Dissertation
submitted to the
Combined Faculties of the Natural Sciences and Mathematics
of the Ruperto-Carola-University of Heidelberg, Germany
for the degree of
Doctor of Natural Sciences

Put forward by
M.Sc Benjamin Hendricks
Born in: Seeheim-Jugenheim, Germany
Oral examination: November 11th 2015

Reading the Chemical Evolution of Stellar Populations in Dwarf Galaxies

Referees: PD. Dr. A. Koch
Prof. Dr. R. Klessen

Abstract

In this thesis I present observations and analyses addressed to understand the individual evolution of dwarf galaxies and the interdependency with their local environment. My study focuses on the Fornax dwarf spheroidal galaxy, which is the most massive galaxy of its type in the Local Group, hosting stars with a broad range in age and metallicity. Additionally, it is the only intact dwarf spheroidal with an own globular cluster system. Therefore, it provides a superb laboratory to gain insights about the formation and chemical enrichment processes of baryonic matter in Galactic halos. In particular, I have used individual alpha-element abundances obtained from high-resolution spectra to characterize, for the first time, the chemical evolution of Fornax over its entire age and find a surprisingly low early chemical enrichment efficiency with respect to other dwarf galaxies. Comparison with chemical evolution models show that Fornax must have experienced a systematically increasing star formation efficiency with time in order to bring the observations in agreement with the model predictions. One emerging evolutionary scenario is that Fornax experienced major accretion events in the past, so that its current properties are not indicative of the chemical enrichment environment at ancient times. A similar chemical analysis for the globular cluster H4 and nearby field stars in Fornax reveals, that H4 is depleted in all analyzed alpha-elements and falls on top of the observed field star [α/Fe] sequence, while its abundance pattern disagrees with the properties of Milky Way halo field stars and clusters. Thus, I propose a chemical enrichment coupling of the globular cluster population and field stars in Fornax. This finding provides tight constraints on the origin of alpha-depleted globular clusters in the Milky Way and will enable the chemical enrichment characterization of distant galaxies from integrated-light cluster analysis where field stars are too faint for detailed chemical analysis.

In dieser Arbeit werden hochaufgelöste Spektren von Sternen in Zwerggalaxien analysiert, mit dem Ziel die Evolution dieser Galaxien und deren Interaktion mit ihrer direkten galaktischen Umgebung zu verstehen. Im Mittelpunkt der Analyse steht Fornax, eines der massereichsten Systeme seiner Art, mit einer komplexen Population an Feldsternen und einem eigenen System an Kugelsternhaufen. Diese Konstellation bietet ideale Voraussetzungen, um entscheidende Erkenntnisse über die chemische Entwicklung von Sternen und Sternhaufen in Galaxien zu sammeln. Hierzu wurden im Speziellen chemische Häufigkeiten aus der Alpha-Elementgruppe ermittelt. Daraus konnte erstmalig die chemische Entwicklung von Fornax über dessen gesamte Entwicklungsgeschichte rekonstruiert werden. Das Resultat der Untersuchung ergab eine überraschend ineffektive chemische Entwicklung zu frühen Zeiten im Vergleich zu Galaxien ähnlicher Konstitution. Ein Vergleich mit Modellen für chemische Anreicherung ergab, dass eine stetig anwachsende Anreicherungseffizienz nötig ist, um die beobachteten Charakteristiken in Fornax mit Modellvorhersagen in Einklang zu bringen. Ein sich daraus ergebendes Entwicklungsszenario ist die Verschmelzung von mehreren Sub-Fragmenten, deren individuelle chemische Entwicklung zunächst unter anderen Bedingungen erfolgen konnte als die jetzige Galaxie. Des weiteren wurde die chemische Anreicherungscharakteristik von Kugelsternhaufen in Fornax untersucht. Ich konnte zeigen, dass deren chemischer Fingerabdruck mit dem der Muttergalaxie übereinstimmt, und nicht dem Muster von Sternhaufen oder Feldsternen in der Milchstrasse folgt. Die daraus abgeleitete Schlussfolgerung, dass Kugelsternhaufen als Marker für die chemische Entwicklung ihrer Muttergalaxie verwendet werden können, ermöglicht neue, detaillierte Erkenntnisse über die Herkunft von Kugelsternhaufen in der Milchstrasse, und kann darüber hinaus als Diagnostik in weit entfernten Galaxien verwendet werden, deren individuelle Sterne zu leuchtschwach sind.

Contents

List of Figures

List of Tables

Acknowledgements

Zu allererst möchte ich Dir danken, lieber Andreas, für die wohldosierte wissenschafltiche Betreuung, für Deine flexible Interpretation von Kernarbeitszeiten, und für alles was Du mir ermöglicht hast. Ich weiss nicht wie, aber Du hast es immer geschafft die Peitsche im Zuckerbrot zu verstecken. For the help in supervising and/or refereeing my work, I would also like to thank Norbert Christlieb, Ralf Klessen, Glenn van de Ven, Luca Amendola, and Avon Huxor.

The Landessternwarte has always been a place I enjoyed working at. For this, I would like to thank:
Matthias, für deinen Humor und die Art und Weise wie du die Dinge ins rechte Licht rückst. Hans, für die vielen Diskussionen über astronomische Probleme. Es war grossartig, dass Du immer ein offenes Ohr für alles hattest; und immer etwas zu erzählen. Holger Mandel, for having an eye on the non-profit part and the heritage of the LSW. Anders, running the bar with you was great fun! Christian Fendt, für die Barbecues und die ruhige Hand mit der Du die IMRPS führst. Ulla Anslinger, für Ihre unkomplizierte Abwicklung des administrativen Papierkrieges, und Ihre endlose Geduld mit meinem Unvermögen diesen zu gewinnen.

Scattered over the wold, there are people who bring sunshine to my day. Thank you:
Racin' Masen, for being the best. I really cannot think of anything dark you couldn't turn into bright. Mike The-One Palmer and Melissa, for serving as our first address in Canada. Evan and Jumbo, for the whiskey and philosophy at rattlesnake-rock. Felix, für deine Ehrlichkeit und die vielen Worte. Raphael, chèr ami, for riding the kayak with me between mountains and whales. Rika, dafür dass du mit mir den Teufel höchtpersönlich zur Weissglut getrieben hast. Nikolay, for the ultimate snowshoe adventure, and for letting me win at darts from time to time. Ron, für dein Universum ausserhalb der Astronomie. Ryan, for caring and calling the police when I seemed lost in the mountains. Finally, THEZONE.FM and BERMUDAFUNK, for providing seriously good music.

Dear hockey gang: Jochen, Ute, Jane, Eric, Lucas, Sebastian, Simon, David, Patrick, Pavel, Johannes, Wolfgang, Wei, und Kai. This team helped me through the first cold winter in Heidelberg. You guys become a family.

Mama und Papa, ihr seid mein Seil und doppelter Boden, ich danke euch für so viel. Auch im Namen der Katze.

Kleine Katze, schnurr, brr, mau, mrrr. Du verstehst schon.

Katrin, you are my house, my garden, and my thunderstorm.

Für Dich, der Du die Sterne bewunderst in der Nacht. Für Dich, den Verrückten, der verrückt lebt, verrückt redet, und alles auf einmal will, der nie gähnt oder Phrasen drischt, sondern wie ein Römisches Licht die ganze Nacht lang brennt, brennt, brennt.

1

Introduction

`“Ah! if poets could vanquish space, explore the planets, discover other worlds, other beings; vary unceasingly for my mind the nature and form of things, convey me constantly through a changeful and surprising Unknown, open for me mysterious gates in unexpected and marvellous horizons, I would read them night and day.”`

– Guy de Maupassant

It was not before 1918, when our Galaxy, the Milky Way (MW), was first measured by Harlow Shapley using variable stars in globular clusters as standard candles, which placed us, the human observer, at an estimated distance of 10 kpc to the center of a flattened spiral galaxy spanning more than 30 kpc in space. This picture has been refined rapidly (and is still being refined) with the improvement of telescope-, instrument-, and computational capabilities, so that by now the structure and composition of the MW is known to great detail. However, less is known about how the picture of visible baryonic matter we observe today gradually fell into place. The fundamental principles of large-structure assembly is no more understood than the governing physics which regulate the evolution of galaxies. Specifically, it is not clear how the individual components of our Galaxy (i.e., bulge, discs, halo) have been formed, and what were the initial building blocks. At the same time, we do not know if the local case study of the MW serves as a representative, universal concept, or whether the observed picture is instead a rather unique outcome resulting from complex interactions within its specific environment. The goal of this thesis is to improve our understanding of galactic structure formation and its subsequent evolution through the observations of galaxies, and in particular through the investigation of stars that reside within dwarf galaxies in the halo of the MW.

1.1 A Zoo in the Galactic Halo

The halos of our Galaxy and its neighbour, the Andromeda Galaxy, are inhabited by a variety of different kinds of satellite stellar systems in varying numbers with different morphology and intrinsic properties. For observational astronomers these objects provide a unique opportunity to study, from the outside, self-contained stellar systems in direct proximity. The satellites of the MW are fully resolved into individual stars. The brightest amongst them provide sufficient light to feed high-resolution spectrographs and hence reveal detailed chemical abundances and high-precision dynamical information. The photometric properties can be studied from the much fainter stars on the main sequence of their evolution, yielding the ages of individual members and consequently details about the star formation history of the system. Thus, each individual stellar population provides unique insights into the formation and evolution of the individual stars and their combined entity.

1.1.1 Stellar Populations and their Observed Properties

The satellites of the MW can be separated into galaxy-like systems and globular-cluster-like systems, where the former group is distinct from the latter by having a larger physical extent at a given total luminosity. In other words, the cluster-like systems are denser (see Figure 1.1).

Cluster-like Systems

Classical *globular clusters* (GCs) are the densest stellar systems known, and typically contain stars with the combined luminosity of $\sim 10^5 - 10^6\,M_\odot$ (Harris 1996). They belong to the oldest objects in the universe with ages mostly $\geq 10\,\mathrm{Gyr}$, and consist of essentially a single stellar population with negligible spread in age and/or heavy element abundances. However, today it is well established that GCs host at least two sub-populations with a significant spread and (anti-)correlation between various light elements (e.g. Gratton et al. 2004, Gratton et al. 2012 and references therein). Therefore it is likely that these systems had a more complex formation history than at first indicated by their apparent coeval stellar population. GCs are generally pressure supported systems with a varying degree of rotation (van de Ven et al. 2006, Lane et al. 2011, Kacharov et al. 2014) and no significant contribution of Dark Matter (DM). The MW also hosts some "oddballs" with similar structural and dynamical parameters compared to classical GCs but with some spread in heavy elements amongst the stars, or with some measurable spread in age (e.g. M22, M54, NGC 2419, ωCen; Cohen 1981, Da Costa et al. 2009, Mucciarelli et al. 2012, Johnson & Pilachowski 2010). These outliers display similar structural characteristics to the recently discovered *ultra-compact dwarf galaxies* (UCDs), found in nearby galaxy clusters (Hilker et al. 1999), as well as to systems classified as *galactic nuclei* at the center of elliptical galaxies (Côté et al. 2006). It is therefore possible that these three groups of objects share a common origin, and that the peculiar cluster-like systems in the halo of the MW are the stripped cores of now dissolved galaxies (e.g., Bassino et al. 1994, Bekki et al. 2001, Bekki & Freeman 2003). Since very recently, the apparent gap in structural parameter space between classical giant elliptical galaxies and GCs becomes populated with the discovery of various *transition type* objects (e.g. Norris et al. 2014, Laevens et al. 2015), and thus the contrast between the initially distinct groups becomes more and more blurred.

Galaxy-like Systems

Satellite galaxies in the MW appear in two different forms: the *dwarf irregular* galaxies (dIrrs) are found at large distances ($\geq 250\,\mathrm{kpc}$) and, as indicated by the name, display an irregular morphology, including bulge- or bar-like components. They have total luminosities of $\geq 10^7 L_\odot$ (Mateo 1998) and harbour large amounts of neutral hydrogen in which stars are actively formed. Star formation histories, derived from deep photometric surveys, indicate that stellar populations formed continuously or in bursts from $\sim 12\,\mathrm{Gyr}$ until today (e.g., Cole et al. 2014), and hence it is likely that dIrrs originate from the first epoch of galaxy formation subsequent to the Big Bang.

The *dwarf spheroidal* galaxies (dSphs) display a quite different picture. Unlike dIrrs, dSphs are typically located closer to the host galaxy ($\leq 300\,\mathrm{kpc}$) and thus can be clearly associated with either the MW or M31 (McConnachie 2012). Similar radial separations have been found in clusters and groups of galaxies outside the Local Group like CenA or Sculptor (Karachentsev 2005, Tully et al. 2015). Dwarf spheroidals have luminosities of $\sim 10^7 L_\odot$ (Mateo 1998) and are symmetric in shape with an elliptical form. Although their oldest stellar populations are of comparable age to GCs and dIrrs, in contrast to the latter they do not contain any measurable amounts of gas and consequently do not show any star formation activity. Therefore, dSphs are defunct galaxies with a completed star formation history and chemical evolution. Their star formation activity is limited to a finite period and lasted only a few Gyr for the smallest systems while it continued almost until today for the most massive galaxies (Weisz et al. 2014). Dynamical studies have shown that dSphs are pressure supported and embedded in a massive DM halo, which dominates the dynamical properties—and possibly the chemical evolution—of these galaxies (Walker et al. 2009b). Given their small distances and great ages, dSphs likely have completed one or several orbits around the MW during their lifetime, which makes them specifically interesting objects to study the environmental impact on galaxy evolution.

Owing to the immense data provided by extensive sky surveys (e.g., SDSS, DES, or Pan-STARRS), over the last view years extremely sparse and faint galaxies have been discovered (e.g., Willman et al. 2005, Koposov et al. 2008 Belokurov et al. 2010, Laevens et al. 2015), with $L \sim 10^3 L_\odot$, and hence with total luminosities marginally brighter than a single supergiant star. These dim objects have tentatively been named *ultra faint galaxies* (UFDs). In average they are located even closer to the MW than the dSphs (McConnachie 2012), an effect which is possibly caused by a selection bias, as more distant UFDs are likely to have escaped detection. Photometry paired with spectroscopic information shows that stars in these galaxies are exclusively old, but with some spread in age and metallicity (Brown et al. 2012, Kirby et al. 2015). Their similar morphological and chemical properties to dSphs may be an indication that UFDs are simply the natural extension of the very same object to lower luminosities and sizes, coming into view owing to advancing telescope power, instrument sensitivity, and statistical detection methods.

With regard to the above considerations, it is important to note that there is no accepted convention about how many types of different stellar systems exist, and about the observational properties that should be used to assign a specific system to one type or the other. It seems likely that at least some of the classifications do not demarcate an intrinsically unique type of object, but rather reflect a specific evolutionary stage of some other type, whose properties have been either altered by time through internal feedback, or by interactions with its environment. As an example, dSphs and dIrrs may emerge from a similar primordial type of galaxy, but while the remoter systems evolve in relative isolation and are observed as irregulars, the satellites close to a massive host may loose their gas through environmental interactions such as ram-pressure stripping and evolve to spheroidals.

1.1.2 Predictions from a ΛCDM Universe

Lambda Cold Dark Matter (ΛCDM) is the commonly accepted fundamental cosmological framework for the evolution of space and the formation of galaxies within it. It implies two “dark” components, one in form of energy (Λ) and the other in form of matter (DM). While the dark matter component contribute about 25% to the total energy budget in the universe, the dark energy is estimated to be responsible for about 70% (Planck Collaboration et al. 2014). This leaves not more than $\sim 5\%$ for luminous baryonic matter, the only building block we experience in our daily lives and which we can observe directly with astronomical facilities. Although the dark components currently cannot be described in any more detail except their impact on the universal and local energy and

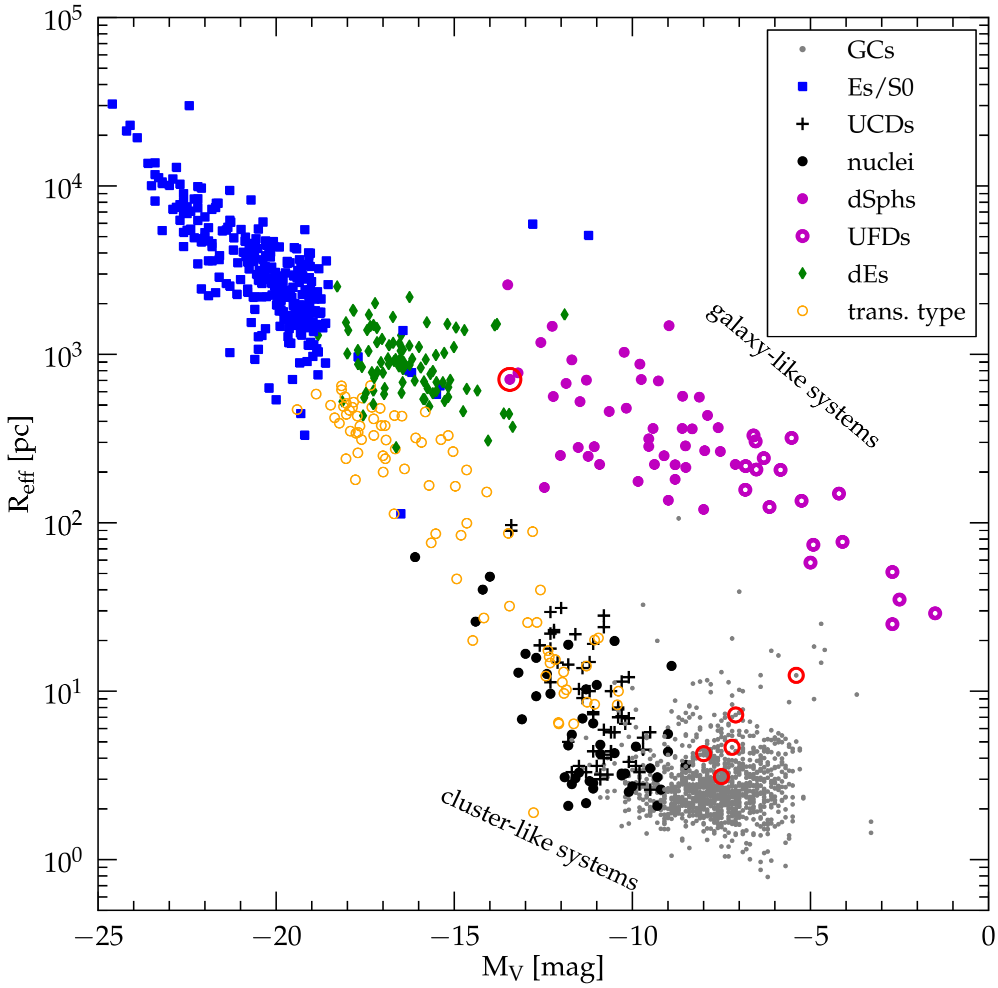

Figure 1.1: Effective radius (R_{eff}) versus absolute V-band magnitude for pressure supported stellar systems. The Figure incorporates data from Misgeld & Hilker (2011), Norris et al. (2014), and references therein. In addition to the dynamically hot systems, the typical location of dIrr galaxies is indicated. The Fornax dSph galaxy and its five GC systems play the central role in this thesis and are highlighted with red circles.

mass balance, the concept of ΛCDM has proven remarkably successful in describing and predicting various processes, e.g., the evolution and structure formation in the early universe (Moore et al. 1999, Madau et al. 2001), or the chemical fusion processes in the first minutes after the Big Bang. Today, most N-body simulations that aim to model the large-scale evolution of structure and galaxy formation over a Hubble time therefore adopt ΛCDM (e.g., Springel et al. 2008). Such simulations enable us to vision the assembly statistics and evolution of galaxies over many magnitudes in mass and over evolutionary significant timescales (i.e. billions of years). Individual subcomponents can be modelled in greater detail to account for gravitational interactions between dark- and baryonic matter as well as hydrodynamical feedback between the baryons (Diemand & Moore 2011). In this way, predictions for galactic environments comparable in size to the Local Group can be made and compared with the observed picture obtained from the visible baryonic component within this framework (e.g., Oñorbe et al. 2014). The outcome of such simulations have shaped significantly our current perception on galactic structure formation.

Numerical simulations within a ΛCDM framework predict a strictly hierarchical growth of structure. At first, matter assembles by the merger of primordial DM overdensities. These gravitational agglomerations then form the first galaxies by accreting and binding baryons within their environment (White & Rees 1978). Importantly, the models predict that galaxies as massive as our MW cannot form through a monolithic collapse within a single massive halo as originally proposed by Eggen et al. (1962). In contrast, they *grow* by merging with—and accretion of—smaller units. The satellite galaxies we observe today in the Galactic halo may be the very remnants of these initial building blocks.

The above described bottom-up assembly of massive galaxies should leave a wealth of observational traces in the morphological, dynamical, and chemical signatures of both the MW and its satellite systems (Moore et al. 1999, Bullock & Johnston 2005, Johnston et al. 1996). A great interest has grown therefore in analyzing the observed properties of Local Group stars and stellar systems, searching for merging signatures, and interpreting the results with respect to the cosmological model; an area which is now called *near field cosmology*.

This way it has been found that, while a ΛCDM universe is in good agreement with the observed (baryonic) large scale structure (e.g., Wambsganss et al. 2004), disagreements emerge on smaller scales, challenging the general concept, or at least its fine-tuning. For example, the number of observed satellite systems associated with the MW (or M31) is smaller by at least one order of magnitude compared to what is predicted from simulations, the so-called *missing satellite problem* (Kauffmann et al. 1993): the MW only hosts a few tens of dwarf galaxies, while ΛCDM predicts a number in the order of 10^3. This discrepancy has evoked much interest, and considerable effort has been put to explain the missing satellites, e.g., by large scale reionization (Gnedin & Kravtsov 2006) or baryonic feedback (Governato et al. 2012) that naturally impose a minimum halo mass in order to permanently retain baryons, and thus makes them visible for the observer. Furthermore, in ΛCDM the most luminous satellites naturally reside in the most massive DM halos, and therefore high central velocity dispersions should be expected within the brightest of them. In the MW, however, such high dispersions have not been observed. Thus, it seems that not only the smallest, but also the largest satellites are missing in the Local Group (the *too big to fail problem*; Boylan-Kolchin et al. 2011).

The dwarf galaxies of the Local Group are the closest candidates of cosmological building blocks we can observe. They are resolved in individual stars and bright enough to study their photometric and spectroscopic properties in detail. Therefore they play an important role to assess the cosmological framework of structure formation, and the subsequent evolution of galaxies. As a consequence, these galaxies also provide the key to understand the properties and evolution of the MW (e.g., Helmi et al. 2006).

1.2 The Galactic Kitchen: How Elements Form and What They Can Tell

The fundamental building block for all chemical elements is a proton, i.e., an ionized hydrogen core (H^+). The fusion to heavier species with larger atomic numbers Z and mass numbers A are exothermic reactions (until ^{56}Fe, which has the highest binding energy of all elements) and produce considerable amount of energy because the mass of the fused product is less than the sum of the original particles: $E = \Delta mc^2$. However, for fusion to be ignited, the atom's charge barrier has to be overcome, which requires a combination of high temperature and density.

The recycling of fused elements to the interstellar medium (ISM) can happen during either stellar evolutionary stages (stellar winds), or during the explosion of the star in a core-collapse- or thermonuclear Supernova (SN II and SN Ia, respectively). While the detailed abundance yield depends on the mass and the pre-enrichment of the star itself, the net-effect is always an increase of the mean metallicity $\langle Z \rangle$[1] of the ISM into which the materials have been recycled to. This process is called *chemical enrichment*.

The chemical species in stars (and elsewhere) as we observe them today have been formed through two fundamentally different and chronologically distinct processes: the *Big Bang Nucleosynthesis* (BBN) and the *fusion processes within stars*. A separation should also be made between fusion processes that occur in hydrodynamical equilibrium in the interior of stars where the mechanical balance of temperature and pressure determines the reactions, and those that are ignited during out-of-equilibrium events, such as SN explosions, in which case the physics of the explosion also has impact on the chemical yield.

From evolutionary models of stars and their nucleosynthetic yield, we know that the fusion products within a star depend on the initial ratio of ^{1}H to ^{4}He (mainly through the mean molecular weight μ), and therefore our understanding of the two major chemical enrichment mechanisms are interdependent and eventually tightly linked to the adopted cosmological model.

Big Bang Nucleosynthesis

In the hot Big Bang model, the temperature during the first $\sim$ 15 minutes is high enough to form the first elements heavier than ^{1}H. In the very first second after the Big Bang, no bound particles exist and the proton-to-neutron ratio is maintained in thermal equilibrium. As the temperature steadily drops with the expansion of the early universe, these weak interactions stop and, in a first step, deuterium (^{2}H) is formed from a proton through the capture of a free neutron. Subsequently, further reactions proceed to produce helium nuclei (^{3}He and ^{4}He) through proton- and neutron-capture, as well as traces of lithium (^{7}Li) either directly through the capture of ^{4}He from ^{3}H, or via the decay of ^{7}Be. The net reactions of BBN therefore are

BIG BANG NUCLEOSYNTHESIS

$$^1\mathrm{H} + \mathrm{n} \longrightarrow {}^2\mathrm{H} + \gamma$$

$$^2\mathrm{H} + {}^2\mathrm{H} \longrightarrow {}^4\mathrm{He} + \gamma$$

$$^3\mathrm{H} + {}^4\mathrm{He} \longrightarrow {}^7\mathrm{Li} + \gamma$$

Then, with the ongoing expansion of the universe, the temperature continuously drops below the limit for further reactions to take place, and the primordial BBN yields are conserved. The detailed relative abundances depend upon the cosmological parameters that define the exact conditions, and is, amongst others, sensitive to the fraction of neutrons that can be initially bound to ^{2}H. Observations estimate relative fractions of (H, He, Li) = (0.75, 0.25, $\sim 10^{-9}$), in overall good agreement to model predictions (Coc et al. 2012)[2]. All elements heavier than ^{7}Li have to be formed exclusively within the lifecycle of stars.

Stellar Nucleosynthesis

While the detailed chemical processes within stars—as well as their final contribution to the chemical enrichment of the ISM (their individual yield)— depend on many factors (such as mass, primordial composition, internal rotation, binary-interaction), all stars with masses $M \geq 0.08 M_\odot$ at first

---

[1] The metallicity $\langle Z \rangle$ denotes the relative mass fraction of all elements heavier than ^{4}He.

[2] The only exception is lithium, for which lower abundances have been observed compared to model predictions.

burn ^{1}H to ^{4}He during their life on the main sequence of their evolution. This process is called *H-burning* and is realized either through the *pp-chain* (proton-proton chain) for stars with $M \leq 1.15 M_{\odot}$ or via the *CNO-cycle* for stars with higher masses.

PP-CHAIN 0

$$^{1}\mathrm{H} + {}^{1}\mathrm{H} \longrightarrow {}^{2}\mathrm{H} + \mathrm{e}^{+} + \nu_{e}$$
$$^{2}\mathrm{H} + {}^{1}\mathrm{H} \longrightarrow {}^{3}\mathrm{He} + \gamma$$

PP-CHAIN I

$$^{3}\mathrm{He} + {}^{3}\mathrm{He} \longrightarrow {}^{4}\mathrm{He} + 2\,{}^{1}\mathrm{H}$$

PP-CHAIN II

$$^{3}\mathrm{He} + {}^{4}\mathrm{He} \longrightarrow {}^{7}\mathrm{Be} + \gamma$$
$$^{7}\mathrm{Be} + \mathrm{e}^{-} \longrightarrow {}^{7}\mathrm{Li} + \nu_{e}$$
$$^{7}\mathrm{Li} + {}^{1}\mathrm{H} \longrightarrow 2\,{}^{4}\mathrm{He}$$

PP-CHAIN III

$$^{3}\mathrm{He} + {}^{4}\mathrm{He} \longrightarrow {}^{7}\mathrm{Be} + \gamma$$
$$^{7}\mathrm{Be} + {}^{1}\mathrm{H} \longrightarrow {}^{8}\mathrm{B} + \gamma$$
$$^{8}\mathrm{B} \longrightarrow {}^{8}\mathrm{Be} + \mathrm{e}^{+} + \nu_{e}$$
$$^{8}\mathrm{Be} \longrightarrow 2\,{}^{4}\mathrm{He}$$

CNO-CYCLE

$$^{12}\mathrm{C} + {}^{1}\mathrm{H} \longrightarrow {}^{13}\mathrm{N} + \gamma$$
$$^{13}\mathrm{N} \longrightarrow {}^{13}\mathrm{C} + \mathrm{e}^{+} + \nu_{e}$$
$$^{13}\mathrm{C} + {}^{1}\mathrm{H} \longrightarrow {}^{14}\mathrm{N} + \gamma$$
$$^{14}\mathrm{N} + {}^{1}\mathrm{H} \longrightarrow {}^{15}\mathrm{O} + \gamma$$
$$^{15}\mathrm{O} \longrightarrow {}^{15}\mathrm{N} + \mathrm{e}^{+} + \nu_{e}$$
$$^{15}\mathrm{N} + {}^{1}\mathrm{H} \longrightarrow {}^{12}\mathrm{C} + {}^{4}\mathrm{He}$$

Above central temperatures of 10^{8} K, ^{4}He will additionally burn into ^{12}C through the *triple alpha-process*, or *He-burning*. This happens for all stars heavier than $0.5 M_{\odot}$.

TRIPLE-ALPHA

$$^{4}\mathrm{He} + {}^{4}\mathrm{He} \longrightarrow {}^{8}\mathrm{Be}$$
$$^{8}\mathrm{Be} + {}^{4}\mathrm{He} \longrightarrow {}^{12}\mathrm{C}$$

Eventually, heavier elements are formed through subsequent higher levels of fusion (*C-*, *N-*, *Ne-*, *O-*, and *Si-burning*), which, however, can only take place in stars with main-sequence masses above $\sim 8 M_{\odot}$. As a consequence, the chemical yield from stars in the lower mass regime (below $8 M_{\odot}$) is characterized by a significantly different chemical abundance pattern as compared to the enrichment signature of massive stars, with a tightly constraint mass limit between the regimes.

^{56}Fe is a cornerstone for stellar fusion processes, as it holds the highest binding-energy per nucleon of all elements and consequently provides the condition of lowest energetic potential amongst all nucleons. Therefore, if temperatures are high enough ($\sim 5 \times 10^{9}$ K), a state of nuclear statistical equilibrium is reached in which all lighter elements are transformed preferentially into ^{56}Fe through explosive Si-burning or the alpha-rich freezeout. Such temperatures are only reached in the core of the most massive stars or during a SN explosion of type I and II, which both produce about equal amounts of ^{56}Fe in time, if their relative rates of occurrence are taken into account (Woosley & Weaver 1995).

Elements above the iron-peak group (which, besides Fe, includes ^{42}Sc and all nuclei between $23 \leq Z \leq 30$ from ^{46}V to ^{60}Zn) with $Z > 30$ are endothermic constructs and are not effectively produced by reactions between charged nucleons. Their main production path involves the capture of neutrons. Individual isotopes are either formed through slow accumulation of neutrons in irregular alternation with β-decay of unstable species (*s-process*), or a rapid capture (*r-process*) when the density of free neutrons is high, and the capture process can happen on timescales faster than that of the β-decay.

1.2.1 Groups of Elements

Different chemical elements form through different nucleosynthetic pathways and on different timescales. If the precise formation channels of the individual species are understood, their abundance pattern in stellar atmospheres can be used to learn, e.g., about the chemical enrichment, age, and origin of the stars, the mass distribution of the enriching progenitors, and eventually to read the chemical evolution of the stellar system they belong to. Depending on the element and the evolutionary phase of the star, the observed chemical abundance either reflects the pure composition of the material it has formed from, or may incorporate internal fusion products (i.e. processed protostellar material) that have been mixed (dredged-up) to the surface of the star.

H and He are considered as *primordial elements*, since they are the only species produced to significant amounts outside of stars during the BBN.

The *light elements* (e.g. C, N, O, Na, and Al) have different formation sites, but many are formed during H-, He-, or C-burning in massive stars. Several of these elemental abundance can change during the evolution of a star due to the dredging-up of processed material from deeper layers or the exchange of such material in close binary systems.

The *alpha-elements* are those nuclei which are formed through the capture of one or several ^{4}He, also known as alpha-particle. Alpha capture takes place in all burning stages higher than H-burning, using ^{12}C as an initial seed, and produces a sequence of alpha-species ,e.g.,

$$^{12}\mathrm{C}(\alpha,\gamma)^{16}\mathrm{O}(\alpha,\gamma)^{20}\mathrm{Ne}(\alpha,\gamma)^{24}\mathrm{Mg}(\alpha,\gamma)^{28}\mathrm{Si}(\alpha,\gamma)^{32}\mathrm{S}(\alpha,\gamma)^{36}\mathrm{Ar}(\alpha,\gamma)^{40}\mathrm{Ca}(\alpha,\gamma)^{44}\mathrm{Ti}.$$

Elements with higher Z mainly form through different channels, and are not part of the alpha-group of elements. Of interest in the understanding of galactic chemical evolution are mostly O, Mg, Si, Ca, and Ti, as those elements produce strong absorption features in the optical or near-infrared spectra of relatively cool stars belonging to the main sequence or the red giant branch.

Iron-peak elements include, beside Fe, ^{42}Sc and all nuclei between $23 \leq Z \leq 30$ from ^{46}V to ^{60}Zn). Similar to Fe, they are mainly and to great amounts produced in nuclear statistical equilibrium during SNe explosions when temperatures are sufficiently high. Since iron-peak elements (and specifically the easily observable Fe) are the natural endpoint of any nuclear fusion process, they are not reprocessed to higher elements in subsequent generations of stars. Thus, the iron abundance accumulate over time. The [Fe/H][3] in a star can therefore be used as a first order proxy for the star's relative age compared to other stars within the same galaxy, or, strictly speaking, within an environment that experiences the same chemical enrichment efficiency. Because SN of type Ia emerge from low-mass progenitors (with at least one white dwarf involved), iron-peak elements are the only species heavier than ^{16}O that are produced to significant amounts in stars well below $\sim 8M_{\odot}$.

---

[3] The bracket notation expresses the logarithmic ratio between the number of atoms per unit volume for two elements A and B relative to the sun: $[\mathrm{A/B}] = \log(N_A/N_B)_{star} - \log(N_A/N_B)_{\odot}$.

Heavy elements (or neutron-capture elements) with $Z > 30$ are endothermic fusion products and are not effectively produced by reactions between charged nucleons. Isotopes are formed through capture of neutrons during the s-process and r-process. Most heavy elements are formed through both production channels, but there are some species that can be produced almost exclusively through s-process reactions (e.g., Sr, Y, Ba), or by rapid neutron capture (e.g., Eu, Dy).

1.2.2 Reading the Chemical Signatures of the Alpha-Elements

The alpha-elements are an important tool to understand the detailed chemical enrichment history of stars and clusters in galaxies. In order to produce alpha-elements, a star must experience advanced fusion processes, and, as a consequence, these elements are almost exclusively produced in high-mass stars ($M \geq 8M_{\odot}$) and injected to the ISM during core-collapse SN II events. Massive stars have short lifetimes of not more than $\sim 50\,$Myr, and hence recycle the processed material to the galactic ISM almost instantaneously. In contrast, SNe of type Ia produce primarily iron-peak elements (only $\sim 2\%$ of the alpha-elements are produced in SNe Ia, if the relative rate of occurrence is taken into account) and may not contribute to a system's ISM for the first billion years after a generation of stars have been formed. Thus, the [α/Fe] ratio in a star is a way to trace the relative contributions from SN II to SN Ia products in the ISM. As a result, the [α/Fe] ratio is enhanced for the first, oldest and metal-deficient stars and subsequently drops with time and increasing [Fe/H] as soon as SNe Ia start to contribute significantly to the enrichment, seen as a *knee* in the abundance ratio (called the *time-delay model*; Tinsley 1979). Consequently, the evolution of [α/Fe] vs [Fe/H] reveal the extent to which the galaxy can enrich its ISM before SNe Ia set in, and hence is a measurement for the *chemical enrichment efficiency* of the system (Matteucci & Brocato 1990, Lanfranchi & Matteucci 2003).

The individual alpha-elements are all built during the evolution of massive stars, and hence display a similar evolution as a function of [Fe/H]. Therefore, in order to increase the effective precision of the derived abundance values, it can be helpful to combine several alpha-elements into a mean abundance ratio, so that $\alpha = \sum_{i=1}^{n} (\alpha_i)/n$.

Their exact nucleosynthetic origin, however, differs; O and Mg are produced through He-, C-, and Ne-burning during hydrostatic equilibrium (i.e., during mechanical balance of radiation pressure and gravity) and the production of these elements is therefore only governed by the initial stellar parameters (Woosley & Weaver 1995). In contrast, Si and Ca form during hydrostatic and explosive O-burning and hence are created at significant amounts within the SN event itself. Their abundance therefore not only depend on the stellar parameter but also on the physics of the explosion itself which may yield to differences compared to the hydrostatic elements, and to some intrinsic scatter in [α/Fe] at a given [Fe/H]. Moreover, Ti is only an alpha-like element, because it is not synthesized through the subsequent captures of alpha-particles but has its main formation site during explosive Si-burning and in the alpha-rich freezeout during the SN explosion. It thus behaves like an alpha-element and can be used to analyze galactic chemical evolution (e.g., Nissen & Schuster 2010, Boeche et al. 2014), but is sometimes also referred to as a member of the iron group (Timmes et al. 1995).

In addition to the outlined differences amongst individual alpha-elements, the explosive species Ca, Si and Ti may also be produced during SN Ia explosions (Tsujimoto et al. 1995), although the exact yield ratios are not known. In contrast, the hydrostatic elements O and Mg are exclusively produced in SN II, with only negligibly small yields from SN Ia (Tsujimoto et al. 1995, Nomoto et al. 1984, Maeda et al. 2010). Combining the above considerations, the exact [α/Fe] abundance ratio and the observed trend with [Fe/H] can show some intrinsic differences between individual elements, and it is good practice to interpret them as individual tracers, and not to use the individual species interchangeably.

1.2.3 Internal and Environmental Effects on Chemical Evolution

The above outlined model for the evolution of the alpha-elements is true in an idealized scenario where a homogeneously mixed galaxy resides in an unperturbed DM halo in which the galaxy does not encounter gravitational or physical interactions with its environment or any sort of internal perturbance. The observed reality, however, deviates from this simplified model, and internal and environmental effects have to be considered for the best possible interpretation of the observed chemical properties. In this context it is important to emphasize that the process of chemical enrichment is a combination of both a galaxy's ability to produce chemical elements and its ability to subsequently retain them within the gravitational potential.

- The *star formation efficiency* within a galaxy is the primary determining factor for the [Fe/H] position of the knee in the alpha-element evolution. A higher efficiency enables the galaxy to produce more metals and thus to enrich to larger [Fe/H] before SN Ia set in. In the MW, the star formation efficiency is known to vary with radius and the available amount of gas, and it is likely connected to the density, temperature, and velocity dispersion of the ISM. Thus, it might vary during the evolution of a galaxy. A high star formation efficiency also mildly lifts the abundance of the alpha-enhanced plateau, due to a larger average mass of SN II.

- The *initial mass function* (IMF) indicates the relative distribution of stellar masses in a generation of stars and has impact on the observed chemical properties. Specifically the abundance of the hydrostatic elements O and Mg is correlated with the SN II progenitor mass, and hence a top-light IMF (i.e. an IMF lacking of the most massive stars) produces lower [α/Fe] ratios (e.g., Arnett 1971, Woosley & Weaver 1995). Top-light IMFs have been proposed for dwarf galaxies with the basic argumentation that the size of star-forming molecular gas clouds depends upon the total gas mass within a galaxy. As a consequence, dwarf galaxies cannot produce as massive stars as it is observed for the MW (Weidner & Kroupa 2005, Kroupa & Weidner 2003, Oey 2011). One consequence of a top-light IMF would be an underabundance of O and Mg compared to the explosive alpha-elements within a star. Such patterns have been observed, e.g., in Sagittarius by McWilliam et al. 2013), and proposed as a possible origin for the difference in the observed [α/Fe] between Sagittarius and the MW. However, the IMF cannot explain the existence of the knee, except it actually varies during the evolution of a galaxy. Such variations could be caused, for example, by a change in the available amount of gas, or the metallicity of the ISM, as suggested, e.g., by Kahn (1974).

- Similar to the IMF, the *binary fraction* of a stellar generation is an important parameter for the frequency of SN Ia (e.g., Greggio 2005) and therefore also can alter the chemical evolution sequence of the alpha-elements if it changes with time or amongst galaxies.

- An important aspect in the evolution of dwarf galaxies is the outflow of gas. Such *galactic winds* occur when the thermal energy of the gas overcomes the gravitational potential of the DM halo and remove significant amounts of (potentially) star forming material. Generally, a strong wind restricts the time for chemical enrichment before the gas is fully removed and star formation stops. It has been found that galactic winds are necessary to reproduce the observed chemical properties in many dwarf spheroidal galaxies (Kirby et al. 2013, Romano & Starkenburg 2013). They also play an important role to completely remove the ISM in these systems and make them the gas-free galaxies we observe them today(Lanfranchi & Matteucci 2007). In an [α/Fe] vs [Fe/H] diagram, the intensity of the galactic wind affects the slope of the knee, where a stronger wind results in a steeper slope due to the larger relative contribution of SN Ia compared to the mass of the ISM.

- *Incomplete Mixing* may also play a role in the proper interpretation of chemical abundance evolution (e.g. Marcolini et al. 2008, Leaman 2012). If the expelled material from SN explosions is not distributed evenly within the galaxy but remains locally concentrated, stars forming within such "pockets" may have exotic abundance ratios that do not follow the otherwise observed trends. Such outliers have been found in some dwarf spheroidals (e.g., Koch et al. 2008, Venn et al. 2012) and may constitute 10% or more of an observed sample.

Although dSphs have stellar masses typically $\leq 10^7 M_\odot$, there is a high complexity among their chemical and dynamical properties (e.g., Grebel et al. 2003, Tolstoy et al. 2009). Recently, Weisz et al. (2014) have found significant scatter in the SFH of Local Group dSphs, even if only galaxies of otherwise similar characteristics are compared, which indicates that a diversity of environmental influences must have had significant impact on the evolution of theses systems. That environmental effects happen between the MW and its satellite companions is best seen in the case of the now-disrupting Sagittarius dwarf galaxy (Ibata et al. 1995). Such interactions can have contrary effects: while tidal- and ram pressure stripping can induce strong galactic winds and thus slow down or even quench star formation in the satellite (Mayer et al. 2006), the accretion of gas or merger events may trigger SF bursts and by that alter the chemical enrichment history. Given their shallow gravitational potentials compared to larger galaxies, dSphs should be most sensitive to such effects, which makes them important testing grounds to understand the frequency and impact of the afore-mentioned external influences. In addition to the "local" case of Sagittarius, environmental effects like ram pressure stripping, tidal stirring and gas inflow have been observed in galaxies within the Fornax and Coma galaxy cluster (see Kormendy & Bender 2012 and references therein) and it seems not to be a question if, but only to which extent they played a role for the galaxies within the much sparser populated Local Group.

However, not all effects (internal and environmental) have been established through observations and/or hydrodynamical and chemical models. While differences in the position of the knee and the level of depletion have been observed in various Local Group galaxies, other, more subtle, effects on the evolution of the alpha-elements like the precise enhancement of the plateau for stars with low [Fe/H], the slope after the onset of SN Ia, or variations in the IMF are still conceptual models and could not (yet) be significantly constrained from current observations.

1.2.4 Chemical Evolution of Dwarf Galaxies: Some Insights and many open Questions

Historically, Wallerstein (1962) discovered that metal-poor MW halo stars showed excesses of Mg, Si, Ca and Ti, relative to Fe; later, Conti et al. (1967) found similar excesses for O. Subsequently, it was proposed that these alpha-enhanced stars formed in an early epoch before SN Ia started to contribute to the chemical mixture of the ISM and thus provide a powerful and sensitive tool to measure the chemical enrichment efficiency in a galaxy and its early chemical evolution (Tinsley 1979). In the coming decades, alpha-enhanced stars at low [Fe/H] and a similar trend with metallicity as it has been observed for the Galactic halo also have been found in the MW disc (e.g., Gratton & Sneden 1987), and bulge (McWilliam & Rich 1994).

However, it was not before the era of 8-m class telescopes and the use of powerful multi-object spectrographs at the beginning of the 21st century, that detailed chemical abundances for stars in dwarf galaxies could be studied (Shetrone et al. 1998, Bonifacio et al. 2000, Shetrone et al. 2003). With increasing sample sizes, it was found that—strikingly—these small galaxies displayed a different alpha-element signature than their larger hosts (Sbordone et al. 2007, Letarte et al. 2006, Koch et al. 2008). Specifically, the observations showed that the alpha-elements deplete earlier (i.e. at lower metallicity) compared to the MW, and subsequently deplete to sub-solar [α/Fe] ratios at high metallicities (see Tolstoy et al. 2009 and references therein). These discrepancies in the chemical properties between the MW and its satellites challenge the simple building-block scenario within a ΛCDM framework, in which significant fractions of the MW should be composed of former dwarf galaxies. In Figure 1.2 the current census of alpha-element fingerprints is shown for individual Galactic Satellites in comparison to the signature observed in the MW.

The currently most popular explanation for this discrepancy follows the concept of the time-delay model and presumes a lower chemical enrichment efficiency for low-mass systems like the MW satellite galaxies. This theory has been bolstered by recent observations, that indicates an extended alpha-enhanced plateau to higher [Fe/H] for the most massive satellites Sagittarius and the Magellanic Clouds, while lower-mass satellites tend to display low alpha-abundances already at low [Fe/H] (e.g. Sbordone et al. 2007, Pompéia et al. 2008, Cohen & Huang 2009, Vargas et al. 2013). Furthermore, this concept seem to match well with the long-established luminosity-metallicity relationship for galaxies over a large range of magnitude (e.g., Lequeux et al. 1979, Skillman et al. 1989), that has been recently extended to the lowest-mass satellite galaxies by Kirby et al. (2013).

However, only very few dwarf galaxies (Sagittarius, Carina, and Fornax) have been studied based on a statistically large sample of member stars in order to characterize their global properties. For *none of these* the chemical evolution could be traced over a major part of their lifetime. For the faintest of these galaxies, the UFDs, only very view, very metal-poor giant stars have been observed, with no clear conclusion about their alpha-enrichment (Gilmore et al. 2013, Vargas et al. 2013). Very recently, similar first attempts have been made for M31 satellite galaxies, but the extremely faint stars and the sparse data did not reveal more than a general discrepancy to the MW halo, and a significant scatter amongst the individual satellites (Vargas et al. 2014). Therefore, until today, the key questions remain unanswered: How does chemical enrichment evolve over the lifetime of dwarf galaxies, and what is the true variety amongst—and within—the individuals? Which mechanisms trigger and sustain the complex and varied star formation and chemical-enrichment histories of these galaxies? And finally: How does that fit into a complete picture of interdependent evolution in the local environment and in a cosmological frame of galaxy evolution?

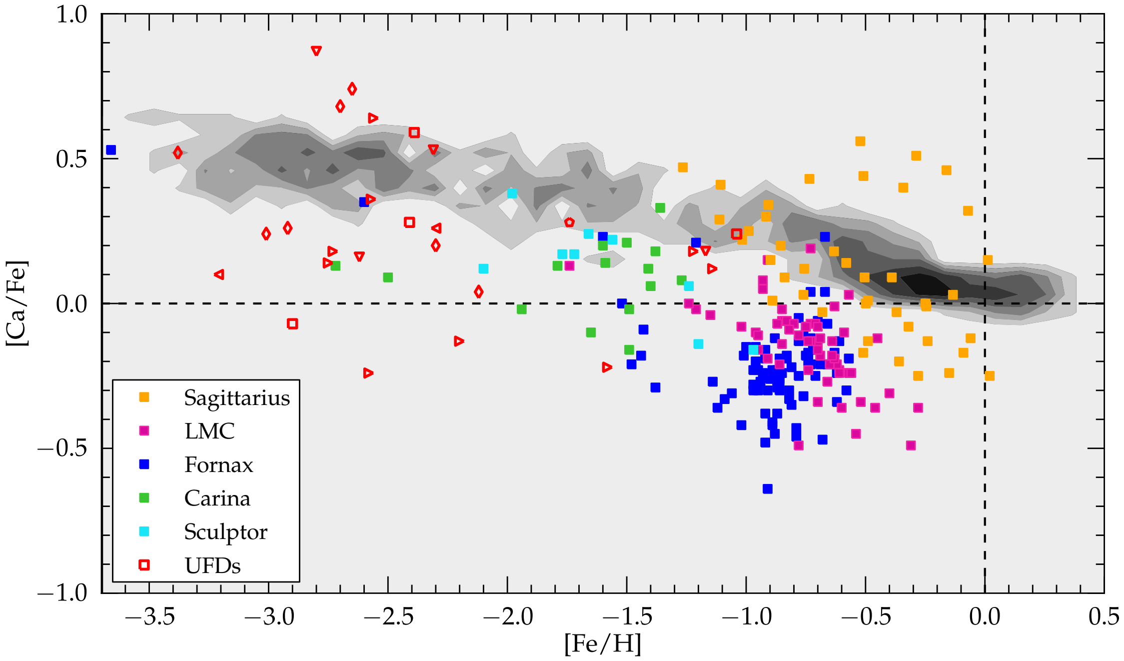

Figure 1.2: Census of existing chemical information for the alpha-element Ca in a compilation of several satellite galaxies of the MW: Sagittarius stars are shown in orange (Sbordone et al. 2007, Carretta et al. 2010a, McWilliam et al. 2013), LMC stars in magenta (Pompéia et al. 2008), Fornax in blue (Letarte et al. 2010, Shetrone et al. 2003, Tafelmeyer et al. 2010), Carina in green (Koch et al. 2008, Shetrone et al. 2003), Sculptor in cyan (Shetrone et al. 2003, Geisler et al. 2005). Several UFDs studied by Vargas et al. (2013) at lower resolution are shown as open circles (Segue I), diamonds (ComBer), squares (Ursa Major II), left-handed triangles (Leo IV), right-handed triangles (Ursa Major I), pentagons (Leo T), and inverted triangles (CVn II). The pattern of MW disc and halo stars are shown as a logarithmically-scaled number density distribution of arbitrary units (data from Venn et al. 2004 and Roederer et al. 2014)

1.3 The Fornax dwarf spheroidal galaxy

Fornax is a key galaxy to understand galactic chemical evolution on small scales. Discovered in 1938 by Harlow Shapley, it is now considered a “classical” dwarf spheroidal galaxy. It is one of the most massive Galactic satellites with $M_V = -13.5$ (see Figure 1.1) some few $10^7\,M_\odot$ (McConnachie 2012) and hosts stars of a broad range of metallicities (Battaglia et al. 2006), embedded in a dark matter halo with mass-to-light ratio of $\sim 10-30$ (McConnachie 2012). Located at an approximate distance of $\sim 140\,\mathrm{kpc}$, Fornax is resolved into individual stars, which therefore become available for photometric and spectroscopic investigation. Previous chemical and photometric studies have shown a complex and extended SFH that includes stars ranging in age from $\sim 12\,\mathrm{Gyr}$ to 250 Myr with a significant SF peak around 3–4 Gyr ago (Stetson et al. 1998, de Boer et al. 2012b, del Pino et al. 2013). The metallicity-distribution-function (MDF) from several spectroscopic studies (Battaglia et al. 2006, Coleman & de Jong et al. 2008) shows distinct peaks in [Fe/H], which can be interpreted as an inhomogeneous, bursty SFH. Battaglia et al. (2006) also found a strong radial metallicity gradient in Fornax, where younger generations of stars with higher [Fe/H] are more centrally concentrated in the galaxy compared to stars with low [Fe/H], which are distributed equally over all galactic radii.

Fornax hosts its own population of five GCs (see Figure 1.3). Four of them are metal-poor with [Fe/H]≤ -2.0 (Letarte et al. 2010), old (Buonanno et al. 1998) and alpha-enhanced (Letarte et al. 2010, Larsen et al. 2012b), and by that resemble typical MW halo clusters. The remaining cluster (named H4, following Hodge 1961) is an outlier in many respects: it is significantly more metal-rich, around [Fe/H]$= -1.4$ (Strader et al. 2003, Larsen et al. 2012b), and possibly younger than the other clusters (Buonanno et al. 1999).

Recent proper motion studies with both ground-based telescopes (Walker et al. 2008, Méndez et al. 2011) and the Hubble Space Telescope (Dinescu et al. 2004, Piatek et al. 2007) agree that the current orbital position of Fornax is close to perigalacticon, which it passed less than 1 Gyr ago. Most of these studies furthermore predict an orbital period of $\sim 6\,\mathrm{Gyr}$, which implies that Fornax experienced at least two full orbits around the MW during its evolution. In contrast to these studies, Méndez et al. (2011) derive a significantly longer orbital period of 21 Gyr paired with an extremely high eccentricity. While the orbital history may play an important role in the evolution of dSphs concerning a potential environmental harassment, the evident discrepancies illustrate the large uncertainty in these properties, in particular for long look-back times.

Although it seems as if Fornax (almost) continuously formed stars during the last $\sim 13\,\mathrm{Gyr}$ (de Boer et al. 2012b), many questions remain unanswered: did Fornax evolve in relative isolation or did it experience merger events (Coleman et al. 2004, Battaglia et al. 2006, Yozin & Bekki 2012, Amorisco & Evans 2012, Bate et al. 2015). There is also discussion about the mixing efficiency within the galaxy and the impact of SF bursts on the ISM. Should one expect to find local inhomogeneities caused by a few individual supernova explosions (Marcolini et al. 2008)? Did Fornax re-accrete and subsequently form stars from some of the gas initially lost in galactic winds (Ruiz et al. 2013, D’Ercole & Brighenti 1999)? Furthermore, it is not clear whether the MW or other environmental influences played an important role in the chemodynamical evolution of Fornax. Has the SFH been influenced by periodic tidal interactions (Nichols et al. 2012)? Did ram pressure stripping, caused by AGN shock shells from the MW in the past, trigger SF bursts and simultaneously remove large quantities of its (former) gas reservoir (Nayakshin & Wilkinson 2013)? Finally, why did Fornax form GCs – while most other dwarfs did not – and why are they not yet dissolved (Peñarrubia et al. 2009)? Consequently, it is not known if and how many stars in the field were in fact stripped from existing GCs or are the remnants of already completely dissolved clusters (Larsen et al. 2012a).

Most of these aspects are clearly not problems specific to the Fornax dSph but concern all satellite systems in the Local Group. Constraining open questions about the evolutionary pathway of Fornax will therefore have a direct implication on our understanding of the nature of dwarf galaxies in general.

1.4 This Thesis

Speaking in simple terms, previous studies have shown that the chemical enrichment *differs* amongst satellite systems and between satellite systems and the MW. We do not know, however, the details of their individual evolution (*how* do they differ?), nor do we know the key-regulating physical parameters that are responsible for the observed variations (i.e., *why* do they differ?).

The work presented here aims to address these critical questions by studying in detail the dynamical and chemical properties of different resolved populations in the Fornax dSph galaxy and interpret the results with respect to the properties observed in other satellite systems of the MW and M31. The results shall help

i) to unravel the individual evolution of satellite galaxies, to understand chemical enrichment within galaxies on small scales, and to connect the mechanisms of the satellite galaxies to the more complex stellar systems, like our MW.

ii) to understand the interdependence between the MW and its dwarf galaxy population with the goal to obtain insights to the build-up of the Galactic halo and, vice versa, the Galactic impact on the evolution of dwarf galaxies.

iii) to constrain the evolution of our Galactic environment and by that contribute to the comprehension of the fundamental underlying cosmological framework.

The analyses are mainly based on spectroscopic observations with *FLAMES* at the Very Large Telescope and *M2FS* at the Magellan Telescope. The observations have been exclusively carried out, reduced and analyzed for this project. Figure 1.3 shows a DSS image of the Fornax dSph, in which I highlight the pointings and fields-of-view of the conducted observing programs.

The results are presented in three main chapters:

In Chapter 2, I uncover and analyze the full chemical evolution of Fornax from its oldest stars to stellar populations younger than $\sim 3\,\mathrm{Gyr}$. The results are put into context to chemical evolution models and the observed field star properties in other dwarf galaxies and the MW. The content is mainly based on the published work by Hendricks et al. (2014a).

In Chapter 3, I present a detailed census for the chemical and dynamical properties of stellar populations in the outskirts of Fornax as compared to the central region of the galaxy. The observed differences *within* the galaxy are used to understand differences *amongst* individual dwarf satellites. The content is mainly based on the published work by Hendricks et al. (2014b).

In Chapter 4, I investigate the chemical signatures of GCs in Fornax in comparison to the field star population, from which we obtain important conclusions on the link between the chemical enrichment of GCs with respect to their host galaxy, and the origin of chemically peculiar GCs in the MW and M31. The content is mainly based on the work by Hendricks et al. (2015, submitted to A&A).

In Chapter 5, I summarize my main findings with respect to the key questions raised during the introduction of this thesis.

Finally, in Chapter 6, the impact of upcoming instruments and telescope facilities is discussed. Moreover, I give an outlook to future work on this topic, emerging from my results and highlight the critical questions to be asked in the future.

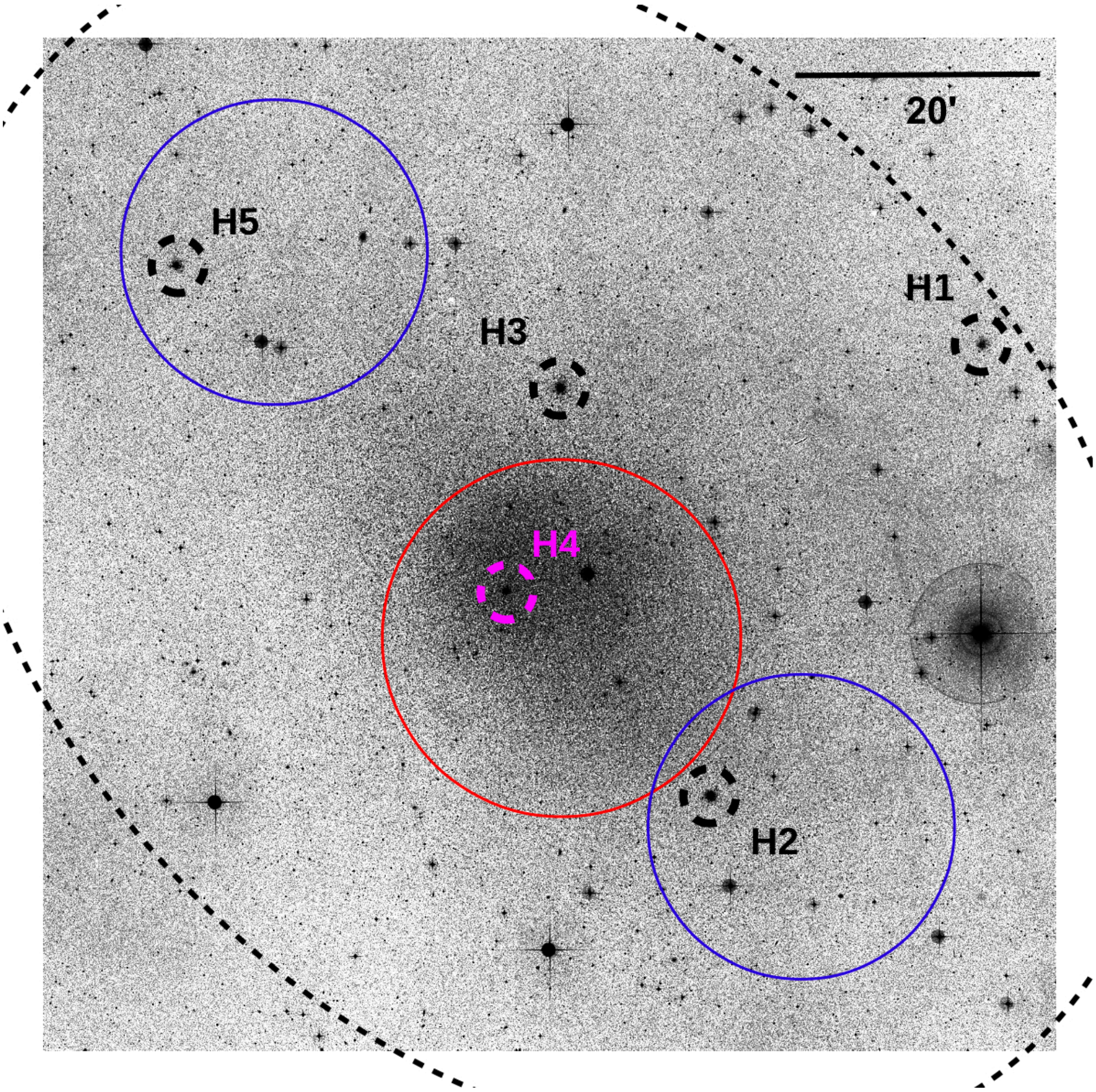

Figure 1.3: DSS image of the Fornax dwarf spheroidal galaxy. The dashed ellipse indicates the tidal radius of the galaxy with a diameter of ∼ 2.3° along the major axis. The position of the five GCs are highlighted. H4 is the cluster located close to the center of the galaxy. We carried out two programs to collect spectroscopic data of individual stars in the galaxy: the blue circles show the approximate pointing and 12.5′ field-of-view of our VLT *FLAMES* observations in the outer parts of the galaxy (presented in Chapter 2 and 3). The red circle indicate the area which we observed with *M2FS* at the Magellan Telescope, covering a radius of 14.65′ (presented in Chapter 4).

2

The Metal-Poor Knee in the Fornax dSph[1]

`“A large rich cluster with remarkable characteristics appears on photographs received from the Boyden Station. Since nothing quite like it is now known, a detailed though preliminary description is given in the following pages...”`

– Harlow Shapley upon his discovery of the first dwarf spheroidal galaxy in the year 1938

2.1 Introduction

It has been shown for several dSphs, that the alpha-element evolution is significantly different from the MW. Generally, their knee—if detected at all—lies at lower [Fe/H] than for MW halo field stars (see, e.g., Tolstoy et al. 2009), and the individual alpha-element ratios become more depleted (e.g., Letarte et al. 2010, Koch et al. 2008, Sbordone et al. 2007). Additionally, the position of the knee varies between individual dSphs (e.g., Cohen & Huang 2009, 2010). This apparent variation in the chemical enrichment process has been linked mainly with the total stellar mass of the individual galaxy, where faint, low-mass dwarfs show lower enrichment efficiencies. The same simplified argument also applies for the observed difference between dwarfs and the MW (Matteucci & Brocato 1990).

Unfortunately, for most of these galaxies, the detailed evolution of the alpha-elements is not well known yet. Until today the observed sample of metal-poor stars in dSphs with high-resolution spectroscopy is small. One reason for the lack of data in this metallicity regime is the generally small fraction of metal-poor stars ($[\mathrm{Fe/H}] \leq -2.0$) in dSphs (Helmi et al. 2006). Second, to optimize galaxy membership, most large surveys target their central regions, which are known to be more metal rich than the outer parts (e.g., Battaglia et al. 2006, Koch et al. 2006, Kirby et al. 2011a). Although the few published abundances suggest that, at the metal-poor end, the alpha-elements in dSphs overlap with the metal-poor MW halo (Shetrone et al. 2003, Tafelmeyer et al. 2010),

---

[1] The work presented in this chapter was done in collaboration with Andreas Koch, Gustavo A. Lanfranchi, Corrado Boeche, Matthew Walker, Christian I. Johnson, Jorge Penarrubia, and Gerard Gilmore. The results were initially published in Hendricks et al. (2014a).

the only galaxy for which the position of the knee is well-defined is Sculptor (see Starkenburg et al. 2013)[2]. For Fornax, Letarte et al. (2010) provides the only existing high-resolution study. They determined the alpha-depleted level for metal-rich stars, but only detected very few stars with $[\mathrm{Fe/H}] \leq -1.3$, which did not allow for the determination of the knee, nor the chemical evolution at lower metallicities.

Here, we show the results for three alpha-elements (Mg, Si, Ti) in Fornax, determined from high-resolution spectroscopy, covering the full range in [Fe/H]. We are able to define the position of the knee and trace the evolution of the alpha-elements from the alpha-rich, iron-poor plateau, to the alpha-depleted level at the metal-rich side of the knee. In Section 2.2, we summarize our data and the reduction steps to obtain our abundances, which are subsequently presented in Section 2.3. In Section 2.4, we compare our results to chemical evolution model predictions. Finally, in Section 2.5 we will discuss our findings in regard to possible formation and evolution scenarios of Fornax.

2.2 Data

Our sample of 431 targets in Fornax were selected from optical V and I broadband photometry (Walker et al. 2006) within a broad selection box around the red giant branch (RGB), spanning down to the horizontal branch magnitude. The targets are distributed in two opposite fields along the major axis of the galaxy, aiming specifically for stars in the outer part of Fornax which has a higher fraction of ancient, metal-poor stars, compared to the central region (Battaglia et al. 2006). Our fields also cover two of the five known GCs of Fornax (H2 and H5, Hodge 1961). Figure 2.1 shows the location of our targets in comparison to previous, comprehensive high- and low-resolution studies. The spectra have been obtained in November 2008 with *FLAMES* at the VLT, where we used *GIRAFFE* in *MEDUSA* high-resolution mode (HR 21, $R \sim 16,000$, $8484-9001$ Å). With a total integration time for each pointing of 8 hours we obtain a typical signal-to-noise ratio (S/N) of $20-50$ per pixel.

To extract and calibrate our spectra, we use GIRBLDRS (GIRAFFE Base-Line Data Reduction Software, Geneva Observatory; Blecha et al. 2003)[3]. The individual reduction steps include flat-field correction, bias subtraction and dark corrections, as well as wavelength calibration. Each exposure has been split up in 8 frames and we median-combine them in order to remove cosmic rays and other artifacts in the spectra. Since the near-infrared is strongly affected by sky emission features, a proper subtraction is crucial for accurate spectral analysis. For this reason, we have written a code which accounts for the different flux throughput in each particular fibre with respect to the dedicated skyfibres and also for small wavelength shifts between the sky- and the target fibres by matching only the strongest few emission features via χ^2-minimization and subsequently apply the same scaling to the whole spectrum.

For the majority of our spectra, we were able to derive metallicities from the Calcium Triplet ($\lambda_{CaT_1} = 8498.03$, $\lambda_{CaT_2} = 8542.09$, $\lambda_{CaT_2} = 8662.14$). We use the sum of a Gaussian and a Lorentzian function to fit the profile of the second and third CaT lines and determine equivalent widths (see, Cole et al. 2004, or Koch et al. 2006). Classically, the calibration from CaT equivalent width to [Fe/H] is based on GC measurements (e.g., Armandroff & Zinn 1988, Armandroff & Da Costa 1991, Rutledge et al. 1997). It has been shown in several studies, that these GC-based calibrations of the CaT metallicity is in good agreement with high-resolution abundance measurements from iron lines only in the metallicity regime between $-2.0 \leq [\mathrm{Fe/H}] \leq -0.5$ (Battaglia et al. 2008, see also Hendricks et al. (in prep.)). To obtain [Fe/H] from the CaT EWs, we therefore use the recently

---

[2] The data, however, never have been explicitly published, or have been made public.

[3] http://girbldrs.sourceforge.net

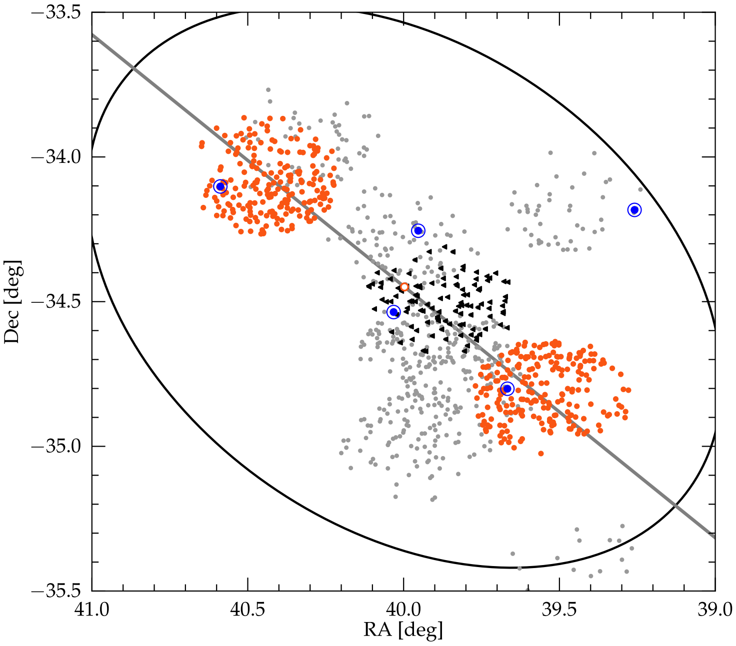

Figure 2.1: Location of our targets (red dots) in the field of Fornax. GCs are marked as blue symbols, and previous spectroscopic studies using low-resolution (Battaglia et al. 2006; gray dots) and high-resolution (Letarte et al. 2010; black triangles) are also shown for comparison. To guide the eye, the nominal tidal radius with $r_t \approx 1.15^\circ$ is shown.

published calibration-equations by Carrera et al. (2013), who made a dedicated effort to extend the calibration range to metallicities as low as −4.0 dex.

We determine radial velocities for each star by comparison to a synthetic CaT template spectrum using FXCOR within the IRAF environment, which yields a precision of ∼2–3 km s^{-1}. The derived RVs are then used to weed out foreground stars and background galaxies, with a similar iterative clipping procedure as described in Walker et al. (2006).

Since two Fornax GCs were included in our target fields, and the chemical enrichment history of GCs can be significantly different from that of the host galaxy, we exclude from our present sample stars within 60″ (equivalent to ∼ 4 cluster core-radii) of the cluster centers.

2.2.1 The Alpha Elements

Individual abundances are determined using SP_ACE (Stellar Parameters and Chemical abundances Estimator, Boeche et al. 2013, Boeche et al. in prep). This new code is the evolution of the RAVE chemical pipeline (Boeche et al. 2011, Kordopatis et al. 2013), capable of deriving stellar parameters and elemental chemical abundances during the same analysis process. It uses a library of Generalized Curve Of Growths which are the extension of the well known curve of growths in the 3-dimensional stellar parameter space with variables T_{eff}, log g, and [X/H]. Because the relatively low S/N and the limited wavelength range of our spectra does not allow a robust estimation for the atmospheric parameters within the code, we derive these parameters from optical $V-I$ colors, using the empirical calibration equations given in Alonso et al. (1999) with a reddening law of $A(V)/E(B-V) = 3.1$ and a line-of sight reddening $E(V-I) = 0.04$ (McConnachie 2012).

Micro-turbulence is assumed to be a function of $T_{\rm eff}$, and log g, and is calculated using a third-order polynomial given in Boeche et al. (2011).

2.2.2 Statistic and Systematic Uncertainties in Chemical Abundances

The major source for systematic uncertainties in the derived abundances comes from the photometric estimation of $T_{\rm eff}$ and log g. To estimate this effect, we propagate the uncertainty of our photometry to $T_{\rm eff}$ and log g and rerun the abundance code on our full sample by separately varying each parameter. By that, we obtain individual systematic uncertainties for each star, defined by its specific photometric error. Typical values for δ[Fe/H] and δ[X/Fe] are below 0.1 dex for all abundance ratios.

We estimate the statistical uncertainty for individual abundances with a subset of the synthetic spectra compiled by Kirby (2011c). These spectra cover a broad range in metallicities and additionally offer the option to vary the alpha-abundance between $[\alpha/\mathrm{Fe}] = -0.2$ and $+0.5$ dex. First we trim the spectra to our observed wavelength range and convolve them to the resolution and pixel scale of our data. Then we create a set of 50 spectra for each point in the parameter space and add random poissonian noise mimicking a S/N of 30, a typical value for our observed spectra. The standard deviation in the derived abundance for each set eventually serve as our estimate for the random error. Note, that we used spectra with $[\alpha/\mathrm{Fe}] = 0.0$, but the dependance of the error on the actual alpha-abundance is small. Typically, we find the combined uncertainty from all discussed aspects for our abundances to be smaller than 0.15 dex in the metal-poor regime, and smaller than 0.1 dex in the metal-rich regime (see Figure 2.2).

2.3 Results

The derived abundance ratios for three alpha-elements Mg, Si, and Ti are shown in Figure 2.2. Here, we only use stars with a $\mathrm{S/N} \geq 25$ and also removed results, for which our code only converged with χ^2-values greater than three sigma from the mean. From the described selection, we obtain a sample of 58, 69, and 67 stars with measured Mg, Si, and Ti, respectively.

From our data we sample the alpha-distribution continuously between $[\mathrm{Fe/H}] \geq -2.5$ and $[\mathrm{Fe/H}] \leq -0.7$ dex. As can be seen in Figure 2.2, a knee in the distribution around $[\mathrm{Fe/H}] \approx -1.9$ is clearly visible, especially in the evolution of Mg. For the other two elements the sampling in the metal poor area is less clear, but it is evident that both Si and Ti are already depleted to a sub-solar level ($[\alpha/\mathrm{Fe}] \leq 0.0$) at metallicities below -1.5 dex. Therefore, from Si and Ti it is still possible to set a strong upper limit for the iron abundance that marks the onset of SN Ia. We also find stars more metal poor than the knee to lie on the same alpha-rich plateau observed in the MW halo, whereas stars above $[\mathrm{Fe/H}] \approx -1.4$ seem to lie on a depleted plateau, significantly below the MW level at a corresponding iron abundance. Note that our mean abundances agree very well with the values derived by Letarte et al. (2010) at the overlapping metal-rich end. Since their sample has been taken exclusively from the central part of the galaxy, while our data come from outer fields, the agreement between the two datasets indicates that there is no difference in the level of depletion as a function of galactocentric distance or stellar density, at least within 2-3 half-light radii of the galaxy.

Although Mg, Si, and Ti are expected to share a common general evolution, their exact origin differs; while Mg is almost exclusively synthesized in SNe II, Si and Ti may also be produced in SN Ia explosions. Therefore, we might expect the decline in [Mg/Fe] after the knee to be steeper than [Si/Fe] and [Ti/Fe] (see, e.g., Lanfranchi & Matteucci 2004). In our sample, we observe this difference most clearly between Mg and Si (see also Table 2.1). If the position of the knee, however, solely depends on the SNe Ia time-delay, its location should be the same for all stars sharing the same chemical enrichment environment.

In order to quantify our results, we first construct a toy model (see Cohen & Huang 2009), which uses the evolution of alpha-elements in the MW halo as template and assumes a constant plateau for stars more metal poor than the knee, and a second plateau for alpha-depleted stars. The two plateaus are linked with a linear slope. Accordingly, we create a piecewise function with the level of both plateaus in [X/Fe] ($P1$, $P2$), the onset of the knee (K) and the slope of the linear decline (s) as free parameters, which we subsequently derive by error-weighted χ^2-minimization. The result is overplotted on the abundance pattern for each Element in Figure 2.2 and the corresponding parameters are listed in Table 2.1.

Element	K	$P1$	$P2$	s
[Mg/Fe]	−1.88	0.35	−0.14	−0.93
[Si/Fe]	−2.49	0.40	−0.13	−0.43
[Ti/Fe]	−2.05	0.44	−0.06	−1.04
[α/Fe]	−2.08	0.35	−0.13	−0.67

Table 2.1: Fiducial points for the chemical evolution of Mg, Si, and Ti in Fornax from our toy model. For Si and Ti, no clear plateau is visible until the lower end of our sampled metallicity range, and the derived parameters are ambiguous. To derive the fiducial points for [α/Fe] we combine all three elements where possible, and otherwise use any combination of only two species.

Most remarkably, the onset of the knee is located at $K = -1.88$ dex for Mg, and -2.08 dex for a combination of all available elements. The very low [Fe/H] at which we observe the knee in Fornax is unexpected for two reasons. First, chemical evolution models in previous studies that reproduce the observed MDF, consistently predict a knee at [Fe/H] ≈ -1.4, 0.5 dex higher than what we find from our data (Kirby et al. 2011b). The second puzzling point arises when we compare our results to the findings from other dSphs, and specifically to Sculptor. For the latter galaxy the position of the knee is well determined at [Fe/H] ≈ -1.8 (Starkenburg et al. 2013)— similar to what we find for Fornax— although Sculptor's stellar mass is estimated to be around 10 times smaller. Vice versa, Sculptor's mean metallicity is lower by more than 0.6 dex, although the evolution of alpha-elements indicates a similar enrichment efficiency. Since we compare absolute magnitudes, and consequently luminous masses, it is important to note that recent estimates have attributed Fornax also a larger M/L-ratio than Sculptor (McConnachie 2012). This is in conflict with the concept of more massive galaxies being more efficient in building up heavy elements, with a knee consequently at higher [Fe/H]. Using absolute magnitudes from McConnachie (2012) as well as previous estimations of knee-positions in other dwarf galaxies for Sculptor (Starkenburg et al. 2013), Draco, Ursa Minor, Carina, Sagittarius (Cohen & Huang 2009, Cohen & Huang 2010), and Hercules (Vargas et al. 2013), Fornax' knee clearly falls out of an otherwise fairly linear relation (see Figure 2.3). If the same mechanism was at play in all the dwarfs, Fornax' stellar mass should not exceed a few 10^6 solar masses. Since not all studies we selected here do define the knee with the same method we applied for Fornax, we do not add individual uncertainties for the position of the knee in [Fe/H], which are generally in the order of ~ 0.2 dex for the brighter galaxies (Sagittarius, Fornax, Sculptor) and larger than that for the rest. Note, that for the faintest dSphs like Boötes or Hercules with $M_V \geq -7$, the expected drop in [α/Fe] is at such low metallicities that a linear model without plateau and knee also gives a reasonable fit to the data (e.g., Gilmore et al. 2013, Vargas et al. 2013).

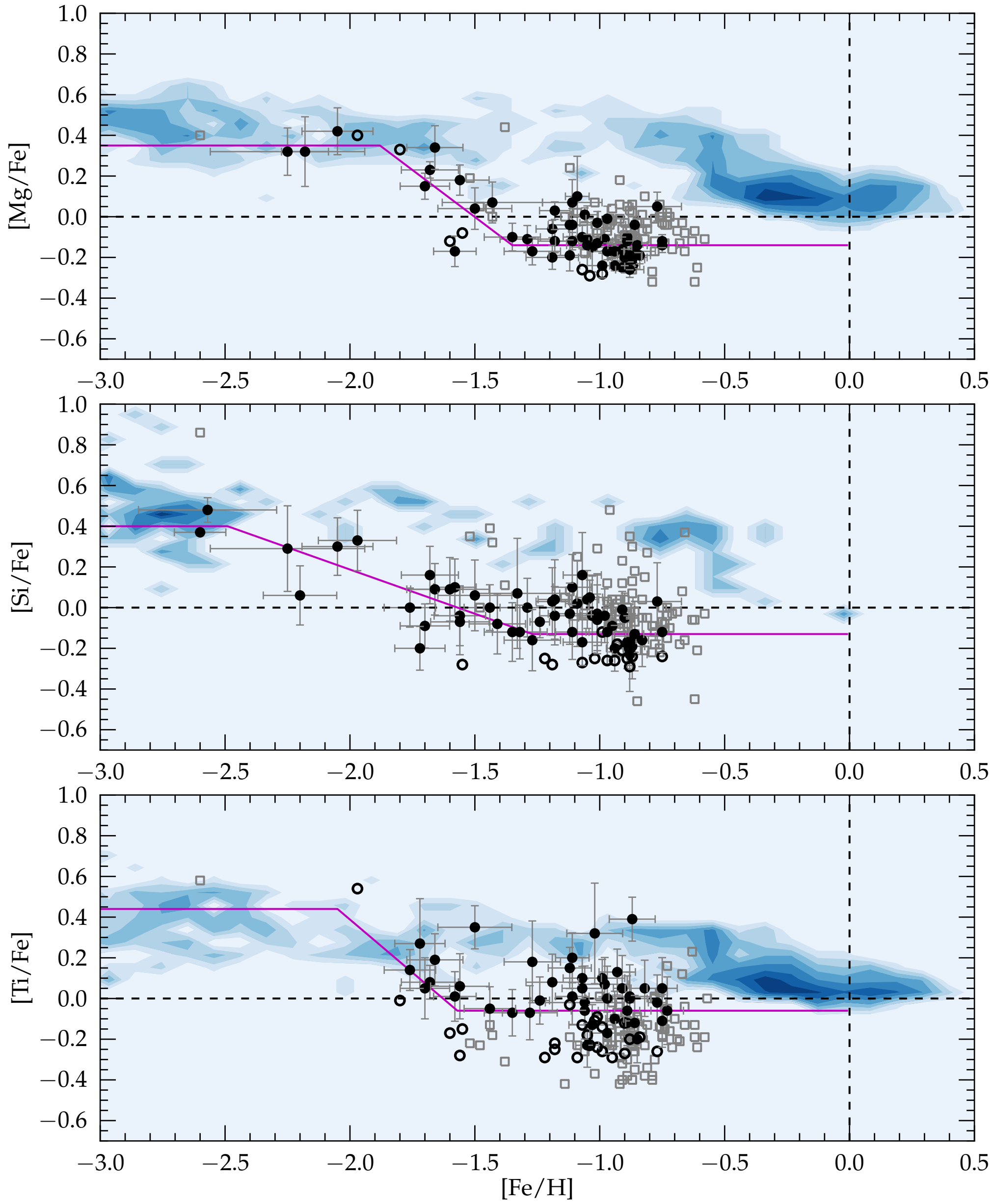

Figure 2.2: Evolution of three alpha-elements in the Fornax dSph (from top to bottom; Mg, Si, Ti). Our sample from two outer fields is shown with black symbols and is supplemented with previous results for inner-field stars (Letarte et al. 2010; gray squares). Open black circles indicate stars for which no adequate upper and lower abundance limit could be derived. For comparison, the evolution of alpha-elements in the MW halo and disks is shown as blue contours (data from Venn et al. 2004 and Roederer et al. 2014). A toy model (see text) is overplotted for each element and shows a clearly defined knee in the evolution of Mg at [Fe/H] ≈ -1.9. The position of the knee is less clearly defined for Si and Ti, but can be ruled out to be more metal rich than -1.8 dex.

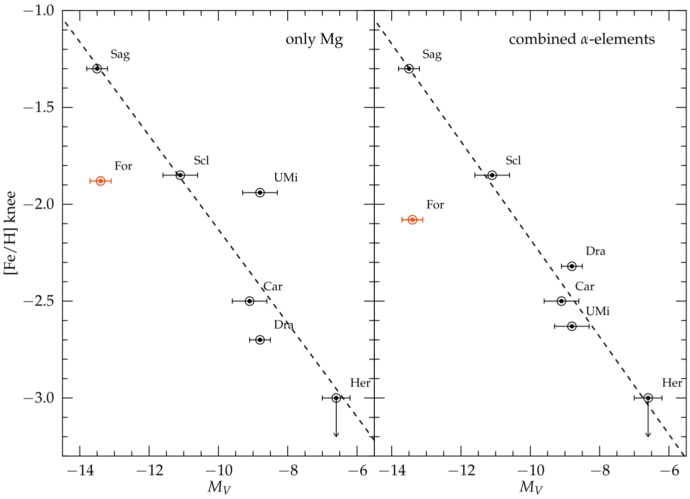

Figure 2.3: Position of the knee in the alpha-element distribution in several dwarf galaxies as a function of absolute magnitude. Uncertainties in M_V have been adopted from McConnachie (2012). Note, that Sagittarius might have been as much as two magnitudes more luminous in the past (Niederste-Ostholt, et al. 2010). In the left panel we only use [Mg/Fe], in the right panel we use a combination of all available alpha-elements. The dashed line indicates the best fitting linear relation, when we exclude Fornax from the sample. The metal-poor knee of Fornax does not fall in an otherwise linear relation and either questions the formation scenario of this galaxy, or the understanding of chemical enrichment in dSphs.

2.4 Comparison to Chemical Evolution Models

Chemical evolution models are a useful tool to analyze the enrichment history of dwarf galaxies; by matching the predicted evolution to the observed chemical abundances it is possible to put constraints on different SF and enrichment scenarios. In the recent past, the chemical evolution of alpha-elements in dSphs have been modelled for many individual galaxies. In a series of papers Lanfranchi et al. (Lanfranchi & Matteucci 2003, Lanfranchi & Matteucci 2004, Lanfranchi & Matteucci 2010) as well as Kirby et al. (2009) and Kirby et al. (2011b) consistently found that, in order to reproduce the observed abundances and the metallicity distribution in the galaxies, the models have to be characterized by a very low star formation efficiency compared to the MW Halo and solar neighbourhood to reproduce the low values of $[\alpha/\mathrm{Fe}]$, in combination with a strong and efficient galactic wind to explain the observed MDF and the lack of gas in these systems today. For most systems (except Carina) a single SF period with a spatially and timely invariant SF efficiency has been used, yielding a good fit to the observed properties (including $[\alpha/\mathrm{Fe}]$, $[\mathrm{s,r/Fe}]$, the MDF, and the present day gas- and stellar mass).

Since our data provide a continuous sequence of abundances from $[\mathrm{Fe/H}] \approx -2.5$ to -0.7 dex, we can make use of the Lanfranchi & Matteucci (2003) chemical enrichment models, which are specifically developed to reproduce the properties of dSphs. These models adopt up-to-date nucleosynthesic yields for intermediate-mass stars and SNe (Ia and II) as well as the effects of SNe and stellar winds on the energetics of the ISM. The main features as well as the theoretical prescriptions of the model are described in detail in Lanfranchi & Matteucci (2003) and at this point we only summarize the key features and the specifications we made in order to adjust the model to Fornax.

In the model, Fornax is supposed to be formed by infall of pristine gas until a mass of $\sim$

$5 \times 10^8 M_\odot$ is accumulated inside a radius of 450 pc. During and after the infall stars are formed according to a Salpeter initial mass function (IMF; Salpeter 1955) and a pre-defined SFH. The models allow the outflow of gas through galactic winds and assume infall of primordial gas in the formation of the galaxy, but do not assume inflow from external gas or reaccretion of previously expelled material. The predicted position of the knee is sensitive to mainly two key parameters. First, the star formation efficiency (ν), which scales the star formation rate (SFR) in the galaxy to the amount of available gas. Second, the wind efficiency (ω_i; the index indicates a differential treatment of individual chemical species) determines the relation between the SFR and a galactic wind which removes thermally heated gas from the galaxy as soon as it is surpassing its gravitational potential (see Lanfranchi & Matteucci 2007 for a detailed discussion). Since a strong galactic wind causes the removal of potentially star forming gas, ν and ω_i both regulate the actual SFR, and by that the chemical enrichment efficiency of the galaxy.

In the following we will present and discuss two conceptually different scenarios: First, we adopt a continuous SFH and in a second model we mimic an interrupted, bursty SF with changing key parameters. As we will see below, the exact choice of SFH will have an important impact on the predicted evolutionary signatures.

2.4.1 Metallicity Distribution Function

In order to construct different SF scenarios, we use Fornax' MDF to constrain the possible parameter space of ν and ω_i for the galaxy, while we simultaneously force the models to reproduce the present luminosity, stellar mass, as well as the absence of gas or ongoing SF.

The MDF in Fornax shows a radial variation with a more metal-rich profile towards the center of the galaxy. Therefore the MDF derived from our outer sample is somewhat different compared to the one shown, e.g., in Battaglia et al. (2006), and it is not trivial to decide which MDF reflects the chemical evolution of the alpha-elements. If we assume that the parameters for SF- and wind efficiency are mainly determined by *global* properties like the DM halo mass, a global MDF would be the appropriate comparison. If instead these parameters are *locally* defined for a specific radius or position in the galaxy, our abundances should be compared to the metallicity distribution from our sample. In Figure 2.4 we therefore show two versions of the MDF in Fornax: First, we derive a *local* MDF from our sample, for which we use the CaT metallicities. Here, we apply the same selection criteria as for the alpha-elements (RV-membership, removal of possible GC stars), only with a lower threshold for the S/N (≥ 10), yielding a sample of ~ 350 stars. The second version is a weighted MDF, for which we use the extended sample of CaT metallicities (~ 1000 stars) from Battaglia et al. (2008) and use the same approach as outlined in Larsen et al. (2012b) and Romano & Starkenburg (2013) to correct for the varying degree of completeness as a function of galactocentric distance. Note that the derived CaT metallicities in the two distributions shown here have been calibrated with different equations, and therefore small variations can be expected in the zero point and in the scaling of the MDF.

In each model fit, we searched for the parameters which best reproduce the peak at [Fe/H] ≈ -1.0 dex, which is the prominent feature in *both* MDFs. Therefore, we consider the choice of ω_i and ν to be fairly robust against possible spatial biases in the MDF caused by incomplete sampling. The best fitting parameters for each model are summarized in Table 2.2 and the detailed SFHs are illustrated in Figure 2.6. The model predictions for the MDF and the alpha-element evolution are shown in Figure 2.4 and 2.5, respectively.

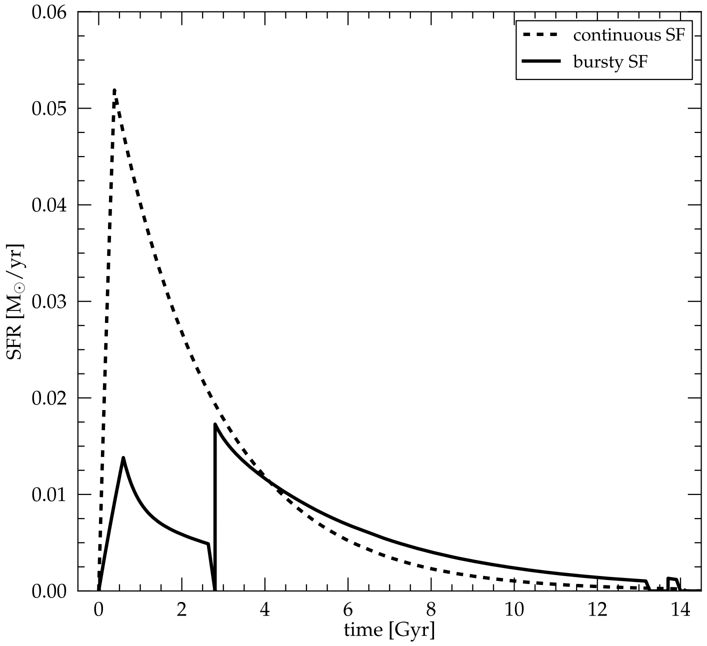

Figure 2.4: Two different concepts for the SFH in Fornax: the dashed line shows the SFR as a function of time for our continuous model (see main text), and the solid line indicates the SFR resulting from the bursty model. The time is measured since the Big Bang.

Model Characteristics	continuous	bursty
Episodes of SF	1	3
Periods (Gyr)	0.0 – 14.0	0 – 2.6; 2.8 – 13.2; 13.7 – 14.0
ν (Gyr^{-1})	0.380	0.095; 0.348; 0.469
ω_i	-5.40	-5.65
τ (Gyr)	2.42	3.75
M_{init} $(M_\odot)$	5.0×10^8	5.0×10^8
M_{final} $(M_\odot)$	3.8×10^7	2.2×10^7
IMF	Salpeter	Salpeter

Table 2.2: Best fitting parameters for the chemical evolution models of the Fornax dSph: SF efficiency (ν), wind efficiency (ω_i), and infall timescale (τ). Note, that the actual SF in the models does not continue to the present day, due to the removal of the gas by galactic winds. The indicated periods for the SF episodes only serve as the input corner points for the model.

2.4.2 Continuous Star Formation

In the model with a continuous SF, the alpha-enhanced plateau at low [Fe/H] is caused by a pollution of the ISM from only SN II at early times. The model shows a slight decrease in the $[\alpha/\mathrm{Fe}]$-ratio already before the knee, since the average SN II progenitor mass is decreasing steadily with time, and the ISM is already polluted by a few Ia SNe. The onset of a significant number of SN Ia is observed as a knee in the alpha-evolution which causes a steep drop in the $[\alpha/\mathrm{Fe}]$-ratio. In the continuous model, this ratio keeps dropping in the subsequent evolution, since the rate of SN II is practically constant, while the number of SN Ia keeps rising. At late times, this effect is enhanced by

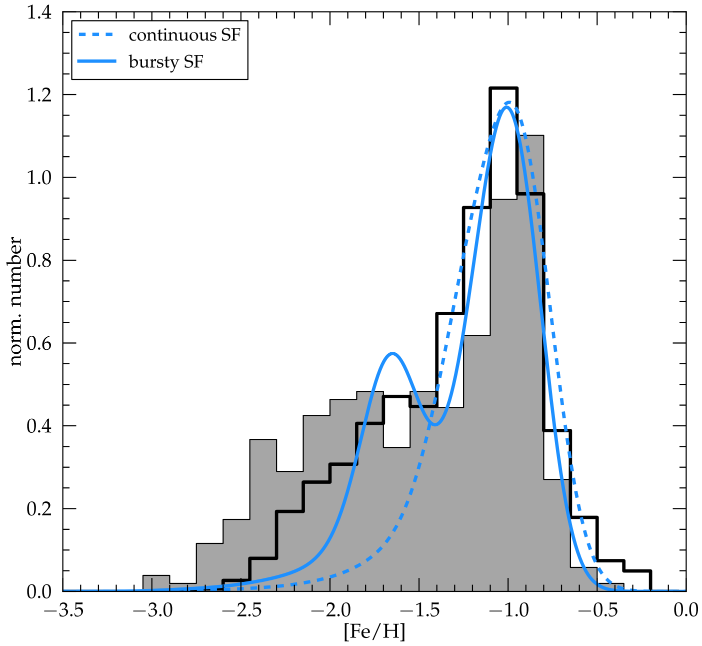

Figure 2.5: Observed MDF in comparison to the chemical evolution model fits for a continuous (dashed blue line) and bursty SF (solid blue line). The filled histogram represents the local outer MDF, constructed from our sample is shown, while the outlined histogram uses the larger sample from Battaglia et al. 2008 and is corrected for radial variations in the coverage (see main text). Both model fits are error-convolved by 0.15 dex in [FeH], a typical value for ours and Battaglia's CaT metallicities. While the observed distributions are normalized so that the integral over the area equals to one, we scale the models in order to give the lowest χ^2 to the global MDF.

the onset of the galactic wind. The removal of gas decreases the SFR and, consequently, the number of SN II, which leads to lower injection of O and Mg (and to some extent Ca and Si) in the ISM. Iron, on the other hand, still pollutes the medium even after the end—or during an interruption—of SF due to the longer lifetimes of SN Ia progenitor stars.

The continuous model is still in agreement with our observations for $[\mathrm{Fe/H}] \leq -1.9$, but it predicts a knee not before $[\mathrm{Fe/H}] \;\; -1.3$, about 0.5 dex higher than we observe in the data. For Mg and Si we find that the models systematically over-predict $[\alpha/\mathrm{Fe}]$ at a 2σ level between $-1.6 \leq [\mathrm{Fe/H}] \leq -1.1$. Ti has a somewhat larger observational scatter, and the mismatch is less pronounced.

It is important to stress, that we tested a variety of different parameter combinations in order to shift the knee towards lower [Fe/H], which we find only to be possible with a significantly lower SFR (either due to a low SF efficiency or a strong galactic wind at early times). This, however, is inevitably in disagreement with the high-metallicity peak in the iron distribution, existent in both the local and the global MDF, which can only be reproduced with a high SF efficiency and a late galactic wind. In other words, the high-metallicity peak in the MDF in combination with the metal-poor knee in the evolution of the alpha-elements *rule out* an evolutionary set-up with continuous SF and constant SF efficiency.

Generally, a model with continuous SF also fails to reproduce a second plateau after the knee which we observe at a sub-solar level in our data. A possible reason for this mismatch could be an incompleteness-bias of our sample towards more alpha-enhanced stars, especially because SP_ACE is only capable to derive abundances for $[\alpha/\mathrm{Fe}] \geq -0.3$ (lower abundances fall outside of the interpolation grid and will be flagged). However, this scenario is unlikely, since SP_ACE gives the highest level of completeness at high metallicities, and we are able to derive abundances for more than 75% of all stars with $[\mathrm{Fe/H}] \geq -1.0$ from our sample.

2.4.3 Bursty Star Formation

A bursty SF—that is a SFH with periods of intense SF separated by less active phases or even a complete shut down—presents a completely different scenario to the evolution of individual elements and the resulting MDF. Now, we do not only enable the SF to shut off and on several times along the evolution, but also allow for *different* SF efficiencies during each burst.

With only three individual bursts, it is now possible to reproduce all crucial features in the alpha-evolution, as well as the general appearance of the MDF. Generally, a gradual increase of the SF efficiency for subsequent bursts, makes it possible to bring the low [Fe/H] of the alpha-elements in accordance with the metal-rich peak in the MDF.

Similar to the continuous model, the plateau at very low metallicities is caused by the enrichment of the ISM exclusively from SNe II. But now, the knee occurs at significantly lower [Fe/H]. This is caused mainly by the low SF efficiency we assigned to the first SF episode, which prevents the galaxy to build up iron as fast as in the case of continuous SF. In addition, the pause of SF after 2.6 Gyr is accompanied by a lack of young, massive SN II polluters at this point, which leads to an additional drop of the $[\alpha/\mathrm{Fe}]$-ratio in the ISM (see dashed evolution segments in Figure 2.5). The onset of the second burst of SF 200 Myr later with a higher SF efficiency has the opposite effect on the evolution of the alpha-elements; the average mass of a SN II explosion jumps up, which not only stops the abundance ratio to drop, but actually causes a temporary increase in $[\alpha/\mathrm{Fe}]$, observed as a bump in the evolution. The third burst has a similar effect (visible at $[\mathrm{Fe/H}] \approx -0.9$ dex), but since it occurs at late times when the galactic wind has already removed the majority of the gas, we do not expect a large fraction of stars along this sequence.

The "bouncing'-effect caused by the interruption in star formation is in very good agreement with our data. It is possible that the sub-solar plateau which we observe in the evolution of the alpha-elements—and which is also observed in other dSphs—is in fact the interpretation of one or several bumps, caused by interruption in the SF during the evolution of the galaxy, possibly accompanied by a change in the SF efficiency.

Note that, while both models do reproduce the metal-rich part (including the peak) in the MDF, the bursty SF scenario also yields the better fit to the observed distribution below -1.5 dex (see Figure 2.4). However, it still slightly underestimates the fraction of most metal-poor stars with $[\mathrm{Fe/H}] \leq -1.9$. The introduction of an additional, brief SF episode to the model at very early times with high SF efficiency would give a better fit to the data. Another possible explanation for the discrepancy between model and observed MDF at the lowest metallicities arises from the high specific frequency of GCs in Fornax: Recently, it has been proposed that Fornax' field population hosts a significant fraction of GC stars, stripped from the star cluster population associated with this galaxy (Larsen et al. 2012b). These authors estimate that as much as 1/4 of the metal-poor population in this galaxy might originate from GCs. Four of the five existing globulars in Fornax have metallicities below -2.0 dex (e.g., Strader et al. 2003, Larsen et al. 2012a, Letarte et al. 2006) and from the extended CaT metallicity sample provided in Battaglia et al. (2008), we can estimate the relative stellar fraction with $[\mathrm{Fe/H}] \leq -2.0$ to be only ~ 0.08. A significant number of dissolved GC stars in the field could therefore plausibly explain the discrepancy between the observed and the model MDF.

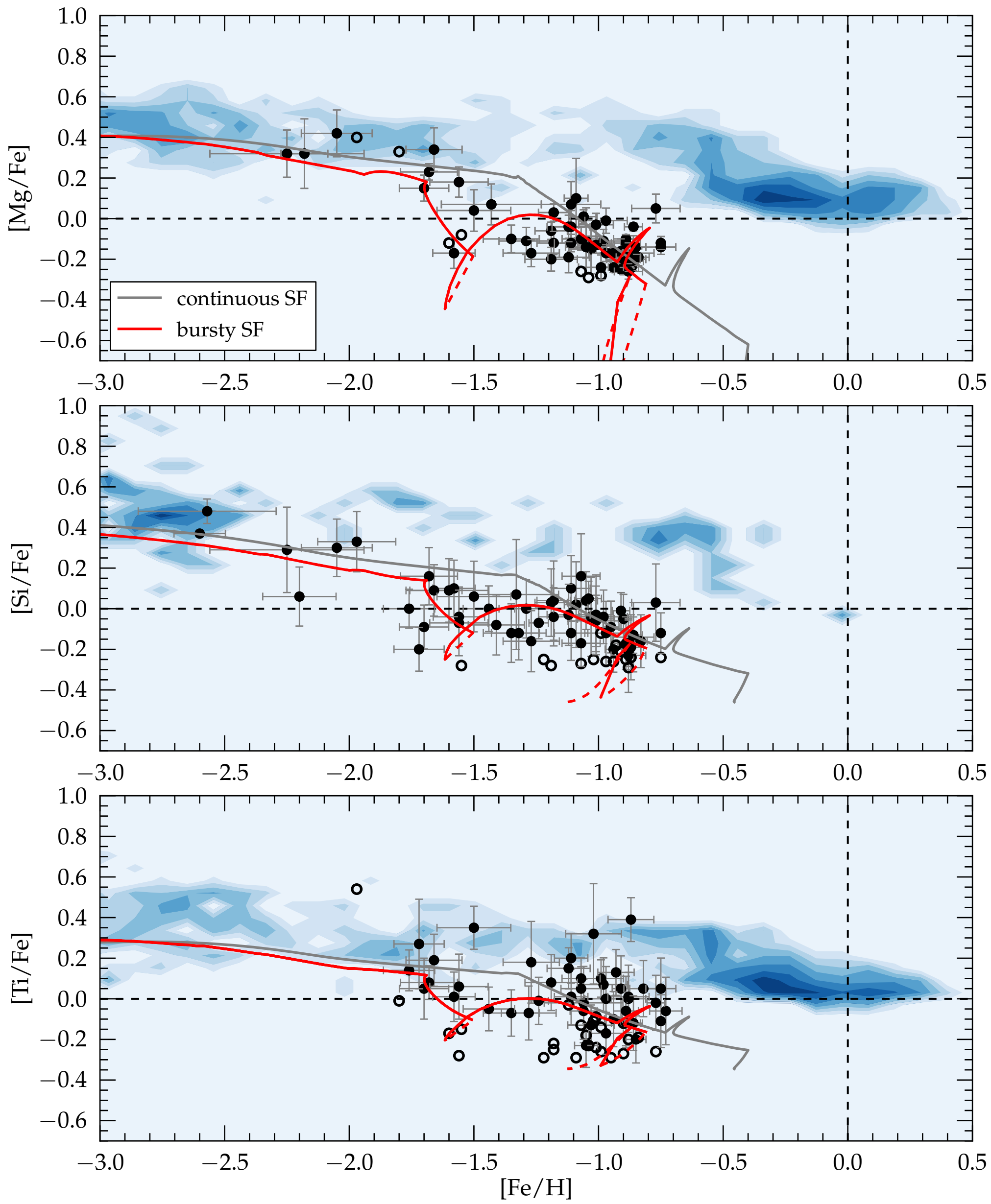

Figure 2.6: Model fits to the observed distribution of the alpha-elements Mg, Si, and Ti. The best fitting continuous model is shown in gray, and the bursty SF model in red. Times with no SF are indicated as dashed segments. While the continuous SF model predicts a knee in the evolution at [Fe/H] about 0.5 dex too high, we can reproduce the metal-poor knee as well as the sub-solar plateau in the alpha-elements on the metal-rich side of the knee with a bursty model allowing for changes in the SF efficiency.

2.5 Discussion

We find a clear knee in the evolution of the alpha-elements as a function of [Fe/H]. Such a feature has been observed for field stars in the MW halo, and is also predicted by chemical evolution models as the delayed onset of SNe Ia. The fact that we find Fornax' knee to be as metal-poor as the knee in the ~ 10 times less massive and ~ 0.6 dex more metal-poor Sculptor dSph prompts the question, if, or to what extend the total stellar mass of these galaxies determined their general efficiency to build up heavy elements over time.

By comparing our results to chemical evolution models we find that a continuous SF cannot bring the knee in the alpha-elements into a consistent evolutionary scenario with the observed MDF in Fornax. In contrast, a bursty SFH with gaps between the individual SF episodes and significant variations between the SF efficiencies can not only explain the combination of the metal-poor knee and a metal-rich MDF, but at the same time provides an explanation for the alpha-depleted plateau in the data, which we find impossible to reproduce with a continuous SFH.

Although it is surprising that a uniform SFH in Fornax does not agree with the observations, it is not striking that the match between model and data improves when the synthetic SFH is designed more flexible by allowing time-dependent key parameters. Therefore it is important to evaluate the assumptions we made for the model with respect to their physical implications for the galaxy and with regard to the the findings from previous studies.

The assumption of major SF episodes separated by several hundred Myr is not in agreement with the photometric SFH reconstruction in de Boer et al. (2012b), who found a continuous SF present at all ages out to a radius of 0.8 degree. On the other hand, MDFs constructed from large samples of CaT-measurements in Battaglia et al. (2006) and Coleman & de Jong et al. (2008) show that the distribution of stars is not homogeneous, but peak at several—in fact three or four—metallicities. The MDF from our sample shows similar signatures at the same metallicities (see Figure 2.4)[4]. Additionally, Amorisco & Evans (2012) find that each of the three more metal-rich populations can be distinguished by distinct kinematic properties, with a possible counter-rotation between the components, indicating a clear dynamical distinction between the populations. Having in mind that the age resolution in photometric SFH studies gradually decreases (to several Gyr) towards older ages due to a smaller color-sensitivity of old RGB stars, together with the fact that iron abundances for stars from the CaT (as used in de Boer et al.) become systematically uncertain at lower metallicities, it is possible that an interruption of SF before the ISM is enriched to $[\mathrm{Fe}/\mathrm{H}] \approx -1.5$ cannot be resolved in such studies. Finally, several discrete SF episodes have been observed in the Carina dSph (e.g., Monelli et al. 2003 an references therein), which gives an empirical validity for this evolutionary concept in dSphs. Therefore, we consider the assumption of distinct SF bursts in Fornax to be reasonable, and the implementation of three episodes in good agreement with previous findings.

The values for the best fitting SF and wind efficiency parameters are of comparable size to the corresponding best fitting parameters in other dSphs; generally the SF efficiency is low and the galactic wind intense compared to MW field stars. While the galactic wind for our model is on the lower end of what has been found for other dwarfs (there: $6.0 \leq \omega_i \leq 13.0$), the individual SF efficiencies for Fornax lie well in the middle of the typical parameter space in other studies, where best fitting values range between $\nu = 0.03\,Gyr^{-1}$ for Draco and $\nu = 3.0\,Gyr^{-1}$ for the massive Sagittarius dwarf. Sculptor, in comparison, is best fitted with $(\nu, \omega_i) = (0.2, 13.0)$.

However, the necessity of a strong variation of the SF efficiency (by a factor of ~ 5) between the first and the third episode in order to explain the data is not a trivial assumption, especially since *all* other dSphs (including Carina) could be successfully modelled with a uniform SF efficiency.

---

[4] A detailed population analysis, motivated by the findings presented in this chapter, will be presented in Chapter 3

What can cause such a drastic change in the SF efficiency in Fornax and the interruption between SF episodes, and which galactic parameters control its SFH?

A hint for a possible explanation comes from the radial metallicity gradient in Fornax (e.g., Battaglia et al. 2006). If the location of SF moves through the galaxy from outward in, and assuming that the SF efficiency depends on the radial position in the DM potential of the system, the net effect would be a time-dependence of the SF efficiency. In such a scenario, the star formation could be altered and stopped periodically by radiative heating of the ISM from SNe II. Hydrodynamical simulations have shown, that SNe II explosions can transfer sufficient thermal energy into the medium to produce local cavities in the density distribution and halt the SF process until the gas has cooled and fallen back to reignite the SF process (e.g., Ruiz et al. 2013, D'Ercole & Brighenti 1999, see also Nichols et al. 2012 for an alternative explanation of periodic SF in dSphs).

Another evolutionary scenario is that Fornax experienced one, or several merger events with other gas-rich systems. For massive galaxies it has been shown that the SFR can be enhanced by a factor of up to 10, when they interact in close pairs or mergers (Scudder et al. 2012). If this also holds for less massive systems, a merger scenario for Fornax could lead to a variation in the SF environment with time, and simultaneously explain the gap in stellar mass between Fornax and Sculptor, despite their apparently very similar early chemical enrichment history. In this case, the initial DM halo that defined the early chemical evolution of Fornax would have been less massive and might have formed initially only the metal-poor population of the MDF observed today. Through subsequent accretion events, the galaxy could have gained additional mass, and subsequently formed its enriched populations—with varying SF efficiencies.

In fact, there are several studies supporting a merger event for Fornax, from a number of observational aspects. Coleman et al. (2004) identify shell-like overdensities in their photometry and de Boer et al. (2013) show that stars in these features are significantly younger than in its direct environment. MDFs constructed in Battaglia et al. (2006) and Coleman & de Jong et al. (2008) show, that the distribution of stars is not homogeneous, but peak at several metallicities. Battaglia et al. (2006) also find a distinct bimodality in the radial velocity distribution for the most metal-poor component, suggesting this subpopulation to be in an dynamically unrelaxed state. Note, that we find a similar distribution for this population in our kinematics (Hendricks et al. 2014b). The distinct kinematic properties for different populations in Fornax found by Amorisco & Evans (2012) also support a merger scenario, and in fact these authors propose a “bound-pair" as a likely evolutionary scenario. In recent simulations dedicated to the complex kinematic and chemical structure observed in Fornax, Yozin & Bekki (2012) are able to reproduce both the photometric overdensities as well as the peculiar velocity bimodality for metal-poor stars in a scenario where Fornax has experienced a merger event between 3.5 and 2.1 Gyr ago. Note, however, that a bimodal velocity distribution in old stars, as observed in Fornax, may also be the result of stripped GC stars in a triaxial DM potential profile (Peñarrubia et al. 2009), whereas the fairly young shell structure (~ 2 Gyr) would require a significantly younger progenitor system.

The necessity of a bursty SFH with variations in the SF efficiency we propose here for the Fornax dSph arises from model predictions, and we do not know to what extent these models reflect the actual conditions in the galaxy. From observational side, the most promising way to test for the episodic nature of SF in Fornax—independent of its evolutionary interpretation—would be a deep photometric study of this galaxy, which is able to resolve the subgiant branch at $V \approx 23.5$ mag, and by that uncover possible distinct stellar population sequences. (e.g.,Smecker-Hane et al. 1996, or Monelli et al. 2003 for Carina). Evidence for past mergers could be found in local overdensities of stars with the same velocity or [Fe/H] characteristic or galactic streams in the periphery of the galaxy. If the chemical enrichment efficiency inside Fornax changes with radius, we should expect to find different evolutionary sequences of, e.g., the alpha-elements from samples taken at different galactocentric distances. This, however, is a difficult endeavour since the fraction of metal-poor stars in the central region is extremely small.

On the other hand, the chemical evolution in a merger scenario is associated with an inflow of stars as well as pristine or enriched gas to an existing system. It is therefore beyond the capabilities of the models we use here, and new chemical and hydrodynamic models are needed in order to support or rule out different evolutionary pathways.

If Fornax actually grew from several smaller building blocks, it has to be asked whether this is an exception, or if it is a common evolutionary path for dwarf galaxies. In case Fornax instead did evolve in an isolated environment, and in fact did not gain a major part of its mass from external sources, the inevitable alternative is to introduce a new parameter to the chemical enrichment problem of this galaxy, such as a radial gradient of the SF and wind efficiency.

3

Insights from the Outskirts: Chemical and Dynamical Properties in the Outer Parts of the Fornax dSph[1]

3.1 Introduction

Knowledge of the detailed chemodynamical properties in satellite galaxies evolved particularly with the advent of powerful, fiber-fed multi-object spectrographs, which enable us to obtain simultaneously precise velocity information and chemical abundances for a large number of stars. Therefore, today large samples of more than 50 stars with at least metallicity[2] and velocity measurements exist for all of the more luminous dSphs associated with the MW: Carina (Koch et al. 2006, Lemasle et al. 2012), Sextans (Battaglia et al. 2011), Sculptor (Tolstoy et al. 2009), Draco and Ursa Minor (Kirby et al. 2011a), Leo I and II (Koch et al. 2007a,b), Sagittarius (Carretta et al. 2010a), and Fornax (Pont et al. 2004, Battaglia et al. 2006).

The majority of the abovementioned studies make use of the CaT absorption lines in the near-infrared as an indicator for [Fe/H] (Armandroff & Zinn 1988,Rutledge et al. 1997), motivated by the fact that the CaT is the strongest feature in the near-infrared spectra of late-type giant stars. Thus, it can be analyzed even from low- to medium-resolution spectra ($R \leq 10\,000$) with low signal-to-noise (S/N$\sim 10-20$), where individual iron lines can hardly be used (but see Kirby et al. 2008 for an alternative approach). Unfortunately, the CaT-[Fe/H] calibration relies, among others, on log g, $\mathrm{T}_{\mathrm{eff}}$, and [Ca/Fe], which limits the validity of empirical calibration equations and makes them uncertain especially at extreme metallicities, where few or no calibrators can be found (e.g., Battaglia et al. 2008).

Combining spectroscopic and photometric information is particularly powerful, because thus stellar ages can be derived and links between dynamical and chemical properties can help to identify and distinguish different origins of individual subpopulations. For Fornax, Battaglia et al. (2006) provide 562 spectra distributed throughout the galaxy. Half of these stars are located within an

---

[1] The work presented in this chapter was done in collaboration with Andreas Koch, Matthew Walker, Christian I. Johnson, Jorge Penarrubia, and Gerard Gilmore. The results were initially published in Hendricks et al. (2014b).

[2] Throughout the remainder of this chapter, the terms *metallicity* and *[Fe/H]* will be used interchangeably.

elliptical radius $r_{ell} \leq 0.3$[3], about equivalent to Fornax' core radius (see Battaglia et al. 2006). Additionally, Pont et al. (2004) provide a sample of 117 stars from the central area with maximal radii of $\sim 0.2°$, and Kirby et al. (2011a) analyzed 675 Fornax field stars within a similarly small radius. Finally, Walker et al. (2009) provide [Fe/H] measurements from Mg absorption features. These data however show large systematic variations compared to direct Fe or CaT-measurements and therefore are not well suited for direct comparison with other samples and for absolute [Fe/H] analysis. Several recent chemodynamical studies use the Battaglia-sample (Coleman & de Jong et al. 2008, Amorisco & Evans 2012) or adopt a central subsample of the same targets for high-resolution follow-up (Letarte et al. 2010). Therefore, the outer radii of Fornax are still poorly analyzed despite the fact that the chemical evolution shows clear radial trends within its gravitational potential. Consequently, a complete picture of the chemical evolution of Fornax is only possible if the chemodynamical characteristics at all radii are known, and their differences are understood. This is specifically important with regard to possible accretion events since they most likely leave imprints in the outer parts of a galaxy (e.g., Naab et al. 2009, Brodie et al. 2014). Simultaneously, the existing sample of metal-poor ([Fe.H] ≤ -2.0) stars in Fornax, which bear the information on early chemical evolution, is still limited (≤ 60 throughout the whole galaxy).

Here we present a chemodynamical analysis for a large sample of stars in the Fornax dSph obtained at large radii within the galaxy. The sample is intended to obtain insights from the outskirts of Fornax and, in combination with the existing samples, provide a tool to pin-down and understand the chemical and dynamical *differences* within this complex galaxy.

In Section 3.2, we summarize our data and describe the CaT-analysis and radial velocity (RV) measurements in detail. In Section 3.3, we test different calibration equations for the CaT and discuss possible systematic differences. In Section 3.4, we determine individual stellar ages and discuss the resulting age-metallicity relation (AMR) and age-RV-relation with respect to the chemical enrichment history of Fornax. Special attention is given to the treatment of statistical and systematic uncertainties in the age determination. In Section 3.5, we show the metallicity distribution function (MDF) of our sample and investigate different subpopulations. Section 3.6 contains our analysis of radial properties, of both metallicity and stellar ages, within our sample. Finally, in Section 3.7 we summarize our results and highlight the implications to the evolution of Fornax.

3.2 Data

The spectra for this study were obtained in November 2008 with FLAMES at the VLT (program ID 082.B-0940(A)). We used GIRAFFE in MEDUSA high-resolution mode (HR 21, $R \sim 16000$, $8484 - 9001$ Å). With a total integration time for each pointing of 8 hours we obtain a typical S/N of $20 - 50$ per pixel. As shown in Figure 2.1, the targets are distributed in two opposite fields along the major axis of the galaxy. We specifically targeted stars in the outer part of Fornax at distances $r_{ell} \approx$ 0.4–0.8°. Our sample contains 431 bona-fide Fornax members and was selected from optical V and I broadband photometry (Walker et al. 2006) within a broad selection box around the RGB. The targets sample the full color range of the RGB and reach down to the horizontal branch luminosity with the intention to equally include the most metal-rich and metal-poor populations as well as the full age range (see Figure 3.1).

The spectroscopic sample we use in this study is the same as presented in Hendricks et al. (2014a), which emphasized a detailed chemical abundance analysis for several alpha-elements. Here, we will discuss in detail the reduction and analysis of the dynamical properties and metallicities derived from the CaT. We point the reader to the aforementioned paper for details about the

---

[3] $r_{ell} = [x^2 + y^2/(1-\varepsilon)^2]^{1/2}$, where x and y denote the distances along the major and minor axis, respectively. In the following, we adopt a position angle of 41.0° and $\varepsilon = 0.30$ from Irwin & Hatzidimitriou (1995).

pre-reduction process of the spectra and the high-resolution chemical abundance analysis to obtain [Fe/H] from iron absorption features, as well as the individual alpha-elements.

For all but Section 3.3 we will use [Fe/H] as derived from the CaT and not the direct measurements from Fe absorption features. The main reason is that the CaT can be evaluated for spectra at practically all S/N and over the full range of metallicity. In contrast, we obtain [Fe/H] from Fe absorption lines only for a smaller subsample (331 out of 401 with CaT measurements) with higher S/N. This sample is additionally biased towards metal-rich stars for which [Fe/H] can be obtained more easily. Several parts of our analysis, however, require an unbiased sample which reflects the actual distribution of chemical enrichment. Such a set can only be provided from CaT measurements, with the additional advantage of being directly comparable to previous studies in Fornax and other dSphs, which are based on CaT metallicities.

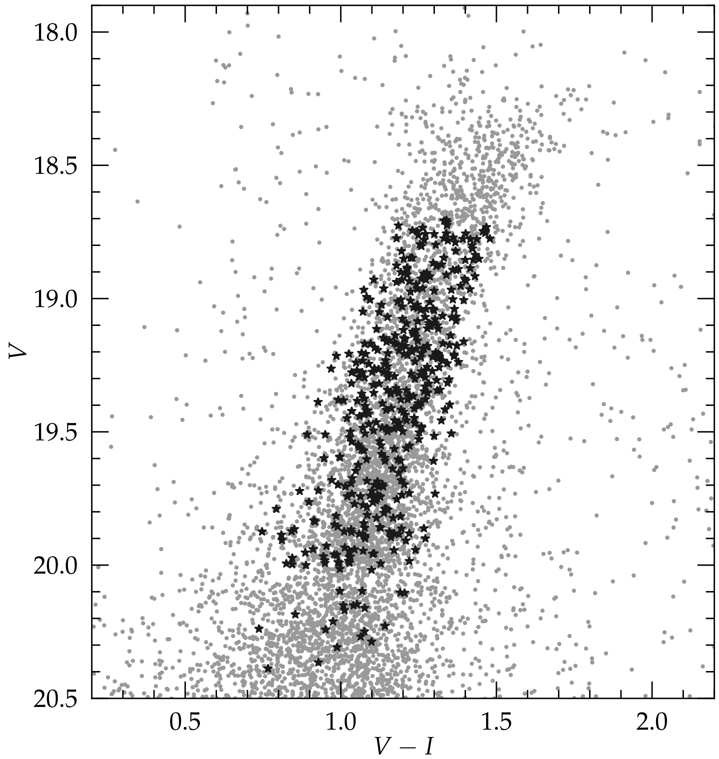

Figure 3.1: Location of our targets (black symbols) on top of the RGB of Fornax drawn from the photometry, which we use for target selection.

3.2.1 Radial Velocities and Galaxy Membership

We determine the line-of-sight radial velocity (RV) for each star via Fourier cross-correlation with a synthetic CaT template spectrum (Kleyna et al. 2004) using FXCOR within the IRAF environment, which yield typical fitting errors $\leq 1\,\mathrm{km\,s^{-1}}$. The evaluation of dynamical properties – especially the intrinsic velocity dispersion – fundamentally relies on accurate error estimates for the individual stellar velocities. Hereby the systematic bias increases dramatically as the fraction between the velocity error and the true dispersion becomes larger (Koposov et al. 2011). Although we expect our velocity error to be an order of magnitude smaller than the true velocity dispersion in Fornax, we tested the accuracy of our error estimates using stars with multiple, individual measurements. For 15 stars in our sample we have 12 individual measurements, respectively, and Figure 3.2 compares the standard deviation from individual repeated measurements (σ_{true}) to the mean error determined by FXCOR (σ_{fxcor}) as a function of [Fe/H]. We find good agreement between these two numbers, with a mean ratio $\sigma_{\mathrm{fxcor}}/\sigma_{\mathrm{true}} = 0.97 \pm 0.10$, and practically no trend with metallicity.

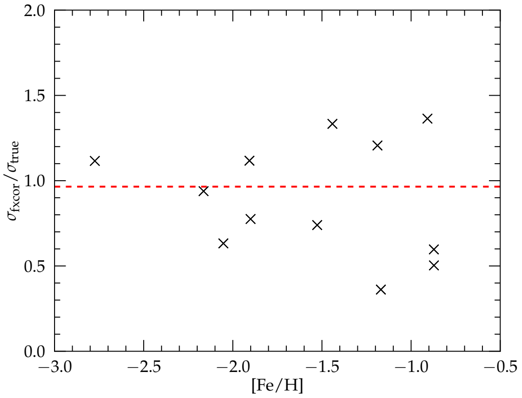

Figure 3.2: Comparison of the mean velocity error from FXCOR and the standard deviation of multiple measurements for a subset of targets. Almost all ratios fall within 0.5 and 1.5 and are scattered around a mean value of $\sigma_{\mathrm{fxcor}}/\sigma_{\mathrm{true}} = 0.97 \pm 0.10$, indicated by the red horizontal line. Three stars without [Fe/H] information are not shown here but have error-ratios of 1.92, 0.83, and 1.04, respectively.

The derived RVs can be used to assess the membership of each target star to Fornax and to weed out foreground stars. Previous studies have shown indications of an intrinsic velocity distribution in Fornax that deviates significantly from a Gaussian distribution (Battaglia et al. 2006). For this reason, we make use of the biweight estimator (Beers et al. 1990, see also Walker et al. 2006), which is more robust against underlying non-Gaussian populations than a simple n-σ-clipping. However, its characteristic distribution width (S_{BI}) corresponds to a Gaussian standard deviation if the data are normally distributed. To reach a membership completeness of 99%, we clip the data at $2.58 \times S_{BI}$, where S_{BI} is redetermined in an iterative process until convergence. See Figure 3.3 for the distribution of RVs in our sample and a visualization of the clipping limits.

Next, we visually inspect our spectra and exclude those from the sample with either an apparent non-stellar origin (e.g., background galaxies, quasars, etc.) or spectra with strong telluric remnants within the environment of the three CaT lines. Additionally, we only keep stars in our final sample with a S/N per pixel of ≥ 10, to guarantee a reliable and accurate determination of velocities and CaT equivalent widths (EWs).

Our target fields also cover two of the five known GCs (H2 and H5; Hodge 1961) associated with Fornax. Because the chemical enrichment history of GCs can be significantly different from that of the field star population, we flag possible GC stars (those within $60''$ around the cluster centers) in our sample and exclude them in our chemical and dynamical analysis. See Section 3.2.4 for a separate analysis of these stars and derived properties for the GCs.

Applying all selection criteria discussed here, our sample of bona-fide Fornax field stars consist of 378 stars, plus 13 possible GC members.

Located at a Galactic latitude of $b = -65.7^\circ$ (McConnachie 2012), we expect the foreground contamination for Fornax to be minimal (see also Battaglia et al. 2006). To estimate the number of foreground stars in our sample, we use the Besançon Model for stellar population synthesis

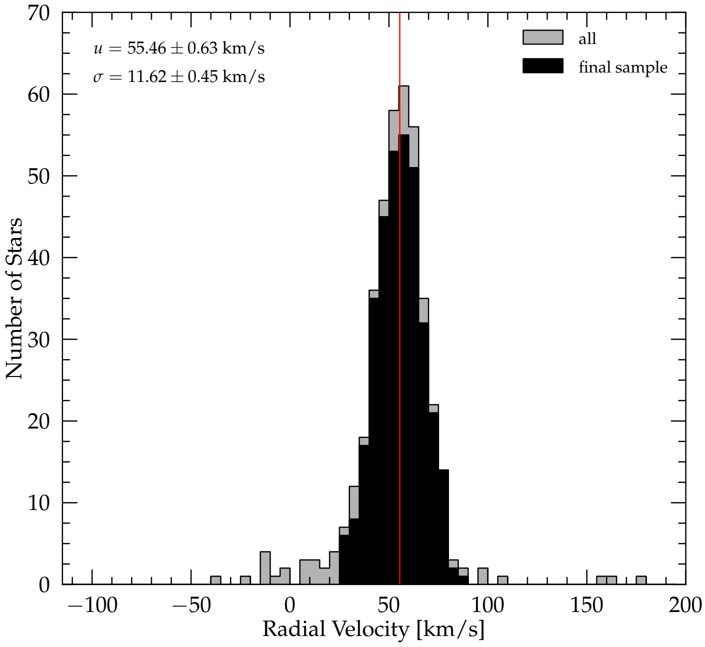

Figure 3.3: Radial velocity distribution of stars in our sample. The red vertical line indicates the mean systemic velocity ($RV_{sys} = 55.46\,\mathrm{km\,s^{-1}}$). Stars that pass the iterative clipping procedure and the visual inspection described in the text are highlighted in black. The maximum allowed velocity deviation from the mean is $\pm 30.70\,\mathrm{kms^{-1}}$.

of the MW (Robin et al. 2003) and extract all synthetic field stars up to the distance of Fornax ($d = 147\,\mathrm{kpc}$), in a solid angle equivalent to our combined pointing area ($A = 0.139\,\mathrm{deg}^2$), and within the same photometric selection box that we used for the initial target selection. We find ~ 30 foreground stars matching these criteria. When we further consider the fraction of stars inside this box that were finally selected for spectroscopy, and furthermore take into account that the velocity clipping already rejects all stars with radial velocities outside of the clipping range, we expect only a handful of foreground stars in our final sample, which is negligible for the further analysis.

To determine the systemic RV (RV_{sys}) and its intrinsic velocity dispersion (σ_{sys}) from the cleaned sample of Fornax field stars, we use the maximum-likelihood statistics described in Walker et al. (2006) which yields $RV_{sys} = 55.46 \pm 0.63\,\mathrm{km\,s^{-1}}$ and $\sigma_{sys} = 11.62 \pm 0.45\,\mathrm{km\,s^{-1}}$. These numbers are in good agreement with previous measurements from Battaglia et al. (2006) who found $RV_{sys} = 54.1 \pm 0.5\,\mathrm{km\,s^{-1}}$ and $\sigma_{sys} = 11.4 \pm 0.4\,\mathrm{km\,s^{-1}}$, or Walker et al. (2009) who obtained $RV_{sys} = 55.2 \pm 0.1\,\mathrm{km\,s^{-1}}$ and $\sigma_{sys} = 11.7 \pm 0.9\,\mathrm{km\,s^{-1}}$ from a more evenly distributed sample within the tidal radius of the galaxy. The mean velocities for the southwestern and the northeastern fields are practically the same within the uncertainties ($RV_W = 54.50 \pm 0.61\,\mathrm{km\,s^{-1}}$ and $RV_E = 56.26 \pm 0.68\,\mathrm{km\,s^{-1}}$, respectively), which supports previous findings that Fornax' rotational component is dynamically insignificant (Walker et al. 2006).

3.2.2 CaT-Metallicities

The CaT is one of the most prominent absorption features in the near-infrared part of stellar spectra. Its three lines are located at 8498.02 Å, 8542.09 Å, and 8662.14 Å, respectively. Because the CaT line-strength varies as a function of metallicity, it has been used as an indicator of [Fe/H] in a variety of Galactic and especially extragalactic systems for which detailed high-resolution spectra, in combination with high S/N, are extremely time expensive. For our spectra with $R \sim 16\,000$ and a S/N typically around 30, the CaT can be used to derive metallicities for a large majority of stars.

CaT metallicities are typically determined in two steps. At first the EWs of the three absorption features are derived by fitting the line profiles in a continuum-normalized spectrum with some analytic function. The next step is to transform the CaT EWs into [Fe/H]. Those calibrations not only relate the change in the CaT line profile as a function of iron abundance, but also remove effects of stellar atmospheric parameters, in particular surface gravity. Published calibration equations, which correlate the CaT EWs to the intrinsic [Fe/H] of a star, depend on the exact approach of measuring the CaT-EWs (see Section 3.3 for a detailed discussion). In the past, there have been different approaches to derive a star's [Fe/H] from the CaT. While originally all three lines were used with equal weights (Armandroff & Zinn 1988, Cole et al. 2004), Rutledge et al. (1997) applied a weighted sum of the lines to account for their different line strengths. In recent years, however, most analyses are solely based on the two strongest (CaT_2, CaT_3) lines (e.g. Koch et al. 2006, Battaglia et al. 2008, Starkenburg et al. 2010) due to concerns that the weakest line adds more noise to the final result. We will follow that argumentation and restrict our analysis to CaT_2 and CaT_3.

Here, we adopt the respective line- and continuum bandpasses given in Armandroff & Zinn (1988), and also follow their approach in correcting for traces of a continuum trend in the vicinity of the lines by fitting a linear function through the median of each continuum bandpass to both sides of the line.

Next, we determine the EW from the actual line profile. Usually, a simple Gaussian is not sufficient to model the shape of the lines appropriately, because it significantly underestimates the broad damping wings of the CaT. This is specifically significant for strong lines and hence for high metallicities, which would consequently introduce an unwanted bias (Rutledge et al. 1997). On the other hand, a simple integration of the flux over the line bandpass (as originally performed by Armandroff & Zinn 1988) also sums weaker lines of other elements inside the interval, which possibly have different dependencies on the metallicity and atmospheric parameters than the CaT. While Rutledge et al. (1997) use a Moffat function to account for the damping wings, Battaglia et al. (2008) and later Starkenburg et al. (2010) use a Gaussian with an additional empirical correction term defined by the integrated flux within the line. In our work, we use the sum of a Gaussian and a Lorentzian function to fit the CaT lines and determine the EW from numerical integration, which provides a good fit for both metal-poor and metal-rich stars (see Figure 3.4). This approach has been used in several previous studies (e.g., Cole et al. 2004, Koch et al. 2006) as well as for the determination of recent CaT-[Fe/H] calibration relations (Carrera et al. 2013).

To ensure reliable results, we visually inspect each fit and exclude stars where the function fails to reproduce a reasonable continuum level or the shape of the fit does not agree with physical expectations. We can derive reliable EWs for 346 field stars and 13 additional stars that are likely GC members.

Finally, we use the recently published calibration equations of Carrera et al. (2013) to obtain [Fe/H] from the derived CaT-EWs. These authors made a dedicated effort to extend the classical calibration range of GC-based calibration from $[\mathrm{Fe/H}] \approx -2.0$ to metallicities as low as -4.0 dex.

To obtain uncertainties for the CaT-metallicities, we first use the covariance matrix of each line fit to determine σEW from the individual uncertainties in each free fitting parameter and their dependencies. To propagate the error through the calibration equation, we use the uncertainties for the individual calibration indices from Carrera et al. (2013) and estimate the uncertainty on the luminosity-normalization as $\sigma(V - V_{HB}) = 0.10$. From this, we find a median error for our CaT-metallicities of $\sigma[\mathrm{Fe/H}] = 0.10$ dex. Although we find that the minimum uncertainty increases with

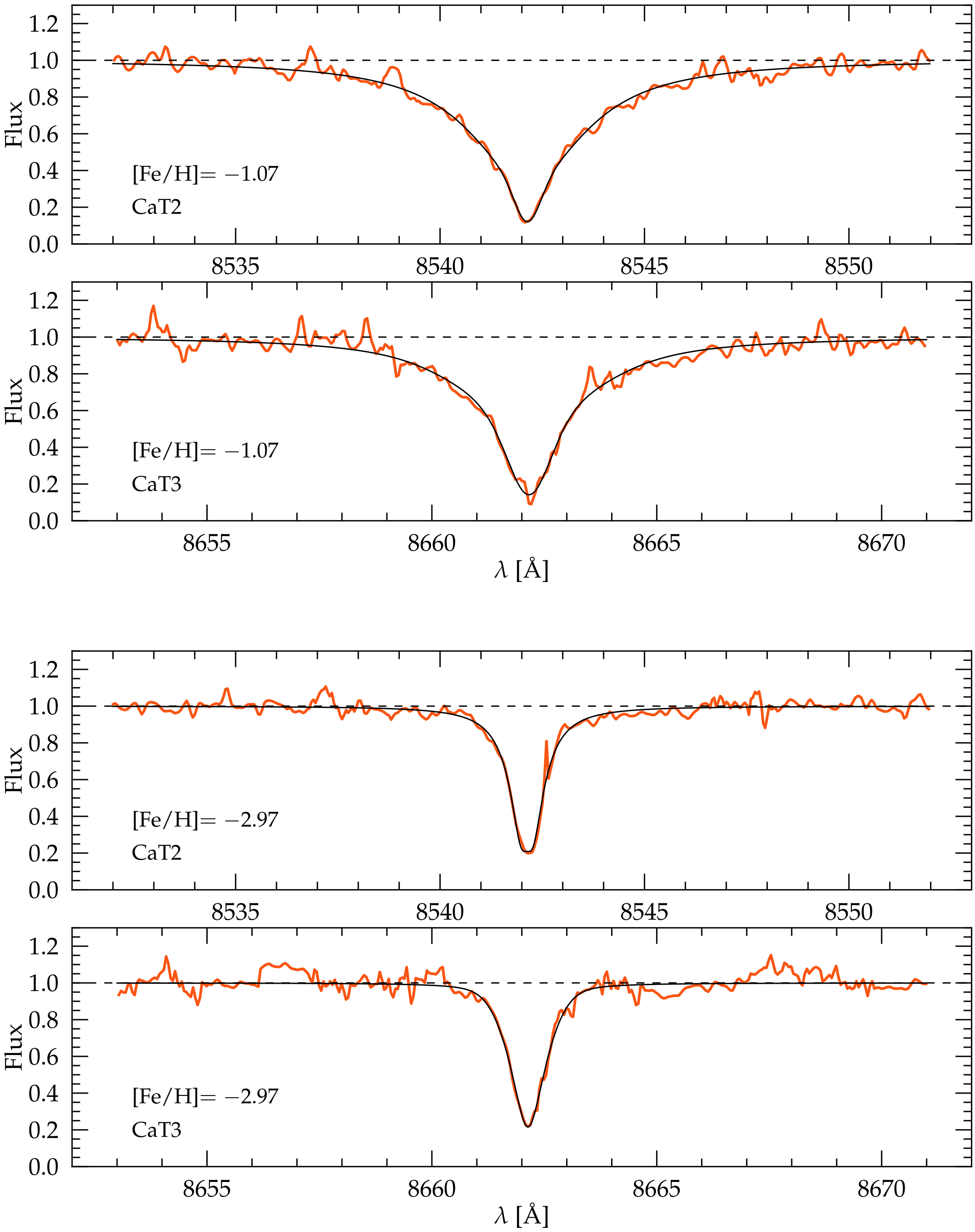

Figure 3.4: Determination of the EW from the CaT, using continuum-normalized spectra in the case of a metal-rich target (upper two panels) and a metal-poor star (lower two panels). A combination of a Gaussian and a Lorentzian function (black line) is fit to the absorption features in order to account for the strong damping wings, particularly for the metal-rich stars. The plotted wavelength range represents the adopted line bandpasses. The S/N of both targets is ~ 30, a typical value for our sample.

metallicity due to the larger wings of the lines, the mean uncertainty at each metallicity is about constant because the scatter towards higher $\sigma[\mathrm{Fe/H}]$ is larger for metal-poor stars.

As a crosscheck for our uncertainties derived from individual line fits, we made a second approach with the analytical formula proposed in Cayrel (1988), based solely on the S/N and resolution of the spectra:

$$\sigma\,\mathrm{EW} = 1.725\,\sqrt{\sigma_{Gauss}}\,S/N. \tag{3.1}$$

In the above equation, σEW depends on the Gaussian width of the lines. Because a combined function of a Gaussian and a Lorentzian does not provide this information directly, we determine σ_{Gauss} by fitting a *pure* Gaussian to the absorption features. Both error estimates are shown in Figure 3.5, which shows that the analytic estimates are in good agreement to the uncertainties derived from the line-fitting covariance matrix.

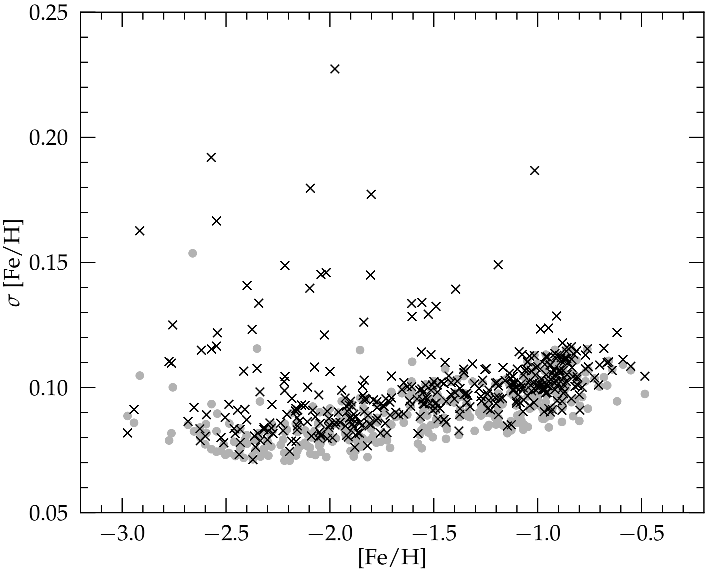

Figure 3.5: Statistical uncertainty of our CaT metallicity values. Black crosses are errors obtained from our line fits and gray points represent errors derived with the analytic formula from Cayrel (1988).

3.2.3 The Mg I Line at 8806.8 Å as Dwarf-Giant Index

Recently, the neutral Mg line at 8806.8 Å has been proposed as an indicator of stellar surface gravities, and hence may separate possible foreground dwarfs from RGB galaxy members (Battaglia & Starkenburg 2012). Since our spectra cover both the CaT and the Mg I-feature, we can identify additional foreground contamination, which has not been removed through the radial velocity clipping. We derive the Mg I EW by simple integration over a 3 Å-interval around the line center in the continuum-normalized spectra. Battaglia & Starkenburg (2012) use a broader (6 Å) interval around the line, but we find that this includes a contaminating Fe I line located at 8804.6 Å, which we avoid with the smaller integration corridor.

In Figure 3.6, the MgI EWs are plotted against the EWs from the two strongest CaT lines. We observe a group of obvious outliers with Mg I EWs more than 0.2 Å above the majority of stars that are located on a well defined sequence. The two populations indicate that the proposed method is generally a useful dwarf-giant separator. However, as can be seen in Figure 3.6, the separation function given in Battaglia & Starkenburg (2012) does not yield an optimal cut to these outliers, which may be explained by the different CaT EW fitting technique applied to their data (see Section 3.3). We therefore decide to simply remove stars ≥ 0.15 above the median Mg-EW at any given CaT-EW, which concerns five stars from our previous sample, in addition to the already flagged RV outliers. We note that this number is in excellent agreement with our contamination estimate based on comparison with the Besançon Model (see Section 3.2.1).

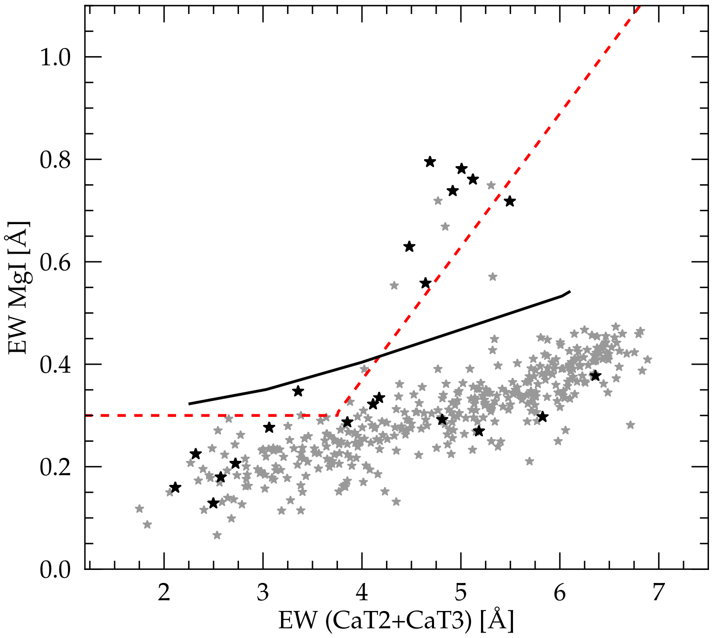

Figure 3.6: EWs of the two strongest CaT lines in comparison to Mg I at 8806.8Å. Foreground dwarfs have higher log g and display a stronger Mg-line at given [Fe/H] compared to giant stars. Results from our sample are shown as gray symbols, and stars which previously have been excluded based on their velocities are highlighted in black. The data show a clear sequence of RGB stars with a few (dwarf) foreground contaminants well above the general trend. The separation-criterium from Battaglia & Starkenburg (2012) is indicated as a red dashed line, but does not provide a good cut for our sample. Our own separation limit is indicated as a black solid line and removes only outliers ≥ 0.15 above the median Mg line strength at a given CaT EW.

3.2.4 The GCs H2 and H5

The chemical composition, age, and dynamical information of extragalactic GCs give important clues about their evolution and the evolution of their host galaxy (Brodie & Strader 2006). While their ages help to understand GC formation mechanisms (van den Bergh 1981), detailed abundance analysis of their stellar content helps to constrain the chemical enrichment processes within the cluster and in the environment of their formation (see, e.g., Gratton et al. 2004).

The GCs in Fornax have been studied intensively in the past and their metallicities and RVs have been determined with various methods. However, due to their limited spatial extent, most spectroscopic studies relied on integrated light analysis (Strader et al. 2003, Larsen et al. 2012b), and so far only Letarte et al. (2006) carried out a detailed abundance analysis for a small number of *individual* stars in three of the clusters.

Two Fornax GCs (H2 and H5) were included in our target fields, and it is therefore likely that some stars in our sample are GC members. To identify bona-fide GC members, we first select stars within $60''$ (equivalent to the tidal radius) around the respective cluster centers: $(\alpha, \delta) = (02^h38^m40^s.1, -34°48'05''.0)$ for H2 and $(02^h42^m21^s.15, -34°06'04''.7)$ for H5. For all stars in question, we have reliable [Fe/H] abundances from the CaT and precise RV measurements. Unfortunately, the S/N for these stars is not sufficient to determine alpha-elements.

Besides a visual clustering of stars around the coordinates, we find a striking similarity in metallicity and radial velocity for both sub-groups around H2 and H5, respectively (see Table 3.1). When we exclude the star (ID 278) with significantly lower RV compared to the other candidates [4], we find $[\mathrm{Fe/H}] = -2.08 \pm 0.05$ and $RV = 59.36 \pm 0.31\,\mathrm{km\,s^{-1}}$ for H2 and $[\mathrm{Fe/H}] = -2.03 \pm 0.08$ and $RV = 59.39 \pm 0.44\,\mathrm{km\,s^{-1}}$ for H5. From our limited sample, these two systems have an identical metallicity and systemic RV, within the uncertainties. Our numbers are in excellent agreement with previous findings: Larsen et al. (2012b) measures a metallicity of -2.1 ± 0.1 and a radial velocity of $60.6 \pm 0.2\,\mathrm{km\,s^{-1}}$ for H5 from integrated light spectroscopy and Letarte et al. (2006) obtained $[\mathrm{Fe/H}] = -2.10 \pm 0.1$ and $RV = 63.8\,\mathrm{km\,s^{-1}}$ from three individual stars in H2. Consequently, for H2 we provide the largest sample of individual spectroscopic RV and [Fe/H] measurements to date.

ID	GC	$[\mathrm{Fe/H}]_{\mathrm{CaT}}$	σ[Fe/H]	RV $[\mathrm{km\,s^{-1}}]$	σRV $[\mathrm{km\,s^{-1}}]$
94	H2	−2.21	0.11	67.18	0.94
95	H2	−2.28	0.09	61.91	1.29
97	H2	−2.05	–	62.31	0.76
99	H2	−2.15	0.09	60.04	1.43
199	H2	−1.95	0.09	60.02	0.97
201	H2	−2.06	0.08	62.98	1.06
202	H2	−1.92	0.08	53.00	0.69
203	H2	−2.16	0.09	56.75	0.87
206	H2	−1.91	0.08	56.84	0.96
278	None	−1.87	0.09	37.54	1.57
423	H5	−2.15	0.09	58.93	0.76
426	H5	−2.05	0.08	59.81	1.07
427	H5	−1.88	0.08	59.43	1.52

Table 3.1: Chemodynamical parameters for candidate GC members in our sample. We have excluded ID 278 as a possible member for H5 due to its low line-of-sight velocity.

3.3 Testing the CaT-Calibration

Originally, the CaT was calibrated to GCs with known metallicity (e.g. Armandroff & Zinn 1988, Rutledge et al. 1997, and more recently by Battaglia et al. 2008, Koch et al. 2006, and Carretta et al. 2009). The calibration limits – set by the metallicity range of the GCs that were used – were then extended with open clusters towards higher [Fe/H] (Cole et al. 2004). At this point, a linear relation between the strength of the CaT lines was assumed, with a zero-point that is linearly correlated with the stellar luminosity and thus gravity. Recently, extensive tests have shown that both correlations

---

[4] We also find a significantly lower age for this star compared to the other candidates, which gives further support that it is not an actual member of H5 (see Section 3.4)

show non-linear trends when wide ranges of either [Fe/H] and/or luminosity are sampled (Battaglia et al. 2008, Starkenburg et al. 2010). In recent years, Starkenburg et al. (2010) and Carrera et al. (2013) developed new CaT-calibrations that add quadratic terms to the equations, with the goal to extend the acceptable calibration range to both sides in [Fe/H], and particularly towards more metal-poor stars in order to remove the existing bias from the metal-poor tail in extragalactic metallicity distribution functions.

We have a large, homogeneous sample of stars with sufficient spectral resolution and S/N in order to determine [Fe/H] *independently* from both the CaT and from detailed analysis of individual Fe-lines in our spectra. This provides a unique opportunity to test the different existing CaT-calibrations over a range of more than 2 dex from [Fe/H] $= -2.8$ to -0.5. In the following, and in the remainder of this work, we will refer to [Fe/H] measured from the CaT as *CaT-metallicities*, while *Fe-metallicities* indicate iron abundances derived from individual iron lines. For a detailed description of the latter, see Hendricks et al. (2014a)

Here, we test three different equations to calibrate our EWs to [Fe/H]:

- i) A classical GC-calibration from Koch et al. 2006:

  $$[\mathrm{Fe/H}] = -2.77 + 0.38W', \tag{3.2}$$

  with

  $$W' = EW_{2+3} + 0.55(V_\star - V_{HB}), \tag{3.3}$$

  where EW_{2+3} denotes the sum of the two strongest CaT lines, and $(V_\star - V_{HB})$ is the relative V-band magnitude of a star above the horizontal branch.

- ii) The semi-synthetic calibration from Starkenburg et al. (2010), who take into account the non-linear behavior of the EWs by adding a quadratic term to the calibration equation that is derived from synthetic line analysis:

  $$\begin{aligned}[\mathrm{Fe/H}] &= a + b \times (V_\star - V_{HB}) + c \times \sum EW_{2+3} \\ &+ d \times (\sum EW_{2+3})^{-1.5} \\ &+ e \times \sum EW_{2+3} \times (V_\star - V_{HB}),\end{aligned} \tag{3.4}$$

  with

  $$(a,b,c,d,e) = (-2.87, 0.195, 0.458, -0.913, 0.0155).$$

- iii) The most recent calibration from Carrera et al. 2013, who use a combination of open clusters, GCs, and metal-poor field stars to derive a purely empirical calibration following the same non-linear form as given in Eq. 4. They find

  $$(a,b,c,d,e) = (-3.45, 0.11, 0.44, -0.65, 0.03).$$

  According to the relative line strength of the three CaT features given in Carrera et al. (2013), we have to divide each EW-term by 0.81 in order to account for the fact that we only use the two stronger CaT-lines, and not all three as is done in their paper.

It is important to note that in i) and iii), CaT EWs were fit with a sum of a Gaussian and Lorentzian, which is also our approach to measure the line strength, but ii) uses an analytic correction term to an initial Gaussian fit as described in Battaglia et al. (2008).

The results from the different calibrations are shown in Figure 3.7. We find, in agreement with Battaglia et al. (2008), that a classical GC-calibration is only valid between $-1.8 \leq [\mathrm{Fe/H}] \leq -0.6$, and shows strong deviations at lower metallicities, where the CaT-metallicity becomes systematically too metal-rich by ≥ 0.5 dex (see also Koch et al. 2008). When we use the calibration of Starkenburg et al. (2010), we do not observe a significant trend in our CaT-metallicities compared to the Fe-metallicities at low [Fe/H]. However, there is a zero-point offset between the two approaches. When we fit a linear function to the residuals ($\Delta[\mathrm{Fe/H}] = x_1 \times [\mathrm{Fe/H}]_{\mathrm{HR}} + x_0$), we obtain $x_1 = 0.15 \pm 0.05$ and $x_0 = -0.04 \pm 0.07$ as best fitting parameters, indicating a negligible dependance on [Fe/H], but with an offset of ~ 0.2 dex at $[\mathrm{Fe/H}] = -1.5$. That results in too metal-rich CaT-metallicities. Finally, the Carrera-calibration equations agree remarkably well with our Fe-metallicities. As can be seen in the lowest panel in Figure 3.7, there is neither a dependance of the derived CaT-metallicity on [Fe/H] nor a significant zero-point shift. A similar fit of a linear function gives best fitting parameters of $x_1 = 0.10 \pm 0.04$ and $x_0 = 0.15 \pm 0.06$, corresponding to an exact match at $[\mathrm{Fe/H}] = -1.50$ dex.

To investigate the origin of the zero-point offset between the two most recent calibration equations, we make use of the CaT-catalog from Battaglia et al. (2008) – an extended version of the catalog published in Battaglia et al. (2006) – for which these authors provided not only [Fe/H] but also the underlying EWs (from here on “B08-sample”, G. Battaglia, priv. comm.). When we compare the MDF derived from the different datasets we find excellent agreement for the dominant and narrow peak metallicity in the MDF at ~ -1.0 dex (see also Section 3.5) when we a) use the Carrera-calibration or the Koch et al. (2006) GC-calibration for our data, or b) the Starkenburg-calibration or the Battaglia et al. (2008) GC-calibration for the B08-sample. In contrast, when we apply the Starkenburg-scale to our data, the peak appears ~ 0.2 dex too metal-rich. Vice versa, the peak in the B08-sample becomes too metal-poor by the same amount when we apply the Carrera-calibration on their EWs (see Figure 3.8). Strikingly, both calibrations for which our sample peaks at ~ -1.0 dex use the sum of a Gaussian and a Lorentzian to fit the line profiles, as we do to derive our EWs. Similarly, the calibrations that bring the B08-sample to peak at the same metallicity applied an empirical correction to a Gaussian fit, corresponding to the approach in Battaglia et al. (2008). We therefore conclude that the actual fitting approach for the CaT absorption features can have significant effects on the derived EWs and is most likely the reason for the 0.2 dex-offset between the Carrera- and the Starkenburg-calibration equations, when applied to our sample.

In summary, we find that both the Starkenburg- and the Carrera-calibration show good agreement with high-resolution results between $-3.0 \leq [\mathrm{Fe/H}] \leq -0.5$, but only if EWs are derived with the corresponding method to the applied calibration. Otherwise, systematic offsets on the order of ~ 0.2 dex in the derived CaT-metallicity can be introduced at all metallicities. This could result in systematic discrepancies of up to ~ 0.5 dex between independent CaT-studies.

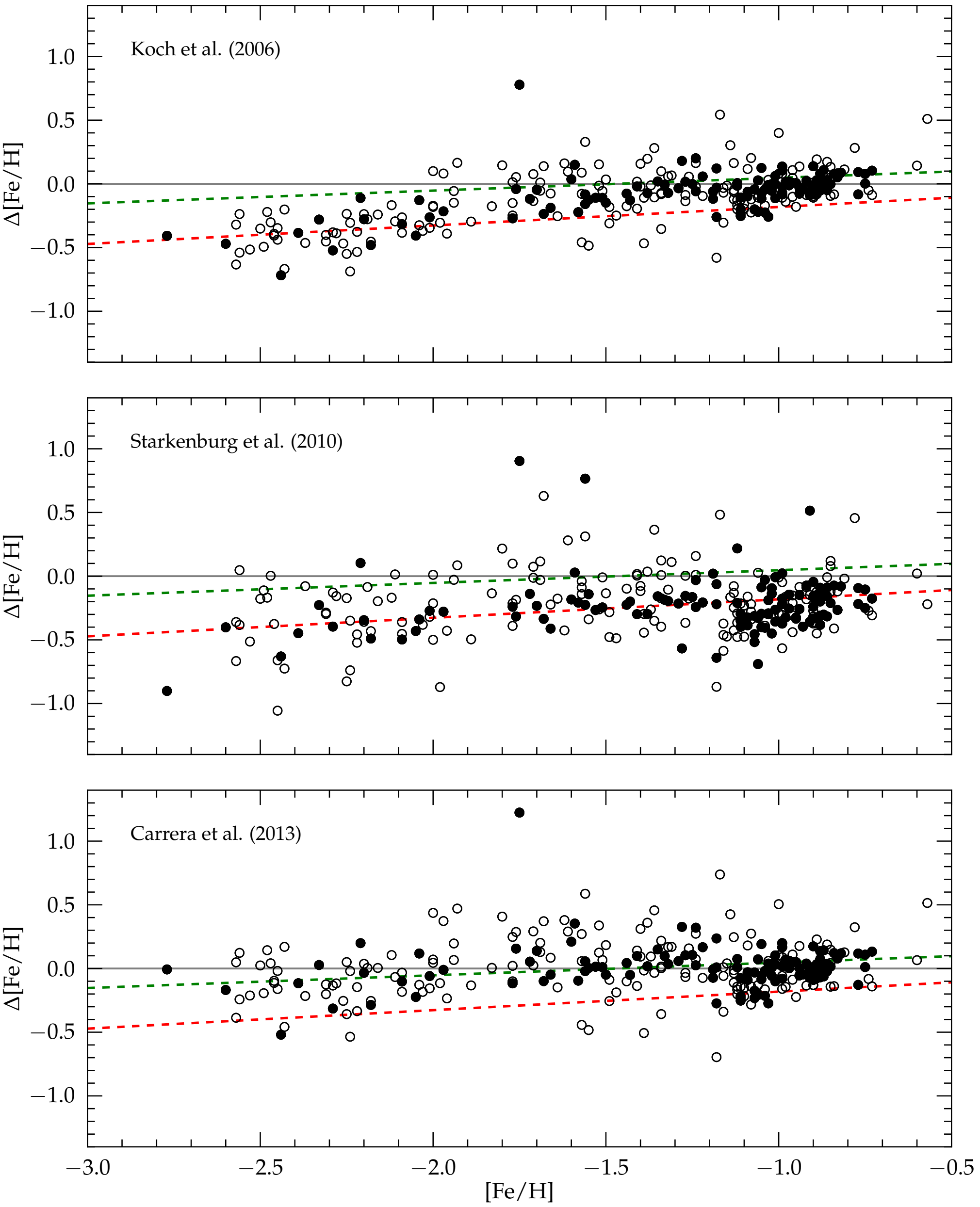

Figure 3.7: Comparison of different CaT-[Fe/H] calibrations to independent Fe-abundances from iron-line analysis for the same sample of stars. In each panel $\Delta[\mathrm{Fe/H}] = Fe - CaT$. We show the results for our complete sample in open circles and highlight stars with $S/N \geq 25$ and $\sigma[\mathrm{Fe/H}] \leq 0.15$ with filled symbols. The red and green dashed line in each panel indicate the best linear fit to the Starkenburg- and Carrera-calibration, respectively, and reveal a constant ~ 0.2 dex-offset between them. The latter one yields a better fit to our data. The classical GC-calibration in the top panel shows a clear systematic trend for $[\mathrm{Fe/H}] \leq -1.8$, resulting in CaT-metallicities too metal-rich by as much as 0.5 dex.

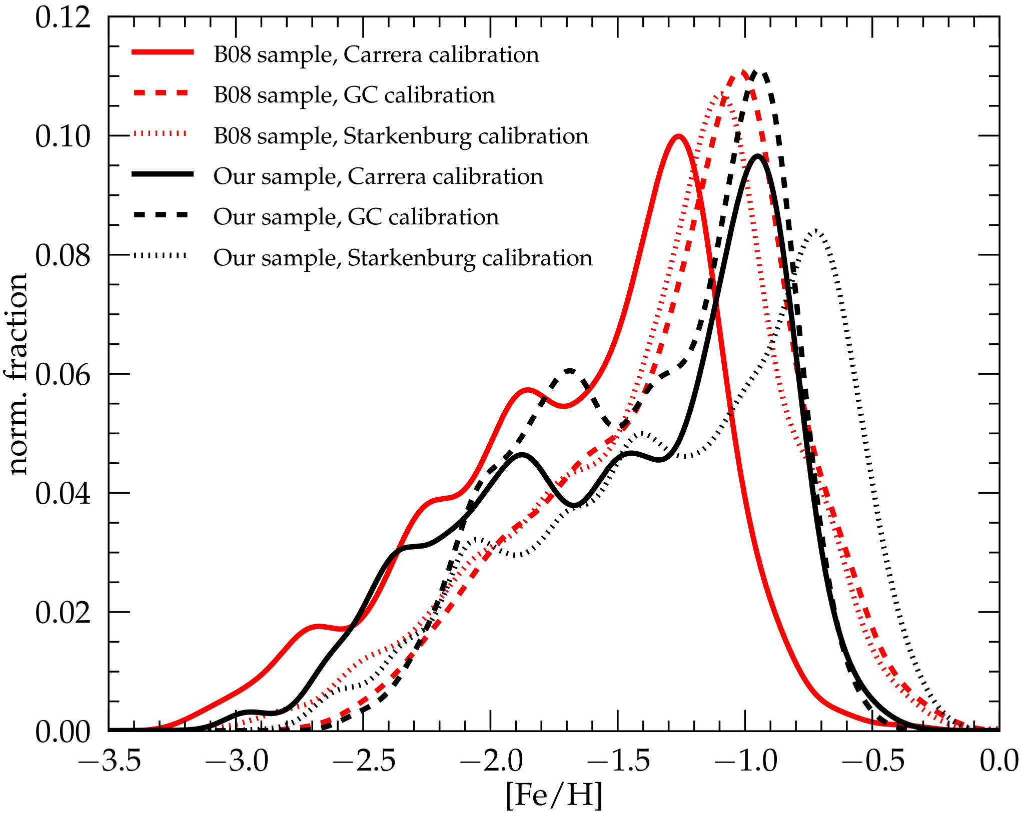

Figure 3.8: Comparison between different CaT-[Fe/H] calibrations applied to two independent datasets. The B08-sample (see text) has been analyzed with an empirical correction to a Gaussian fit, whereas our EWs have been determined from a combined Gaussian and Lorentzian function. With respect to the position of the prominent peak in the distribution, a good agreement for the zero-point in [Fe/H] between both sets is obtained when the line-fitting technique in the calibration relation and the scientific sample is the same. In contrast, different line-fitting approaches can result in significant offsets of more than 0.5 dex between the samples.

3.4 The Age-Metallicity Relation

An accurate age-metallicity relation is a powerful tool to determine a galaxy's chemical enrichment history (e.g., Carraro et al. 1998, Haywood et al. 2013). Unfortunately, the determination of stellar ages from isochrone fitting suffers from several systematic and statistical uncertainties. On the one hand, the position of a star in the CMD depends on both chemical composition and age. Precise individual [Fe/H] and $[\alpha/\mathrm{Fe}]$ information is required to break this degeneracy. On the other hand, assumptions for the distance modulus and interstellar reddening and extinction are necessary and therefore pose a significant source of systematic uncertainty. The analysis is additionally based on the assumption that a given set of isochrones correctly predicts stellar evolutionary sequences for stars of given age and chemistry and consequently relies – among other things – on assumptions about mixing length, core-overshooting, and mass loss in the models. On top of these sources of error, the age-sensitivity of stellar positions on the RGB is weak, and large random errors are introduced from even small uncertainties in the stellar photometry. This is specifically true for old populations where the uncertainties can exceed several Gyr. Therefore, we dedicate a separate discussion to the individual statistical and systematic uncertainties governing relative age estimates in Section 3.4.3.

Previous studies like those of Pont et al. (2004), Battaglia et al. (2006), Lemasle et al. (2012), or more recently de Boer et al. (2012b), make use of individual metallicity measurements for large samples of stars in dSphs to derive their AMR. Other studies like del Pino et al. (2013) use only photometric data and try to break the age-metallicity degeneracy by finding the best model fit for a wide grid of possible age-[Fe/H] combinations. From our sample, we not only have precise metallicities for the majority of our stars, but also know alpha-element abundances for some of them, which enables us to reconstruct the alpha-enrichment for stars at a given [Fe/H] (see Hendricks et al. 2014a). Therefore, we are – for the first time – able to derive stellar ages in Fornax from isochrones *individually* tailored for the stellar [Fe/H] *and* $[\alpha/\mathrm{Fe}]$.

Precise photometric information is required in order to obtain a reasonable statistical uncertainty on stellar ages when measured for RGB stars. Originally, the main purpose of our photometry was the target selection, and consequently the photometric precision is lower than in dedicated photometric studies. For stars in our sample typically $\sigma(V-I) \approx 0.06$ and $\sigma V \approx 0.05$, which is too poor for a detailed age analysis (see Section 3.4.3). Therefore, we make use of the recently published photometric catalog from de Boer et al. (2012b), which covers the entire field of Fornax and provides B and V magnitudes for stars from the tip of the RGB down to the main sequence turn-off at $V \approx 23.5$. For stars in our magnitude range, their photometric precision is typically $\sigma(B-V) \approx 0.005$ and $\sigma V \approx 0.004$, and thus an order of magnitude better than our own photometric information. When we allow for a maximum astrometric deviation of $\delta(RA, Dec) = 1''$, we are able to match $\geq 95\%$ of all stars in our sample with a star from the de Boer catalog.

For our age-analysis, we use the Dartmouth-isochrone database[5] (Dotter et al. 2008), which provides stellar evolutionary sequences for $-2.5 \leq [\mathrm{Fe/H}] \leq +0.5$ over a wide range of alpha-abundances ($-0.2 \leq [\alpha/\mathrm{Fe}] \leq +0.8$). We use their [Fe/H]-interpolation program to generate isochrones for the exact stellar CaT-metallicities. The spacing in their grid of $[\alpha/\mathrm{Fe}]$ is 0.2 dex, so that we can anticipate a maximum discrepancy of 0.1 dex between the isochrone and the actual stellar value, which we assign by placing its CaT-metallicity on the empirical fiducial evolutionary alpha-sequence for Fornax determined in Hendricks et al. (2014a).

The foreground reddening in the direction to Fornax is low ($E(B-V) \approx 0.03$). However, from the reddening maps provided in Schlegel et al. (1998) we find that there is some fluctuation within the field of Fornax. Peak-to-peak differences are as large as $\delta E(B-V) \approx 0.05$ when the entire

---

[5] http://stellar.dartmouth.edu/models/index.html

area within its tidal radius is assessed, and $\delta E(B-V) \approx 0.015$, within the area of the two fields covered by our sample. Although these numbers appear small at first, they introduce a bias in the photometric color several times larger than the intrinsic photometric errors. Therefore, the color bias can cause systematically different ages of ≥ 1 Gyr for stars at different position in the galaxy, if a constant value is assumed (see Section 3.4.3). To avoid such systematics, we use the Schlegel et al. reddening maps to determine an individual reddening value for each star in our sample, based on its astrometric position. The resolution of the reddening maps (FWHM $= 6.1'$) provides information for ~ 13 individual positions in each field. Individual reddening values have then been derived through numerical interpolation, and the V-band extinction is computed assuming a standard reddening law so that $A(V)_\star = 3.1 \times E(B-V)_\star$.

Finally, individual ages are determined through linear interpolation of the age-color relation at the corresponding V-band magnitude of the star, providing continuous results despite the discrete grid of isochrone ages. Since the isochrones only provide fiducial evolutionary tracks for [Fe/H] ≥ -2.5, but our sample inlcudes a significant number of stars below that limit, we additionally derive lower age limits for stars between $-3.0 \leq$ [Fe/H] ≤ -2.5, by adopting the most metal-poor isochrone available for these stars. All isochrones are shifted according to a distance modulus of $(m-M)_0 = 20.84$, corresponding to a distance of 147 kpc, adopted from the most recent measurement of Pietrzyński et al. (2009).

In Figure 3.9, we show the resulting AMR for Fornax. Because the age-precision fundamentally depends on the photometric quality and the uncertainty in [Fe/H], we only show stars for which $\sigma(B-V) \leq 0.01$ and $\sigma[\mathrm{Fe/H}]_{\mathrm{CaT}} \leq 0.15$. We further restrict our sample to stars with $V \leq 19.5$ mag, due to a significantly lower age-sensitivity of isochrones at fainter magnitudes. Finally, we exclude all stars for which $\Delta([\mathrm{Fe/H}]_{\mathrm{CaT}} - [\mathrm{Fe/H}]_{\mathrm{Fe}}) \geq 0.3$.

Overall, we find a clear correlation between age and [Fe/H], where older stars are more metal-depleted. The very few young but metal-poor stars can most likely be assigned to a small fraction of either foreground stars or AGB interlopers, which may be present in our sample. It is striking that the detailed chemical enrichment appears different for the two distinct fields from which our sample is taken. The most likely origin of the systematic difference in individual stellar ages is a zero-point difference within the photometry, since the angular separation between Field 1 and 2 is almost 1°, and the photometry for each field thus originates from different pointings. Therefore, small variations in the photometric zero-points for each field can be expected. Specifically, we find that a constant shift of only $\Delta(B-V) \approx 0.05$, applied to one of the fields, is sufficient to bring the AMR of both fields in agreement (see Section 3.4.3 for a detailed discussion).

For Field 1, we find an extremely fast enrichment for ages older than ~ 8 Gyr, after which the enrichment becomes shallow and [Fe/H] only increases by ~ 0.3 dex over ~ 6 Gyr, indicating a non-linear evolution of [Fe/H] with time. Finally, the chemical enrichment seems to steepen again for stars younger than 4 Gyr, which hints at a sudden increase in SF activity at this epoch. Interestingly, this AMR shows similarities with the chemical enrichment pattern of the Magellanic Clouds (Pagel & Tautvaisiene 1998). However, the SFH of Fornax has to be somewhat different from these systems, given the larger fraction of old, metal-poor stars in Fornax compared to both the Large- and the Small Magellanic Clouds (Cole et al. 2000, Dobbie et al. 2014). From Field 2, the evolution of [Fe/H] appears slightly more linear with only a smooth flattening in chemical enrichment over time and generally younger ages. As we will discuss below, a comparison to chemical evolution models favors the ages derived from Field 1 to be the sample with the more accurate photometric calibration. The observed scatter in the AMR of both fields can be caused by statistical uncertainties in the photometry and chemical abundances of the stars, or it can be introduced by systematic outliers like foreground dwarfs and AGB stars. Taking these effects together, the observed scatter does not give a hint for a significant intrinsic spread.

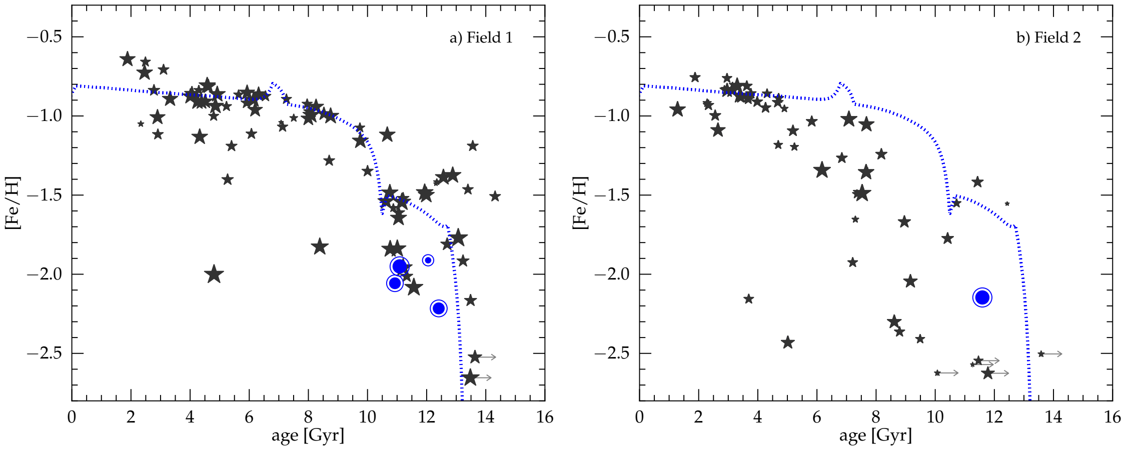

Figure 3.9: Age-metallicity relation for Fornax field stars within the two distinct fields of our study. **Left:** South-Western field centred at $(\alpha,\delta) = (02^h38^m06^s.5, -34°49'52''.7)$, **Right:** North-Eastern field centred at $(\alpha,\delta) = (02^h41^m49^s.6, -34°03'55''.5)$. The observed differences between the AMR of Field 1 and 2 are most likely due to small zero-point variations in the photometry (see text). Symbol sizes in both panels reflect the statistical precision of the photometry and [Fe/H], where larger symbols indicate a better quality. Symbols with a right-handed arrow label additional stars with $-3.0 \leq [\mathrm{Fe/H}] \leq -2.5$, which fell outside the lower isochrone range and for which we adopted $[\mathrm{Fe/H}] = -2.5$ to derive lower age limits. Blue symbols highlight stars which we identified as members of the GC H2 (left panel) and H5 (right panel), respectively. The dotted blue line in both panels shows the model prediction for the best fitting SFH from Hendricks et al. (2014a), when we assume the age of Fornax to be 13.3 Gyr. While stars from Field 2 appear systematically younger than the model, the AMR from Field 1 shows excellent agreement with the predicted sequence. In contrast, in order to obtain a reasonable fit for Field 2, Fornax could not be significantly older than 10 Gyr, a scenario which can be ruled out from previous photometric and spectroscopic age estimations. From the well populated AMR of Field 1, we find a fast enrichment in [Fe/H] until $\sim$ 8 Gyr ago, after which the enrichment becomes extremely shallow so that a wide range of ages accumulate at $[\mathrm{Fe/H}] \approx -1.0$. Finally the chemical enrichment seem to steepen again for stars younger than 4 Gyr, indicating a sudden increase in SF activity at this time.

Chemical evolution models for dSphs (e.g., Lanfranchi & Matteucci 2003) naturally predict the AMR for an assumed SFH of a galaxy. In a recent study, these models have been used to constrain the SFH in Fornax from chemical element information (Hendricks et al. 2014a). In Figure 3.9, we overplot the predictions for our best-fitting evolutionary scenario from that work. This model is characterized by three major SF bursts and an increasing SF efficiency over time. Generally, the model predicts an extremely fast enrichment at early times and an almost flat [Fe/H]-plateau after the first few Gyr, as we observe in the data. When we set the age of Fornax in the model to 13.3 Gyr, we find an excellent agreement with the AMR as seen in Field 1 while ages derived from stars in Field 2 appear systematically younger than the model prediction. The age assumption for Field 1 seems reasonable when compared to previous studies that consistently found stars $\geq$ 12 Gyr in Fornax (Battaglia et al. 2006, de Boer et al. 2012b). In contrast, to obtain a reasonable model agreement for Field 2, the assumed age of Fornax needs to be $\leq$ 10 Gyr, a scenario which can be ruled out from previous photometric and spectroscopic age estimations of Fornax' oldest populations. Specifically, the lower age limit of Fornax should be constrained by its GC population, and at least three of the five globulars are older than 12 Gyr (Strader et al. 2003).

Here, we are also able to derive ages for one star in the GC H5 and four stars in H2 (blue symbols in Figure 3.9). As expected, all stars from both clusters have about the same age ($\sim$ 12 Gyr). The

GCs fall on top of the observed field-star sequence, indicating a similar early chemical enrichment of the ISM out of which the clusters and the field population formed. Here, it would clearly be of interest to have precise [Fe/H] and age information for the GC H4, which is presumably significantly more metal-rich and possibly younger than the remainder of Fornax' GC population. Placed in the AMR of the field stars, this GC could help to answer the question of whether the proto-GC material was enriched in the same way as the field of the galaxy. Note, that star ID 278, which we dubbed as a field star in the line-of-sight to GC H5 from its RV signature, also has a significantly younger age estimate (7.40 Gyr) in our analysis. This supports our previous assumption that it is not an actual member of the cluster.

Finally, it is worth noting that we do not observe any difference in the AMR when we split our sample into subgroups of stars with $r_{ell} \leq 0.6^\circ$ and $r_{ell} \geq 0.6^\circ$, and therefore do not see signs of a differential chemical enrichment at different galactocentric distances. However, we cannot rule out such differential effects due to our limited radial coverage. It would be desirable to have a spectroscopic sample of stars with accurate, homogeneous photometry over the whole tidal range to test this hypothesis.

3.4.1 Chemical vs. Photometric SFH

The star formation history of Fornax has been studied recently by de Boer et al. (2012b) and Weisz et al. (2014), both using a photometric approach to derive the most likely scenario from synthetic CMD fitting. While de Boer et al. (2012b) use ground-based photometry with an extended spatial coverage from the center of the galaxy out to $\sim 0.8^\circ$, the results of Weisz et al. (2014) are based on deep HST photometry of Fornax that however only covers the central parts of the galaxy. Both (photometric) studies find an extended SFH for Fornax, starting ≥ 12 Gyr ago and lasting to very recent times, with a fairly constant SF rate during most of this period. Interestingly, de Boer et al. (2012b) additionally report a radial variation in the SFH within the galaxy such that in the outer parts a larger fraction of stars have been formed at early times, compared to the SFH in the central region.

While the above-mentioned studies present a purely empirical SFH from photometry, the scenario proposed by us is based on a physical model adjusted to fit the chemical properties of the galaxy. The observed AMR in our study supports a SFH with extended episodes of SF interrupted by short periods of low activity and characterized by an increasing SF efficiency over time, as has been used in our previous paper to fit the chemical evolution of alpha-elements and the MDF in Fornax (see Hendricks et al. 2014a). The AMR additionally shows evidence of an increase in SF activity ~ 4 Gyr ago, seen as a sudden increase in [Fe/H] thereafter.

Because the gas available to serve as star forming material within the galaxy decreases over time, our proposed scenario with increasing SF efficiency predicts a roughly constant SF rate, as also observed in Weisz et al. (2014). From the upper panel in Figure 3.10, it is clear that there is no fundamental difference between these two scenarios. However, our model predicts a generally larger fraction of stars produced at old times, a trend which can be explained when taking the different radial positions of the samples and the radial trend in Fornax' SFH into account. While Weisz et al. (2014) exclusively evaluate the central parts of the galaxy, our sample covers exclusively the outer parts, where a shift towards earlier SF is expected (de Boer et al. 2012b). In addition, a lack of recent SF – consequently a lack of young stellar populations – predicted by the model, could be compensated for by an additional episode of SF triggered by external effects like a merger event or the re-accretion of previously expelled gas. Such environmental impacts on the evolution of Fornax cannot be considered in our simple leaky-box model. This scenario would not only account for the discrepancies between the predicted and observed SFH, but could simultaneously explain the observed sudden increase in [Fe/H] at this time within the galaxy.

Finally, the time-resolved SFR shown in de Boer et al. (2012b) is in excellent agreement with our model when we consider only the radial areas which overlap with the spatial extend of our sample (i.e., annuli 4 or 5 in their paper). Their observations, as well as our scenario, predict a slightly higher SFR at early times, until $\sim 9.5\,\mathrm{Gyr}$ ago, after which the SFR drops continuously (see lower panel in Figure 3.10). Hereby, it is important to stress that short gaps ($\leq 1\,\mathrm{Gyr}$) between the bursts of SF – as proposed in our scenario – are not in conflict with the continuous SFH derived from synthetic CMD fitting because these studies are unlikely to resolve short-time variations (de Boer et al. 2012a).

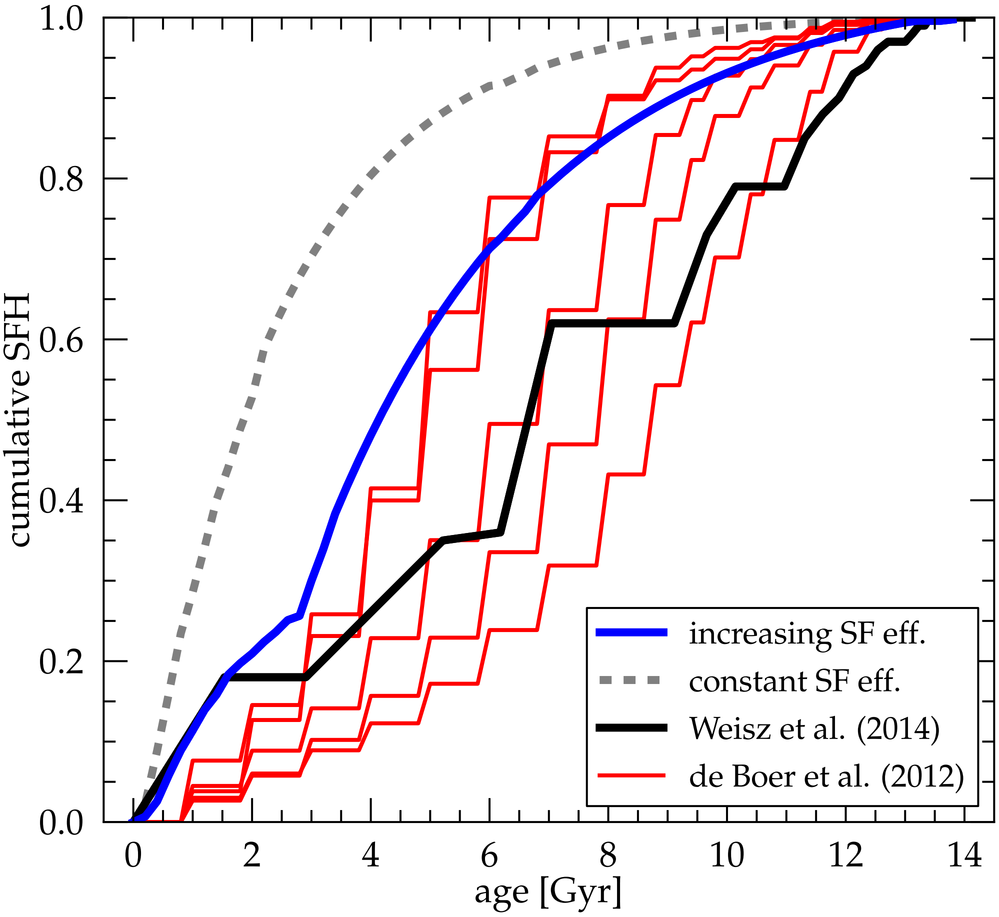

Figure 3.10: Comparison between the photometric SFH from Weisz et al. (2014) (black) and our proposed evolutionary scenario (blue) based on the chemical evolution for the alpha-elements, the MDF, and the observed AMR in the outer parts of Fornax. The red lines show the radially resolved SFHs for five distinct radial positions in Fornax from de Boer et al. (2012b). Our history results matches best with the photometric sequence obtained from the outermost radii used in de Boer et al. (2012b).

3.4.2 Signs for different Dynamical Populations

Signs of dynamical peculiarities in Fornax field stars have been reported in several previous studies. Battaglia et al. (2006) were the first to report a larger velocity dispersion in the central region of the galaxy with bimodal RVs among central metal-poor stars compared to the more enriched populations. Later, a significant variation in the velocity dispersion between the metal-rich and the metal-poor stellar component was confirmed by Walker & Peñarrubia (2011). Subsequently, Amorisco & Evans (2012) found that when stars with different metallicities are split into three subgroups, each of them shows signs of a distinct dynamical behavior, leading to the conclusion that a merger event in the past (preceded by a "bound-pair" scenario) may be a possible explanation.

As can be seen in Figure 3.11, we also observe complex dynamics in the outskirts of Fornax. Using the CaT-metallicities, we determine both the mean RV and the intrinsic velocity dispersion as a function of [Fe/H], following the same algorithm described in Section 3.2.1. We find that the velocity dispersion steadily increases from $\sigma_{sys} \approx 7.5\,\mathrm{kms}^{-1}$ for $[\mathrm{Fe/H}] \geq -1.0$ to dispersions as high as $15\,\mathrm{kms}^{-1}$ for the most metal-poor stars. While different velocity dispersions for stellar populations in Fornax have been previously reported, here we are able to show that these variations not only concern a specific population in the galaxy but are instead part of a continuous trend from the most metal-poor to the most metal-rich stellar components in Fornax. Such a dynamical pattern would be expected for a tracer population in the central parts of a dark matter dominated halo, undergoing an outside-in SF.

Figure 3.11 also indicates that individual metallicity subgroups have significantly different systemic line-of-sight velocities. To stress this fact, we overplot seven distinct subsamples and their intrinsic uncertainties to the floating mean, which indicates that stars between $-2.2 \leq [\mathrm{Fe/H}] \leq -1.5$ display a larger RV than the rest. However, because our sample is locally constrained, it is possible that we do not observe global trends with [Fe/H] but instead local inhomogeneities within the galaxy.

In Figure 3.12 we show the individual distribution of line-of-sight velocities at different metallicities and ages. When we follow the radial velocities of stars with increasing age (left panel in Figure 3.12), the velocity dispersion not only increases systematically towards older stars, but the stars show a slightly bimodal RV distribution: stars with ages ~ 7 Gyr and younger have a small velocity dispersion around the galactic mean motion, older stars are equally distributed between high ($\sim 70\,\mathrm{km\,s}^{-1}$) and low ($\sim 45\,\mathrm{km\,s}^{-1}$) RVs. These observations suggest that the non-Gaussian dynamical pattern of metal-poor stars, reported by Battaglia et al. (2006) for the inner regions of the galaxy, in fact has a continuation to larger radii.

The existence of a non-Gaussian dynamical distribution of stars only within a specific population bears the risk of introducing a selection bias to any stellar sample, if membership is assigned with a sigma-clipping procedure based on stellar velocities. In this scenario, preferably members of the population which is not in dynamical equilibrium would be excluded from the sample, in the case of Fornax the oldest and most metal-poor stars. We therefore re-examine those stars in our sample which we excluded from the analysis due to deviant velocities. From 11 candidates with CaT-metallicities, 9 have $[\mathrm{Fe/H}] \leq -1.4$, and by that fall, e.g., in the metallicity range of the existing GC systems in Fornax. However, these metallicities also show the expected [Fe/H] pattern of Halo foreground contaminants (e.g., Schörck et al. 2009, Ryan & Norris 1991).

It is important to note that the determination of σ_{sys} assumes a (Gaussian) distribution of velocities for stars in dynamical equilibrium. If a significant fraction of a stellar system shows kinematical substructures (McConnachie et al. 2007) or bimodalities (Battaglia et al. 2006), as may be the case for Fornax, the use of the projected velocity dispersion profile to interpret the dynamical state of galaxy field stars in Fornax, e.g. for mass estimations, is ambiguous.

3.4.3 Discussion of Age Uncertainties

Parameters that contribute to the age uncertainty (σage) of our targets are the photometric errors (in color and magnitude), the uncertainty in metallicity and $[\alpha/\mathrm{Fe}]$, which define the set of isochrones

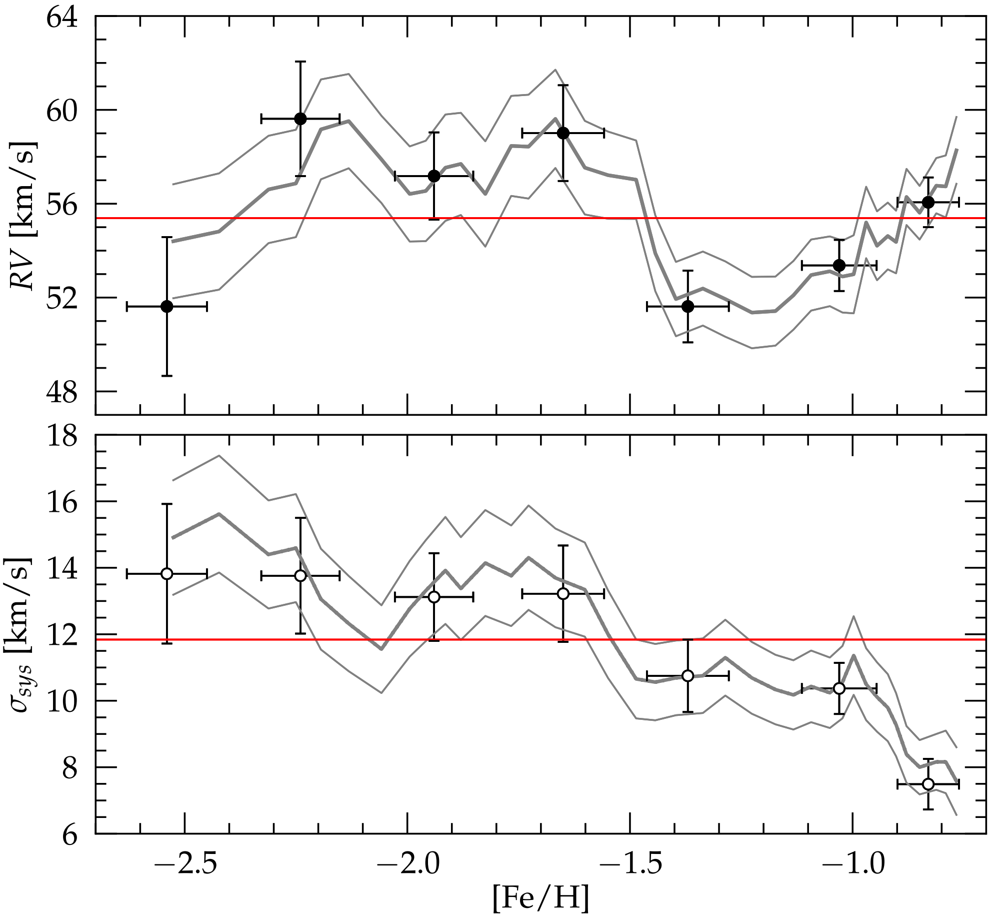

Figure 3.11: Top: Radial velocities over the full range of [Fe/H] covered by our sample. The thick and thin solid lines represent the floating mean and the 1σ-uncertainty interval for subsamples of 80 stars. Measurements for seven independent metallicity intervals with 0.3 dex in size have been additionally taken and are shown as black dots. While the vertical error-bars indicate the intrinsic uncertainty for each bin, the horizontal bars represent the standard deviation of [Fe/H]-values in each bin. The red line marks the mean systemic RV for the whole sample. We do not observe a significant trend in RV with [Fe/H], but the data show signs that there exist different velocity subgroups. **Bottom:** Same as in the top panel, for the velocity dispersion. A clear trend is visible with higher σ_{sys} towards lower [Fe/H].

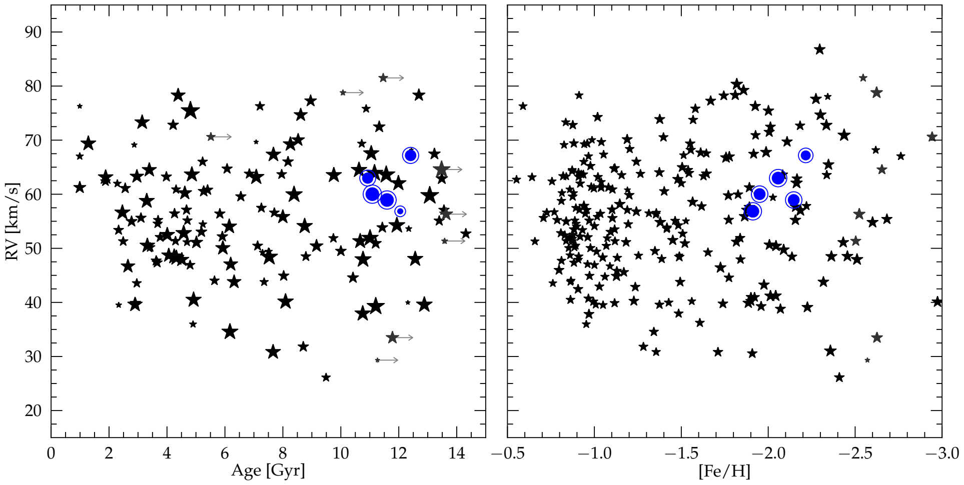

Figure 3.12: Left: Individual radial velocities as a function of age. Symbols with a right-handed arrow show stars which fell out of the lower metallicity range of the isochrones and therefore only lower age limits could be determined. **Right**: Radial velocities as a function of [Fe/H]. In both panels, an increase of the velocity dispersion with decreasing [Fe/H] or age is visible. The RV distribution becomes non-Gaussian for stars older than ~ 8 Gyr or below $[\mathrm{Fe/H}] = -1.5$. In the right panel, we plot all stars with a valid CaT-measurement, whereas in the left panel we restrict our selection to the same sample shown in Figure 3.9. As before, larger symbols indicate stars with higher photometric and chemical precision and blue symbols highlight stars associated with the GCs H2 and H5.

used for each star, as well as uncertainties in the distance modulus and interstellar reddening. In our case, *all* of the above-mentioned sources have a significant impact on the total precision and accuracy with which individual stellar ages can be derived. However, absolute ages also depend on the chosen set of isochrones and moreover to the uncertainties in the underlying stellar physics. Therefore, the total age uncertainty includes assumptions on mixing length, core-overshooting, mass loss, etc. in the models, which to discuss is beyond the scope of this study. In the following, we consequently limit our discussion to uncertainties in relative ages and discuss the net-effects of σmag, $\sigma color$, $\sigma[\mathrm{Fe/H}]$, and $\sigma[\alpha/\mathrm{Fe}]$ on the age when derived from RGB stars and under the assumption that the adopted model sequences predict the stellar position in a CMD correctly.

The major sources for statistical error in the age determination are the photometric color uncertainty – in our case $\sigma(B-V)$ – as well as the intrinsic error in the assumption of the stellar metallicity ($\sigma[\mathrm{Fe/H}]$) and alpha-abundance ($\sigma[\alpha/\mathrm{Fe}]$). Typical photometric uncertainties for stars in our sample with $V \leq 19.5$ are $\sigma(B-V) \approx 0.005$ and $\sigma V \approx 0.003$. For $\sigma[\mathrm{Fe/H}]$ and $\sigma[\alpha/\mathrm{Fe}]$, typical values are 0.1 dex and 0.15 dex, respectively.

The adopted distance modulus has a strong systematic effect on the age determination, especially for stars close to the tip of the RGB. For Fornax, a variety of standard candles have been used to determine the distance, including Cepheids (Greco et al. 2005), tip-RGB magnitudes in the optical (Buonanno et al. 1999, Bersier 2000) and NIR (Pietrzyński et al. 2009), as well as the luminosity of the red clump (Bersier 2000, Pietrzyński et al. 2003). While some studies state an intrinsic error of ~ 0.1 dex (corresponding to a true distance error of ~ 8 kpc), one has to take into account that *all* photometric standard candles require empirical calibrations that are dependent on the assumed metallicity and age in the system (e.g., Valenti et al. 2004). Because generally GCs are used to calibrate the photometric standard candles, some systematic differences can be expected when applied to the field star population in a galaxy. Consequently, for systems like Fornax, which show a significant intrinsic variation in [Fe/H] and age, the total uncertainty of the distance modulus is likely higher than the above stated number, even for up-to-date measurements. Here, we adopt $(m-M)_0 = 20.84 \pm 0.12$, the most recent distance determination from Pietrzyński et al. (2009), determined from the tip-RGB magnitude in the NIR. The quoted uncertainty is not only the intrinsic (statistical+systematic) error of their method, but is also a reasonable reflection of the variation between different existing distance values from various studies in the past (see Table 3 in their paper).

Although the line-of-sight foreground reddening in the direction to Fornax is small (see previous Section), the reddening maps from Schlegel et al. (1998) have a zero-point uncertainty of 0.016 in $E(B-V)$ and a pixel-to-pixel statistical uncertainty of $0.16 \times E(B-V)$, which corresponds to $\sigma(B-V) \approx 0.005$ in our field-of-view. These numbers are similar in size compared to $\sigma(B-V)$ in the photometry and therefore add significantly to the overall error in the age analysis.

Taken together, $\sigma color$ is mainly of statistical nature and dominated by a combination of $\sigma(B-V)$ from the photometry and $\sigma E(B-V)$ from the reddening maps. In contrast, σmag is dominated by the systematic uncertainty in the distance modulus.

In order to quantify age uncertainties for stars in our sample of different [Fe/H] and age, we generate a fine grid of isochrones between $-2.5 \leq$ [Fe/H] ≤ -0.8 and for ages between 2 and 15 Gyr with steps of 0.1 dex and 0.5 Gyr, respectively. Then, for each point in this parameter space, we determine the age difference when we vary σmag, $\sigma color$, σ[Fe/H], and $\sigma[\alpha/\mathrm{Fe}]$ according to their estimated values. All calculations are performed for a star at a distance to the tip of the RGB of 0.5 mag (in our case $V = 19.0$ mag), which is typical for our sample.

The results are shown in Figure 3.13. Generally, ages for older stars become more uncertain. As can be seen in panel a), $\sigma(B-V)$ causes $\sigma age \leq 0.5$ Gyr for the majority of younger and metal-rich populations, which rises to $\sigma age \approx 1$ Gyr for the oldest stars. From panel c) and d), we find that both σ[Fe/H] and $\sigma[\alpha/\mathrm{Fe}]$ introduce a statistical uncertainty to our ages which varies between $\sigma age \leq 2$ Gyr for most of our targets up to $\sigma age \approx 5$ Gyr for old but metal-rich targets. However, since this region is not covered by "real" stars (see Figure 3.9), the maximum uncertainty introduced by chemical input parameters should not exceed 3 Gyr. One of the strongest impacts on stellar age comes from the uncertainty in the distance modulus. From panel b), we find that while young stars are accurate to better than 2 Gyr, old stars become systematically uncertain to as much as 3-4 Gyr.

It is important to note that the effect of all error-afflicted parameters in the age determination process are highly asymmetric. Specifically, the results are more uncertain towards iron-depleted stars. However, to minimize the cases where a stellar age falls outside the grid of available isochrones, and therefore to maximize the available parameter space in our grid, in Figure 3.13 we evaluate only the difference between the actual and the younger age, and the errors needs to be multiplied by a factor of ~ 1.5 to obtain the error towards older ages.

In summary, for most of our young and metal-rich targets $\sigma(B-V)$, σ[Fe/H], and $\sigma[\alpha/\mathrm{Fe}]$ will cause an error in age of less than 0.2, 1, and 1 Gyr, respectively. Consequently, a total statistical age uncertainty of $\sigma age \approx 1.5$ Gyr can be expected in our analysis, topped with a possible systematic shift of at least 1 Gyr on the age. For the oldest and metal-poor stars, we obtain a statistical error of ~ 2.5 Gyr and a systematic accuracy ~ 2 Gyr. Therefore, it is important to stress that the ages, specifically of old stars, should be interpreted with caution, and a sample with both better photometric accuracy and a better knowledge about the distance to Fornax is needed to reduce the systematic impact on our results.

At this point, we can revisit the difference in the AMRs between the two distinct pointings in our sample which are shown in Figure 3.9. First, it should be noted that the large majority of stars in both fields share a common distance to the center of Fornax. Therefore, we can rule out that the bias we observe is caused by radial variations in the chemical enrichment. Other than that, the different trend in the ARM could be caused by systematic differences in the CaT-metallicities. We can rule out systematics in [Fe/H] for several reasons: first, the spectra have been taken with the same instrument and have been processed and analyzed with the same pipelines. We do not find a zero-point difference between the MDFs for both fields. Second, there is a subsample of our dataset that was also analyzed in Battaglia et al. (2006), and we do not observe any systematic offset between the two sets, although it includes stars from both fields. Finally, there is no difference between the two fields when the results are compared to [Fe/H] independently determined from iron absorption lines. The only systematic source left is the photometric information for our stars, and in fact we see strong evidence that differences in the photometric zero-points are the reason for the putative difference in the chemical enrichment path between Field 1 and 2. Due to the wide separation of the two fields (almost 1°in the sky), the photometry for each of these two subsamples comes from different pointings (see Figure 1 in de Boer et al. 2012b). Although the authors used an overlap in the individual frames to find a common photometric zero-point for all fields, a remaining uncertainty of 0.03 mag in each filter is typical (see, e.g., Coleman & de Jong et al. 2008) and the zero-point difference in any photometric color can therefore be expected to be different by ~ 0.04 mag. This offset is almost an order of magnitude higher than the statistical error evaluated in Figure 3.13 and consequently can cause age differences from 2 to 4 Gyr, depending on the age and metallicity of the star. Therefore, the offset between the AMRs shown in Figure 3.9 is most likely the result of small zero-point variations in the photometry at different positions in the galaxy.

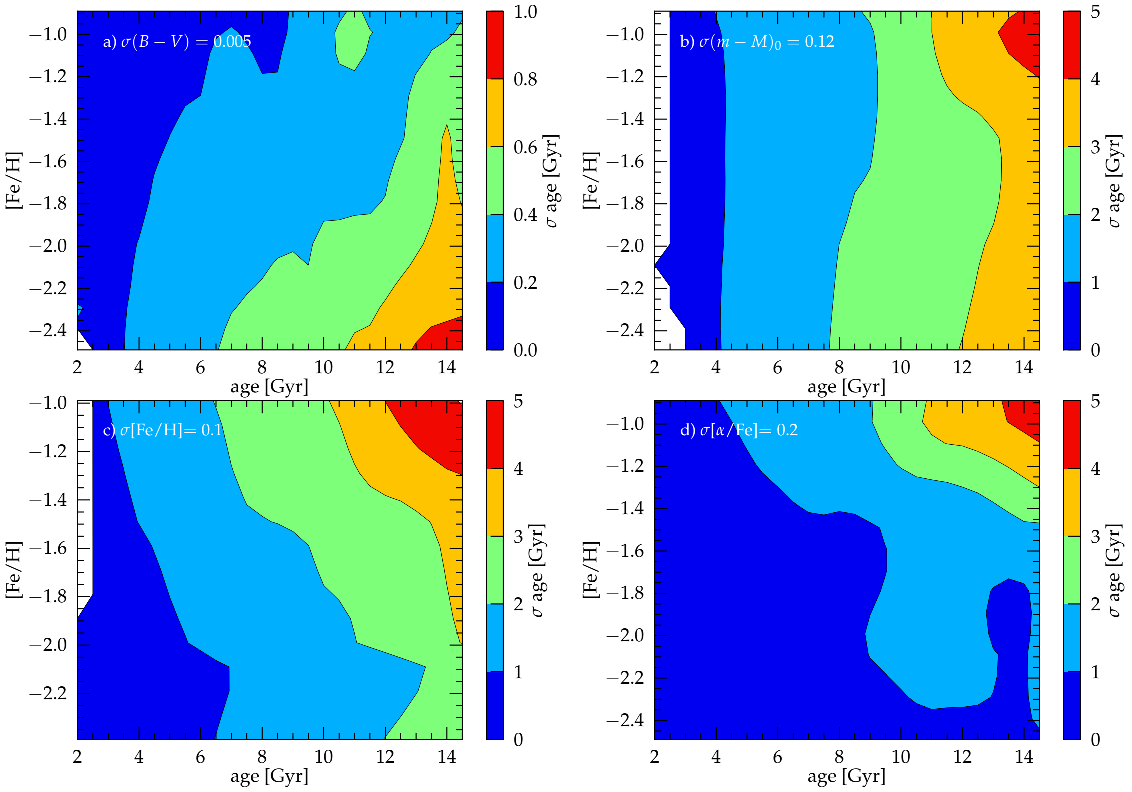

Figure 3.13: Assessment of different sources of uncertainty on our ages. **a)** shows the correlation between $\sigma(B-V)$ and σage. Here we choose $\sigma(B-V) = 0.005$, a typical value for our photometry. The resulting age uncertainty is generally small (≤ 1 Gyr) and increases from young, metal-rich, to old and metal-poor stars. In **b)** the effect of 0.12 mag variation in the distance modulus on the derived stellar ages is shown. For shorter distances, generally younger ages are obtained with an increasing effect for older stars. In **c)** the sensitivity of our age analysis on the assumption of stellar metallicity is shown. Similar to the photometric uncertainty, the effect increases with stellar age but is significantly larger for typical uncertainties of $\sigma[\text{Fe/H}] = 0.1$. Finally, **d)** shows the age sensitivity on the adopted $[\alpha/\text{Fe}]$, relative to a solar ratio which reveals a very similar and only slightly smaller effect on stellar ages than $\sigma[\text{Fe/H}]$.

3.5 The Metallicity Distribution Function

The MDF gives important insight into the integrated chemical enrichment history of a galaxy and it can help to constrain different enrichment scenarios, especially when it is used in combination with detailed enrichment models (e.g., Kirby et al. 2011a, Lanfranchi & Matteucci 2010, Hendricks et al. 2014a). Asymmetries or distinct peaks in the MDF can be signs of intense, burst-like star formation or accretion events in the past. Because dSphs may possibly have contributed to the build-up of the Galactic Halo, the metallicity budgets of dwarf galaxies are also important keys to better understand if, and to what extent these systems have donated their populations to our Galaxy (e.g. Helmi et al. 2006, Starkenburg et al. 2010).

3.5.1 Distinct Stellar Populations in Fornax?

The MDF drawn from our complete sample of 340 field stars is shown in Figure 3.14. The binning size is chosen according to the median uncertainty $\sigma[\mathrm{Fe/H}] = 0.10$ dex for our CaT-metallicities. To remove possible binning-biases, we also show the error-convolved interpretation of the same distribution. In addition to the field stars, we also plot the metallicities of stars which we have previously identified as GC members (see Section 3.2.4), as well as the small sample of stars which fall outside of our RV-membership criterion (see Section 3.2.1) but may nonetheless be members of the galaxy with non-Gaussian dynamics. In the following, we will use the term *population* only for stars who share the same age, while stars with same metallicity will be denoted as a *group*, motivated by the fact that these groups can in fact host several generations of stars.

Generally, the MDF is dominated by a prominent metal-rich group at $[\mathrm{Fe/H}] \approx -1.0$ and a significant fraction of stars at lower metallicities, down to -3.0 dex. The mean metallicity of our sample is $[\mathrm{Fe/H}] = -1.48$ at a mean radius of $r_{ell} = 0.57°$. The sample displays two more spikes in the metallicity distribution: one peaking at -1.9 dex, indicating a large metal-poor group, and a second one located at $[\mathrm{Fe/H}] \approx -1.4$.

The small group of GC stars coincides with the metal-poor peak in the field-star MDF. Therefore, it is possible that this overdensity is the result of accreted GC stars during earlier evolution. Such a scenario is discussed in Larsen et al. (2012a), who estimate the total fraction of former GC stars in the field star population of Fornax to be $\geq 20\%$. The "contamination" of a galaxy by a significant fraction of GC stars might also be the case for other dwarf galaxies (Larsen et al. 2014), and should be considered when the MDF is used to interpret the chemical evolution history of these systems.

The peak at ≈ -1.0 dex has been observed in all previous studies in more central areas (Pont et al. 2004, Battaglia et al. 2006, and Letarte et al. 2010), and we still find it to be the prominent feature at larger radii. However, this population practically disappears for $r_{ell} \geq 0.65$ (see Section 3.6). Battaglia et al. (2006) also find a significant group of more metal-poor stars (which they define by $[\mathrm{Fe/H}] \leq -1.3$) and a very metal-rich group at $[\mathrm{Fe/H}] \approx -0.6$. In a later study, Amorisco & Evans (2012) show that there are indeed distinct dynamical properties among the three subgroups of stars. Our MDF suggests that the "metal-poor" group shows an additional peak at $[\mathrm{Fe/H}] = -1.4$ and therefore may in fact be composed of several distinct populations. Although the number of stars in our analysis is still too small to rule out an artifact from small-number statistics, it is remarkable that *all* previously mentioned studies display a peak or a bump in the MDF at $[\mathrm{Fe/H}] \approx -1.4$, which supports our findings (see also Coleman & de Jong et al. 2008 who find three peaks at $[\mathrm{Fe/H}] = -1.0$, -1.5, and -2.0).

When we use the Kaye's Mixture Modeling (KMM) algorithm of Ashman et al. (1994) to divide the sample in several Gaussian-shaped metallicity populations, we find that at least 4 populations are required to obtain an adequate fit to the sample. Importantly, the metal-rich peak is extremely well resembled with a single Gaussian fit. In contrast, it is likely that at least the metal-poor populations (≤ -1.8 dex) should not be described by a Gaussian profile, and we consider these stars to be part of one or several non-Gaussian groups. With these assumptions, we find that the [Fe/H]-groups in our sample peak at -0.97 dex, -1.45 dex, and -2.11 dex, with relative contributions to the overall sample of 45%, 18%, and 37%, respectively. The position of the latter group is determined from the weighted combination of the two most metal-poor Gaussian fits.

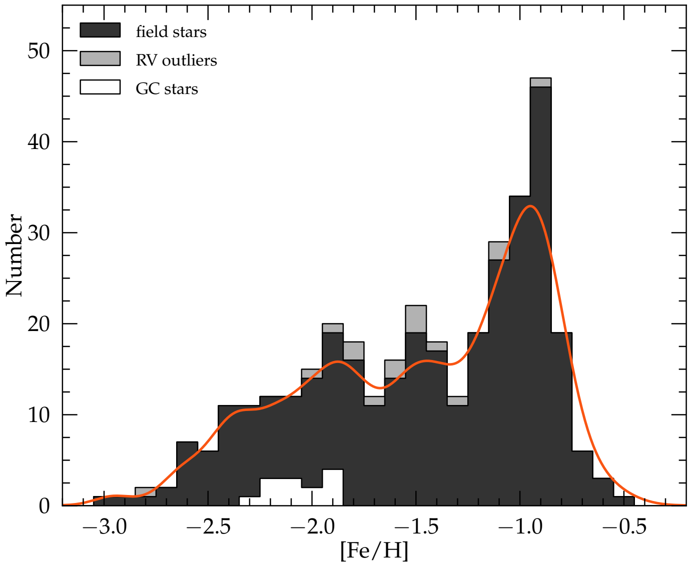

Figure 3.14: MDF from our sample of stars in two outer fields at $r_{ell} \sim 0.6°$in the Fornax dSph. Different shadings show different components in our sample, where we explicitly highlight the stars which we removed in the process of the radial-velocity clipping. We note that this selection process did not introduce any bias to our sample. The red line is the error-convolved version of the underlying field-star histogram.

3.5.2 Comparison between Fornax and Sculptor

Fornax is about ten times more massive than Sculptor today, but both systems share a similar early chemical enrichment history drawn from their α-element evolution (Hendricks et al. 2014a). When their SFHs are compared, the major difference between them seems to be that Sculptor stopped star formation $\sim$ 7 Gyr ago (de Boer et al. 2012a), while Fornax kept forming stars almost until today (Stetson et al. 1998, de Boer et al. 2012b).

The metal-rich peak in the MDF of Fornax as drawn from our sample is strikingly narrow, and in fact can be fit with a single Gaussian profile using a FWHM corresponding to the statistical uncertainty of our CaT-metallicities and thus indicating a very low intrinsic metallicity scatter within the group. In Figure 3.15, we indicate the mean stellar age for each individual metallicity interval of the MDF. Thus, it becomes clear that the metal-rich group does not consist of a one coeval population, but is in fact a mixture of stars between 4 and 8 Gyr. Consequently, practically all stellar populations in Fornax that formed after the end of SF in Sculptor are combined in this metal-rich group of stars.

It is possible that this late, intense episode of SF in Fornax was either caused by a late merger event or an otherwise triggered event of SF, e.g., through re-accretion of previously heated or expelled gas as discussed in Ruiz et al. (2013) or D'Ercole & Brighenti (1999), or triggered by environmental influences like tidal interactions or ram pressure shocks. In order to mimic a SFH in Fornax which *lacked* such an event and any SF younger than $\sim 8\,\mathrm{Gyr}$, we use the previously determined *KMM* parameters to fit the prominent, narrow peak with a single Gaussian profile and then simply subtract this group from the convolved histogram of the full sample (see Figure 3.16).

The metallicity distribution of Sculptor in Figure 3.16 is adopted from the recent study of Romano & Starkenburg (2013). Specifically, it has been derived from the centrally constrained sample of Kirby et al. (2008) and the sample from Battaglia et al. (2008) that provides the metallicity distribution of stars in the outer parts. Therefore, Sculptor's MDF represents a balanced distribution of stars from the central area to the very outskirts of the galaxy.

Remarkably, the truncated MDF, rescaled to the now smaller stellar budget, exactly matches the MDF of Sculptor. The small group at $[\mathrm{Fe}/\mathrm{H}] \approx -0.7$, visible in the truncated MDF of Fornax, has been previously identified in more central regions of this galaxy (e.g Amorisco & Evans 2012), and is likely composed of stars younger than 2 Gyr. Therefore, the distribution of metals in Fornax and Sculptor becomes identical at exactly the point when the additional SFH of Fornax with respect to Sculptor is removed from the sample. Consequently, it is likely that these two systems have a very similar enrichment history before Sculptor stopped forming stars 7 Gyr ago. Such a synchronous evolution between the two galaxies would be in good agreement with their similar alpha-element evolution (Hendricks et al. 2014a), which requires a similar chemical enrichment at least during the first $\sim 1\mathrm{Gyr}$.

Vice versa to a scenario in which Fornax late SF is caused by a late accretion of additional material, the difference in the late evolution of the two galaxies can possibly be evoked by their individual ability to *retain* their reservoir of gas. Starting with a similar initial mass, the observed properties in their MDF and in the evolution of alpha-elements would be evoked if Sculptor lost a significant fraction of its gas through tidal stirring, whereas Fornax did not. Such a scenario may be supported by the orbital properties of both galaxies because Sculptor's estimated perigalactic distance (about 68 kpc) is by a factor of ~ 2 smaller than that of Fornax (Piatek et al. 2006), and it is likely to follow an orbit with higher excentricity. In this case, Sculptor did experience stronger (and more frequent) tidal forces, which could explain the early loss of gas. We note, however, that orbital parameters for both dSphs come with large uncertainties and it does not seem advisable to draw strong conclusions from them.

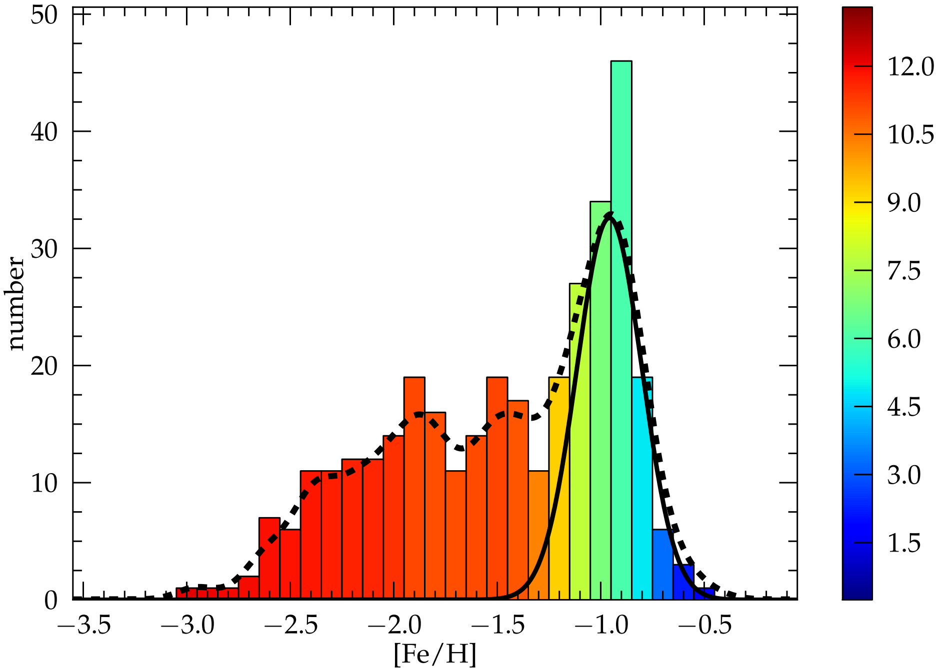

Figure 3.15: As Figure 3.14, but with an additional color-scale indicating the mean age of stars in each metallicity interval. The colors range from zero age (blue) to 13 Gyr (red). The dashed line is the error-convolved version of the underlying histogram and the solid curve shows the best-fitting Gaussian to the distribution of stars around [Fe/H]= −1.0 dex (see text for details).

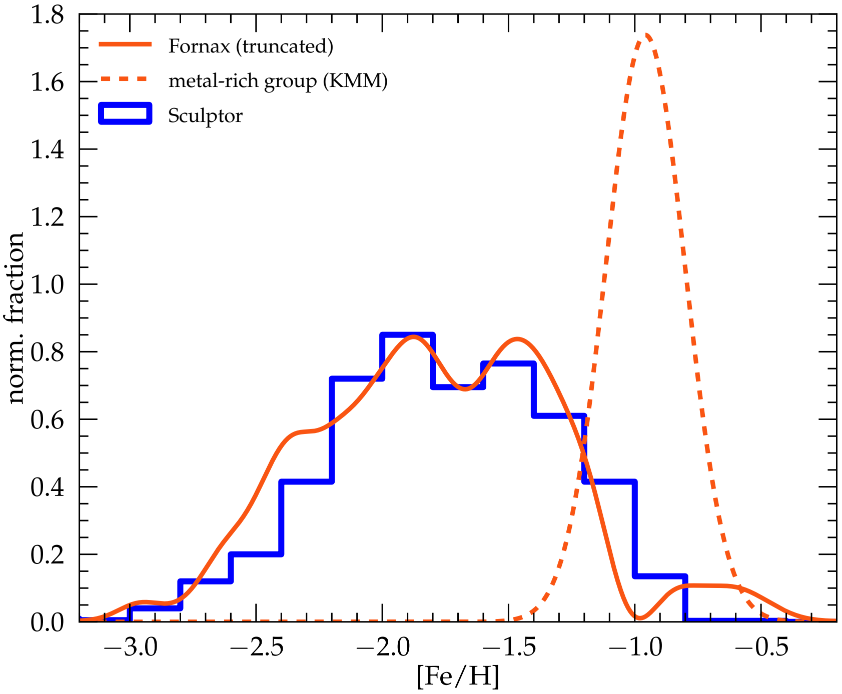

Figure 3.16: Fornax' and Scuptor's MDF show striking similarity when the metal-rich group in Fornax is fit with a Gaussian and removed from the convolved distribution. Fornax' MDF (solid orange line) and the subtracted peak (dashed orange line) have been rescaled such that the truncated MDF resembles the same total area as Sculptor's MDF.

3.6 Radial gradients

Fornax displays a significant radial metallicity gradient, where the metal-rich stars tend to be found closer the center of the galaxy (Battaglia et al. 2006). From photometric studies we know that this observation corresponds to an actual age gradient within the galaxy (Stetson et al. 1998, de Boer et al. 2012b, del Pino et al. 2013). A radial population gradient seem to be a common feature among dSphs (e.g., Harbeck et al. 2001, Leaman et al. 2013), and it is commonly interpreted as a gradual concentration of the remaining gas within a galaxy towards the center of its gravitational potential accompanied with an outside-in SF. Alternatively, radial gradients could be the result of a differential binding energy with galactocentric radius within the galaxy. In this case, internal and environmental gas-removing processes such as SN feedback, tidal interactions, or ram-pressure stripping will more easily remove potential star forming material from the outer parts of the galaxy, while the most centrally located gas will exhibit the highest likelihood of being held in the galaxy, and can subsequently serve as a birthplace for new generations of stars.

Our sample is focused on the chemodynamical properties of stars primarily in the outer parts of Fornax, and consequently is not well suited to study overall radial trends in this galaxy. However, since the stars were selected between $r_{ell} \sim 0.4$-$0.8°$, we can observe a general population-trend for different radii.

Figure 3.17 shows the MDF when we separate the stars between those with a galactocentric distance shorter than 0.6°and those located at larger radii. It is clearly visible that the more centrally concentrated stars have a more metal-rich distribution than the stars in the outermost areas. In the inner MDF, all three peaks from the full sample are present, and the metal-rich group is the dominant feature. In contrast, when only the outer stars are examined, the peak at $[\mathrm{Fe/H}] \approx -1.0$ is barely visible (and will disappear for $r_{ell} \geq 0.65°$), and we find an even distribution of stars over the entire metallicity range.

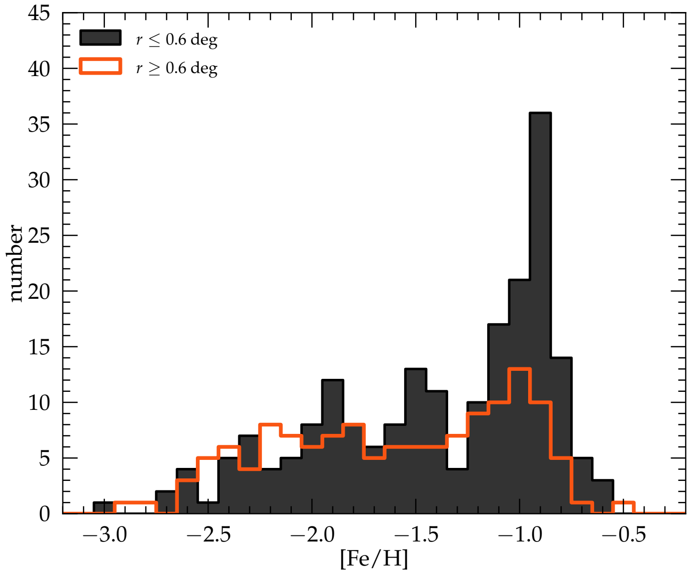

Figure 3.17: Radial variations in the MDF of Fornax. Stars with $r_{ell} \leq 0.6°$(black) are clearly dominated by the metal-rich peak at $[\mathrm{Fe/H}] = -0.97$ and two other subgroups are visible. The MDF outside this interval (red) indicates an almost equal distribution between stars of all metallicities.

To investigate the detailed trend of [Fe/H] with r_{ell}, we first sort the stars in our sample by increasing distance to the center and then compute a floating mean for a subsample of 80 stars. The result is shown in the top panel of Figure 3.18. We find that the mean metallicity drops steadily from [Fe/H] ~ -1.2 dex at 0.4°to -1.8 dex for stars at 0.8°. The bump in the distribution with a steeper trend for $r_{ell} \geq 0.65°$is present in both fields independently, which indicates that we are observing a real feature caused most likely by a clearly defined upper radial boundary for stars belonging to the metal-rich group (and consequently with ages younger than $\sim$ 8 Gyr). When we approximate the radial decline of [Fe/H] with a linear function, we find a slope of -1.28 ± 0.25 dex/degree, corresponding to -0.50 ± 0.10 dex/kpc (and -0.37 ± 0.07 dex/r_c) when we assume $r_c = 0.293°$and $d = 147$ kpc.

We can perform a similar analysis for the radial distribution of stellar ages, shown in the bottom panel of Figure 3.18. Here we cannot make use of the full sample of stars with CaT-metallicities but have to restrict our analysis to the same selection of stars we presented in Section 3.4. Interestingly, we do not find a significant trend of the mean stellar age with galactocentric distance. The mean correlation appears flat with a slope of -1.73 ± 1.96 Gyr/degree.

In addition to the statistical uncertainties, it is possible that we introduce a systematic bias in the radial age trend since the youngest stars (which are most abundant at small radii) are not fully sampled when stars along the tip of the RGB are investigated. Furthermore, the photometric error of stars causes *only* members from the oldest and youngest populations to be discarded in the analysis because only they can fall outside of the isochrone range, due to their statistic and systematic uncertainties. Therefore, it is hard to draw conclusions about the quantitative distribution of stellar ages from spectroscopic samples like ours because it requires a large statistical sample with no selection bias and a negligible number of systematic outliers like AGB interlopers or incorrect assumptions about [α/Fe] for individual stars.

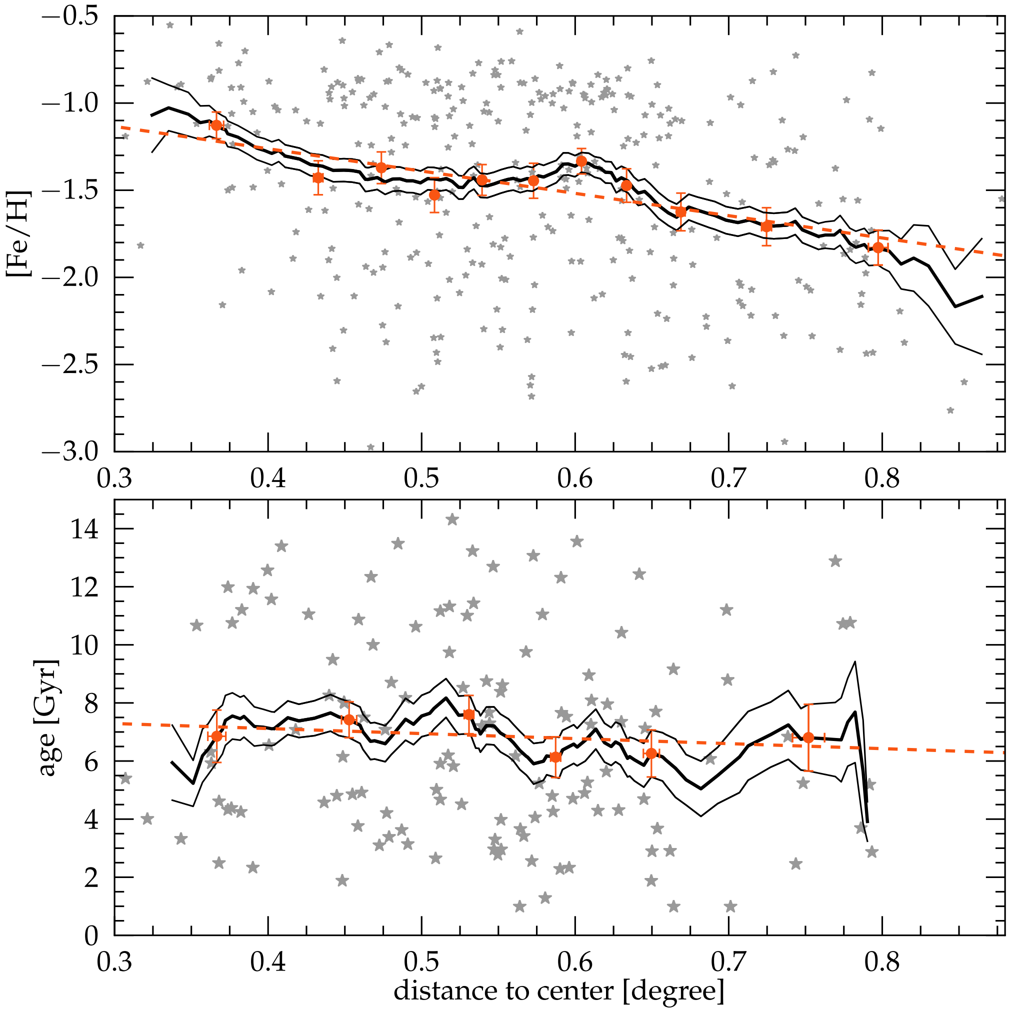

Figure 3.18: Top: Radial metallicity gradient in our sample. The floating mean [Fe/H] (thick black line) shows a clear decrease of [Fe/H] with distance to the galactic center. The thin black lines indicate the 1-σ uncertainty interval. Red symbols show the same trend from independent subsamples of ~ 30 stars and the red dashed line shows the best linear fit to this trend. The data are in reasonable agreement for a linear slope, for which we find best fitting parameters of -1.28 ± 0.25 dex/degree, corresponding to -0.50 ± 0.10 dex/kpc. Small, gray symbols show the actual distribution of star in our sample. **Bottom:** No significant radial age trend in our sample within the spatial coverage of our sample. When a linear function is fit to the data, we find a slope of -1.73 ± 1.96 Gyr/degree.

3.7 Summary

We have presented precise radial velocities and CaT-metallicities for a large sample of 340 stars in two distinct outer fields of the Fornax dSph from intermediate resolution spectra ($R \sim 16000$). While the inner regions of Fornax have been studied in detail by, e.g., Pont et al. (2004), Battaglia et al. (2006), or Letarte et al. (2010), the outer region of this galaxy has not been studied systematically although it is known that Fornax – like dSphs in general – displays a strong variation in its chemodynamical properties with distance to the galactic center (Battaglia et al. 2006). The present analysis is intended to fill this gap and should help, in combination with the existing spectroscopic samples in Fornax, to decipher its evolution and reduce the level of selection bias for important galactic parameters. In the following we summarize our detailed results:

- Stars in our sample show a wide range in metallicity, between $[\mathrm{Fe/H}] = -0.5$ and -3.0 dex. The MDF in the outer fields of Fornax is dominated by a distinct metal-rich group of stars at $[\mathrm{Fe/H}] = -0.97$, which is seen out to $\sim 0.65°$, where it disappears abruptly. In total, we observe three subgroups at $[\mathrm{Fe/H}] = -0.97$, -1.45, and -2.11 with a relative contribution to the total sample of 45%, 18%, and 37%, respectively. Our sample contains 75 stars with $[\mathrm{Fe/H}] \leq -2.0$, increasing the database of rare metal-poor stars in Fornax by a factor of two.

- When we remove the most metal-rich (and youngest) populations from our sample, the truncated MDF becomes identical to the one observed in Sculptor. This striking similarity is strong evidence that these systems evolved identically at early times, with the only difference that Fornax experienced a late and intense episode of SF, which could have been triggered through a merger event (Yozin & Bekki 2012), by re-accretion of previously expelled gas (Ruiz et al. 2013, D'Ercole & Brighenti 1999), or by environmental influences like tidal interactions.

- Our data confirm a radial gradient of [Fe/H] with galactocentric distance in Fornax. The gradient within our radial coverage reasonably resembles a linear slope with -1.28 ± 0.25 dex/degree. In contrast, we do not observe a significant age gradient for increasing radii for which a similar fit yields -1.73 ± 1.96 Gyr/degree. However, the age-gradient should be interpreted with caution since the available sample is small and the analysis is likely to suffer from systematic selection biases.

- We use the independent [Fe/H] measurements from individual iron lines in our spectra to test different CaT-calibrations over more than 2 dex in [Fe/H]. We find best agreement with the calibration equations provided in Carrera et al. (2013), but classical GC-calibrations yield CaT-metallicities systematically too large for stars below $[\mathrm{Fe/H}] \approx -1.8$. Finally, we identify the actual approach of fitting the CaT absorption features as a possible source of systematic offsets in the calibration, leading to systematic shifts between different datasets as large as 0.5 dex in [Fe/H]. To avoid such effects, the same line-fitting technique should be applied to the stars as has been used to derive the calibration equations of choice.

- We can associate nine stars from our sample to the GC H2 and three stars to H5. We find $[\mathrm{Fe/H}] = -2.04 \pm 0.04$ and $RV = 59.36 \pm 0.31\,\mathrm{km\,s^{-1}}$ for H2 and $[\mathrm{Fe/H}] = -2.02 \pm 0.11$ and $RV = 59.39 \pm 0.44\,\mathrm{km\,s^{-1}}$ for H5, in excellent agreement with previous findings. In the case of H2, we provide the largest sample of individual measurements for RV and [Fe/H].

- We combine our information about [Fe/H] with $[\alpha/\mathrm{Fe}]$ for individual stars to derive ages for these targets with object-specific isochrones. The general trend in the AMR indicates a chemical enrichment in three-phases: a steep increase in [Fe/H] at early ages followed by a significantly slower and almost flat enrichment for stars younger than ~ 8 Gyr. Finally, the AMR show signs for a second, fast enrichment in metallicity during the last 3 Gyr, subsequent to a strong, young stellar population in the galaxy. This picture shows that the dominant metal-rich population in this galaxy does not reflect a single stellar population, but instead contains stars of at least 5 Gyr in age during an evolutionary phase where the ISM was not significantly enriched. These observations are in good agreement with predictions from our earlier chemical evolutionary model where the SF efficiency increases with time in a series of bursts – a scenario which also possibly explains the peculiar, metal-poor position of the knee in the evolution of [Mg/Fe] (see Hendricks et al. 2014a). However, the model does not predict a significant fraction of young stars with ages $3-5$ Gyr, nor the subsequent steep increase in [Fe/H] which we observe in the data. Therefore, we tentatively propose that this younger population(s) may have been the result of an externally triggered SF episode, for which a simple leaky-box model does not account for.

- Our evolutionary scenario agrees well with the empirical SFH from Weisz et al. (2014), except in two aspects: First, our model predicts a larger fraction of old stars. This difference can be explained with the radial SFH gradient in Fornax observed in de Boer et al. (2012b). Second, our model neither predicts a significant fraction of stars younger than ~ 5 Gyr nor a significant fraction of SF during that time. This difference can possibly be explained with an environmentally-triggered episode of SF.

- The few individual GC stars in our sample fall on top of the field-star AMR within the respective uncertainties. This implies a similar chemical enrichment of the protostellar material out of which both GC and field stars formed. However, given the large uncertainty on ages – especially for old, metal-poor stars – we cannot rule out the possibility of small or moderate differences in the chemical enrichment between the two environments.

- A detailed analysis of several sources of statistical and systematic uncertainties in the age determination shows that the total error is dominated by systematic effects. Hereby, the uncertainty in the distance modulus poses a major source of error that can alter the derived ages of stars by several Gyr, depending on their intrinsic age and metallicity. Furthermore, we identify small zero-point variations between photometric frames as an additional source of systematic error, which in our case evokes an apparently different chemical enrichment pattern for the two galactic areas we investigate. Given the high sensitivity of ages on photometric parameters, a star-by-star reddening correction becomes necessary, even for galaxies with very low line-of-sight interstellar extinction.

- When we combine the dynamical and chemical information of our sample, we find that different populations also display complex dynamical properties, which has been previously observed for the inner regions of Fornax (Battaglia et al. 2006, Amorisco & Evans 2012). Specifically, the velocity dispersion continuously increases from $\sigma_{sys} \approx 7.5\,\mathrm{kms}^{-1}$ to $\geq 14\,\mathrm{kms}^{-1}$ from the highest to the lowest metallicities. The large velocity dispersion at low metallicities is probably the result of a non-Gaussian velocity distribution among stars older than ~ 8 Gyr, with a flat distribution of RVs between 40 and 70 $\mathrm{km\,s}^{-1}$. These complex dynamical signatures can be a sign of accreted stellar systems.

- Finally, we do not observe significant differences in the chemical and dynamical properties between the two distinct fields of our survey at the same radii but opposite sides, which suggests that there are only small *random* local variations within the galaxy.

This work confirms that there are significant differences between the inner regions of dSphs and their outer parts, where some details can only be revealed if a statistically large number of stars is available at different radial positions in a galaxy. Our sample still lies well within the tidal radius of the galaxy (with a significant fraction of stars only out to $r_{ell} = 0.75^\circ$). However, the tidal radius of Fornax reaches out to $\geq 1^\circ$, and a significant number of members can be expected beyond that radius. In order to get a full picture of Fornax' history, it is important to add to the existing stars, for which we already have basic chemodynamic information, a sufficiently large sample of stars taken from the *real* periphery of the galaxy, at radii $\geq 0.8^\circ$and beyond the tidal radius. The same necessity applies to other dSphs, for which the available – photometric and spectroscopic – samples are, in most cases, even stronger biased towards the center of these objects.

4

Evidence for a Chemical Enrichment Coupling of Globular Clusters and Field Stars in the Fornax dSph[1]

4.1 Introduction

Globular clusters (GCs) are an intriguing class of stellar systems and have been objects of interest for many decades. When resolved, they offer a unique possibility to study their effectively coeval and mono-metallic stellar populations in detail. In distant galaxies, unresolved globular clusters serve as luminous beacons that can still be analyzed when individual field stars are too faint to observe (e.g. Brodie & Strader 2006).

While the chemical (self-)enrichment in GCs *after* their formation has been studied in great detail in the recent past (see, e.g., Gratton et al. 2012 and references therein), relatively little is known about the chemical enrichment of these systems *before* their formation; that is, the chemical evolution of the proto-GC gas embedded in a galactic environment. Specifically, it is not clear whether GCs—despite their undoubtedly unique formation mechanism—reflect the chemical properties of the field stars in the host environment they are born in, or whether they instead display distinct chemical enrichment properties.

Globular clusters in the Milky Way (MW) halo are found to be almost exclusively alpha-enhanced over the entire observed range of metallicities (Pritzl et al. 2005), indicating a fast chemical enrichment of the material from which they formed. Simultaneously, they fall on top of the enhanced [α/Fe] plateau displayed by the field stars (e.g., Venn et al. 2004), and therefore no clear distinction between a uniform enrichment scenario and a coupling with the field star properties can be made (see Figure 4.1). A similar picture is found for the GC system in Andromeda (M31) where a large number of clusters have been studied recently by Colucci et al. (2014) and Sakari et al. (2015), using integrated-light spectroscopy. Although the alpha-evolution of field stars in M31 is not known given the extremely faint magnitudes of individual stars, the [α/Fe] values of the GCs agree well with the field stars and the GCs of the MW. Notably, the clusters on the high-metallicity

---

[1] The work presented in this chapter was done in collaboration with Corrado Boeche, Christian I. Johnson, Matthias J. Frank, Andreas Koch, Mario Mateo, and John I. Bailey. The results were initially published in Hendricks et al. (2015, submitted to A&A).

end in the sample of Colucci et al. (2014) possibly show lower alpha-abundance ratios and may follow the knee of MW field stars, which could be a hint for a common chemical enrichment pattern between field stars and clusters.

Both galaxies host a few, but interesting, outliers with significantly lower [α/Fe] ratios with respect to the field stars at comparable metallicity: Terzan 7, Palomar 12, and the younger system Ruprecht 106 in the MW (Sbordone et al. 2005, Cohen 2004, Brown et al. 1997), G002 and PA17 in M31 (Colucci et al. 2014, Sakari et al. 2015). While Terzan 7 and Palomar 12 are commonly associated with the currently disrupting Sagittarius dwarf galaxy (see Law & Majewski 2010 and references therein), the other clusters are orphans without a known parental system. Only because of their abnormal chemical signatures is it speculated that they have formed in smaller satellite systems with slower chemical enrichment, and have subsequently been stripped from their hosts during the accretion (e.g., Villanova et al. 2013, Colucci et al. 2014). In this scenario, the GCs *need* to share the fingerprint of slow chemical enrichment inherent to the host galaxy. Furthermore, it would be possible to generally use clusters with peculiar alpha-abundances for chemical tagging of accreted systems.

The only Local Group galaxy known to host GCs while its stars are simultaneously alpha-depleted at a metallicity of Ruprecht 106 or G002 is the Fornax dwarf spheroidal. This galaxy therefore may provide a unique test case to address the key questions of whether GCs share the chemical enrichment pattern of their host galaxy and, as a consequence, whether it is possible to use peculiar alpha-abundances (i.e., those deviating from the field stars) for chemical tagging of accreted systems. Fornax hosts its own population of five GCs (see Figure 1.3). Four of the Fornax GCs are metal-poor with [Fe/H]≤ -2.0 (Letarte et al. 2010), old (Buonanno et al. 1998) and alpha-enhanced (Letarte et al. 2010, Larsen et al. 2012a), and by that resemble typical MW halo clusters. The remaining cluster (named H4, following Hodge 1961) is an outlier in many respects: it is significantly more metal-rich, around [Fe/H]$= -1.4$ (Strader et al. 2003, Larsen et al. 2012a), and possibly younger than the other clusters (Buonanno et al. 1999). Most importantly, it has only recently been shown that field stars in Fornax become alpha-depleted at very low metallicities, with a knee in the alpha-evolution most likely below [Fe/H]≈ -1.9 dex (Hendricks et al. 2014a, Lemasle et al. 2014). As a consequence, H4 is located at a metallicity where the field stars in Fornax are clearly alpha-depleted. This contrasts with the composition characteristics of similar metallicity MW field stars, which are alpha-enhanced. Therefore, H4 provides a unique opportunity to test if GCs share the chemical enrichment pattern of their host galaxy, and if it is possible to use peculiar alpha-abundances to chemically identify accreted systems such as Ruprecht 106 in the MW or G002 in M31.

Despite its importance for understanding GC formation and evolution in Fornax, H4 is the only cluster in the galaxy for which no individual member stars have been analyzed to date. H4 is located very close to the center of the galaxy and is therefore severely contaminated by field stars. Additionally, it happens to be the most compact of all Fornax GCs, and at a distance of ~ 147 kpc its core radius amounts to only $2.64''$ (Mackey & Gilmore 2003). From ground-based telescopes, H4 is only resolved into individual stars in its outer regions where the fraction of cluster member and field star contaminants is about equal.

In the chapter, three likely individual member stars of the cluster H4 have been identified. For one of them, we derived detailed chemical abundances and put them in direct comparison with field stars of both the Fornax dwarf spheroidal and the MW at similar metallicity. The goal of this work is to shed light on the question of whether or not the chemical enrichment history of field stars within a galaxy is imprinted on its GC system. In Section 4.2, we summarize our target selection, observing setup, and data reduction. Section 4.3 gives details about the chemical analysis, which is subsequently presented in Section 4.4 together with an age analysis of H4. In Section 4.5, we discuss the impact of our findings with respect to the nature of alpha-depleted GCs, the nature of H4 itself, and the chemical enrichment properties of Fornax. Finally, in Section 4.6, we summarize our main results.

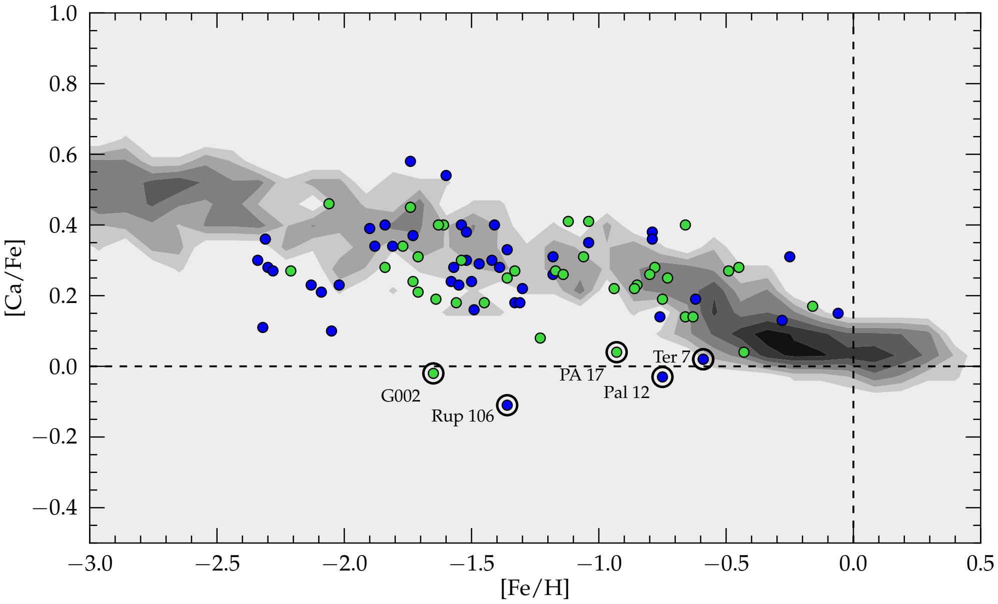

Figure 4.1: Literature compilation of the chemical abundance pattern of Ca as a function of [Fe/H]. Symbols show GCs in the MW from Pritzl et al. (2005) (blue) and M31 (green) from Colucci et al. (2014) and Sakari et al. (2015). The pattern of MW disc and halo stars are shown as a logarithmically-scaled number density distribution of arbitrary units (data from Venn et al. 2004 and Roederer et al. 2014). Outliers with significantly lower [Ca/Fe] are highlighted with large open black circles.

4.2 Data Acquisition and Reduction

Finding individual and bright member stars in H4 is a challenging endeavour. A multi-object spectrograph is necessary in order to efficiently observe cluster members. Furthermore, the cluster's large distance, with accessible targets located at $10-60''$ from the cluster center, means that the instrument must be capable of densely packing many objects onto a small spatial scale. To avoid contamination, the apertures also need to be small and able to be placed on the field-of-view with high precision. Finally, with most targets fainter than $V = 19.0$ mag, exposure times to obtain sufficient signal-to-noise for a chemical analysis are long and suffer from accumulating cosmic rays.

4.2.1 Observations, Instrument, and Setup

For this project, we used the Michigan/Magellan Fiber System (*M2FS*, Mateo et al. 2012) and MSpec spectrograph, a fiber-fed spectrograph mounted on the Nasmyth-east port of the Magellan-Clay 6.5m telescope at Las Campanas Observatory. For *M2FS*, we used the *Bulge_GC*1 setup and $125\,\mu$m slit (see Johnson et al. 2015), which allows a simultaneous observation of up to 48 targets at a resolving power of $R \approx 28\,000$ and a continuous wavelength coverage from 6140 to 6720 Å. The observations have been carried out during three consecutive nights in December 2014.

With 8 individual exposures, a total of 6.7 hours have been observed on target with typical seeing conditions around $0.8''$.

4.2.2 Target Selection

Due to the central location of H4 in the field of the Fornax dwarf galaxy, the cluster is heavily contaminated by Fornax field stars. The contamination fraction in the outer half of the cluster tidal radius is higher than 50%, and still amounts to $\geq 20\%$ around the cluster center (see Section 4.4.1). A careful target selection is critical to maximize the fraction of actual H4 members, while simultaneously avoiding blended stars in the heavily crowded area. In addition to bona-fide H4 cluster members, we also deploy some of the fibers on bright field stars in the vicinity of the cluster to allow a direct comparison between cluster and galactic properties.

GC Candidates

For our target selection, we used archival Hubble Space Telescope imaging taken with the Wide-Field Planetary Camera 2 (WFPC2) in programme 5637 (PI: Westphal). The data consist of two deep (1100 s) and one shallow (60 s) exposure in both of the F555W (V) and F814W (I) bands, and were first published by Buonanno et al. (1999). We retrieved the pipeline-reduced individual images from the STSCI archive and performed point-spread function fitting photometry using HSTPHOT (version 1.1; Dolphin 2000), following the same procedure described in more detail in Frank et al. (2012). Briefly, residual shifts of the images were determined by initially running HSTPHOT on each image separately and cross-matching the resulting catalogs. After the creation of cosmic-ray masks, the well-aligned deep exposures in each filter were coadded, and the F555W deep coadded image was used as a detection image in the simultaneous photometry from all frames.

The output of HSTPHOT provides charge-transfer-efficiency- and aperture-corrected magnitudes in the HST system (F555W and F814W), as well as magnitudes transformed to the Johnson-Cousins V and I bands, based on the updated calibration and photometric transformation coefficients of Dolphin (2009). In the following, we use these V and I band magnitudes.

For astrometry, we created a mosaic of all F555W-band exposures (see Figure 4.2) using MULTIDRIZZLE (Koekemoer et al. 2006), and transformed the photometric catalogs of the camera's four individual chips to this reference image, in order to correct for geometric distortion. We corrected for shifts in absolute R.A. and Dec by matching our catalog to the 2MASS astrometric system (Cutri et al. 2003), using the VIKING survey DR1 source catalog (Edge et al. 2013) as an intermediate step in the cross-match because the 2MASS point source catalog is very sparse in the $\sim 2.6' \times 2.6'$ field-of-view of the WFPC2 pointing.

Possible targets are selected from the RGB and comprise stars from the RGB-tip down to magnitudes as faint as $V = 20.5$ mag. Although the RGB is fairly broad with a possible color split for the brightest stars, it is not clear whether this is a signature of the GC population on top of a field stars mix or whether it simply reflects the intrinsic spread in the field star population. Therefore, we did not further constrain our selection to a specific part of the RGB, as for example done in Carretta et al. (2010a) for the case of M54 in the center of the Sagittarius dwarf spheroidal, where a cleaner separation between populations could be made. We also refrain from placing an individual fiber at the (unresolved) center of the cluster. The analysis of the resulting integrated-light spectrum would be inferior to classical drift-scan methods because the integrated spectrum does not consist of an entire population (which can be modelled varying levels of accuracy) but may contain only some dozens of stars of essentially unknown origin and parameters.

Blending is a serious problem for stars in H4, specifically in the inner regions of the cluster where membership likelihood is highest, and we have to take into account the additional seeing from ground-based observatories in contrast to the HST images. To quantify the amount of blending and to exclude significantly flux-contaminated stars in advance, we calculate a *separation index*, developed by Stetson et al. (2003). In detail, we use the magnitude of each star in the HST catalog to calculate its flux, which we subsequently smooth with a Gaussian profile according to the seeing of our observations. We then calculate the flux ratio between the target star and all neighbours in the environment at the star's central position and express the result as a magnitude (m_{sep}). Finally, we exclude all stars from our target list with a flux contamination higher than 5%, equivalent to $m_{sep} \geq 3.25$. Our final targets typically have $m_{sep} \geq 5.0$, and by that suffer less than 1% contamination from neighbouring stars (see Figure 4.3).

Field Stars

Field star targets of the Fornax dwarf spheroidal were selected from the catalog of Battaglia et al. (2008), which provides Calcium Triplet metallicities for nearly 1 000 bright RGB stars that are cleaned from most of the contaminating Galactic halo foreground by velocity cuts. From this catalog, we purposefully picked rare, metal-poor stars with [Fe/H]≤ -1.4 dex to trace the alpha-element evolution at the metallicity of H4 and at the expected position of the [α/Fe] knee. The selected field stars belong to the upper part of the RGB and consequently have similar magnitudes to the H4 candidate stars. Since they are located close to the cluster itself, our field star targets are all located in the central part of Fornax ($r \leq 0.3°$) and hence within the core radius of the galaxy.

4.2.3 Data Reduction

The general spectroscopic data reduction process follows the description in Johnson et al. (2015). Using IRAF routines, the individual amplifier images on each CCD were separately trimmed, bias corrected and subsequently rotated, translated, and combined into one exposure per CCD. Next, we used the IRAF task DOHYDRA to extract the individual orders of each spectrum. This task has been written to extract spectra taken with the WIYN and Blanco Hydra spectrographs, and it can be applied to most multifiber echelle data sets. The routine includes aperture identification and tracing, scattered light removal, flat-field correction, throughput- and wavelength-calibration, and a basic cosmic-ray removal. Sky-subtraction within DOHYDRA is skipped and performed later using a master-sky frame from the combined sky fibers of both CCDs.

It is important to emphasize that DOHYDRA is called separately on each of the six orders for individual spectra. As a consequence, the extracted parts of any full spectrum underwent an *individual* data reduction process and therefore possibly display different systematic signatures imprinted by the individual extraction steps. This allows us to verify the robustness of our analysis against such possible systematics by comparing the results from different orders (see Section 4.3.2).

After sky subtraction, the individual exposures have been summed using a weighted average based on the typical S/N of the brightest targets in each frame, to maximize combined signal-to-noise. The heliocentric velocity was removed from each frame prior to co-addition in order to account for differences of up to $0.7\,\mathrm{km\,s^{-1}}$ between individual frames. Finally, the spectra are continuum normalized and the full wavelength range is recovered by combining the individual orders.

Compared to the data in Johnson et al. (2015), our targets are extremely faint, with long individual exposure times and low signal-to-noise (≤ 10 per pixel) within the individual exposures. This introduces some complications in the data reduction and requires some additional steps. First, given the long individual exposure times of up to 1 hour, the images suffer from severe cosmic-ray contamination for which DOHYDRA cannot properly account. The multitude of cosmic-ray features

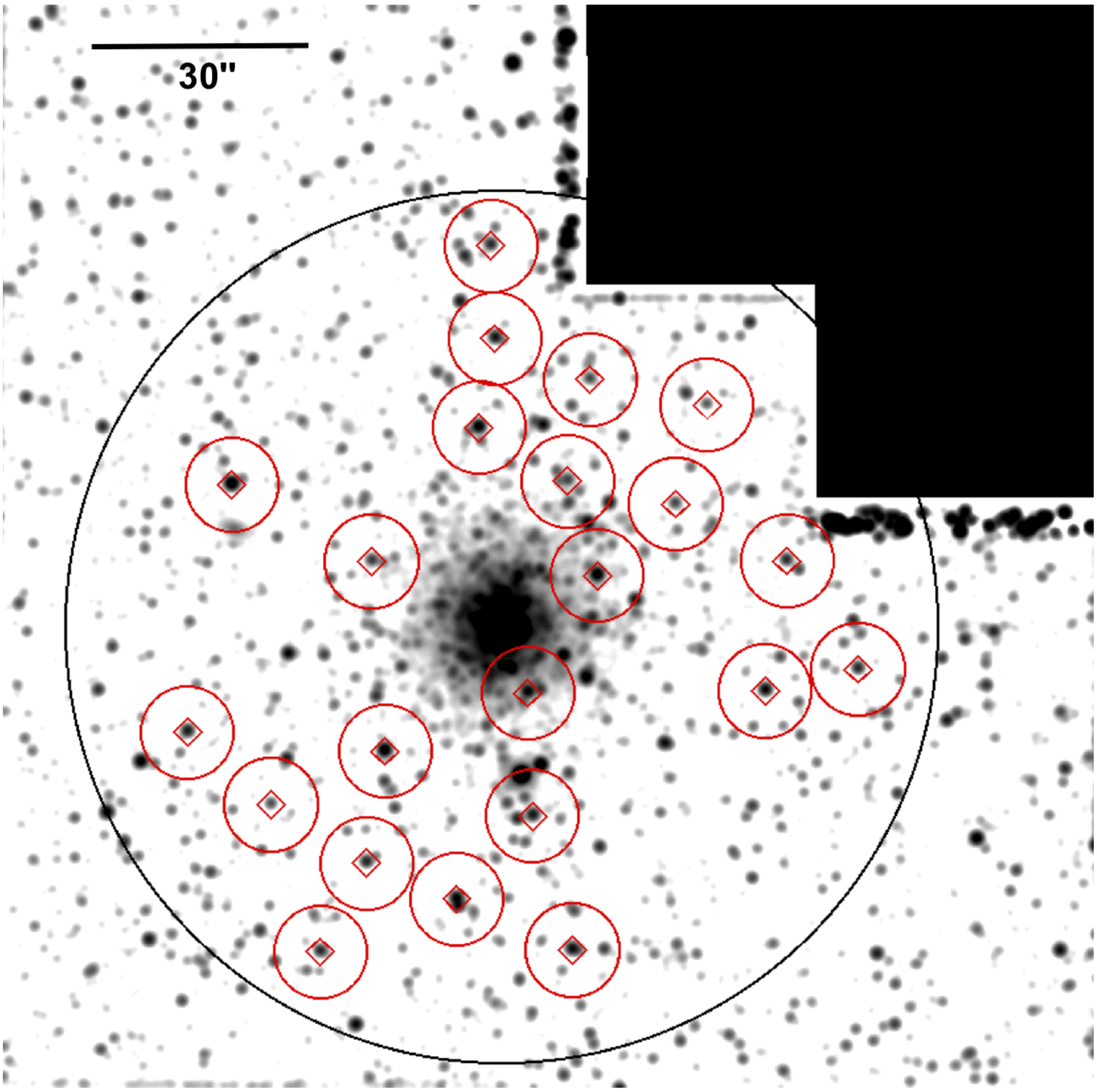

Figure 4.2: Location of our targets in the GC H4, shown on the WFPC2 F555W-band mosaic and artificially degraded to a ground-based seeing of $1''$. The tidal radius of the cluster ($r_t = 1'$) is shown in black and our targets are highlighted with red symbols. Red boxes are $2'' \times 2''$ and mimic the actual fibesize while the circles are $6.5''$ in radius and visualize the minimum allowed spacing between individual fibers for *M2FS*.

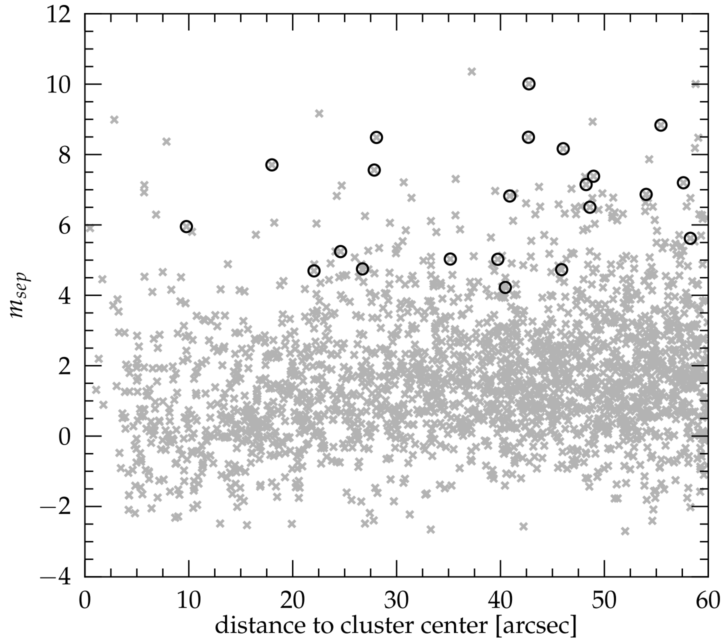

Figure 4.3: Plot of the separation index defined in the text for stars in the GC H4 as a function of central distance. Gray crosses denote all red giant stars projected on the sky near the cluster, and our targets are highlighted with black circles. While $m_{sep} = 0.0$ means that half of the star light comes from blending neighbours, $m_{sep} = 4.0$ and 5.0 means $\sim 2.5\%$ and 1.0% contamination, respectively.

not only possibly spoil absorption features in the spectra, but also may pose a problem for fiber tracing, throughput calibration, and later to sky subtraction and continuum placement. For this reason, we use the Python implementation of LACOSMIC[2] (van Dokkum 2001) on our 2d images prior to the DOHYDRA task, which yields a significant improvement on our results. However, we cannot be sure if absorption features, initially affected by cosmic-rays, are recovered to their intrinsic, unbiased properties. Therefore, we generate a cosmic-ray mask in order to flag any regions in a spectrum which have been possibly biased by cosmic-ray removal. Unfortunately, DOHYDRA does not propagate bad pixel masks through the reduction. We therefore perform the extraction process twice, once on the images with and once on the images without previous correction by LACOSMIC. Then, we flag all wavelength regions where we observe a significant (≥ 5 sigma of continuum noise) difference between the extracted versions. Finally, we combine the regions from all individual exposures to build the cosmic-ray mask. Later, we will use this mask to test the robustness of our abundances by excluding these regions during the analysis (see Section 4.3.2).

Despite the initial throughput calibration, we observe flux variations between individual fibers, including science and sky fibers. This necessitates a sophisticated sky-subtraction for which we use the SKYTWEAK task in IRAF. The SKYTWEAK task allows for wavelength shifts and rescaling of the flux in the master-sky spectrum to minimize residuals of the most prominent emission features. The master-sky is generated by the average of 5 sky fibers distributed among both CCDs, and includes a min-max rejection algorithm to clear the spectrum of any remaining cosmic-rays or other contamination. In low singal-to-noise spectra with flux only ~ 10 times above the sky level, sky residuals will have a non-negligible impact on any chemical analysis. Similar to the cosmic-ray

---

[2] available online at http://obswww.unige.ch/~tewes/cosmics_dot_py

mask, we therefore generate a *sky-mask* where we flag wavelength regions with initially strong sky emission lines and test the sensitivity of our chemical analysis to these regions. The reddest order in our setup (order 57; 6653 - 6720 Å) does not contain any significant sky emission features that can be used for rescaling. As a consequence, the level of sky subtraction is less reliable than for the other orders, and we therefore exclude this region from the chemical analysis for all stars.

Finally, some orders of some spectra are affected by an internal Littrow ghost reflection (e.g., Burgh et al. 2007; see also Johnson et al. 2015, their Figure 1). Such regions are clearly visible as a strongly deviating continuum flux, and we exclude these regions from the forthcoming analysis.

After data reduction, we obtain a total of 40 science spectra (18 field stars and 22 stars within the tidal radius of H4). The signal-to-noise distribution, measured at ~ 6388 Å, ranges from ~ 40 per pixel for the brightest targets to ≤ 10 for the faintest objects. We estimate the final resolution of our spectra from the width of several clean sky emission lines and find a constant $R = \lambda/\Delta\lambda \approx 28\,000$ over the full wavelength range.

4.3 Data Analysis

4.3.1 Radial Velocities

We determine radial velocities for each star using he IRAF task FXCOR and a template spectrum convolved to the resolution of our observations. As template we used a synthetic spectrum[3] with $T_{\rm eff} = 4250\,$K, $\log g = 1.0$, and [Fe/H]$= -1.4$, which is close to what we expect for H4 cluster members and suitable for our complete sample.

To obtain the most precise velocity determination, we use only one of the orders (order 55; 6406 - 6515Å) because it contains a series of deep, unblended absorption lines, it is relatively free of strong sky emission, and it does not contain broad lines nor strong telluric bands. Where applicable, we test the outcome with other orders and find consistent results within the uncertainties.

Velocity uncertainties reported by FXCOR are typically $\leq 1.0\,\mathrm{km\,s^{-1}}$ (between 0.2 and $2\,\mathrm{km\,s^{-1}}$, depending on S/N). We additionally estimate the uncertainty from the standard deviation of the individual exposures for each star, which yield very similar results to the FXCOR values. Although less critical than for the chemical analysis, we want to make sure that our velocities are not strongly biased by residual artifacts from sky emission or cosmic rays. Therefore, we determine velocities once using the full wavelength range of order 55 and once without the masked regions in the sky- and cosmic-ray mask. Reasurringly, the differences are small and usually at or below the level of the statistical errors.

4.3.2 Chemical Analysis

SP_ACE

For the chemical analysis of our spectra we use the newly developed code SP_ACE (Stellar Parameters and Chemical Abundances Estimator; Boeche & Grebel (2015)), an evolution of the RAVE chemical abundance pipeline (Boeche et al. 2011). In short, the code employs a full-spectrum-fitting technique to derive stellar atmospheric parameters and chemical abundances by means of a χ^2-minimization procedure. The reference spectra are generated with a library of general curve-of-growth models for a given line-list within the desired wavelength range. We point the interested reader to Boeche & Grebel (2015) for a detailed description of the method, the code itself, and its performance on synthetic and real spectra.

---

[3] Obtained from the Coelho et al. (2005) library of high resolution synthetic stellar spectra.

A major advantage of fitting entire wavelength regions is that the amount of information extracted from the data is improved compared to an individual line analysis, specifically because blended absorption features of the same and of different species can be incorporated in the analysis. As a consequence, reliable results can be obtained for many chemical elements, even in spectra of low resolution and/or low signal-to-noise (e.g. Kirby et al. 2008, Caffau et al. 2013, Conroy et al. 2014, Choi et al. 2014, or Hendricks et al. 2014a). Another advantage is that the iterative fitting procedure of the full spectrum within SP_ACE is able to take into account the knowledge about individual absorption features for the continuum placement, which otherwise can have an unwanted biasing effect on the derived continuum level and therefore on the derived chemical abundances (e.g. Kirby et al. 2008). The limited luminosity (and hence distance) range in which classical, high-resolution, and high signal-to-noise chemical abundance analysis can be carried out can thus be expanded to extragalactic targets, such as MW satellites or unresolved systems in the Local Group.

While it seems generally possible to perform a chemical analysis with $\sigma[\mathrm{X/Fe}] \leq 0.2$ even on low-resolution spectra with $R \sim 3000$ (e.g. Kirby et al. 2008, Conroy et al. 2014), SP_ACE is theoretically capable to determine robust abundances for $R \geq 2000$ and is specifically tested between $R = 2000 - 20\,000$. Therefore, we degrade our spectra slightly to a resolution of $R \approx 16\,000$ to place them on the well-calibrated regime of SP_ACE and also to obtain a higher signal-to-noise per resolution element. For the fainter stars, this improves the proper placement of the continuum and reduces the confusion between noise and weak absorption lines within the fitting procedure. Nonetheless, we test the consistency of the derived chemical abundances to results obtained using the original $R \approx 28\,000$ resolution, and find low scatter and no systematic changes in the results (see Section 4.3.2).

The most critical problem for an automated, full-spectrum analysis routine is its susceptibility to artifacts related to fitting sky and cosmic ray residual features, which may lead to problems in the continuum placement. Spectra of lower signal-to-noise, as we analyze here, are specifically vulnerable to these points. To address this issue, we visually inspect the model fit to each spectrum and remove individual pixels or wavelength areas from the fit in cases where they can be clearly identified as the origin for a mismatch. This "visual mask" is iteratively refined for each of our targets until we either obtain a satisfactory fit or no obvious cause for a poor fit can be identified. In the latter case, the spectra will have large χ^2-values, and we treat their outcome with care. On top of this, we reject absorption features that are problematic to model (in our wavelength range, e.g., H_α or the Telluric feature blueward of 6320 Å).

In summary, we supply four different pixel masks to SP_ACE which define wavelength regions to ignore in the analysis. While use of the visual mask and the regions containing the Littrow ghost feature are mandatory in order to obtain reliable results, the cosmic-ray and sky masks only have a negligible impact on our results. We only use the cosmic-ray and sky masks later to test the robustness of the chemical analysis against possible inaccuracies in the correction for sky emission and cosmic ray contamination during the process of data reduction.

Atmospheric Parameters

Generally, SP_ACE is capable to derive stellar atmospheric parameters within the fitting process. However, given the fairly low signal-to-noise of our spectra, a more robust result can be achieved when $\mathrm{T_{eff}}$ and $\log g$ are estimated from multi-band photometry. Specifically, we use V and I magnitudes from our HST photometry and derive temperatures $\mathrm{T_{eff}}$ and bolometric corrections from the empirical equations given in Alonso et al. (1999). For the reddening, we adopt $E(B-V) = 0.08$ from Greco et al. (2007) and apply an object-specific transformation described in Hendricks et al. (2012) (specifically their Eq. 3 and 4) to obtain $E(V-I) = 0.11$, suited for a red giant of [Fe/H]$= -1.0$ dex, $\mathrm{T_{eff}} = 4250$ K, and $\log g = 1.5$. Adopting a standard reddening law ($R_V = 3.1$), we furthermore obtain a V-band extinction of $A_V = 0.248$. We assume no significant differential reddening within our field-of-view.

For surface gravities, $\log g$, we then used the standard relation:

$$\log g = \log g_\odot + \log \left[\left(\frac{T_\mathrm{eff}}{T_{\mathrm{eff},\odot}} \right)^4 \left(\frac{M}{M_\odot} \right) \left(\frac{L_\mathrm{bol}}{L_{\mathrm{bol},\odot}} \right)^{-1} \right]. \tag{4.1}$$

Here, we apply a distance modulus of $\mu_0 = 20.84$, adopted from Pietrzyński et al. (2009). In order to account for a possibly large age spread among stars in our sample, we used Dartmouth Isochrones (Dotter et al. 2008) and a simple linear age-metallicity relation to assign individual masses to our targets. Specifically, we obtain a variation of stellar mass from $1.27\,M_\odot$ for stars with [Fe/H]$= -1.0$ to $0.79\,M_\odot$ for a stars with [Fe/H]$= -2.0$. Finally, the micro-turbulence is assumed to be a function of $\mathrm{T_{eff}}$ and $\log g$, and is calculated with a third-order polynomial given in Boeche & Grebel (2015). The atmospheric parameters are iteratively determined with updated stellar metallicities from SP_ACE.

Consistency Tests

As outlined in the previous sections, several of the assumptions we make during data reduction and analysis may have systematic effects on the derived chemical abundances. Therefore, we perform a series of consistency tests to assess the robustness of our analysis against these factors. Specifically, we test:

a) the results obtained using the full wavelength range (minus the mandatory pixel masks) compared to the outcome using only one of the five individual orders. The motivation of this test is that each order underwent an individual reduction and extraction process, including wavelength calibration, throughput calibration, (tweaked) sky subtraction, and continuum fit, and therefore may display individual systematic biases.

b) the results obtained using the full wavelength range compared to the outcome when additional sky emission regions are flagged out, using the sky-mask. The test is motivated by the necessity for a tweaked sky subtraction to compensate for inaccurate throughput calibration.

c) the results obtained using the full wavelength range compared to the outcome when additional cosmic ray regions are flagged out, using the cosmic-ray mask. The test is motivated by the necessity for a cosmic-ray subtraction prior to spectrum extraction, due to the long individual exposure times.

d) the results obtained using a slightly degraded resolution of $R \approx 16\,000$, compared to the original $R \approx 28\,000$.

e) the results obtained using artificially altered atmospheric parameters by $\Delta\mathrm{T_{eff}} = +200\,\mathrm{K}$.

f) the results obtained using artificially altered atmospheric parameters by $\Delta\log g = +0.3$.

Results for [Fe/H] are shown in Figure 4.4. We did not find any global systematic bias in the derived abundance for any of the tested scenarios (except for the artificial temperature and gravity variations). We also did not find any trends with metallicity, and the scatter for all cases is typically well within ±0.2 dex. Importantly, all five individual orders yield consistent results, but with some scatter caused mostly by the limited line information within the smaller wavelength range. A change in $\mathrm{T_{eff}}$ by $+200\,\mathrm{K}$ results in Δ[Fe/H]≈ -0.2 dex for stars with low metallicity and decreases to smaller offsets towards more metal-rich stars. A change in log g by $+0.3$ has practically no effect amongst metal-deficient stars, and yields Δ[Fe/H]≈ -0.1 for stars of high metallicity.

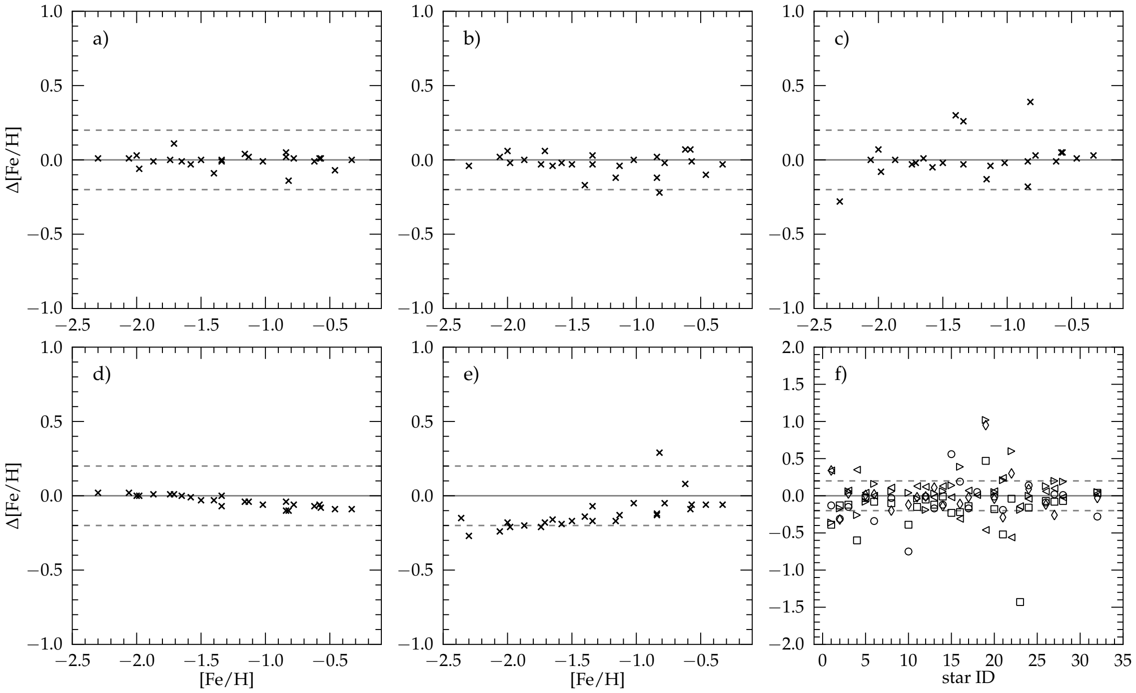

Figure 4.4: Consistency tests for chemical abundances derived with SP_Ace. All plots show the difference between the derived [Fe/H] and various changes to the spectrum as described in the text: **a)** with cosmic ray regions flagged out; **b)** with sky emission regions flagged out; **c)** adopting the initial resolution of $R = 28\,000$; **d)** $\Delta \log g = 0.3$; **e)** $\Delta T_{\text{eff}} = 200K$; **f)** all five orders analyzed separately (orders 52, 53, 54, 55, 56: circle, diamond, square, left-handed triangle, right-handed triangle). Given the limited wavelength range and the limited chemical information, not every individual order in each spectrum provides a result. Additionally, some orders in some stars are more affected by the different pixel masks and hence might show larger offsets.

Uncertainty Estimates

Statistical uncertainties are estimated within SP_Ace and expressed as a separate upper and lower limit of the derived [X/H] elemental abundances ($[X/H]_+$ and $[X/H]_-$)[4]. Here, the upper and lower limit express the 68% probability with no guarantee that the semi-error expresses the 34% limit (see Boeche & Grebel 2015 for more details). For the errors in relative abundances ([X/Fe]), we simply calculate the semi-errors as quadratic sum of the upper and lower semi-errors (e.g., $\sigma[X/Fe]_+{}^2 = \sigma[X/H]_+{}^2 + \sigma[Fe/H]_+{}^2$) and therefore overestimate the error slightly by ignoring the covariance terms between [Fe/H] and [X/H] in a full-spectrum-fitting approach. Uncertainties for [Fe/H] range from ≤ 0.1 dex to ~ 0.3 dex, depending on the brightness and the metallicity of the star. For [α/Fe] (where α = Ca, Si, or Ti) we obtain similar but somewhat larger errors. Iron-peak element (V, Cr, Co, Ni) ratios typically show uncertainties as small as [Fe/H]. Finally, the statistical uncertainties are included with some systematic error as discussed in the previous section, which limits the final accuracy of our results to $\delta[X/H] \sim 0.1$ dex, even for the brightest targets.

---

[4] When the upper or lower abundance limit falls beyond the internal SP_Ace abundance grid, a null-value is reported.

4.4 Results

4.4.1 [Fe/H], Radial Velocities and Membership Likelihood

Due to its position close to the center of Fornax, stars within the tidal radius of H4 are severely contaminated by field stars of the galaxy. A membership likelihood determination and a clear assignment of our program stars to either the cluster or the field is crucial because the chemical properties of H4 *compared* to the field is a major goal of this study.

Here, we use three observed properties to determine the membership likelihood of a target stars to the cluster H4: The star's proximity to the cluster center (r_{GC}), its radial velocity v, and its iron abundance [Fe/H] (here m). Generally, the probability for a given star with properties $\{P\}$ to be a member of the cluster H4 is given by

$$P_{\mathrm{H4}}(\{P\}) = \frac{N_*(\{P\}\,|\,\mathrm{H4})}{N_*(\{P\}\,|\,\mathrm{H4}) + N_*(\{P\}\,|\,\mathrm{field})}, \tag{4.2}$$

where $N_*(\{P\}\,|\,\mathrm{H4})$ is the number of H4 members with properties $\{P\} = p_1,\ p_2,\ \ldots\ p_i$ and similarly $N_*(\{P\}\,|\,\mathrm{field})$ denotes the number of field stars which share the same parameter space.

Using our HST photometric catalog, we first obtain an initial membership probability from the stellar density profile of the cluster, which we fit with a King profile ($K(r_{GC})$; King 1966), and extrapolate the function inwards to the unresolved center for radii $\leq 12''$ (see Figure 4.5). Notably, the contamination rate is high both at radii beyond half the tidal radius (($\geq 50\%$) and near the cluster center ($\approx 20\%$).

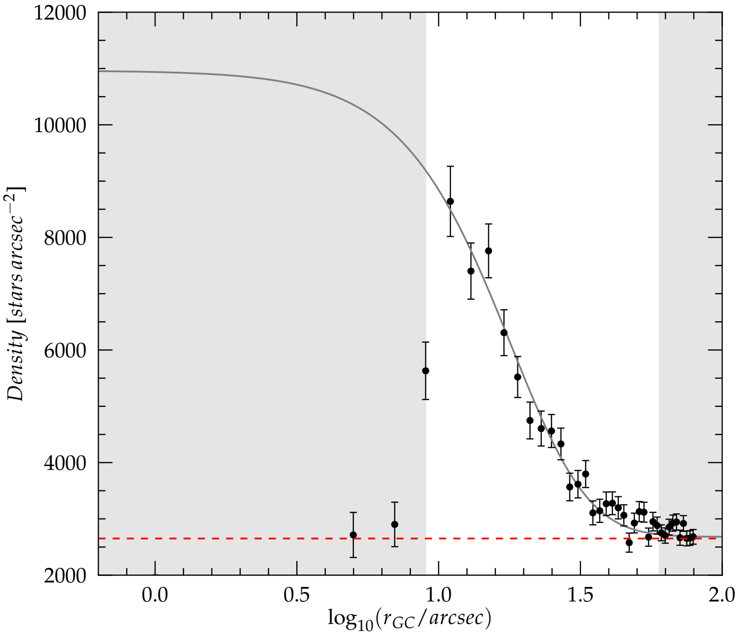

Figure 4.5: Stellar density profile of the GC H4 from HST photometry. The gray line is a King-profile fit to the data at radii beyond $r_{GC} = 12''$. The red line indicates the background level that we determine from the stellar density outside the tidal radius of the cluster. The white area in the figure shows the radial zone from which we pick our targets. At smaller radii, the cluster is not resolved with ground-based telescopes, and stars at larger radii have a very low probability to be a member of the cluster.

The fraction of stars above the uniform background compared to the background level (ρ_b) itself yields the membership probability $P_{\mathrm{H4}}(r_{GC})$ for a given star with distance r_{GC} to the cluster center:

$$P_{\mathrm{H4}}(r_{GC}) = \frac{N_*(r_{GC}\,|\,\mathrm{H4})}{N_*(r_{GC}\,|\,\mathrm{H4}) + N_*(r_{GC}\,|\,\mathrm{field})} = \frac{K(r_{GC})}{K(r_{GC}) + \rho_b}. \tag{4.3}$$

The unfortunate circumstance of heavy contamination is somewhat compensated by the fact that H4 members show a distinctly different radial velocity and [Fe/H] compared to the field stars. The radial velocity of the cluster has been measured in integrated-light studies by Larsen et al. (2012a) and Dubath et al. (1992), who consistently report values of 46.2 and 47.2 $\mathrm{km\,s^{-1}}$, respectively. Therefore H4's radial velocity is lower by $\sim 9\,\mathrm{km\,s^{-1}}$ compared to the mean galactic motion of Fornax, which approximately corresponds to the velocity dispersion of the galaxy at this metallicity (see Hendricks et al. 2014b). Additionally, H4's metallicity is measured around [Fe/H]$= -1.4$ (Larsen et al. 2012a, Strader et al. 2003), and is therefore significantly lower than the galaxy average of ~ -0.9 dex in the central part of Fornax.

When we combine the metallicity m , the velocity v, and the proximity to the cluster center r_{GC}, we can put a tight membership probability for our stars:

$$\begin{aligned} P_{\mathrm{H4}}(r_{GC}, v, m) &= \frac{N_*(r_{GC}, v, m\,|\,\mathrm{H4})}{N_*(r_{GC}, v, m\,|\,\mathrm{H4}) + N_*(r_{GC}, v, m\,|\,\mathrm{field})} \\ &= \frac{K(r_{GC}) \times p(v, m\,|\,\mathrm{H4})}{K(r_{GC}) \times p(v, m\,|\,\mathrm{H4}) + \rho_b \times p(v, m\,|\,\mathrm{field})}. \end{aligned} \tag{4.4}$$

Here, $p(v, m\,|\,\mathrm{H4})$ denotes the probability for an H4 member star to display the properties v and m. Similarly, and $p(v, m\,|\,\mathrm{field})$ is the equivalent expression for field stars.

We extract the chemical and dynamical properties for the contaminating field stars from the catalog provided in Battaglia et al. (2008), which provides Calcium-Triplet metallicities and radial velocities for nearly 1000 stars. To take into account radial variations of these properties within Fornax, we only consider 406 objects which are located at similar radii to the cluster, and specifically stars with $r \leq 0.3°$.

We do not know the exact properties of H4 given that all information is derived from integrated-light analysis. With the risk of systematic misplacement of its actual properties, we assume that all H4 members fall within certain limits of [Fe/H] and v where $p(v, m|\mathrm{H4}) = 1$, but do not have a preferred position within these intervals. Consequently, there is a zero likelihood to find a member outside these limits. We set the allowed parameter space for H4 members between $-1.65 \leq$ [Fe/H] ≤ -1.3 and $42.5 \leq v \leq 52.5\,\mathrm{km\,s^{-1}}$, constrained by previous integrated-light measurements that take into account their measurement error and a possible systematic bias in the methodology. For the velocities, we additionally take into account H4's intrinsic velocity dispersion of $\sim 4.5\,\mathrm{km\,s^{-1}}$ (Larsen et al. 2012a, Dubath et al. 1992).

For the field stars, the distributions of [Fe/H] and the radial velocities are not Gaussian functions nor are they any other evident analytical shape. We therefore abandon the attempt to model the complex distribution in a combined parameter space. Instead, we assess the contamination fraction $p(v, m\,|\,\mathrm{field})$ empirically from the fraction of field stars that fall within the allowed parameter box of H4 and find $p(v, m\,|\,\mathrm{field}) = 0.020$. Under these assumptions—and if its Fe and v identifies a star as a potential cluster candidate—the probability for each of our targets to be an actual member of the cluster, becomes

$$P_{\mathrm{H4}}(r_{GC}, v, m) = \frac{K(r_{GC})}{\rho_b \times p(v, m\,|\,\mathrm{field}) + K(r_{GC})}. \tag{4.5}$$

Finally, we use a bootstrapping technique to estimate the uncertainty for $P_{\mathrm{H4}}(r_{GC}, v, m)$ by constructing a number of equally sized samples where each individual entry is altered randomly within its uncertainties in v and m. In Figure 4.6, we show the derived [Fe/H] abundances and velocities on top of the underlying field star distribution. Most of the stars we selected from within the tidal radius of H4 resemble typical properties of field stars in Fornax, with high metallicities ([Fe/H]≥ -1.2) and velocities of $\sim 45-70\,\mathrm{km\,s^{-1}}$. From the few outliers, one is very metal-poor ([Fe/H]≤ -2.0 dex) and with high radial velocity. This combination may be typical given that previous studies already detected a trend for more extreme velocities amongst metal-deficient stars in the galaxy (Battaglia et al. 2006, Hendricks et al. 2014b). The remaining four all have [Fe/H]≈ -1.5, and three of them show almost identical radial velocities of 47.2, 48.2, and $46.6\,\mathrm{km\,s^{-1}}$. For the last candidate we measure a similar metallicity but a radial velocity about two times larger than the intrinsic dispersion within H4. Strikingly, two of the stars that fall within the acceptable parameter space are also located closest to the center of H4, which strengthens the assumption that they are members of the cluster. For them, we obtain a membership likelihood of $99.2 \pm 0.4\%$ (target r_0010) and $97.7 \pm 1.2\%$ (target r_0016), respectively, but the third star (target b_0018) with larger r_{GC} is still a $71.0 \pm 11.0\%$ member of H4. Given a membership likelihood of at least 2-3 sigma for our best candidates, we will assume that these stars are true cluster members in the following chemical analysis and discussion.

The remaining targets outside the tidal radius of H4 have been picked deliberately from the sparse metal-poor tail of the galaxy, and therefore their [Fe/H]-v distribution does not reflect the dominant distribution of the field star population.

Our chemical analysis yields iron abundances for 30 targets, 15 of which are located within the tidal radius of H4. Of these stars, three "clump" around the fiducial cluster properties. Given this small number, our sample does not allow for an individual estimate of the cluster's chemical or dynamical properties, and—in contrast— we *adopted* these mean cluster parameters from the literature to identify member stars. From our three likely members, we find a weighted (by error and membership likelihood) mean metallically of [Fe/H]$= -1.56$ dex, slightly lower than the values obtained from integrated-light studies. This may not be surprising when we consider that most of the contaminants in integrated-light spectra are undoubtedly more metal-rich than the cluster itself. With a similar explanation, our bona-fide members have weighted mean radial velocity of $47.6\,\mathrm{km\,s^{-1}}$, marginally higher than the integrated-light estimates.

4.4.2 Alpha-Elements

The alpha-elements in stellar atmospheres analyzed with respect to iron reveal the fraction of SN Ia contributions to the star forming material and hence are an indicator for the enrichment efficiency of the galactic environment. The [α/Fe] parameter is known to be distinctively different in the field star population of dwarf galaxies compared to the MW.

In Figure 4.7 we show the results for the alpha-elements Ca and Ti as a function of the stars' iron abundances. For both elements, we find a clear sequence with metallicity. While field stars with [Fe/H]≤ -1.8 tend to have [α/Fe] above solar level, this ratio drops continuously to clearly sub-solar values for [Fe/H]≈ -1.3 and higher. Clearly, our stars show an early depletion in both elements compared to the MW halo. This trend does not allow for a knee in the alpha-iron evolution at [Fe/H] significantly higher than -2.0 dex, which confirms previous findings by Hendricks et al. (2014a) and later Lemasle et al. (2014), and indicates a low chemical enrichment efficiency within the Fornax dSph galaxy. One star falls out of this general scheme by showing high [α/Fe] for Ca and Ti, despite being the star with the highest [Fe/H] in our sample. By that, it better resembles the characteristics of MW disc stars. Therefore, it is possible that this star is a Galactic interloper that does not belong to the Fornax dwarf spheroidal.

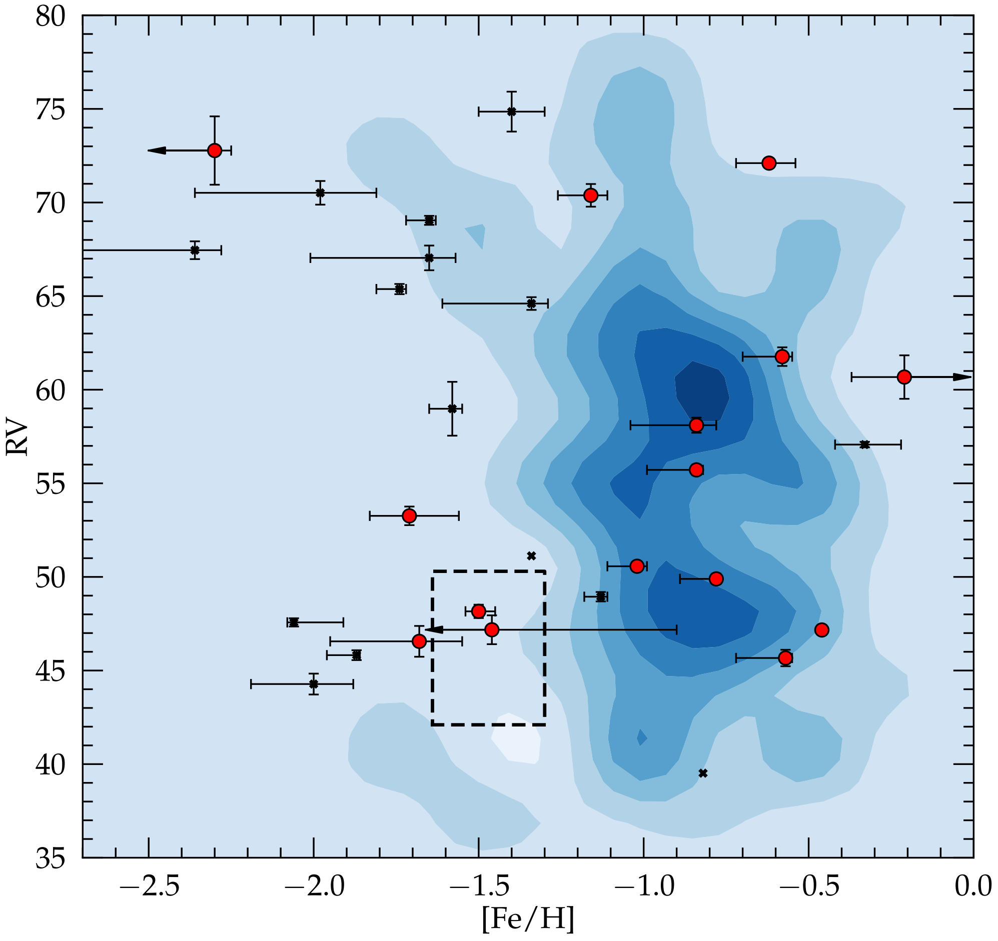

Figure 4.6: Radial velocity and [Fe/H] of our targets stars are overplotted to the field star distribution, visualized as a linearly-scaled density distribution of arbitrary units (blue contours). Stars within the tidal radius of H4 are shown in red. Importantly, three of them group within the parameter space where we expect cluster members (black box). Black symbols are targets outside the tidal radius, which are purposefully selected to be metal-poor and therefore are not representative of the actual field star distribution.

While two of the H4 members in our sample are too faint to determine reliable alpha-abundances, one star (r_0010 with 99.2% membership likelihood) is one of our brightest targets and we can derive precise abundances for Ca, Ti, and, with larger uncertainties, Si. For this star, we measure low [α/Fe] ratios for all three elements. In detail, we find [Ca/Fe]= $+0.05^{+0.09}_{-0.07}$, [Ti/Fe]= -0.27 ± 0.23, and [Si/Fe]= -0.35 ± 0.34, resulting in an average [α/Fe]= -0.19 ± 0.14. Given the high membership likelihood to H4 and the small uncertainties on our abundances, this is a strong indication that H4 is an alpha-depleted GC, with a combined [α/Fe] possibly at or around sub-solar level.

To this point, the only existing measurement of alpha-elements in H4 comes from Larsen et al. (2012a) and is based on integrated-light spectroscopy of the cluster. These authors find [Ca/Fe]=$+0.13 \pm 0.07$ and [Ti/Fe]=$+0.12 \pm 0.05$, which is somewhat larger than our results from an individual member star. The discrepancy might be partially explained with the measurement errors of the respective analyses. Furthermore, it is important to recall the high contamination of more than 20% within the 5″ slit, which has been used to obtain the integrated-light spectrum. These authors carefully try to minimize the impact of this contamination by evaluating the spectrum at different positions, and therefore at different cluster radii. Unfortunately, the options to detect and correct for contamination effects are limited, and the contamination fraction does not change by more than 10% within the central 5″ of the cluster. As a consequence, it is difficult to reconstruct the actual underlying population mix because the contaminating field stars show a broad range of ages and metallicities. Therefore, even with a careful approach, a small bias between results obtained from integrated-light and individual stars can be expected. Overall, however, both studies agree that H4 has lower[α/Fe] than similar metallicity Milky Way GC and field stars.

The Full Picture: Co-Evolution of Field Stars and GCs in Fornax

Important insights can be obtained when the alpha-abundances of all GCs in Fornax are viewed in the context of the field star enrichment in the galaxy. If we combine literature samples of [Ca/Fe] measurements for field stars (43 stars from Lemasle et al. 2014, 85 stars from Letarte et al. 2010) with our own sample from this work (21 stars), we obtain a well defined and coherent alpha-element evolution sequence (see Figure 4.8). The data clearly show that for [Fe/H] below approximately -2.0 dex, field stars are alpha-enhanced and share the typical properties of MW halo stars (see also Tafelmeyer et al. 2010 for one star at [Fe/H]= -3.66 and [Ca/Fe]= $+0.48$). Towards higher metallicities, the [α/Fe] ratio drops and evolves from super-solar to sub-solar values around [Fe/H]≈ -1.5. Although there are no stars in common between the individual field star samples, there is an excellent agreement between the observed properties for all respective metallicities.

The four metal-poor GCs in Fornax are all moderately enhanced in [α/Fe], and have values comparable to clusters found in the halo of the MW. However, the metal-poor Fornax GCs may lie somewhat below the average plateau found in the MW. In detail, for three of the metal-deficient clusters in Fornax, [Ca/Fe] has been measured from three individual stars in each cluster by Letarte et al. (2006). These authors find alpha-enhanced values for all three systems with average values of $+0.18 \pm 0.09$, $+0.22 \pm 0.06$, $+0.24 \pm 0.03$ for H1, H2, and H3, respectively. Additionally, Larsen et al. (2012a) also derive [Ca/Fe] from integrated-light analysis for the metal-poor GCs H3 and H5 and find $+0.25 \pm 0.07$ and $+0.27 \pm 0.05$.

Taking the information from field stars and GCs in Fornax together, two important consequences arise. First, it is very likely that the cluster H4 does have a significantly lower [α/Fe] abundance ratio than the rest of the GC population in Fornax. Second, the clusters in Fornax *follow* the [α/Fe] sequence of the field stars and clearly disagree with with the enrichment pattern of the MW halo. Therefore, there is strong evidence that the chemical enrichment of GCs and field stars in the Fornax dSph is coupled, and that the clusters trace the chemical signatures of the field star population in their host. We will discuss the consequences of such a scenario for other alpha-depleted GCs in

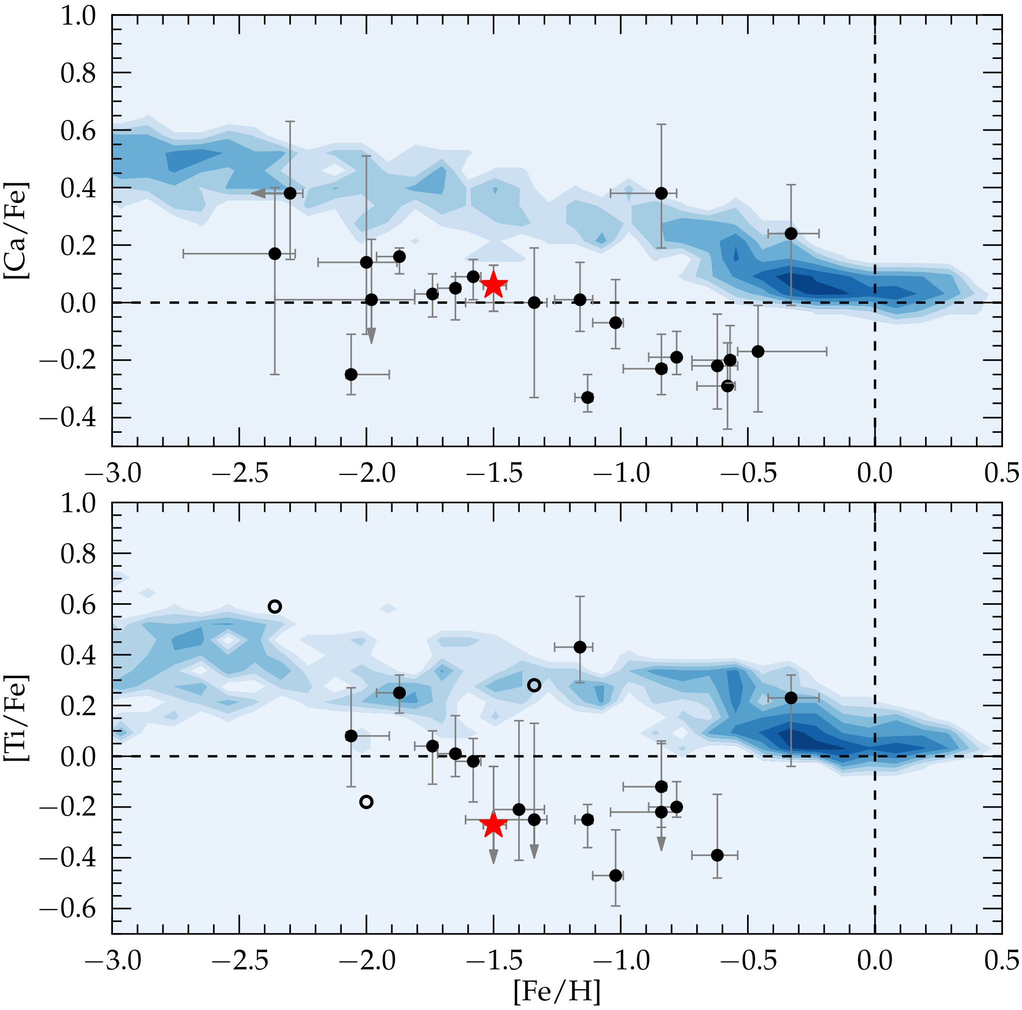

Figure 4.7: Chemical evolution of the alpha-elements Ca (upper panel) and Ti (lower panel) as a function of [Fe/H]. Black dots show the field stars in our sample and the red star highlights the GC H4 star. For visual comparison, the pattern of MW disc and halo stars are shown as a logarithmically-scaled number density distribution of arbitrary units (data from Venn et al. 2004 and Roederer et al. 2014). For both elements, we observe a clear sequence with [Fe/H], and in both cases the H4 member falls on top of this sequence and does not agree with the chemical abundance pattern seen in the MW. Open circles indicate objects for which SP_ACE could not find upper and lower abundance limits, either due to the low quality of the spectrum or because its chemical parameters fall close to the boundary of the allowed abundance grid.

Section 4.5.1.

The evident chemical enrichment pattern also highlights the star formation differences between Fornax and the MW. In the MW, [α/Fe] declines for the field stars but not the GCs, which means that the GCs with, e.g., [Fe/H]≈ -0.3 possibly formed before the field stars of the same metallicity. Such a scenario does not appear to be the case with Fornax where the field stars and GCs follow each at metallicities exceeding the location of the [α/Fe] knee.

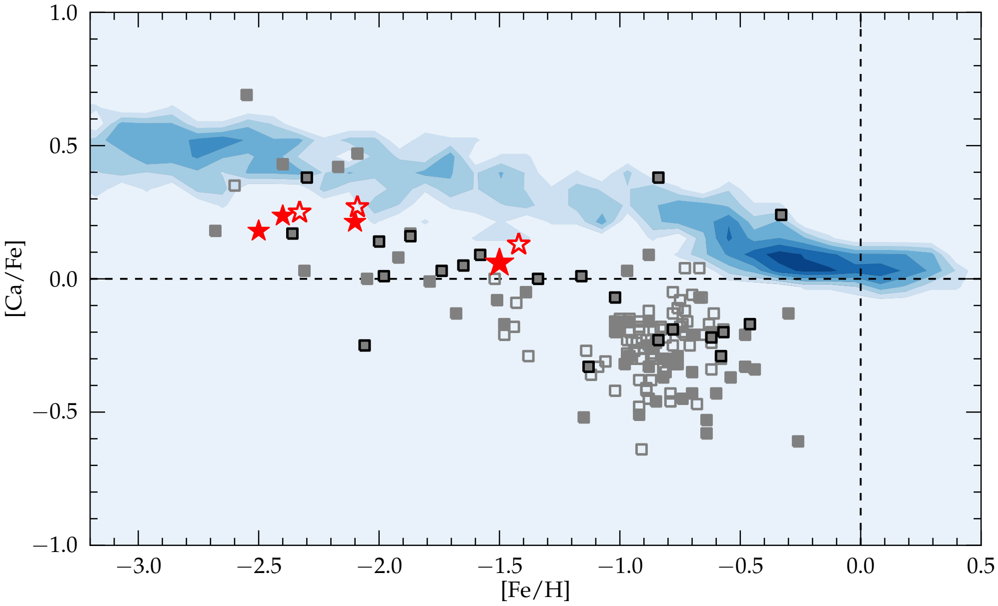

Figure 4.8: Fornax displays a different chemical enrichment pattern from the MW. This is seen in the alpha-element evolution of the field stars *and* the GCs, which show a coupled chemical enrichment. Blue contours show the pattern of MW field stars from Venn et al. 2004 and Roederer et al. 2014. Fornax field stars come from Letarte et al. (2010) (open gray), Lemasle et al. (2014) (filled gray), and this work (filled gray with black edge). Star symbols show the location of the metal-deficient GCs H1, H2, H3 (filled, small red stars; Letarte et al. 2006), H3, H4, H5 (open red stars; Larsen et al. 2012a) and the measurement for H4 presented in this work (filled large red star).

4.4.3 Iron-Peak Elements

It is thought that most iron-peak elements (Sc to Zn: $21 \leq Z \leq 30$, excluding Ti which behaves like an alpha-element) descend from similar nucleosynthetic pathways. While at early times, massive stars and their subsequent SNe II explosions are the only production resource, SNe Ia become the dominant contributor later on, when low mass stars had time to sufficiently evolve. Despite forming a common family of elements, the exact formation channels for individual species are not clear, and in most cases there is no simple scaling with the Fe abundance. For a large fraction of stars in our sample, we obtain abundances for several iron-peak elements to compare with the Galactic trends. The results are shown in Figure 4.9

Nickel. The [Ni/Fe] ratio is generally underabundant by ~ 0.2 dex compared to solar and MW abundance ratios. Such low abundances have been previously observed in Fornax (Letarte et al. 2010, Lemasle et al. 2014) and also in Sagittarius (e.g., Carretta et al. 2010a, Sbordone et al. 2007). The LMC displays a larger scatter in Ni above and below solar (Pompéia et al. 2008). Our results seem to indicate that the sub-solar [Ni/Fe] abundance ratio, which has been perviously found for stars in satellite systems between [Fe/H]≈ -0.5 dex and [Fe/H]≈ -1.5 dex, continues to even lower metallicities.

Chromium. Our Cr abundances lie slightly below the solar abundance ratio and the Galactic trend, although few reliable comparison data are available for [Fe/H]≥ -1.5 dex. They agree well, however, with previous measurements of Fornax field stars from Letarte et al. (2010) and Lemasle et al. (2014), although only a few lines could be measured and the abundances are statistically not very well constrained.

We additionally measure abundances for the iron-peak elements Sc, V, and Co, for which we generally find slightly sub-solar abundance ratios. Unfortunately, there are only very few comparison data available for MW stars, and no previous measurements exist for Fornax. These abundances are therefore not shown in Figure 4.9, and they are only published in the online version of Hendricks et al. (2015, submitted to A&A).

4.4.4 The Age of H4

The relative age of H4 has been a subject of controversy during the last decades, not least because its detailed chemical composition—and specifically the [α/Fe] abundance of its stars—has not been known. Using a relatively clean sample of HST photometry, Buonanno et al. (1999) estimated the relative age of H4 from its photometric offset at different regions in the CMD compared to other clusters in Fornax. From this, the authors found H4 to be ~ 3 Gyr younger than the other four GCs, which are all coeval and resemble typical old ($\sim$ 12 Gyr), metal-poor MW halo GCs like M92 (Buonanno et al. 1998). However, these results were based on the assumption that *all* Fornax clusters display a similar chemical mixture, in disagreement with our findings. Later, Strader et al. (2003) used age sensitive—but alpha-insensitive—spectroscopic indices like H_β and H_γ to constrain relative ages amongst Fornax clusters and found a similar age for H4 compared to the old systems H2 and H3 (they found, however, indications that H5 is slightly younger). If H4 is indeed younger compared to the rest of the GC population, it is not clear how Fornax was able to form this cluster several Gyr later than all of the other more metal-poor clusters in the galaxy. This is specifically intriguing when viewed in the context that similarly young Galactic GCs, such as Ruprecht 106 and Palomar 12, are thought to be accreted from satellite dwarf galaxies (Brown et al. 1997).

Precise relative age estimates of GCs can be obtained when isochrones are fitted to to the resolved main-sequence turn-off (MSTO) region of the cluster. If the chemical composition and the line-of-sight reddening to the cluster are known, the addition of zero-age horizontal branch (ZAHB) model fitting can enable one to achieve a precision well below 1 Gyr (see VandenBerg et al. 2013). However, both the position and shape of the MSTO and the HB luminosity are sensitive to the underlying [α/Fe] ratio. This degeneracy causes a systematic bias in the derived ages of several Gyr for cases where the detailed composition of the cluster is not known.

Provided with a tight constraint on the [α/Fe] abundance in H4, we can now make a new approach to constrain the age of the system and specifically aim to answer the question whether H4 is younger than the remainder of the population in Fornax. To do so, we follow the general procedure described in VandenBerg et al. (2013). Specifically, we derive synthetic ZAHB loci from the lower envelope of synthetic HB models from Dotter et al. (2007) provided on the Dartmouth-Isochrone database[5] and fit them to the observed red horizontal branch of the cluster to set the absolute magnitude scale. Then, the age of the cluster is determined by the best fitting Dartmouth isochrones (Dotter et al. 2008) to the turn-off and subsequent subgiant branch region, after a reddening correction has been applied. To minimize the number of field stars in the CMD, we consider only

---

[5] http://stellar.dartmouth.edu/ models/index.html

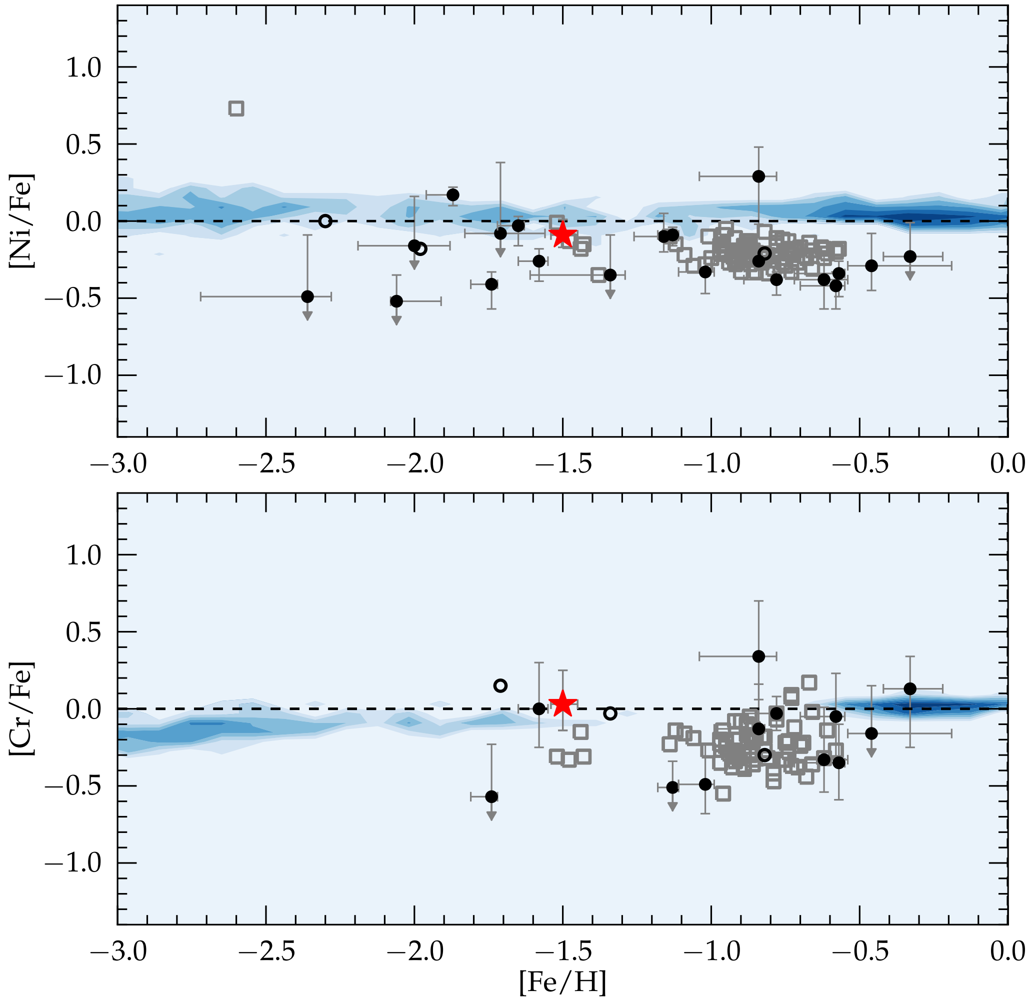

Figure 4.9: [Ni/Fe] and [Cr/Fe] as a function of [Fe/H]. As in Figure 4.7, black dots show the field stars in our sample and the red star highlights the GC H4 star. Contours show the pattern of MW disc and halo stars (data from Venn et al. 2004, Roederer et al. 2014, Reddy et al. 2003, and Bensby et al. 2003). Open circles indicate objects for which SP_ACE could not find upper and lower abundance limits. Gray open squares are Fornax field star measurements from Letarte et al. 2010.

an area within $r_{GC} \leq 15''$ around the cluster center. For all models, we adopt [Fe/H]$= -1.5$ and [α/Fe]$= 0.0$, and a correction for reddening and extinction of $E(V-I) = 0.11$ and $A_V = 0.248$ (see Section 4.3.2 for details about the reddening).

In Figure 4.10 we show the result. From the position of the ZAHB, we find a distance modulus of $\mu_0 = 20.74 \pm 0.4$, in agreement with previous estimates for the distance to the galaxy itself (e.g., Bersier 2000, Rizzi et al. 2007, Pietrzyński et al. 2009). However, this number is slightly higher than the results of Greco et al. (2007) who find $\mu_0 = 20.53 \pm 0.09$ from RR Lyrae stars in H4, if [Fe/H]$= -1.5$ is adopted.

We obtain the best isochrone fit using an age of 10 Gyr, which places H4 at a *younger* age compared to the rest of the population. However, this result should be interpreted with caution since the uncertainty is at least ±1 Gyr, given the poorly defined MSTO at V-band magnitudes around 24.5 and when we consider the still significant fraction of field stars in the CMD with different chemical signatures and ages than the cluster itself. If we further consider inaccuracies in the reddening [6], an age as old as 12 Gyr, comparable to the other Fornax clusters, seems to be still a conceivable possibility.

---

[6] for H4, the estimates range between $E(B-V) = 0.15$ and 0.08, while Fornax itself has a reddening not higher than $E(B-V) = 0.04$ from Schlegel et al. (1998) reddening maps

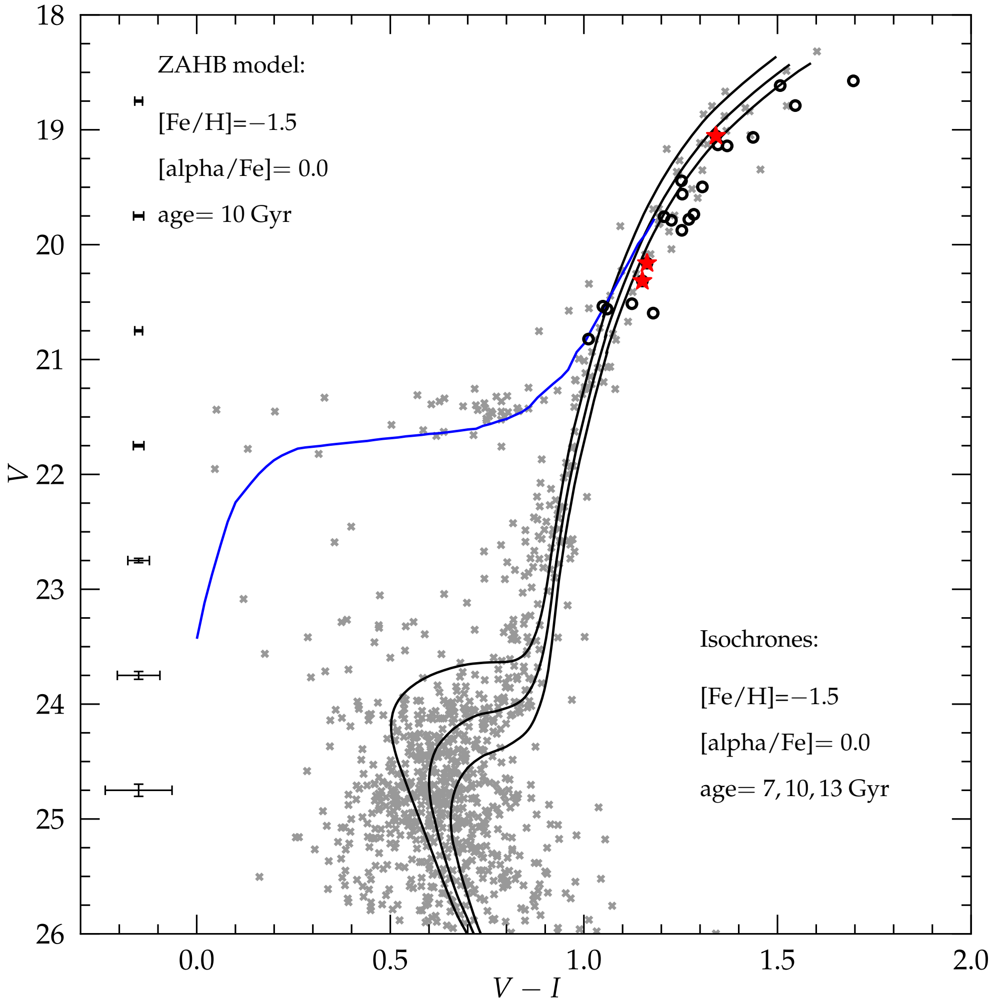

Figure 4.10: Color-magnitude diagram of H4 from our HST photometry. Only stars from the innermost 15″ around the cluster center are shown to minimize the impact of contaminating field stars. Dartmouth Isochrones (Dotter et al. 2008) of 7, 10, and 13 Gyr of age and a 10 Gyr ZAHB model are overplotted to the data. The ZAHB luminosity, however, is not sensitive to age in this regime and therefore the model is representative for all three ages compared here. Red stars indicate the position of the three likely H4 members in our sample and black circles are other targets with H4's tidal radius. The isochrones give a best fit for ages around ∼ 10 Gyr, but uncertainties in reddening and distance to the cluster do not allow a tight age constraint, although the chemical parameters of the cluster are now known.

4.5 Discussion

4.5.1 Origin of Alpha-Depleted GCs in the Halos of Larger Galaxies

The evidence that H4 is an alpha-depleted GC makes it one out of only three known clusters to be depleted at this low metallicity. The other known alpha-depleted clusters are Ruprecht 106 in the MW (Brown et al. 1997, Villanova et al. 2013) and G002 in M31 (Colucci et al. 2014). Importantly, H4 is the only of these clusters which can be clearly associated with a dwarf galaxy, and we may observe in Fornax the first birthplace of a metal-deficient, alpha-depleted GC. The case of Fornax therefore supports speculations which predict similarly depleted clusters in the halo of larger galaxies to originate from dwarf galaxies with low chemical enrichment efficiency (e.g., Colucci et al. 2014).

Following this concept, we can use the properties of accreted GCs to learn about their former host systems. On the one hand, alpha-depleted GCs like Ruprecht 106 and G002 require a host galaxy with a sufficiently low chemical enrichment efficiency to *enable* significant SNe Ia contribution for stars already at such low metallicities. Given that a galaxy's mass is likely the main driver of its enrichment efficiency (e.g.,Matteucci & Brocato 1990, Tolstoy et al. 2009), the host needs to have stellar masses as low as Fornax or the Sculptor dSph (i.e. a few $10^7 M_\odot$), while a system as massive as the Magellanic Clouds can be ruled out. On the other hand, recent studies argue that a large fraction of GCs in the halos of the MW and M31 have not formed in-situ, but instead have been accreted from infalling satellite systems (e.g., Mackey & Gilmore 2004, Leaman et al. 2013, Mackey et al. 2010, Huxor et al. 2011, Elmegreen et al. 2012). Since in both galaxies the large majority of GCs are uniformly alpha-enhanced over a wide range of iron abundance, some clusters with high [Fe/H] and high [α/Fe]-ratios should be of accreted origin. In contrast to Ruprecht 106 and G002, these clusters require a progenitor system with a higher stellar mass than Fornax in order to *prevent* a significant contribution of SNe Ia at these high metallicities. In a ΛCDM universe, such high-mass mergers are increasingly unlikely. Consequently, alpha-enhanced accreted GCs necessarily need to originate from only a very small number of disrupted satellite systems. Strikingly, studying the bifurcated age-metallicity relation amongst disc- and halo GCs in the MW, Leaman et al. (2013) come to a very similar conclusion for both the masses and the number of accreted host satellites carrying GC systems. Finally, the case of Fornax shows that not all GCs within a dwarf galaxy need to have the same chemical signature. Therefore GCs with different [Fe/H] and [α/Fe] could have originated in the same system.

It seems, there is another lesson to be learned from the observation of alpha-depleted GCs. There is no evidence, neither from observations nor from theory, about the lower mass limit for a galaxy to be able to form (and hold) own GCs. The search and detection of alpha-depleted clusters can serve as an empirical upper limit. With decreasing [Fe/H] observed in these peculiar clusters, the lower becomes the required star formation efficiency—and hence mass—of the host. Currently, this limit is set by G002, the most metal-deficient alpha-depleted cluster, with $\text{[Fe/H]} = -1.66$. This cluster consequently requires a host galaxy even smaller than Fornax, and therefore with a maximum mass of $10^7 M_\odot$.

4.5.2 H4: The Nucleus of the Fornax dSph?

H4 is located remarkably close to the center of the Fornax dSph. This, together with its distinguishing higher metallicity compared to the other clusters, has fired speculations about whether H4 is in fact the nucleated core of the galaxy, similar to M54 in the Sagittarius dSph galaxy (Hardy 2002, Strader et al. 2003) or comparable to the suspect accreted nucleus ω Cen (Bekki & Freeman 2003). If this is the case, it is not self-evident if the properties we observe in H4 can be transferred to classical GC systems in other galaxies.

First, M54 and specifically ω Cen display a spread in iron. This characteristic cannot be constrained with our data nor from integrated light. We do not observe sufficient individual stars with sufficient chemical precision in order to place a limit on the intrinsic metallicity spread of the system. Integrated light spectroscopy, on the other hand, only provides a cumulative iron abundance while the necessary information about line-strength variation is lost in the doppler-broadened line profile (McWilliam & Bernstein 2008).

Second, M54 is embedded in the very center of its host galaxy. There is also no clear answer to this critereon. If H4 in fact falls on top of the cusp of the field stellar distribution is a matter of debate because of the asymmetry in Fornax' density profile (Stetson et al. 1998). This results in a "chaotic" behaviour of centroids and inclination angles for elliptical profiles fitted at different radii (Demers et al. 1994). While these authors claim to find H4 at the position where the surface density of stars peaks, Hodge (1961) and later Stetson et al. (1998) find an offset between the peak density and the position of H4. If H4 is the nucleated core of Fornax, it should also be measured at the exact same distance. From ZAHB models we find a best fitting distance modulus of $\mu_0 = 20.74$, which agrees with previous distance measurements for the field star population in Fornax, ranging between $\mu_0 = 20.65$ (Bersier 2000) and 20.87 (Pietrzyński et al. 2003). Given that the actual physical size of the galaxy is between 2 and 3 kpc, and by that several times smaller than the uncertainty on its distance estimations, the existing measurements allow for a placement of H4 right in the center of the galaxy as well as several times outside its tidal perimeter.

Third, M54 moves with the main body of Sagittarius. As outlined in Section 4.4.1, the radial velocity of H4 is determined as precise as $1\,\mathrm{km\,s^{-1}}$ from integrated-light spectroscopy, and is found to be distinctively different to the mean galactic motion by $\sim 9\,\mathrm{km\,s^{-1}}$. This, finally, is evidence that H4 is a classical GC which just coincidentally falls close to the line-of-sight towards the center of Fornax. However, better data will be necessary to further constrain the first and the second aspects, and to eventually obtain a final conclusion on the nature of H4.

4.5.3 Insights from Field Star Evolution at Different Galactocentric Radii

Fornax is one of the best studied of all dwarf galaxies, and the detailed chemical properties of field stars have been an issue in a series of recent papers (Letarte et al. 2010, Hendricks et al. 2014a, Lemasle et al. 2014). It is also the only galaxy where the combined datasets cover a large fraction of its radial extent. Specifically, Hendricks et al. (2014a) and Lemasle et al. (2014) provide the alpha-evolution of stars at $r \approx 0.6^\circ$ (compared to a tidal radius of $\sim 1^\circ$), while the current work, for the first time, yield similar information for the very central area at $r \leq 0.2^\circ$.

In Figure 4.11, we fit a simple step function to the alpha-evolution sequence of all literature samples, similarly to what has been done in Cohen & Huang (2010), or Hendricks et al. (2014a). This toy model has no physical motivation, and is only designed to estimate the position of the knee and the two plateau values of [α/Fe] for both high and low [Fe/H]. When we compare the alpha-evolution at different radial positions in this naive way, we find them to follow essentially the same sequence, which also agrees with the visual impression of the data.

This mutual agreement between the different samples confirms a very slow chemical enrichment in Fornax, seen as a metal-poor knee. Moreover, this means that the chemical enrichment efficiency in the center and the outskirts of Fornax had to be similar, at least at early times. This fact comes a little bit surprising, if one considers that the enrichment efficiency comprises the star formation efficiency on the one side, and the ability to retain the processed stellar yields on the other. Both factors are theoretically sensitive to the density of the ISM and the depth of the gravitational potential, which in turn are both a function of radius.

It is well established that stars in the center of Fornax are of a significantly higher average metallicity than in the outer parts (e.g., Battaglia et al. 2006). The consequence of the above considerations could be that the inner area did not undergo a *faster* chemical evolution, but rather experienced a *longer* star formation history, which eventually caused the observed radial metallicity gradient within the galaxy.

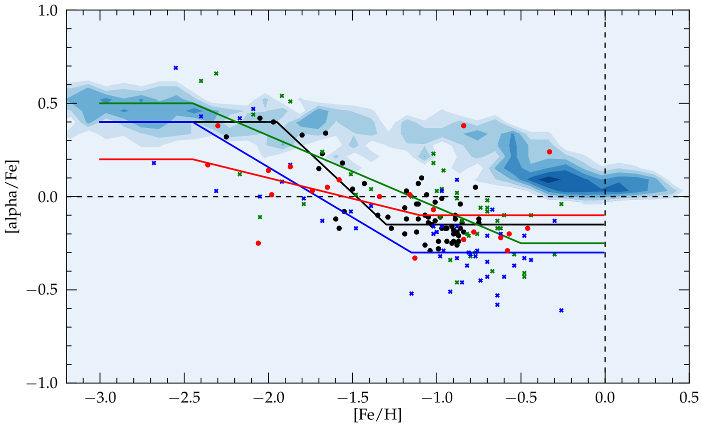

Figure 4.11: Fornax displays very similar chemical enrichment signatures at different radial positions within the galaxy. The evolution of individual alpha-elements is identical within the limited precision of the data. In detail, black points are [Mg/Fe] measured at $r \approx 0.6°$ from Hendricks et al. (2014a), green and blue crosses show [Mg/Fe] and [Ca/Fe] measured at $r \approx 0.6°$ from Lemasle et al. (2014), and red points are the [Ca/Fe] values at $r \approx 0.2°$ from this work. The lines are toy model fits as described in the text to the samples with corresponding color. The contours show the evolution of MW field stars for comparison, averaged for Mg and Ca.

4.6 Summary

In this chapter, we presented radial velocities and high-resolution chemical abundances for Fe, several alpha-elements (Ca, Ti, and Si), and iron-peak elements (V, Cr, Co, Ni) for an individual member star of the peculiar GC H4 and 27 additional stars in the surrounding field at the center of the Fornax dwarf spheroidal galaxy. H4 is difficult to observe due to its central position within the galaxy with severe contamination higher than 30% in the resolved area of the cluster. Our sample has been selected from HST photometry, where we carefully avoided blended stars in a seeing limited scenario. We obtain the first detailed chemical analysis for an individual member star in H4, which we put into context to the chemical signatures of field stars in Fornax from this work and from previous studies. The main results are summarized below:

- Our field star sample cover a wide range in metallicity, with $-2.3 \leq [\mathrm{Fe/H}] \leq -0.4$, and show a distinct change in [α/Fe] as a function of [Fe/H]. In detail, stars are alpha-enhanced at low metallicity where they show similar properties to metal-deficient MW field stars. With increasing [Fe/H], they follow a clear sequence towards sub-solar [α/Fe] ratios.
- The observed field star sequence is in good agreement with previous observations made in this galaxy and does not allow for a knee in the alpha-evolution significantly higher than [Fe/H]~ -2.0 dex, indicative of a low star formation efficiency in Fronax.

- By comparing the alpha-evolution of different field star samples from literature, it is possible to put a tentative constraint on radial chemical enrichment variations within Fornax. We do not find any significant variation for the evolution of a given species with [Fe/H] and therefore speculate that such variations, if existent, have to be small.
- We obtain precise chemical abundances for one star with a 99.2% membership likelihood to the GC H4 and find low alpha-abundances of [Ca/Fe]$= +0.05 \pm 0.08$, [Ti/Fe]$= -0.27 \pm 0.23$, and [Si/Fe]$= -0.35 \pm 0.34$, resulting in an average [α/Fe]$= -0.19$. This makes H4 one out of only three metal-deficient GCs known to be alpha-depleted. Moreover, Fornax becomes the first observed birthplace of such peculiar clusters, which can also be found in the halos of larger galaxies, supporting speculations that these clusters are accreted from now disrupted satellite systems.
- Considered together, the GC population in Fornax follows the chemical signature of the field stars and explicitly disagrees with the properties of Milky Way stars and GCs. We therefore conclude that the chemical enrichment of field and clusters in Fornax is *coupled* and determined by the properties of the common host galaxy.
- If the chemical enrichment signatures of a galaxy as imprinted in the alpha-evolution of its field stars are inherited to its GC population, we can draw inferences from the chemical properties of accreted GCs about their unknown satellite hosts. Following this concept, the alpha-depleted, metal-deficient clusters Ruprecht 106 in the Milky Way and G002 in M31 require a host galaxy similar to, or smaller than Fornax, and consequently with a stellar mass of $\sim 10^7 M\odot$. In contrast, alpha-enhanced GCs with [Fe/H]~ -1, if accreted, require more massive birth places, with masses $\sim 10^8 M\odot$ or more. This argument, however, relies on the assumption that mass is the main parameter to determine the chemical enrichment properties of a galaxy. If, however, other parameters like environmental interactions also play an important role, it becomes more difficult to reconstruct the host galaxies properties in such a way.

Finally, it is important to emphasize that a large portion of our findings (and its interpretation) rely on the properties of only one member star of H4 (two more likely candidates in our sample proved too faint for a detailed chemical analysis). Although the analyzed star is almost certainly a member of the cluster, and despite the robust abundance measurement we could perform on its spectrum, it is possible that its properties are not representative of the average cluster chemical composition. Clearly, in order to confirm the results related to H4 and the subsequent conclusions, it would be desirable to obtain chemical information from more individual members of this cluster in the future.

5

Summary

The work presented here helped to improve significantly our understanding of the individual evolution of dwarf galaxies and the interdependency with their local environment. In particular, I could show that the chemical enrichment efficiency within a galaxy does not simply scale with the present-day luminous mass or mean metallicity of the system. Thus, the chemical enrichment need to be sensitive to additional intrinsic or environmental influences on the galaxy. For Fornax—the prime target of this work—I find high complexity in the chemical and dynamical signatures of field stars, with an additional dependence between chemical-, spatial-, and dynamical properties. Detailed information for stars of *all ages* and at *all radii* is therefore needed to draw a conclusive picture about the star formation and chemical evolution of dwarf galaxies. The coupling between GCs and field star chemical enrichment in Fornax, revealed in this work, provides tight constraints on the origin of globular clusters and will enable the chemical enrichment characterization of distant galaxies from integrated-light cluster analysis. The results, put into context of near-field cosmology, thus helped to unravel the critical issues about fundamental principles of large structure assembly and the governing physics which regulate the evolution of galaxies.

In Chapter 2, I presented alpha-element abundances of Mg, Si, and Ti for a large sample of field stars in two outer fields of the Fornax dwarf spheroidal galaxy, obtained with VLT/GIRAFFE ($R \sim 16\,000$). Due to the large fraction of metal-poor stars in my sample, I was able to follow the alpha-element evolution from [Fe/H] ≈ -2.5 continuously to [Fe/H] ≈ -0.7. For the first time I was able to resolve the turnover from the Type II supernovae (SNe) dominated, α-enhanced plateau down to subsolar $[\alpha/\mathrm{Fe}]$ values due to the onset of SNe Ia, and thus to trace the chemical enrichment efficiency of the galaxy. My data supports the general concept of an alpha-enhanced plateau at early epochs, followed by a well-defined "knee", caused by the onset of SNe Ia, and finally a second plateau with sub-solar $[\alpha/\mathrm{Fe}]$ values. I find the position of this knee to be at [Fe/H] ≈ -1.9 and therefore at significantly lower [Fe/H] than expected from comparison with other dSphs and standard evolutionary models. Surprisingly, this value is rather comparable to the knee in Sculptor, a dSph ~ 10 times less luminous than Fornax. Chemical evolution models reveal that both the position of the knee as well as the subsequent plateau at sub-solar level can hardly be explained unless the galaxy experienced several discrete star formation events with a drastic variation in star formation efficiency, while a uniform star formation efficiency can be ruled out.

One possible evolutionary scenario is that Fornax experienced one or several major accretion events from gas-rich systems in the past, so that its current stellar mass is not indicative of the chemical evolution environment at ancient times. If Fornax is the product of several smaller buildings blocks, this may also have implications of the understanding on the formation process of dSphs in general.

In Chapter 3, I determined radial velocities and [Fe/H] abundances for 340 stars in Fornax using the same sample of stars in the outer parts of the galaxy presented in Chapter 2. The targets were obtained in the outer parts of the galaxy, a region that has been poorly studied. Removal of stars belonging to the most metal-rich population produces a truncated metallicity distribution function that is identical to Sculptor, indicating that these systems shared a similar early evolution, except that Fornax experienced a late, intense period of star formation (SF). The derived age-metallicity relation shows a fast increase in [Fe/H] at early ages, after which the enrichment flattens significantly for stars younger than ~ 8 Gyr. Additionally, the data indicate a strong population of stars around 4 Gyr, followed by a second rapid enrichment in [Fe/H]. A leaky-box chemical enrichment model generally matches the observed relation but predicts neither a significant population of young stars nor strong enrichment at late times. The young population in Fornax may therefore stem from an externally triggered SF event. My dynamical analysis reveals an increasing velocity dispersion with decreasing [Fe/H] from $\sigma_{sys} \approx 7.5\,\mathrm{kms}^{-1}$ to $\geq 14\,\mathrm{kms}^{-1}$. The large velocity dispersion at low metallicities is possibly the result of a non-Gaussian velocity distribution among stars older than ~ 8 Gyr. The sample also includes members from the Fornax globular clusters H2 and H5. In agreement with past studies I find $[\mathrm{Fe/H}] = -2.04 \pm 0.04$ and a mean radial velocity $RV = 59.36 \pm 0.31\,\mathrm{km\,s}^{-1}$ for H2 and $[\mathrm{Fe/H}] = -2.02 \pm 0.11$ and $RV = 59.39 \pm 0.44\,\mathrm{km\,s}^{-1}$ for H5. Finally, I test different calibrations of the Calcium Triplet over more than 2 dex in [Fe/H] and find best agreement with the calibration equations provided by Carrera et al. (2013).

In Chapter 4, I investigated the chemical signatures of GCs in Fornax in comparison to the field star population. The globular cluster H4, located in the center of the Fornax dwarf spheroidal galaxy, is a key object for understanding the formation and chemical evolution of clusters in low-mass galactic environments. H4 is peculiar because the cluster is significantly more metal-rich than the galaxy's other clusters, is located near the galaxy center, and may also be the youngest cluster in the galaxy. Here, I presented detailed chemical abundances derived from high-resolution (R$\sim$ 28 000) spectroscopy of an isolated H4 member star for comparison with a sample of 22 nearby Fornax field stars. I find the H4 member to be depleted in the alpha-elements Si, Ca, and Ti with [Si/Fe]$= -0.35 \pm 0.34$, [Ca/Fe]$= +0.05 \pm 0.08$, and [Ti/Fe]$= -0.27 \pm 0.23$, resulting in an average [α/Fe]$= -0.19 \pm 0.14$. If this result is representative of the average cluster properties, H4 is the only known system with a low [α/Fe] ratio and a moderately low metallicity, embedded in an intact birth environment. Using isochrones adjusted to these chemical properties, I find H4 to be ~ 10 Gyr old, and therefore likely younger than the other four clusters in the galaxy. The field stars in my sample display a clear sequence, seen as an early depletion in [α/Fe] at low metallicities, in good agreement with the results for an independent set of field stars in Fornax presented in Chapter 2 and subsequent results from Lemasle et al. (2014). The cluster H4 falls on top of the observed field star [α/Fe] sequence and clearly disagrees with the properties of Milky Way field stars and globular clusters. I therefore suggest that within a galaxy, the chemical enrichment of globular clusters may be tightly linked to the enrichment pattern of the field star population. The low [α/Fe] ratios of H4 and similar metallicity field stars in Fornax gives evidence that slow chemical enrichment environments, such as dwarf galaxies, may be the original hosts of alpha-depleted clusters in the halos of the Milky Way and M31.

6

Outlook

The great questions about the assembly and evolution of the Milky Way will be powerfully addressed in future surveys. In the next decades, the area of near-field cosmology is expected to be revolutionized by large space- and ground-based programs intended to measure distances, kinematics and proper motions for a large fraction of stars and stellar systems in the Galactic halo, bulge and disc. The anticipated three-dimensional map, paired with velocities for an expected one billion stars, provided by the recently launched astrometric satellite *Gaia* will reveal a major fraction of the existent kinematic substructures and streams as remnants of accretion events in the past. The additional information about space motion and ages for the brighter stars will furthermore facilitate to retrace the evolution of stars and stellar systems in time and thus reconstruct the star formation history and constitution for the early days of our Galaxy. Spectroscopic surveys like the 4m Multi-Object Spectroscopy Telescope (4MOST, expected start of science operations in 2021) or the *Gaia*-ESO survey (GES, from 2012 to 2016) will supplement the dynamical phase-space information with basic chemistry and detailed abundance pattern. Thus, it will be possible to uncover and characterize the legacy of the existent and disrupted satellite galaxies in the stellar halo and disc by precisely identifying relics of tidally-disrupted accretion debris, with the goal to clarify the role of satellites in the build up of the Milky Way.

Such surveys, however, are not able to reach out to most of the satellite galaxies themselves, as the majority of their stellar content falls below the expected magnitude limits of, e.g., *Gaia* and 4MOST. In this chapter, I therefore specifically use the results obtained for the field star population in the Fornax dwarf spheroidal galaxy (Chapter 2 and 3) and its associated GCs (Chapter 4) to give an outlook for future initiatives to further understand the evolution of dwarf galaxies *as individual systems*, and their contribution within the framework of near-field cosmology.

6.1 Contribution of Globular Clusters to the Stellar Content of Dwarf Galaxies

In the previous chapters, conclusions about the dynamical and chemical evolution of dwarf galaxies have been made by the interpretation of field star properties, and some of these conclusions are partially based on evolutionary models. Such models naturally assume that the properties of the baryonic matter within a galaxy's DM halo are dominated by the observed field stars, while GCs have made no significant contribution.

My work shows that the metallicity distribution function in the outer parts of Fornax shows distinct peaks in [Fe/H]. Interestingly two of the peaks roughly coincide with the metallicity of the current GCs in Fornax (see Figure 6.1). Therefore, it may be possible that these peaks do not trace intrinsic star formation variations, but rather denote GC stars that only later dissolved to the field. For example, Larsen et al. (2012b) proposed that as much as half of the metal-poor stars in Fornax originate from the five clusters in the galaxy. In the most extreme scenario, the complete old, metal-poor population of dwarf galaxies could originate from primordial cluster-like building blocks (Assmann et al. 2013). In this case the observed properties about velocity, chemistry, and age—and the conclusions thereof—may be biased, and only a quantitative assessment about the population mix will yield clarification about the true census of field star properties.

In addition to the above described early loss of stars, GCs can also be stripped of their population through tidal interactions over time. In the MW we can observe such a scenario in the cases of Palomar 5 or NGC 5466 (Odenkirchen et al. 2001, Belokurov et al. 2006). In Fornax, there is direct evidence that at least part of the field star population has been accreted through merger events (with systems of unknown nature) in the past. Furthermore, in this work I find signs for a velocity bimodality amongst the metal-poor stars. Such a kinematic bifurcation has been successfully reproduced in numerical simulations of a merger event (Yozin & Bekki 2012), potentially with GCs involved.

One possibility to identify stars that have been born in a GC and are now mixed into the field population of a galaxy is to search for an enhancement in the absorption band strength of the CN molecule compared to a similar feature produced by CH. CN-enhanced stars have been found within the great majority of galactic GCs (e.g., Gratton et al. 2012). It has been identified as an indicator for two distinct stellar populations, with the second and younger population being enhanced in N (and hence CN) , Na, and Mg and depleted in C (and hence CH), O, and Al. Although the origin of this abundance pattern is not fully understood yet, it is approved for being a unique feature to GCs and a CN-CH bimodality has neither been observed in the field nor in other stellar systems like open clusters, or dwarf galaxies, which makes it an unambiguous tracer for GC populations. Light-element bimodality has also been found in extragalactic GCs (e.g., Carretta et al. 2010a) and specifically within all Fornax' GCs (Letarte et al. 2006, Larsen et al. 2014). Therefore, there is strong evidence that the anti-correlation between light elements is a universal feature for GCs, valid beyond the boundaries of the MW.

In comparison to time expensive high-resolution measurements of individual light elements, CN and CH bandstrengh can be obtained with fairly low S/N (~ 20) and at low resolution ($R \leq 1000$), which makes this tracer favourable especially for faint objects (Norris et al. 1981, Briley et al. 1994; see also Figure 6.2). Since it is also sensitive to [Fe/H] and the stellar atmospheric parameters, it is necessary to know these quantities in order to evaluate a stellar population mix of different age and metallicity. In this respect, Fornax is an optimal candidate because it not only hosts several GCs, and thereby potentially stripped cluster stars, but when literature samples are combined with the work presented here, we know the basic chemical and photometric properties of more than a thousand field stars, the by far largest sample of its kind available for any dwarf galaxy.

We can obtain another important insight from the fraction of dissolved GC stars within Fornax. As stated before, typical GCs host at least two stellar populations with an anti-correlated spread between several light elements. A popular formation scenario for this peculiar chemical constellation involves a first generation of massive (i.e. fast recycling) stars, whose partially enriched stellar winds are collected in the cluster center and form a second generation of low-mass stars. Subsequent SNe then cause the cluster to expand, with the result that only about 1/10th of the original mass retains within the eventually bound object (e.g., D'Ercole et al. 2008). Fornax may be a challenge for this formation scenario: Four of its (existing) clusters are metal-poor with

[Fe/H]≤ -2.0 dex. Larsen et al. (2012b) showed that the sparsely populated tail of field stars at similar or lower iron abundance cannot account for an accreted mass of four clusters that have lost a multiple of their currently observed stellar content. Until today, however, all assumptions about the fraction of GC stars in the field of Fornax are purely speculative. If CN-CH fingerprints of typical GC stars can be observed in a statistically large sample, it will be possible to tightly constrain the fraction of dissolved GC stars in the field, and by that the initial upper mass limit for the current GC population in Fornax.

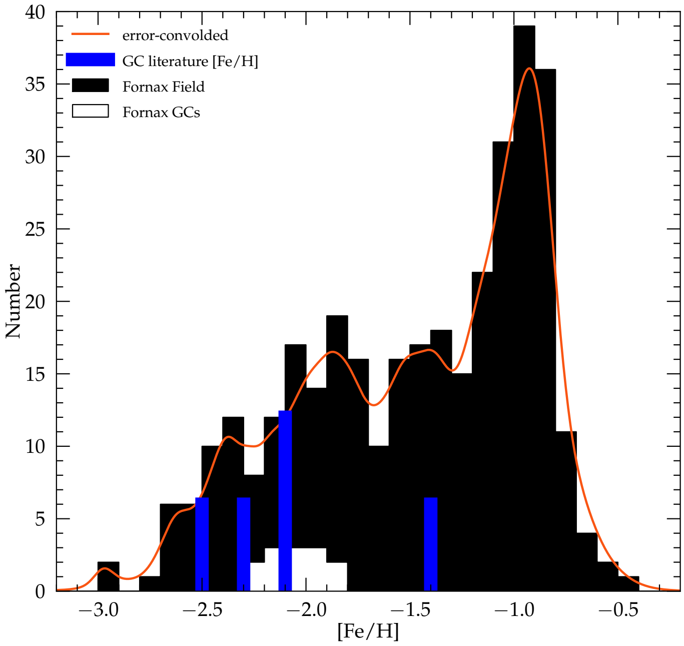

Figure 6.1: Distribution of metals amongst stars in the outer parts of the Fornax dSph. The distribution of field stars is shown in black, and the red line is the error-convolved equivalent. White are individual GC stars within our sample and the blue bars indicate the literature values for all five GCs in Fornax (two clusters are located at [Fe/H]$= -2.1$ dex). It is not known if, and to what extent, GCs contributed to the field star low-metallicity tail of the galaxy.

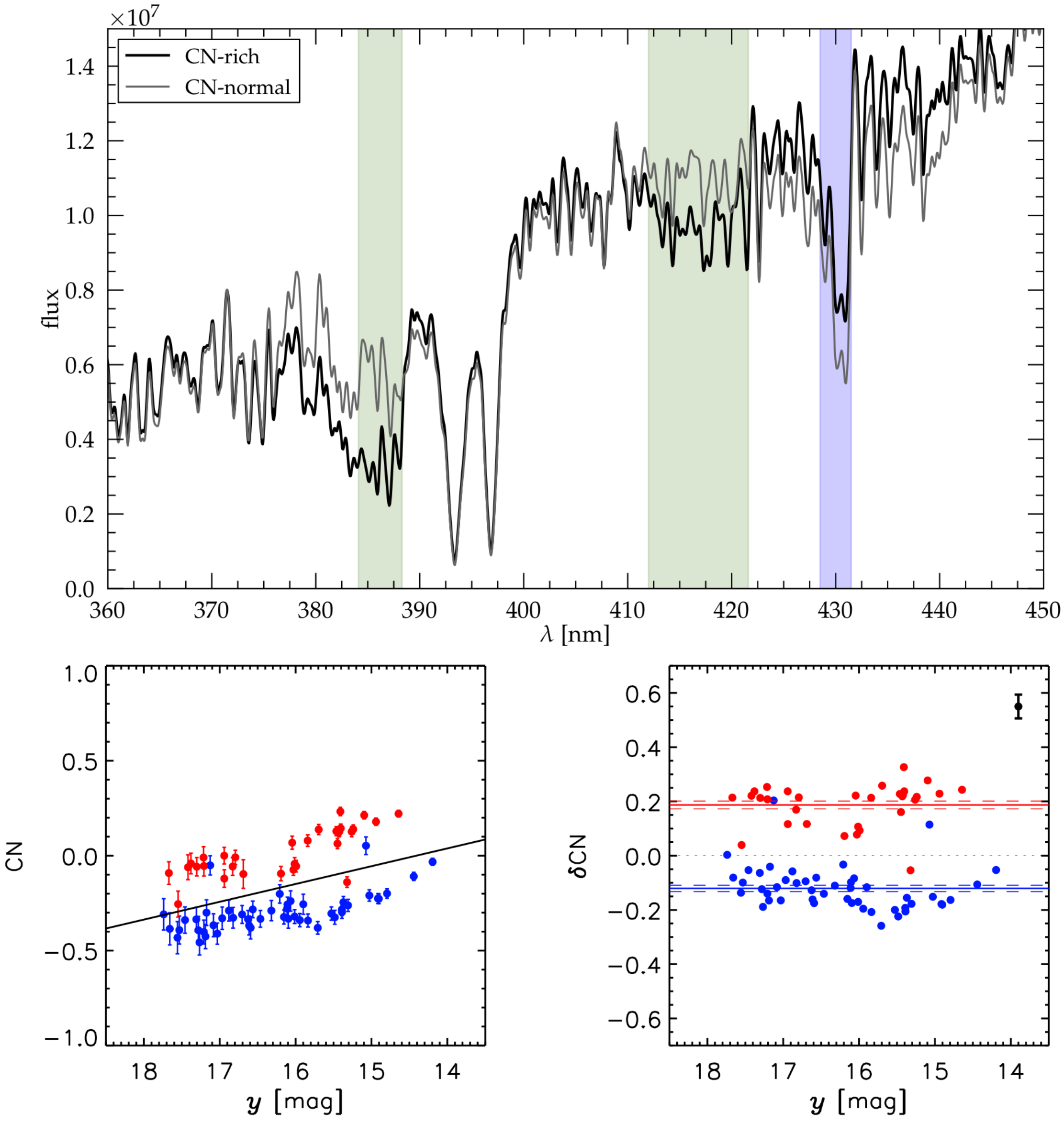

Figure 6.2: Top: Synthetic light-element variations between the two populations within a typical GC as seen in the CN and CH bands in the blue part of the visible spectrum. The shown synthetic spectra are adopted from Sbordone et al. (2011) and mimic two red giant stars with [Fe/H]$= -1.67$ dex and a typical abundance mix for a first-generation star (gray) and second-generation star (black) in a GC. Green areas show the wavelength range of the CN features typically used to discriminate the two generations, and the blue area indicates the CH reference interval.
Bottom: Observed signature of the above shown variations in red giant stars in the GC NGC 288. The red stars belong the second (and hence CN-strong) population. Both populations are plotted as a function of magnitude (lower left), and normalized to the magnitude-dependent bandstrength along the RGB (lower right). The horizontal lines in the right panel indicate the mean value (solid line) and the standard deviation of the mean (dashed lines) for both subpopulations. Figures are adopted from Lim et al. (2015).

6.2 Parametrization of Chemical Evolution

In this work, I presented, for the first time, the full chemical enrichment history of a satellite galaxy traced over more than 10 Gyr of evolution, equivalent to more than 2 dex in [Fe/H]. The results have been discussed by means of the position of the knee and the [α/Fe] values for the enhanced and depleted plateaus when the abundance ratios are plotted as a function of [Fe/H]. Similar attempts have been made with other satellite galaxies before (e.g., Cohen & Huang 2009, Cohen & Huang 2010, Tolstoy et al. 2009) and also during the time of this work (Lemasle et al. 2014, de Boer et al. 2014, Ural et al. 2015). At the moment, however, most of these studies are restricted to a small sample of stars.

The chemical evolution sequence of individual alpha-elements is likely sensitive to a variety of internal characteristics of the galaxy, and possibly also to different environmental effects. As an example, a system inside a more massive DM halo may have higher gas densities and therefore show higher star formation rates than a galaxy in a shallower potential. Vice versa, a satellite galaxy orbiting its host on a close orbit may loose parts of its gas through tidal stirring (while the remainder may be heated), which could result in a lower enrichment efficiency compared to a system on a wide orbit. The downside of such complex dependencies is, that it becomes naturally more difficult to interpret the outcome of present observations. Dependent on the number and interaction of the relevant forces, signatures in the chemical evolution may be significantly misinterpreted.

However, the multitude of information stored in the enrichment pattern of stars within a galaxy could also be a chance to *learn* about the above described physical concepts that govern the chemical enrichment within a galaxy. It is clear, that the evolution of [α/Fe] with [Fe/H] can yield a similar depth of insights to the evolution of galaxies than, for example, a color-magnitude diagram provides about the properties of stellar populations—if the underlying physics are understood.

An essential steps forward will be the development of a meaningful parametrization for the chemical enrichment sequences. Only then we can extract the physical properties from the observations, and become able to compare different systems directly with each other. The foundation for this endeavour would be to build a database of observed fiducial enrichment sequences for many galaxies, based on a large sample of stars spanning the full range of chemical evolution within a given system. The sequences may then serve to accomplish a parametrization is to take into account the critical regulating factors of chemical enrichment, including internal SNe feedback, gas flow, or mixing timescales. For the majority of satellites, the models also need to be capable of allowing for environmental effects.

A step in this direction has been done in this work, by fitting state-of-the-art chemical enrichment models to the observations where the observed enrichment pattern was used to determine the time-dependent star formation- and wind efficiency for the Fornax dwarf spheroidal galaxy. However, currently it seems illusionary to obtain the necessary computational power and physical understanding of the processes in even these simplest of all galaxies, in order to provide models that can take into account all relevant internal and environmental aspects of chemical enrichment in galaxies to a satisfactory level.

Therefore, an alternative approach may be to employ an analytical function with as many as necessary—but as few as possible—variables in order to successfully fit the observed fiducial enrichment sequences within their uncertainties. Thus, it will be possible to consistently evaluate individual enrichment patterns of galaxies and compare the best-fitting empirical parameters directly to each other. In this way, a quantitative comparison can be performed and the significance of parameter variations between individual galaxies can be assessed. Moreover, if there is observational data for a sufficient diversity of systems, the empirical enrichment variables can be used to test for correlations to a broad range of galactic properties such as total luminosity, surface brightness, mass-to-light ratio, orbital period and eccentricity, rotation, IMF, etc., with the final goal to establish the key-regulating factors for the chemical evolution of galaxies in general.

As soon as a parametrization for the chemical enrichment sequences of individual chemical species within satellite galaxies of different type and with different properties is established, it will not only shed light on the physical processes during the evolution of the galaxies. Moreover, it can be used on orphan streams, substructures and stellar clusters to reveal the properties of their now-dissolved hosts.

6.3 Chemical Tagging of Accreted Globular Clusters

In Chapter 4, I find strong evidence that the chemical enrichment properties for a galaxy are also imprinted to its GC system. A coupling between the chemical enrichment of GCs and field stars opens a new observational perspective to infer details about the accretion history of the MW, using the chemical properties of GCs. Specifically, the detailed chemical composition of a cluster can be used to shed light on its origin, whether it formed in situ, or whether it came as a companion of an accreted satellite galaxy. In principal, there are three main diagnostic options, if the precise [α/Fe] ratio within a cluster is known, and depending on the obtained value.

i) *Finding accreted GCs.* It seems to be a robust assumption that *all* (accreted) satellite systems chemically enriched with a *lower* efficiency compared to the MW. Thus, the chemical enrichment fingerprint of satellites will be characterized by a depletion of [α/Fe] already at lower [Fe/H] compared to the MW. As a consequence, any GC which shows a lower alpha-abundance ratio compared to MW field stars or GCs with similar [Fe/H] is most likely of accreted origin. Under the assumption that the chemical enrichment efficiency is scaled to the total mass of the system, the cluster metallicity can be additionally used to set an upper limit on the mass of the host in which the cluster originally formed. Furthermore, if a large sample of GCs is evaluated in this way, it will be possible to put a constraint on the size of the smallest accreted satellite that was able to form GCs, and hence obtain insights to the minimum mass limit required for the formation of GCs.

ii) *Characterizing the hosts of accreted GCs.* There are several alternative indicators from which the accreted origin of a GC can be suspected or approved. For example, extreme radial velocities and/or peculiar proper motions supported the assumption, that Ruprecht 106 is of extragalactic origin. Furthermore, a lower chemical enrichment for dwarf satellites may also be imprinted on the age-metallicity relation for both field stars and clusters. A bifurcation in the GC age-metallicity relation has been found for GCs in M31 (Beasley et al. 2005) and the MW (Leaman et al. 2013). There are also indications that GCs carry information about their formation in their rotational signal (Kacharov et al. 2014). Finally, in the case of M31, the halo GCs are not isotropically distributed, but instead cluster in streams and overdensities (see Figure 6.3) and thus can be identified as accreted systems. In case the accreted origin of a GC is known independent of its chemical fingerprint, the [α/Fe] ratio can be used to infer details about the properties of the now-dissolved host.

iii) *Characterizing the accretion history of the MW and Andromeda.* The above two diagnostics can be combined, if the detailed chemical composition is known for a representative sample of GCs for which the abundances have been determined in a self-consistent manner. Then, it will be possible to reconstruct the accretion history of the galaxy hosting the respective cluster population. From the knowledge about the fraction of GCs with peculiar chemical properties and their distribution of metallicities, conclusions about the type and number of

> accreted satellite systems can be made, or, if this number is already known, inferences about the number of GC-harbouring galaxies can be obtained instead. For one thing, these results provide a critical comparison to the predictions from other diagnostics such as ages, metallicities, or rotational properties. For another, it can be used to challenge the predictions from a ΛCDM cosmological framework in terms of number and mass distribution of accreted satellite systems.

Currently, we know detailed chemical abundances (including [α/Fe]) for not more than half of the MW GCs. Those abundances have been derived from different absorption features, using different solar reference values and different spectroscopic analysis techniques, so that systematic errors become a critical issue in the direct comparison of individual systems (Pritzl et al. 2005). For M31, the situation is worse, and today we only know the detailed chemical fingerprints from a maximum of 20% of all known M31 GCs. Therefore, a significant step towards a better understanding of the accretion and assembly history of the Local Group can be made by isolating peculiar GCs with hints for an extragalactic origin, and perform a *systematic search* for systems with peculiar chemical properties that eventually tells us details about their formation environment. With the integral field unit MUSE at the VLT, a powerful instrument just became available to simultaneously determine metallicities and velocities for tens of thousands of stars within a cluster. Thus, possible candidate systems can effectively be selected. Simultaneously, the obtained radial velocities can be used to identify individual member stars in highly contaminated regions at low galactic latitude. The necessary spectroscopic facilities to obtain the detailed chemical information are already in place: with M2FS at the Magellan Telescopes and FLAMES or UVES at the VLTs, several fiber-fed multi-object spectrographs provide the necessary high resolution, and the telescopes the excuisite light-collecting power in order to target many objects in an affordable amount of time.

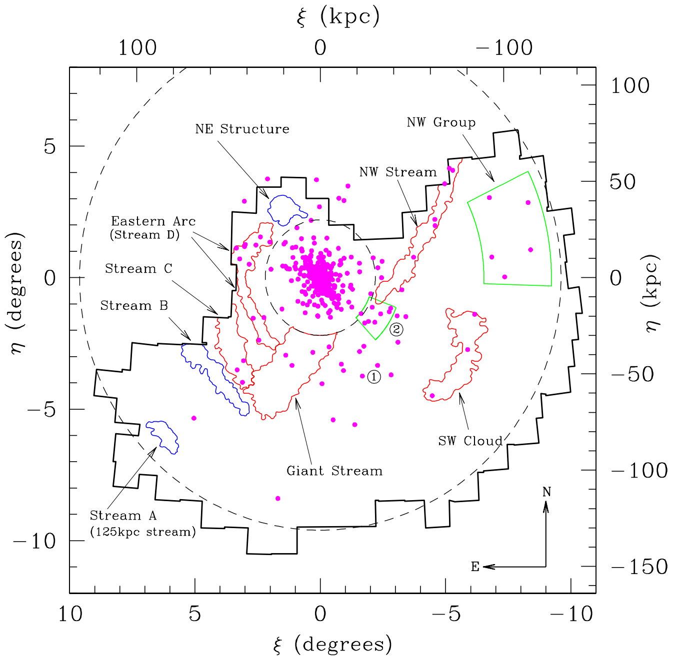

Figure 6.3: Many GCs in the halo of M31 are clustered within streams and groups, and therefore may be of accreted origin. Clusters are shown as magenta points. Red/blue regions indicate stellar substructures associated with multiple/zero GCs. GC overdensities without stellar substructure are shown in green. The dashed circles indicate $R = 30$ and 130 kpc. Figure adopted from Mackey et al. (2010).

When I heard the learn'd astronomer,
When the proofs, the figures, were ranged in columns before me,
When I was shown the charts and diagrams, to add, divide, and measure them,
When I sitting heard the astronomer where he lectured with much applause
in the lecture-room,
How soon unaccountable I became tired and sick,
Till rising and gliding out I wander'd off by myself,
In the mystical moist night-air, and from time to time,
Look'd up in perfect silence at the stars.

– Walt Whitman

Bibliography

Alonso, A., Arribas, S., & Martínez-Roger, C. 1999, A&AS, 140, 261

Amorisco, N. C., & Evans, N. W. 2012, ApJ, 756, L2

Armandroff, T. E., & Zinn, R. 1988, AJ, 96, 92

Armandroff, T. E., & Da Costa, G. S. 1991, AJ, 101, 1329

Arnett, W. D. 1971, ApJ, 166, 153

Ashman, K. M., Bird, C. M., & Zepf, S. E. 1994, AJ, 108, 2348

Assmann, P., Fellhauer, M., Wilkinson, M. I., & Smith, R. 2013, MNRAS, 432, 274

Bassino, L. P., Muzzio, J. C., & Rabolli, M. 1994, ApJ, 431, 634

Bate, N. F., McMonigal, B., Lewis, G. F., et al. 2015, arXiv:1507.06654

Battaglia, G., Tolstoy, E., Helmi, A., et al. 2006, A&A, 459, 423

Battaglia, G., Irwin, M., Tolstoy, E., et al. 2008, MNRAS, 383, 183

Battaglia, G., Tolstoy, E., Helmi, A., et al. 2011, MNRAS, 411, 1013

Battaglia, G., & Starkenburg, E. 2012, A&A, 539, A123

Beasley, M. A., Brodie, J. P., Strader, J., et al. 2005, AJ, 129, 1412

Beers, T. C., Flynn, K., & Gebhardt, K. 1990, AJ, 100, 32

Bekki, K., Couch, W. J., & Drinkwater, M. J. 2001, ApJ, 552, L105

Bekki, K., & Freeman, K. C. 2003, MNRAS, 346, L11

Belokurov, V., Evans, N. W., Irwin, M. J., Hewett, P. C., & Wilkinson, M. I. 2006, ApJ, 637, L29

Belokurov, V., Walker, M. G., Evans, N. W., et al. 2010, ApJ, 712, L103

Bensby, T., Feltzing, S., & Lundström, I. 2003, A&A, 410, 527

van den Bergh, S. 1981, A&AS, 46, 79

Bersier, D. 2000, ApJ, 543, L23

Blecha, A., North, P., Royer, F., & Simond, G. 2003, BLDR Software Reference Manual 1.09, VLT-SPE-OGL-13730-0040

Boeche, C., Siebert, A., Williams, M., et al. 2011, AJ, 142, 193

Boeche, C. & the RAVE collaboration 2013, in IAU Symposium 298, *Setting the scene for Gaia and LAMOST*, in press, arXiv:1309.6460

Boeche, C., Siebert, A., Piffl, T., et al. 2014, A&A, 568, A71

Boeche, C., & Grebel, E. 2015, submitted

de Boer, T. J. L., Tolstoy, E., Hill, V., et al. 2012, A&A, 539, A103

de Boer, T. J. L., Tolstoy, E., Hill, V., et al. 2012, A&A, 544, A73

de Boer, T. J. L., Tolstoy, E., Saha, A., & Olszewski, E. W. 2013, A&A, 551, A103

de Boer, T. J. L., Belokurov, V., Beers, T. C., & Lee, Y. S. 2014, MNRAS, 443, 658

Bonifacio, P., Hill, V., Molaro, P., et al. 2000, A&A, 359, 663

Boylan-Kolchin, M., Bullock, J. S., & Kaplinghat, M. 2011, MNRAS, 415, L40

Briley, M. M., Hesser, J. E., Bell, R. A., Bolte, M., & Smith, G. H. 1994, AJ, 108, 2183

Brodie, J. P., & Strader, J. 2006, ARAA, 44, 193

Brodie, J. P., Romanowsky, A. J., Strader, J., et al. 2014, ApJ, 796, 52

Brown, J. A., Wallerstein, G., & Zucker, D. 1997, AJ, 114, 180

Brown, T. M., Tumlinson, J., Geha, M., et al. 2012, ApJ, 753, L21

Carraro, G., Ng, Y. K., & Portinari, L. 1998, MNRAS, 296, 1045

Bullock, J. S., & Johnston, K. V. 2005, ApJ, 635, 931

Buonanno, R., Corsi, C. E., Zinn, R., et al. 1998, ApJ, 501, L33

Buonanno, R., Corsi, C. E., Castellani, M., et al. 1999, AJ, 118, 1671

Burgh, E. B., Bershady, M. A., Westfall, K. B., & Nordsieck, K. H. 2007, PASP, 119, 1069

Caffau, E., Koch, A., Sbordone, L., et al. 2013, Astronomische Nachrichten, 334, 197

Carrera, R., Pancino, E., Gallart, C., & del Pino, A. 2013, MNRAS, 434, 1681

Carretta, E., Bragaglia, A., Gratton, R., D'Orazi, V., & Lucatello, S. 2009, A&A, 508, 695

Carretta, E., Bragaglia, A., Gratton, R. G., et al. 2010, A&A, 520, A95

Carretta, E., Bragaglia, A., Gratton, R. G., et al. 2010b, ApJ, 714, L7

Cayrel, R. 1988, The Impact of Very High S/N Spectroscopy on Stellar Physics, 132, 345

Choi, J., Conroy, C., Moustakas, J., et al. 2014, ApJ, 792, 95

Coc, A., Goriely, S., Xu, Y., Saimpert, M., & Vangioni, E. 2012, ApJ, 744, 158

Coelho, P., Barbuy, B., Meléndez, J., Schiavon, R. P., & Castilho, B. V. 2005, A&A, 443, 735

Cohen, J. G. 1981, ApJ, 247, 869

Cohen, J. G. 2004, AJ, 127, 1545

Cohen, J. G., & Huang, W. 2009, ApJ, 701, 1053

Cohen, J. G., & Huang, W. 2010, ApJ, 719, 931

Cole, A. A., Smecker-Hane, T. A., & Gallagher, J. S., III 2000, AJ, 120, 1808

Cole, A. A., Smecker-Hane, T. A., Tolstoy, E., Bosler, T. L., & Gallagher, J. S. 2004, MNRAS, 347, 367

Coleman, M., Da Costa, G. S., Bland-Hawthorn, J., et al. 2004, AJ, 127, 832

Coleman, M. G., Da Costa, G. S., Bland-Hawthorn, J., & Freeman, K. C. 2005, AJ, 129, 1443

Coleman, M. G., & de Jong, J. T. A. 2008, ApJ, 685, 933

Cole, A. A., Weisz, D. R., Dolphin, A. E., et al. 2014, ApJ, 795, 54

Colucci, J. E., Bernstein, R. A., & Cohen, J. G. 2014, ApJ, 797, 116

Conroy, C., Graves, G. J., & van Dokkum, P. G. 2014, ApJ, 780, 33

Conti, P. S., Greenstein, J. L., Spinrad, H., Wallerstein, G., & Vardya, M. S. 1967, ApJ, 148, 105

Da Costa, G. S., Held, E. V., Saviane, I., & Gullieuszik, M. 2009, ApJ, 705, 1481

Côté, P., Piatek, S., Ferrarese, L., et al. 2006, ApJS, 165, 57

Cutri, R. M., Skrutskie, M. F., van Dyk, S., et al. 2003, VizieR Online Data Catalog, 2246, 0

Demers, S., Irwin, M. J., & Kunkel, W. E. 1994, AJ, 108, 1648

Diemand, J., & Moore, B. 2011, Advanced Science Letters, 4, 297

Dinescu, D. I., Keeney, B. A., Majewski, S. R., & Girard, T. M. 2004, AJ, 128, 687

Dobbie, P. D., Cole, A. A., Subramaniam, A., & Keller, S. 2014, MNRAS, 442, 1680

van Dokkum, P. G. 2001, PASP, 113, 1420

Dolphin, A. E. 2000, PASP, 112, 1383

Dolphin, A. E. 2009, PASP, 121, 655

Dotter, A., Chaboyer, B., Jevremović, D., et al. 2007, AJ, 134, 376

Dotter, A., Chaboyer, B., Jevremović, D., et al. 2008, ApJS, 178, 89

Dubath, P., Meylan, G., & Mayor, M. 1992, ApJ, 400, 510

Eggen, O. J., Lynden-Bell, D., & Sandage, A. R. 1962, ApJ, 136, 748

Edge, A., Sutherland, W., Kuijken, K., et al. 2013, The Messenger, 154, 32

Elmegreen, B. G., Malhotra, S., & Rhoads, J. 2012, ApJ, 757, 9

D'Ercole, A., & Brighenti, F. 1999, MNRAS, 309, 941

D'Ercole, A., Vesperini, E., D'Antona, F., McMillan, S. L. W., & Recchi, S. 2008, MNRAS, 391, 825

Frank, M. J., Hilker, M., Baumgardt, H., et al. 2012, MNRAS, 423, 2917

Geisler, D., Smith, V. V., Wallerstein, G., Gonzalez, G., & Charbonnel, C. 2005, AJ, 129, 1428

Gilmore, G., Norris, J. E., Monaco, L., et al. 2013, ApJ, 763, 61

Gnedin, N. Y., & Kravtsov, A. V. 2006, ApJ, 645, 1054

Governato, F., Zolotov, A., Pontzen, A., et al. 2012, MNRAS, 422, 1231

Gratton, R. G., & Sneden, C. 1987, A&A, 178, 179

Gratton, R., Sneden, C., & Carretta, E. 2004, ARAA, 42, 385

Gratton, R. G., Carretta, E., & Bragaglia, A. 2012, A&A Rev., 20, 50

Grebel, E. K., Gallagher, J. S., III, & Harbeck, D. 2003, AJ, 125, 1926

Greco, C., Clementini, G., Held, E. V., et al. 2005, arXiv:astro-ph/0507244

Greco, C., Clementini, G., Catelan, M., et al. 2007, ApJ, 670, 332

Greggio, L. 2005, A&A, 441, 1055

Harbeck, D., Grebel, E. K., Holtzman, J., et al. 2001, AJ, 122, 3092

Hardy, E. 2002, Extragalactic Star Clusters, 207, 62

Harris, W. E. 1996, AJ, 112, 1487

Haywood, M., Di Matteo, P., Lehnert, M. D., Katz, D., & Gómez, A. 2013, A&A, 560, A109

Helmi, A., Irwin, M. J., Tolstoy, E., et al. 2006, ApJ, 651, L121

Hendricks, B., Stetson, P. B., VandenBerg, D. A., & Dall'Ora, M. 2012, AJ, 144, 25

Hendricks, B., Koch, A., Lanfranchi, G. A., et al. 2014, ApJ, 785, 102

Hendricks, B., Koch, A., Walker, M., et al. 2014, A&A, 572, A82

Hendricks, B., Johnson, C. I., Boeche, C., et al. 2015, submitted to A&A

Hilker, M., Infante, L., Vieira, G., Kissler-Patig, M., & Richtler, T. 1999, A&AS, 134, 75

Hodge, P. W. 1961, AJ, 66, 83

Huxor, A. P., Ferguson, A. M. N., Tanvir, N. R., et al. 2011, MNRAS, 414, 770

Ibata, R. A., Gilmore, G., & Irwin, M. J. 1995, MNRAS, 277, 781

Irwin, M., & Hatzidimitriou, D. 1995, MNRAS, 277, 1354

Johnson, C. I., & Pilachowski, C. A. 2010, ApJ, 722, 1373

Johnson, C. I., McDonald, I., Pilachowski, C. A., et al. 2015, AJ, 149, 71

Johnston, K. V., Hernquist, L., & Bolte, M. 1996, ApJ, 465, 278

Kahn, F. D. 1974, A&A, 37, 149

Kacharov, N., Bianchini, P., Koch, A., et al. 2014, A&A, 567, A69

Karachentsev, I. D. 2005, AJ, 129, 178

Kauffmann, G., White, S. D. M., & Guiderdoni, B. 1993, MNRAS, 264, 201

King, I. R. 1966, AJ, 71, 64

Kirby, E. N., Guhathakurta, P., & Sneden, C. 2008, ApJ, 682, 1217

Kirby, E. N., Guhathakurta, P., Bolte, M., Sneden, C., & Geha, M. C. 2009, ApJ, 705, 328

Kirby, E. N., Lanfranchi, G. A., Simon, J. D., Cohen, J. G., & Guhathakurta, P. 2011, ApJ, 727, 78

Kirby, E. N., Cohen, J. G., Smith, G. H., et al. 2011, ApJ, 727, 79

Kirby, E. N. 2011, PASP, 123, 531

Kirby, E. N., Cohen, J. G., Guhathakurta, P., et al. 2013, ApJ, 779, 102

Kirby, E. N., Simon, J. D., & Cohen, J. G. 2015, arXiv:1506.01021

Kleyna, J. T., Wilkinson, M. I., Evans, N. W., & Gilmore, G. 2004, MNRAS, 354, L66

Koch, A., Grebel, E. K., Wyse, R. F. G., et al. 2006, AJ, 131, 895

Koch, A., Wilkinson, M. I., Kleyna, J. T., et al. 2007, ApJ, 657, 241

Koch, A., Grebel, E. K., Kleyna, J. T., et al. 2007, AJ, 133, 270

Koch, A., Grebel, E. K., Gilmore, G. F., et al. 2008, AJ, 135, 1580

Koekemoer, A. M., Fruchter, A. S., Hook, R. N., Hack, W., & Hanley, C. 2006, The 2005 HST Calibration Workshop: Hubble After the Transition to Two-Gyro Mode, 423

Koposov, S. E., Glushkova, E. V., & Zolotukhin, I. Y. 2008, A&A,486, 771

Koposov, S. E., Gilmore, G., Walker, M. G., et al. 2011, ApJ, 736, 146

Kordopatis, G., Gilmore, G., Steinmetz, M., et al. 2013, AJ, 146, 134

Kormendy, J., & Bender, R. 2012, ApJS, 198, 2

Kroupa, P., & Weidner, C. 2003, ApJ, 598, 1076

Laevens, B. P. M., Martin, N. F., Bernard, E. J., et al. 2015, arXiv:1507.07564

Lane, R. R., Kiss, L. L., Lewis, G. F., et al. 2011, A&A, 530, A31

Lanfranchi, G. A., & Matteucci, F. 2003, MNRAS, 345, 71

Lanfranchi, G. A., & Matteucci, F. 2004, MNRAS, 351, 1338

Lanfranchi, G. A., & Matteucci, F. 2007, A&A, 468, 927

Lanfranchi, G. A., & Matteucci, F. 2010, A&A, 512, A85

Larsen, S. S., Strader, J., & Brodie, J. P. 2012, A&A, 544, L14

Larsen, S. S., Brodie, J. P., & Strader, J. 2012, A&A, 546, A53

Larsen, S. S., Brodie, J. P., Forbes, D. A., & Strader, J. 2014, A&A, 565, A98

Law, D. R., & Majewski, S. R. 2010, ApJ, 718, 1128

Leaman, R. 2012, AJ, 144, 183

Leaman, R., Venn, K. A., Brooks, A. M., et al. 2013, ApJ, 767, 131

Lemasle, B., Hill, V., Tolstoy, E., et al. 2012, A&A, 538, A100

Lemasle, B., de Boer, T. J. L., Hill, V., et al. 2014, A&A, 572, A88

Lequeux, J., Peimbert, M., Rayo, J. F., Serrano, A., & Torres-Peimbert, S. 1979, A&A, 80, 155

Letarte, B., Hill, V., Jablonka, P., et al. 2006, A&A, 453, 547

Letarte, B., Hill, V., Tolstoy, E., et al. 2010, A&A, 523, A17

Lim, D., Han, S.-I., Lee, Y.-W., et al. 2015, ApJS, 216, 19

Mackey, A. D., & Gilmore, G. F. 2003, MNRAS, 340, 175

Mackey, A. D., & Gilmore, G. F. 2004, MNRAS, 355, 504

Mackey, A. D., Huxor, A. P., Ferguson, A. M. N., et al. 2010, ApJ, 717, L11

Madau, P., Ferrara, A., & Rees, M. J. 2001, ApJ, 555, 92

Maeda, K., Benetti, S., Stritzinger, M., et al. 2010, Nature, 466, 82

Marcolini, A., D'Ercole, A., Battaglia, G., & Gibson, B. K. 2008, MNRAS, 386, 2173

Martell, S. L., & Grebel, E. K. 2010, A&A, 519, A14

Mateo, M. L. 1998, ARAA, 36, 435

Mateo, M., Bailey, J. I., Crane, J., et al. 2012, Proceedings of the SPIE, 8446, 84464Y

Matteucci, F., & Brocato, E. 1990, ApJ, 365, 539

Mayer, L., Mastropietro, C., Wadsley, J., Stadel, J., & Moore, B. 2006, MNRAS, 369, 1021

McConnachie, A. W., Peñarrubia, J., & Navarro, J. F. 2007, MNRAS, 380, L75

McConnachie, A. W. 2012, AJ, 144, 4

McWilliam, A., & Rich, R. M. 1994, ApJS, 91, 749

McWilliam, A., & Bernstein, R. A. 2008, ApJ, 684, 326

McWilliam, A., Wallerstein, G., & Mottini, M. 2013, ApJ, 778, 149

Méndez, R. A., Costa, E., Gallart, C., et al. 2011, AJ, 142, 93

Misgeld, I., & Hilker, M. 2011, MNRAS, 414, 3699

Monelli, M., Pulone, L., Corsi, C. E., et al. 2003, AJ, 126, 218

Moore, B., Ghigna, S., Governato, F., et al. 1999, ApJ, 524, L19

Mucciarelli, A., Bellazzini, M., Ibata, R., et al. 2012, MNRAS, 426, 2889

Naab, T., Johansson, P. H., & Ostriker, J. P. 2009, ApJ, 699, L178

Nayakshin, S., & Wilkinson, M. I. 2013, MNRAS, 433, 324

Nichols, M., Lin, D., & Bland-Hawthorn, J. 2012, ApJ, 748, 149

Niederste-Ostholt, M., Belokurov, V., Evans, N. W., & Peñarrubia, J. 2010, ApJ, 712, 516

Nissen, P. E., & Schuster, W. J. 2010, A&A, 511, L10

Nomoto, K., Thielemann, F.-K., & Yokoi, K. 1984, ApJ, 286, 644

Norris, J., Cottrell, P. L., Freeman, K. C., & Da Costa, G. S. 1981, ApJ, 244, 205

Norris, M. A., Kannappan, S. J., Forbes, D. A., et al. 2014, MNRAS, 443, 1151

Odenkirchen, M., Grebel, E. K., Rockosi, C. M., et al. 2001, ApJ, 548, L165

Oey, M. S. 2011, ApJ, 739, L46

Oñorbe, J., Garrison-Kimmel, S., Maller, A. H., et al. 2014, MNRAS, 437, 1894

Pagel, B. E. J., & Tautvaisiene, G. 1998, MNRAS, 299, 535

Pasetto, S., Grebel, E. K., Berczik, P., Chiosi, C., & Spurzem, R. 2011, A&A, 525, A99

Peñarrubia, J., Walker, M. G., & Gilmore, G. 2009, MNRAS, 399, 1275

Piatek, S., Pryor, C., Bristow, P., et al. 2006, AJ, 131, 1445

Piatek, S., Pryor, C., Bristow, P., et al. 2007, AJ, 133, 818

Pietrzyński, G., Gieren, W., & Udalski, A. 2003, AJ, 125, 2494

Pietrzyński, G., Górski, M., Gieren, W., et al. 2009, AJ, 138, 459

del Pino, A., Hidalgo, S. L., Aparicio, A., et al. 2013, MNRAS, 433, 1505

Planck Collaboration, Ade, P. A. R., Aghanim, N., et al. 2014, A&A, 571, A1

Pont, F., Zinn, R., Gallart, C., Hardy, E., & Winnick, R. 2004, AJ, 127, 840

Pompéia, L., Hill, V., Spite, M., et al. 2008, A&A, 480, 379

Pritzl, B. J., Venn, K. A., & Irwin, M. 2005, AJ, 130, 2140

Reddy, B. E., Tomkin, J., Lambert, D. L., & Allende Prieto, C. 2003, MNRAS, 340, 304

Revaz, Y., Jablonka, P., Sawala, T., et al. 2009, A&A, 501, 189

Rizzi, L., Held, E. V., Saviane, I., Tully, R. B., & Gullieuszik, M. 2007, MNRAS, 380, 1255

Robin, A. C., Reylé, C., Derrière, S., & Picaud, S. 2003, A&A, 409, 523

Roederer, I. U., Preston, G. W., Thompson, I. B., et al. 2014, AJ, 147, 136

Romano, D., & Starkenburg, E. 2013, MNRAS, 434, 471

Ruiz, L. O., Falceta-Gonçalves, D., Lanfranchi, G. A., & Caproni, A. 2013, MNRAS, 429, 1437

Rutledge, G. A., Hesser, J. E., Stetson, P. B., et al. 1997, PASP, 109, 883

Rutledge, G. A., Hesser, J. E., & Stetson, P. B. 1997, PASP, 109, 907

Rutledge, G. A., Hesser, J. E., & Stetson, P. B. 1997, PASP, 109, 907

Ryan, S. G., & Norris, J. E. 1991, AJ, 101, 1865

Sakari, C. M., Venn, K. A., Mackey, D., et al. 2015, MNRAS, 448, 1314

Salpeter, E. E. 1955, ApJ, 121, 161

Sbordone, L., Bonifacio, P., Marconi, G., Buonanno, R., & Zaggia, S. 2005, A&A, 437, 905

Sbordone, L., Bonifacio, P., Buonanno, R., et al. 2007, A&A, 465, 815

Sbordone, L., Salaris, M., Weiss, A., & Cassisi, S. 2011, A&A, 534, A9

Schlegel, D. J., Finkbeiner, D. P., & Davis, M. 1998, ApJ, 500, 525

Schörck, T., Christlieb, N., Cohen, J. G., et al. 2009, A&A, 507, 817

Scudder, J. M., Ellison, S. L., Torrey, P., Patton, D. R., & Mendel, J. T. 2012, MNRAS, 426, 549

Shapley, H. 1938, Nature, 142, 715

Shetrone, M. D., Bolte, M., & Stetson, P. B. 1998, AJ, 115, 1888

Shetrone, M., Venn, K. A., Tolstoy, E., et al. 2003, AJ, 125, 684

Skillman, E. D., Kennicutt, R. C., & Hodge, P. W. 1989, ApJ, 347, 875

Smecker-Hane, T. A., Stetson, P. B., Hesser, J. E., & Vandenberg, D. A. 1996, From Stars to Galaxies: the Impact of Stellar Physics on Galaxy Evolution, 98, 328

Springel, V., Wang, J., Vogelsberger, M., et al. 2008, MNRAS, 391, 1685

Starkenburg, E., Hill, V., Tolstoy, E., et al. 2010, A&A, 513, A34

Starkenburg, E., Hill, V., Tolstoy, E., et al. 2013, A&A, 549, A88

Stetson, P. B., Hesser, J. E., & Smecker-Hane, T. A. 1998, PASP, 110, 533

Stetson, P. B., Bruntt, H., & Grundahl, F. 2003, PASP, 115, 413

Strader, J., Brodie, J. P., Forbes, D. A., Beasley, M. A., & Huchra, J. P. 2003, AJ, 125, 1291

Tafelmeyer, M., Jablonka, P., Hill, V., et al. 2010, A&A, 524, A58

Timmes, F. X., Woosley, S. E., & Weaver, T. A. 1995, ApJS, 98, 617

Tinsley, B. M. 1979, ApJ, 229, 1046

Tolstoy, E., Hill, V., & Tosi, M. 2009, ARAA, 47, 371

Tsujimoto, T., Nomoto, K., Yoshii, Y., et al. 1995, MNRAS, 277, 945

Tully, R. B., Libeskind, N. I., Karachentsev, I. D., et al. 2015, ApJ, 802, L25

Ural, U., Cescutti, G., Koch, A., et al. 2015, MNRAS, 449, 761

Valenti, E., Ferraro, F. R., & Origlia, L. 2004, MNRAS, 351, 1204

VandenBerg, D. A., Brogaard, K., Leaman, R., & Casagrande, L. 2013, ApJ, 775, 134

Vargas, L. C., Geha, M., Kirby, E. N., & Simon, J. D. 2013, ApJ, 767, 134

Vargas, L. C., Gilbert, K. M., Geha, M., et al. 2014, ApJ, 797, L2

van de Ven, G., van den Bosch, R. C. E., Verolme, E. K., & de Zeeuw, P. T. 2006, A&A, 445, 513

Venn, K. A., Irwin, M., Shetrone, M. D., et al. 2004, AJ, 128, 1177

Venn, K. A., Shetrone, M. D., Irwin, M. J., et al. 2012, ApJ, 751, 102

Villanova, S., Geisler, D., Carraro, G., Moni Bidin, C., & Muñoz, C. 2013, ApJ, 778, 186

Walker, M. G., Mateo, M., Olszewski, E. W., et al. 2006, AJ, 131, 2114

Walker, M. G., Mateo, M., & Olszewski, E. W. 2008, ApJ, 688, L75

Walker, M. G., Mateo, M., Olszewski, E. W., Sen, B., & Woodroofe, M. 2009, AJ, 137, 3109

Walker, M. G., Mateo, M., Olszewski, E. W., et al. 2009, ApJ, 704, 1274

Walker, M. G., & Peñarrubia, J. 2011, ApJ, 742, 20

Wallerstein, G. 1962, ApJS, 6, 407

Wambsganss, J., Bode, P., & Ostriker, J. P. 2004, ApJ, 606, L93

Weidner, C., & Kroupa, P. 2005, ApJ, 625, 754

Weisz, D. R., Dolphin, A. E., Skillman, E. D., et al. 2014, ApJ, 789, 147

White, S. D. M., & Rees, M. J. 1978, MNRAS, 183, 341

Willman, B., Blanton, M. R., West, A. A., et al. 2005, AJ, 129, 2692

Woosley, S. E., & Weaver, T. A. 1995, ApJS, 101, 181

Yozin, C., & Bekki, K. 2012, ApJ, 756, L18

Appendices

A

VLT FLAMES Observations in the outer Parts of Fornax (presented in Chapter 2 and 3)

Table A.1: Chemodynamical parameters for field stars and GC members in Fornax – astrometry, photometry, velocities. Astrometry for all our targets is calibrated to the USNO-1B system. For detailed information see Walker et al. (2006). Tables A.1, A.2, and A.3 list all stars which passed the selection process described in Section 3.2.

ID	α	δ	S/N	RV [km s^{-1}]	σ RV [km s^{-1}]	V	σV	$V-I$	$\sigma(V-I)$
2	2h37m12.20s	−34d51m50.18s	20.7	47.95	0.97	18.938	0.031	1.179	0.039
3	2h37m14.11s	−34d51m30.82s	18.5	39.58	1.22	19.094	0.041	1.301	0.048
4	2h37m16.63s	−34d50m11.18s	17.7	46.48	0.90	19.277	0.042	1.069	0.049
5	2h37m19.31s	−34d43m49.19s	22.6	26.40	1.32	19.457	0.052	1.211	0.059
6	2h37m22.88s	−34d53m40.31s	15.2	56.62	0.91	19.378	0.051	1.272	0.056
7	2h37m25.62s	−34d42m43.70s	29.3	50.91	0.68	19.092	0.029	1.283	0.035
8	2h37m25.99s	−34d52m53.90s	16.1	51.80	0.83	19.169	0.034	1.077	0.045
10	2h37m33.79s	−34d42m14.40s	21.1	38.21	1.39	19.487	0.102	1.146	0.109
11	2h37m35.57s	−34d40m52.72s	19.7	30.82	0.94	19.357	0.060	1.160	0.067
13	2h37m36.74s	−34d42m14.51s	28.9	50.46	0.87	18.965	0.049	1.415	0.054
14	2h37m38.64s	−34d56m52.12s	14.3	68.88	1.27	19.495	0.049	1.105	0.059
15	2h37m39.28s	−34d45m14.18s	29.1	50.65	0.83	19.195	0.039	1.187	0.044
17	2h37m44.01s	−34d43m33.71s	26.0	44.98	0.77	19.157	0.037	1.155	0.045
19	2h37m44.87s	−34d46m13.58s	27.6	51.36	1.03	18.889	0.029	1.378	0.033
20	2h37m45.90s	−34d57m24.19s	19.9	64.71	0.74	19.187	0.043	1.267	0.047
21	2h37m46.57s	−34d51m41.29s	20.8	52.06	2.40	19.480	0.048	1.259	0.056
22	2h37m46.86s	−34d41m44.09s	18.5	63.80	1.60	19.402	0.052	1.253	0.059
23	2h37m47.54s	−34d53m55.72s	24.2	39.60	0.86	18.884	0.025	1.213	0.033
24	2h37m50.29s	−34d48m41.40s	14.2	45.31	1.48	19.961	0.117	0.987	0.135
25	2h37m51.36s	−34d53m35.30s	34.6	48.69	0.77	18.822	0.036	1.195	0.041
26	2h37m51.99s	−34d40m59.59s	24.8	59.77	1.10	19.219	0.049	1.257	0.054
27	2h37m52.28s	−34d41m31.99s	23.3	55.39	0.99	18.910	0.035	1.213	0.042
28	2h37m52.35s	−34d56m21.91s	24.4	47.94	0.73	19.425	0.073	1.201	0.080
29	2h37m52.46s	−34d51m17.21s	23.1	40.15	0.92	19.174	0.061	1.349	0.067
30	2h37m53.39s	−34d54m9.29s	16.9	63.86	0.68	19.609	0.091	1.142	0.100
31	2h37m53.64s	−34d48m2.30s	24.2	46.91	0.95	18.854	0.044	1.426	0.047
32	2h37m53.88s	−34d44m2.11s	25.4	63.54	0.91	18.961	0.042	1.263	0.048
33	2h37m58.02s	−34d44m12.52s	17.0	60.90	0.96	19.147	0.060	1.137	0.065
34	2h37m58.05s	−34d49m9.59s	24.6	48.71	0.99	18.851	0.043	1.444	0.047
35	2h37m58.84s	−34d41m24.61s	14.3	48.31	1.28	19.449	0.065	1.020	0.072
36	2h38m0.47s	−34d38m37.79s	20.8	67.45	0.65	18.947	0.035	1.242	0.039
37	2h38m1.18s	−34d41m28.28s	26.9	51.90	0.64	18.774	0.035	1.331	0.041
38	2h38m1.22s	−34d50m46.61s	23.9	41.22	0.95	19.471	0.068	1.090	0.079

Table A.1 – continued from previous page

ID	α	δ	S/N	RV [km s^{-1}]	σ RV [km s^{-1}]	V	σV	$V-I$	$\sigma(V-I)$
39	2h38m3.80s	−34d53m35.09s	16.2	55.23	1.02	19.608	0.065	1.192	0.073
40	2h38m5.12s	−34d44m7.30s	14.6	72.47	1.84	19.023	0.041	1.131	0.049
41	2h38m7.25s	−34d56m52.51s	20.7	73.86	1.10	19.432	0.071	1.090	0.080
43	2h38m7.78s	−34d51m20.99s	18.3	41.20	0.61	19.412	0.054	1.236	0.061
45	2h38m9.81s	−34d46m52.61s	23.0	52.18	1.05	19.319	0.061	1.283	0.066
46	2h38m10.48s	−34d38m46.10s	30.1	62.89	0.67	18.724	0.039	1.341	0.042
47	2h38m11.12s	−34d49m17.18s	35.2	49.73	0.99	19.282	0.061	1.226	0.066
49	2h38m12.24s	−34d38m53.30s	29.9	44.07	0.67	18.708	0.034	1.332	0.038
50	2h38m12.43s	−34d50m47.62s	16.9	52.42	0.95	19.885	0.112	1.163	0.125
51	2h38m13.91s	−34d46m55.60s	49.6	64.49	0.75	18.705	0.036	1.339	0.040
52	2h38m14.36s	−34d49m52.61s	19.4	51.87	0.90	19.161	0.060	1.395	0.065
53	2h38m15.15s	−34d39m28.80s	22.0	49.40	0.85	19.011	0.043	1.183	0.047
54	2h38m16.51s	−34d43m25.28s	33.6	36.24	0.73	18.762	0.046	1.249	0.050
55	2h38m17.21s	−34d42m59.29s	20.1	40.49	1.13	19.330	0.071	1.271	0.077
56	2h38m18.43s	−34d45m13.28s	31.9	53.61	0.84	18.776	0.040	1.392	0.044
57	2h38m18.85s	−34d50m26.30s	14.4	46.37	0.84	19.764	0.076	1.103	0.093
59	2h38m19.86s	−34d53m47.40s	21.8	54.12	1.00	19.398	0.063	1.350	0.069
60	2h38m20.87s	−34d43m56.39s	22.0	55.83	1.04	18.746	0.037	1.465	0.041
61	2h38m21.48s	−34d47m5.39s	28.5	49.50	0.77	19.013	0.042	1.286	0.047
62	2h38m21.75s	−34d50m59.71s	16.1	40.96	1.43	19.210	0.050	1.364	0.057
63	2h38m23.85s	−34d45m38.41s	21.9	63.15	1.01	19.207	0.052	1.313	0.057
64	2h38m24.09s	−34d41m27.71s	18.3	55.59	1.10	19.485	0.066	1.260	0.072
65	2h38m24.79s	−34d50m24.79s	21.3	53.51	1.12	19.215	0.054	0.986	0.064
66	2h38m25.94s	−34d41m47.69s	26.6	39.77	0.84	19.049	0.045	1.071	0.052
67	2h38m26.37s	−34d46m56.39s	31.5	48.53	0.78	19.051	0.055	1.124	0.062
68	2h38m26.89s	−34d45m37.12s	19.7	52.81	1.00	19.303	0.064	1.348	0.072
69	2h38m28.30s	−34d46m39.68s	27.7	69.26	0.92	18.886	0.043	1.416	0.047
70	2h38m28.57s	−34d53m41.10s	20.2	47.07	0.96	18.789	0.038	1.368	0.043
71	2h38m28.66s	−34d58m27.59s	17.3	79.79	0.99	19.674	0.062	1.037	0.080
72	2h38m29.33s	−34d50m14.32s	23.3	55.62	0.96	19.390	0.060	1.258	0.068
73	2h38m29.63s	−34d41m23.89s	19.2	59.58	1.03	19.271	0.053	1.269	0.058
74	2h38m29.90s	−34d58m57.79s	27.5	39.98	0.78	19.078	0.095	1.303	0.116
75	2h38m31.15s	−34d43m1.42s	19.2	63.61	0.82	18.758	0.036	1.272	0.040
76	2h38m31.54s	−34d52m24.89s	20.3	39.89	1.25	19.943	0.102	1.240	0.115
77	2h38m31.59s	−34d43m39.79s	24.1	74.27	1.08	19.470	0.071	1.184	0.078
78	2h38m32.34s	−34d43m24.10s	22.4	48.04	0.83	18.798	0.041	1.305	0.045
79	2h38m33.01s	−34d40m38.32s	34.7	39.28	0.62	18.876	0.037	1.179	0.043
81	2h38m34.93s	−35d0m17.78s	14.7	30.56	1.05	19.277	0.052	1.035	0.063
82	2h38m36.22s	−34d51m21.71s	37.3	40.11	0.94	18.935	0.040	1.220	0.047
83	2h38m37.13s	−34d50m8.30s	22.9	54.04	1.10	19.006	0.047	1.395	0.050
84	2h38m37.52s	−34d40m35.62s	20.1	50.06	2.29	18.952	0.040	1.385	0.045
85	2h38m38.05s	−34d44m59.60s	22.9	39.52	1.08	18.796	0.047	1.254	0.051
86	2h38m39.01s	−34d59m10.00s	30.3	67.56	0.54	18.713	0.030	1.342	0.035
87	2h38m39.63s	−34d42m10.69s	23.4	43.80	1.00	18.782	0.038	1.344	0.050
89	2h38m40.72s	−34d51m36.22s	29.4	75.82	0.70	18.907	0.042	1.267	0.046
90	2h38m41.24s	−34d52m57.79s	11.0	72.81	1.25	19.367	0.064	1.217	0.071
91	2h38m42.32s	−34d45m42.70s	19.9	48.49	1.07	19.071	0.060	1.357	0.063
92	2h38m42.34s	−34d55m43.28s	16.5	48.65	1.16	19.357	0.057	1.067	0.065
96	2h38m44.10s	−34d45m43.88s	33.7	37.95	0.79	18.756	0.031	1.339	0.036
98	2h38m45.67s	−34d57m48.82s	15.6	78.33	1.00	19.350	0.057	1.160	0.067
100	2h38m46.46s	−34d51m49.90s	26.1	44.91	1.04	19.213	0.054	1.314	0.059
101	2h38m46.73s	−34d42m54.79s	19.3	63.98	0.97	19.411	0.082	1.162	0.088
102	2h38m47.89s	−34d50m59.78s	26.5	64.83	0.91	19.138	0.052	1.353	0.057
103	2h38m48.85s	−34d46m27.08s	25.9	57.67	0.70	19.114	0.048	1.115	0.055
104	2h38m53.62s	−34d55m55.09s	17.4	58.56	0.98	19.403	0.069	1.078	0.078
105	2h38m55.70s	−34d48m2.20s	23.9	62.04	0.91	18.734	0.040	1.263	0.044
107	2h38m56.59s	−34d56m34.91s	15.9	78.05	1.15	19.245	0.051	1.090	0.060
108	2h38m58.31s	−34d48m1.40s	21.2	60.23	1.03	18.967	0.047	1.355	0.050
109	2h38m58.73s	−34d43m33.60s	18.8	60.80	0.86	19.212	0.046	1.214	0.054
110	2h38m59.18s	−34d53m27.82s	25.1	63.66	1.07	19.118	0.053	1.201	0.058
111	2h39m0.38s	−34d48m48.71s	27.4	78.29	1.12	18.847	0.037	1.331	0.041
112	2h39m3.50s	−34d49m59.92s	27.9	54.26	0.84	18.925	0.040	1.258	0.046
114	2h37m41.25s	−34d54m16.09s	15.3	50.09	1.12	19.537	0.047	1.035	0.055
115	2h38m52.50s	−34d54m21.31s	11.6	58.36	1.16	19.699	0.091	1.109	0.099
126	2h37m33.48s	−34d43m53.11s	18.2	39.88	1.49	19.296	0.045	1.076	0.055
127	2h37m35.83s	−34d51m15.30s	11.8	70.92	1.35	19.599	0.075	0.946	0.094
128	2h37m37.23s	−34d46m12.29s	14.7	71.48	2.30	19.843	0.069	1.074	0.080

Table A.1 – continued from previous page

ID	α	δ	S/N	RV [$\mathrm{km\,s^{-1}}$]	σ RV [$\mathrm{km\,s^{-1}}$]	V	σV	$V-I$	$\sigma(V-I)$
129	2h37m38.74s	−34d48m20.20s	15.1	56.31	1.26	19.883	0.076	1.059	0.092
130	2h37m40.34s	−34d42m20.70s	13.3	55.26	0.91	19.044	0.039	1.300	0.043
133	2h37m42.88s	−34d45m0.61s	18.2	44.03	0.96	18.911	0.031	1.339	0.034
135	2h37m43.83s	−34d43m15.60s	11.9	53.31	1.83	19.789	0.061	1.141	0.069
136	2h37m44.13s	−34d41m18.60s	16.3	57.47	1.11	19.295	0.087	1.271	0.091
137	2h37m44.58s	−34d56m40.20s	14.4	39.10	1.44	19.520	0.047	1.029	0.054
138	2h37m45.34s	−34d44m32.32s	16.1	60.55	0.95	19.236	0.043	1.238	0.050
139	2h37m45.42s	−34d48m18.68s	22.7	63.69	0.89	19.065	0.037	1.327	0.041
142	2h37m49.98s	−34d48m11.99s	18.9	57.09	0.87	19.039	0.045	1.365	0.049
143	2h37m50.86s	−34d53m31.70s	13.4	44.24	0.70	19.992	0.121	0.949	0.142
145	2h37m52.49s	−34d41m50.71s	13.8	68.18	0.85	19.354	0.068	1.279	0.071
146	2h37m52.65s	−34d54m48.49s	18.2	40.27	1.95	19.510	0.071	0.950	0.082
147	2h37m53.68s	−34d52m52.61s	23.4	57.84	0.88	19.705	0.074	1.136	0.085
148	2h37m57.62s	−34d49m18.08s	25.3	66.01	0.96	18.890	0.042	1.213	0.047
149	2h37m58.17s	−34d50m25.40s	19.8	54.10	0.78	19.874	0.115	1.011	0.130
150	2h37m58.50s	−34d45m16.49s	25.2	59.95	0.56	18.771	0.037	1.361	0.042
151	2h38m0.46s	−34d38m58.20s	12.8	40.52	0.90	19.363	0.000	1.222	0.000
152	2h38m0.64s	−34d43m51.82s	17.9	56.70	1.01	19.199	0.064	1.229	0.070
153	2h38m1.94s	−34d41m23.39s	19.0	47.91	0.98	19.316	0.058	1.343	0.064
154	2h38m2.21s	−34d42m42.52s	17.2	70.04	1.22	19.177	0.057	1.373	0.064
155	2h38m2.84s	−34d53m31.88s	26.4	42.93	0.78	19.468	0.068	1.238	0.077
157	2h38m3.27s	−34d38m17.59s	15.5	52.71	0.89	19.101	0.045	1.311	0.050
158	2h38m3.93s	−34d39m7.42s	13.9	63.35	1.03	19.324	0.065	1.105	0.070
160	2h38m4.73s	−34d40m31.12s	20.1	63.92	0.91	19.138	0.052	1.175	0.058
161	2h38m4.83s	−34d54m59.62s	19.7	44.87	1.24	19.895	0.106	1.161	0.118
162	2h38m5.53s	−34d38m42.79s	26.1	29.42	0.94	19.039	0.054	1.274	0.061
163	2h38m5.78s	−34d55m43.00s	16.9	55.13	1.02	19.730	0.080	1.220	0.089
164	2h38m6.32s	−34d42m31.10s	23.1	65.48	0.89	19.258	0.060	1.316	0.066
165	2h38m6.80s	−34d57m10.80s	16.8	52.98	1.01	18.800	0.038	1.422	0.042
167	2h38m8.19s	−34d50m56.90s	27.3	54.98	0.95	19.515	0.067	1.300	0.074
168	2h38m8.84s	−34d52m2.78s	26.8	57.05	0.88	19.698	0.091	0.991	0.106
169	2h38m10.53s	−34d41m23.71s	18.9	46.16	0.99	19.168	0.047	1.328	0.052
170	2h38m12.24s	−34d56m32.89s	12.6	72.77	0.88	19.753	0.091	1.180	0.100
171	2h38m13.59s	−34d55m14.30s	11.5	65.23	0.92	20.151	0.132	1.008	0.151
173	2h38m14.51s	−34d41m40.70s	30.7	38.40	0.87	19.379	0.060	1.193	0.066
174	2h38m15.73s	−34d54m9.50s	16.9	54.14	1.10	19.823	0.091	1.115	0.104
175	2h38m17.97s	−34d50m35.92s	33.4	54.83	0.79	19.682	0.086	1.194	0.096
176	2h38m19.34s	−34d39m5.40s	14.4	48.71	1.08	19.484	0.061	1.133	0.067
177	2h38m19.69s	−34d41m30.98s	15.4	48.47	1.19	19.275	0.055	1.101	0.063
178	2h38m20.96s	−34d40m41.48s	21.5	57.76	0.71	19.038	0.051	1.297	0.058
179	2h38m21.08s	−34d48m53.21s	12.8	45.98	1.05	19.881	0.097	1.171	0.110
180	2h38m23.12s	−34d44m6.50s	22.0	42.45	1.04	19.457	0.068	1.323	0.073
181	2h38m23.51s	−34d48m37.91s	45.4	77.61	0.78	19.023	0.047	1.246	0.053
182	2h38m25.71s	−34d41m27.31s	16.8	69.66	1.09	19.113	0.044	1.313	0.049
183	2h38m26.39s	−34d38m27.31s	13.5	55.10	0.70	19.216	0.046	1.364	0.051
184	2h38m27.03s	−34d39m10.51s	18.4	62.27	0.85	19.275	0.050	1.138	0.057
185	2h38m27.97s	−34d50m15.68s	27.0	40.91	1.31	19.848	0.105	0.980	0.121
186	2h38m28.64s	−34d52m35.11s	21.2	53.50	0.91	19.609	0.088	1.298	0.093
187	2h38m29.40s	−34d53m18.38s	19.2	64.98	1.37	19.855	0.000	0.990	0.000
188	2h38m30.46s	−34d52m31.30s	13.4	55.80	1.08	19.968	0.113	1.031	0.131
189	2h38m31.56s	−34d38m54.38s	16.6	59.30	1.38	19.488	0.075	1.171	0.080
190	2h38m31.73s	−34d48m24.01s	25.7	75.43	1.15	19.270	0.057	1.052	0.073
191	2h38m32.60s	−34d40m28.81s	13.6	53.07	1.07	19.384	0.057	1.053	0.064
192	2h38m32.94s	−34d39m53.60s	14.9	67.66	1.06	19.366	0.051	1.233	0.058
193	2h38m36.22s	−34d40m25.10s	21.3	51.29	1.11	19.083	0.038	1.370	0.042
194	2h38m37.65s	−34d54m33.41s	10.5	61.25	2.05	19.994	0.115	1.128	0.131
195	2h38m37.78s	−34d52m57.50s	20.0	67.22	0.63	19.506	0.077	1.078	0.086
197	2h38m39.93s	−34d44m11.29s	18.1	44.75	0.82	19.171	0.054	1.179	0.062
200	2h38m44.11s	−34d57m4.61s	11.1	56.26	1.22	19.757	0.098	1.112	0.110
204	2h38m44.60s	−34d41m8.20s	16.7	62.71	1.12	19.352	0.060	1.278	0.065
205	2h38m44.80s	−34d59m14.21s	10.8	70.55	1.02	19.336	0.057	1.177	0.067
207	2h38m45.31s	−34d49m18.19s	40.6	57.62	1.63	19.095	0.046	1.288	0.053
208	2h38m45.70s	−34d52m21.40s	28.6	64.27	0.94	18.855	0.044	1.400	0.048
209	2h38m45.79s	−34d55m37.81s	11.0	75.54	2.12	19.940	0.097	0.911	0.118
210	2h38m46.54s	−34d50m15.50s	35.5	67.70	0.61	19.008	0.046	1.224	0.051
211	2h38m47.53s	−34d46m25.28s	22.6	48.25	0.93	19.193	0.056	1.118	0.062
212	2h38m47.91s	−34d44m42.00s	17.4	51.32	0.84	19.301	0.062	1.238	0.068

Table A.1 – continued from previous page

ID	α	δ	S/N	RV [km s^{-1}]	σ RV [km s^{-1}]	V	σV	$V-I$	$\sigma(V-I)$
213	2h38m53.16s	−34d47m50.89s	13.3	42.86	0.72	19.464	0.071	1.114	0.081
214	2h38m53.60s	−34d45m20.59s	20.8	50.51	0.96	19.003	0.038	1.360	0.043
215	2h38m54.94s	−34d43m23.41s	12.6	51.20	0.90	19.265	0.071	1.121	0.076
216	2h38m55.29s	−34d51m54.50s	14.3	69.71	1.18	19.737	0.071	1.118	0.085
217	2h38m55.30s	−34d55m35.80s	11.6	64.57	1.31	19.457	0.070	1.173	0.077
219	2h38m56.27s	−34d49m23.59s	17.0	45.59	0.90	19.416	0.066	1.335	0.072
221	2h38m56.82s	−34d56m29.00s	10.6	67.85	1.18	19.273	0.060	1.259	0.066
222	2h38m57.95s	−34d54m50.40s	15.9	31.81	0.98	19.506	0.068	1.355	0.076
224	2h39m0.58s	−34d45m6.19s	14.8	52.50	0.97	19.069	0.047	1.271	0.052
225	2h39m2.40s	−34d53m43.69s	10.7	58.84	1.12	19.706	0.081	1.122	0.093
227	2h40m54.24s	−34d5m12.41s	20.1	48.05	1.03	19.900	0.070	1.272	0.081
228	2h40m56.46s	−34d9m2.41s	18.1	65.18	0.85	19.742	0.058	1.126	0.069
229	2h40m59.07s	−34d7m32.20s	30.9	47.71	1.00	19.233	0.037	1.328	0.045
230	2h40m59.26s	−34d0m11.70s	13.8	49.31	2.39	19.960	0.061	0.979	0.086
231	2h41m1.12s	−34d10m59.81s	17.7	50.06	1.51	19.812	0.052	1.085	0.066
232	2h41m1.59s	−34d6m25.20s	19.1	46.70	1.12	19.354	0.048	1.106	0.058
233	2h41m2.02s	−34d8m37.28s	26.3	63.19	0.91	19.176	0.035	1.198	0.043
234	2h41m2.40s	−34d7m29.50s	19.7	48.20	1.54	19.742	0.048	1.021	0.071
235	2h41m4.03s	−34d4m42.82s	23.3	86.77	2.20	19.733	0.045	1.036	0.066
236	2h41m4.04s	−34d9m48.89s	26.8	71.35	0.68	19.184	0.038	1.109	0.048
237	2h41m4.56s	−34d8m22.70s	21.1	47.04	1.56	19.207	0.036	1.026	0.041
238	2h41m6.52s	−34d6m58.72s	24.3	51.73	0.91	19.417	0.043	1.194	0.049
239	2h41m6.97s	−34d3m2.92s	19.3	57.01	1.65	19.860	0.061	1.077	0.076
240	2h41m8.35s	−34d3m23.90s	24.8	31.02	1.15	19.548	0.047	1.056	0.068
241	2h41m8.71s	−33d59m24.00s	20.1	73.87	1.98	19.742	0.058	1.125	0.073
242	2h41m9.44s	−33d57m42.70s	18.1	50.80	1.58	19.697	0.057	1.134	0.066
243	2h41m11.11s	−34d10m57.11s	18.8	56.80	1.32	19.763	0.059	0.898	0.081
244	2h41m11.72s	−34d13m18.59s	22.3	26.12	0.81	19.294	0.034	1.058	0.045
245	2h41m12.08s	−33d57m39.71s	15.6	57.16	1.30	19.881	0.059	1.220	0.075
248	2h41m12.77s	−34d13m1−s	20.3	60.23	0.94	19.654	0.050	1.186	0.061
249	2h41m13.70s	−34d11m40.31s	22.0	37.83	0.96	19.749	0.047	1.106	0.062
250	2h41m19.35s	−33d54m22.61s	10.1	46.24	1.57	20.228	0.065	1.142	0.083
251	2h41m19.81s	−33d59m0.60s	16.5	51.35	3.39	20.169	0.061	1.012	0.084
252	2h41m20.12s	−34d3m0.90s	23.4	43.79	1.39	19.551	0.037	1.129	0.052
253	2h41m21.08s	−34d11m0.10s	25.7	79.24	0.97	19.422	0.040	1.035	0.051
255	2h41m21.96s	−33d56m15.40s	18.2	48.44	1.15	19.583	0.053	1.131	0.063
256	2h41m25.18s	−34d10m50.81s	22.8	66.78	1.13	19.638	0.054	1.166	0.068
257	2h41m26.44s	−34d11m12.70s	26.8	57.12	0.87	19.124	0.035	1.231	0.042
258	2h41m29.33s	−33d59m2.18s	22.8	46.44	1.01	19.624	0.046	1.056	0.062
259	2h41m29.40s	−34d15m17.71s	30.9	66.02	0.74	19.189	0.000	1.243	0.000
260	2h41m29.44s	−34d1m53.62s	17.9	48.78	1.04	19.681	0.053	0.971	0.068
261	2h41m29.52s	−34d10m34.90s	32.0	67.77	0.59	19.434	0.044	1.075	0.052
262	2h41m29.85s	−34d9m39.31s	30.7	76.29	1.21	19.319	0.044	1.123	0.050
263	2h41m30.58s	−34d11m4−s	27.1	56.40	0.84	19.103	0.033	1.289	0.039
264	2h41m31.19s	−34d8m53.30s	26.5	63.24	1.20	19.208	0.033	1.203	0.043
265	2h41m31.39s	−34d2m13.42s	10.1	59.33	2.42	20.104	0.067	1.205	0.089
266	2h41m32.99s	−33d52m3.22s	12.0	40.06	1.86	19.946	0.055	1.072	0.073
267	2h41m33.69s	−34d13m7.50s	38.2	52.79	0.88	19.344	0.037	1.211	0.045
268	2h41m34.28s	−34d10m17.62s	28.4	58.77	0.89	19.158	0.035	1.247	0.039
270	2h41m35.05s	−34d1m23.48s	18.4	59.84	1.51	19.750	0.049	1.117	0.063
274	2h41m37.57s	−34d13m52.10s	25.0	45.84	0.92	19.637	0.046	1.200	0.055
275	2h41m39.27s	−33d56m45.89s	16.3	57.84	1.39	19.866	0.052	1.033	0.066
276	2h41m40.61s	−34d12m17.60s	16.5	66.96	1.50	19.789	0.054	0.793	0.074
277	2h41m41.16s	−34d11m15.68s	22.5	62.78	0.83	19.489	0.000	1.151	0.000
279	2h41m43.58s	−34d8m21.80s	21.2	69.41	0.75	19.535	0.047	1.125	0.055
280	2h41m44.72s	−34d7m48.40s	28.6	64.04	0.81	19.254	0.035	1.150	0.044
281	2h41m44.92s	−33d54m33.59s	18.6	55.91	1.50	19.704	0.048	1.015	0.068
282	2h41m45.03s	−33d53m37.50s	34.3	43.25	0.79	19.069	0.033	1.150	0.039
284	2h41m45.80s	−34d14m19.90s	19.3	48.42	0.64	19.865	0.055	0.851	0.074
285	2h41m47.83s	−34d15m40.21s	24.3	47.36	1.00	19.186	0.040	1.264	0.045
287	2h41m49.78s	−34d15m56.81s	15.3	29.32	1.30	20.018	0.085	1.099	0.098
288	2h41m49.89s	−33d57m2.02s	11.0	63.94	1.72	19.970	0.055	1.027	0.079
289	2h41m50.67s	−34d7m34.50s	21.6	40.21	0.90	19.556	0.048	1.059	0.060
290	2h41m51.05s	−34d1m13.91s	34.3	48.50	0.84	19.232	0.043	1.144	0.047
291	2h41m53.11s	−34d5m16.58s	20.5	70.15	0.98	19.598	0.054	1.142	0.061
294	2h41m56.75s	−34d1m50.30s	16.5	62.08	0.83	19.890	0.068	1.073	0.075
295	2h41m57.81s	−34d15m24.01s	34.5	77.27	0.96	19.133	0.036	1.233	0.043

Table A.1 – continued from previous page

ID	α	δ	S/N	RV [$\mathrm{km\,s^{-1}}$]	σ RV [$\mathrm{km\,s^{-1}}$]	V	σV	$V-I$	$\sigma(V-I)$
297	2h41m58.33s	−33d56m59.89s	16.0	26.63	1.55	20.097	0.091	0.997	0.100
298	2h41m58.35s	−34d10m30.61s	18.0	48.54	1.64	19.928	0.074	0.954	0.087
299	2h42m1.23s	−34d12m53.60s	12.8	66.54	1.90	20.249	0.089	1.076	0.103
300	2h42m3.57s	−34d10m44.69s	18.6	41.21	0.83	19.947	0.061	1.027	0.071
301	2h42m3.64s	−33d56m26.70s	19.9	42.67	1.02	19.570	0.052	1.074	0.058
302	2h42m5.12s	−33d55m9.30s	14.3	51.78	1.30	20.161	0.086	1.077	0.097
303	2h42m7.59s	−33d58m9.80s	15.4	68.20	1.30	20.151	0.085	1.041	0.096
304	2h42m8.47s	−33d59m1.79s	19.9	61.35	1.10	19.567	0.055	1.067	0.060
311	2h42m18.89s	−34d5m7.69s	10.0	63.56	2.06	18.774	0.026	1.179	0.033
312	2h42m19.14s	−34d12m9.79s	13.8	62.74	1.81	20.211	0.085	0.975	0.110
313	2h42m22.42s	−34d10m19.88s	19.5	70.61	1.18	19.857	0.065	1.125	0.077
316	2h42m25.41s	−34d8m24.79s	21.1	70.75	0.77	19.815	0.065	0.985	0.083
317	2h42m32.21s	−34d7m54.91s	23.1	70.92	0.79	19.684	0.060	1.084	0.071
318	2h42m34.20s	−34d10m30.40s	10.5	48.62	1.45	20.239	0.092	0.737	0.119
319	2h42m35.16s	−33d57m4.50s	11.5	55.04	0.92	20.097	0.080	1.069	0.088
320	2h42m35.56s	−33d57m48.10s	11.4	58.62	1.16	20.014	0.069	0.997	0.079
321	2h40m53.64s	−34d2m21.08s	29.3	50.19	1.02	18.893	0.027	1.371	0.034
322	2h40m54.12s	−34d5m36.38s	13.6	56.96	1.26	19.448	0.037	1.236	0.045
323	2h40m55.19s	−33d58m49.12s	10.8	55.00	1.72	19.891	0.058	1.078	0.074
324	2h40m56.53s	−34d3m49.10s	28.5	49.25	0.77	18.780	0.031	1.268	0.037
325	2h40m57.84s	−34d10m22.80s	17.0	43.97	1.06	18.994	0.028	1.083	0.036
326	2h41m0.76s	−34d8m33.11s	23.9	59.97	0.69	18.726	0.029	1.185	0.033
328	2h41m5.98s	−33d58m8.69s	13.4	69.42	2.19	19.318	0.039	1.034	0.052
332	2h41m8.56s	−33d58m23.20s	28.4	56.59	0.99	18.748	0.028	1.246	0.036
333	2h41m8.62s	−34d12m40.50s	16.2	40.25	1.65	19.420	0.044	1.086	0.054
334	2h41m8.99s	−34d4m36.08s	17.2	50.67	1.21	19.240	0.033	1.049	0.047
335	2h41m9.62s	−33d59m39.80s	13.1	63.40	2.13	19.233	0.034	1.070	0.044
336	2h41m9.73s	−34d5m43.40s	19.1	39.92	0.66	19.348	0.032	1.268	0.040
337	2h41m9.86s	−34d1m52.00s	15.2	53.38	1.31	19.178	0.044	1.279	0.048
339	2h41m12.58s	−34d9m23.00s	21.6	73.31	0.86	19.118	0.034	1.241	0.042
340	2h41m13.90s	−34d11m30.01s	27.0	41.13	0.96	18.878	0.033	1.307	0.039
341	2h41m14.58s	−34d12m37.91s	24.2	52.06	1.19	19.102	0.033	1.284	0.040
342	2h41m16.45s	−34d9m31.00s	28.1	33.48	0.95	18.929	0.028	1.106	0.035
343	2h41m17.43s	−33d59m4.88s	19.3	54.56	0.92	18.872	0.024	1.324	0.034
344	2h41m18.22s	−34d7m14.02s	20.2	53.85	1.10	19.093	0.030	1.211	0.037
345	2h41m18.47s	−34d5m16.69s	20.1	34.57	1.35	19.218	0.029	1.317	0.038
347	2h41m20.01s	−34d12m14.62s	28.1	68.37	0.73	18.974	0.034	1.224	0.049
348	2h41m20.55s	−34d3m31.10s	16.6	30.84	1.00	18.758	0.023	1.300	0.049
349	2h41m25.79s	−34d7m40.19s	35.1	72.68	0.56	18.744	0.026	1.230	0.032
350	2h41m25.88s	−34d14m50.21s	24.2	64.50	1.07	18.971	0.027	1.300	0.034
351	2h41m25.95s	−34d14m15.00s	18.7	46.60	0.74	19.498	0.045	1.150	0.058
352	2h41m26.65s	−33d56m11.40s	12.1	51.32	3.55	19.604	0.038	1.184	0.052
353	2h41m26.92s	−34d3m45.68s	14.6	59.57	1.16	19.498	0.037	1.199	0.048
354	2h41m27.08s	−34d4m24.71s	12.7	50.90	1.53	19.944	0.060	1.171	0.073
355	2h41m27.19s	−34d5m3.80s	17.8	56.43	1.03	19.272	0.035	1.294	0.044
356	2h41m28.18s	−34d7m5−s	30.3	71.50	0.93	19.033	0.033	1.234	0.039
357	2h41m28.53s	−34d3m50.29s	14.3	32.53	1.06	19.788	0.051	1.146	0.067
358	2h41m28.96s	−34d8m56.29s	24.7	67.34	0.93	18.892	0.027	1.360	0.031
359	2h41m29.81s	−34d6m44.71s	26.7	61.11	1.04	19.295	0.035	1.151	0.041
360	2h41m30.84s	−34d9m12.38s	34.7	63.30	0.93	18.756	0.025	1.401	0.029
361	2h41m31.87s	−34d6m30.89s	18.7	69.39	0.97	19.162	0.036	1.147	0.041
362	2h41m33.46s	−34d9m35.60s	30.4	43.55	1.00	18.821	0.027	1.369	0.031
363	2h41m34.03s	−34d15m2.30s	27.5	51.10	1.04	18.967	0.029	1.074	0.035
364	2h41m34.24s	−33d58m57.11s	24.9	51.50	0.83	19.393	0.043	1.134	0.060
365	2h41m34.74s	−34d3m10.58s	21.4	43.78	0.82	19.142	0.033	1.242	0.043
367	2h41m37.77s	−34d4m11.71s	27.8	61.28	1.07	19.481	0.032	1.189	0.045
368	2h41m38.92s	−34d7m36.19s	23.8	61.98	0.89	19.291	0.037	1.172	0.044
369	2h41m39.23s	−34d11m48.41s	19.8	74.68	1.19	19.375	0.043	1.076	0.050
371	2h41m41.18s	−33d56m29.40s	26.8	63.78	0.68	18.917	0.024	1.286	0.031
372	2h41m41.85s	−34d7m43.79s	30.6	55.15	1.07	18.866	0.029	1.297	0.035
374	2h41m42.17s	−34d8m16.19s	19.9	48.42	1.04	19.246	0.035	1.141	0.044
375	2h41m42.60s	−33d58m21.11s	22.4	38.79	1.12	19.782	0.000	1.084	0.000
377	2h41m43.65s	−34d5m46.21s	26.4	40.99	1.40	19.739	0.050	1.094	0.064
378	2h41m44.27s	−34d6m38.02s	15.8	57.79	1.57	19.721	0.050	1.100	0.058
379	2h41m45.21s	−34d6m59.18s	12.8	40.71	1.31	20.785	0.161	0.597	0.276
380	2h41m47.32s	−34d3m33.30s	31.6	56.64	0.92	18.929	0.027	1.273	0.032
381	2h41m47.94s	−34d15m52.88s	20.8	76.28	0.91	19.180	0.037	1.276	0.045

Table A.1 – continued from previous page

ID	α	δ	S/N	RV [$\mathrm{km\,s^{-1}}$]	σ RV [$\mathrm{km\,s^{-1}}$]	V	σV	$V-I$	$\sigma(V-I)$
382	2h41m48.81s	−34d15m8.10s	15.8	26.63	0.95	19.908	0.074	1.209	0.085
385	2h41m52.62s	−34d4m48.22s	19.7	78.23	1.32	19.499	0.048	1.031	0.056
386	2h41m52.71s	−34d13m23.09s	31.2	66.87	1.02	19.042	0.030	1.257	0.039
387	2h41m53.09s	−34d2m20.69s	21.4	57.80	0.88	19.149	0.043	1.203	0.046
388	2h41m53.75s	−34d6m39.38s	33.9	62.38	0.94	19.085	0.036	1.247	0.043
389	2h41m54.12s	−34d12m35.39s	40.0	35.97	0.96	18.812	0.031	1.423	0.039
390	2h41m54.36s	−34d5m21.19s	23.0	61.25	1.25	19.204	0.045	1.067	0.052
391	2h41m54.61s	−34d9m32.90s	45.0	60.90	0.97	18.754	0.024	1.464	0.031
392	2h41m55.18s	−33d59m41.39s	15.2	46.60	1.37	19.465	0.051	1.187	0.055
393	2h41m55.39s	−34d0m49.79s	29.3	56.48	0.97	18.851	0.032	1.202	0.035
394	2h41m55.87s	−34d5m54.31s	22.2	50.43	0.74	19.345	0.043	1.183	0.051
395	2h41m56.47s	−34d1m58.58s	18.1	59.40	1.27	19.281	0.050	1.153	0.054
396	2h41m57.81s	−34d12m4.21s	31.7	49.59	1.22	19.224	0.050	1.311	0.057
397	2h41m58.17s	−34d11m18.89s	37.4	44.57	0.99	18.847	0.032	1.224	0.041
398	2h41m58.44s	−34d13m23.09s	24.1	57.09	0.87	19.343	0.043	1.150	0.052
399	2h41m58.47s	−33d55m27.52s	29.8	69.13	1.01	18.926	0.033	1.398	0.035
400	2h41m58.76s	−33d54m10.69s	23.4	60.79	0.87	19.934	0.075	1.013	0.082
401	2h41m59.52s	−33d58m5.99s	24.6	80.36	0.77	19.941	0.065	1.044	0.074
402	2h41m59.86s	−34d10m5.99s	44.9	51.14	0.69	19.205	0.037	1.151	0.045
406	2h42m2.86s	−33d51m52.49s	22.8	54.82	0.89	19.485	0.048	1.071	0.054
407	2h42m5.24s	−34d15m29.09s	27.7	68.19	0.82	19.004	0.056	1.193	0.084
408	2h42m5.96s	−34d1m23.48s	15.4	44.78	0.98	19.564	0.056	1.172	0.061
409	2h42m6.27s	−34d7m52.00s	16.6	82.88	1.46	19.603	0.057	1.083	0.070
411	2h42m9.23s	−33d59m26.81s	25.4	69.36	0.86	19.178	0.044	1.207	0.047
412	2h42m9.48s	−34d6m31.50s	14.8	63.57	0.96	19.693	0.056	1.033	0.067
413	2h42m11.19s	−34d8m21.98s	52.8	67.03	0.81	18.930	0.038	1.196	0.043
414	2h42m11.63s	−34d10m54.80s	20.3	60.73	1.03	19.697	0.063	1.204	0.074
415	2h42m13.91s	−34d10m0.41s	23.6	78.79	0.98	19.262	0.033	1.108	0.047
416	2h42m14.91s	−33d58m49.30s	25.7	58.17	0.93	19.863	0.075	1.195	0.082
417	2h42m15.13s	−34d9m44.39s	15.5	73.76	1.12	19.775	0.058	1.072	0.070
418	2h42m16.59s	−34d7m23.92s	20.8	63.35	0.94	19.528	0.050	1.251	0.059
419	2h42m16.95s	−34d5m18.82s	18.5	60.38	1.54	19.956	0.073	1.107	0.084
420	2h42m17.68s	−33d55m33.82s	30.6	67.04	0.84	19.208	0.041	1.080	0.045
422	2h42m19.01s	−34d7m50.30s	16.2	72.77	1.71	19.994	0.070	0.825	0.080
424	2h42m20.67s	−34d2m5.89s	26.1	55.23	0.98	19.166	0.051	1.173	0.054
425	2h42m21.24s	−34d2m40.81s	11.0	59.97	1.45	19.991	0.072	1.028	0.081
428	2h42m23.89s	−34d9m7.99s	31.7	54.46	0.84	18.964	0.027	1.246	0.037
430	2h42m29.30s	−34d5m59.39s	14.0	60.52	2.31	19.984	0.071	1.025	0.082
431	2h42m31.46s	−34d6m58.61s	19.2	53.04	1.19	19.393	0.036	1.248	0.046

Table A.2: Chemodynamical parameters for field stars and GC members in Fornax – CaT-metallicities, ages, EWs. $[\mathrm{Fe/H}]_{\mathrm{CaT}}$ refers to metallicities determined from the CaT. Column 8 gives the EW of the Mg I line at 8806.8 Å.

Star ID	$[\mathrm{Fe/H}]_{\mathrm{CaT}}$	$\sigma[\mathrm{Fe/H}]_{\mathrm{CaT}}$	age [Gyr]	$\mathrm{EW}_{\mathrm{CaT1}}$	$\mathrm{EW}_{\mathrm{CaT2}}$	$\mathrm{EW}_{\mathrm{CaT3}}$	$\mathrm{EW}_{\mathrm{Mg\,I}}$
2	−1.84	0.10	10.8	0.993	2.363	1.984	0.231
3	−1.37	0.10	12.9	1.097	2.820	2.434	0.351
4	−2.07	0.11	–	0.730	1.954	1.719	0.211
5	−1.33	0.09	13.0	1.139	3.027	2.097	0.356
6	−0.73	0.10	2.5	1.397	3.521	2.921	0.362
7	−1.52	0.09	11.2	1.092	2.803	2.138	0.320
8	−1.35	0.10	4.5	1.090	3.031	2.216	0.325
10	−2.24	0.09	8.4	0.679	1.857	1.387	0.178
11	−1.71	0.09	–	–	2.866	1.515	0.361
13	−1.07	0.11	7.1	1.234	3.343	2.664	0.438
14	−1.01	0.10	–	1.202	3.148	2.611	0.337
15	−2.01	0.08	–	0.279	2.147	1.707	0.224
17	−2.12	–	–	0.945	2.127	1.513	0.239
19	−0.84	0.11	4.3	1.376	3.641	2.933	0.442
20	−1.11	0.10	6.1	1.200	3.278	2.476	0.389
21	−0.96	0.10	6.5	1.392	3.122	2.750	0.416
22	−1.64	0.09	–	0.984	2.641	1.852	0.275
23	−1.01	0.11	2.9	1.432	3.477	2.723	0.399
24	−1.30	0.10	6.7	1.058	2.772	2.094	0.244
25	−2.60	–	–	0.734	1.533	1.287	0.216
26	−1.77	0.09	13.1	0.890	2.503	1.831	0.277
27	−2.68	0.09	–	0.039	1.584	1.029	0.223
28	−2.51	0.08	–	0.600	1.466	1.271	0.183
29	−0.99	0.10	8.1	1.427	3.368	2.649	0.391
30	−1.79	0.10	–	0.969	2.089	1.990	0.194
31	−1.00	0.11	4.8	1.458	3.503	2.736	0.413
32	−1.16	0.10	9.8	1.265	3.162	2.655	0.381
33	−1.10	0.10	8.7	1.329	3.174	2.626	0.397
34	−0.86	0.11	4.1	1.504	3.632	2.921	0.452
35	−1.05	0.10	4.2	1.109	3.254	2.458	0.309
36	−1.92	0.09	13.2	0.600	2.276	1.904	0.250
37	−1.84	0.10	11.0	0.964	2.624	1.824	0.272
38	−2.04	0.08	6.3	0.659	1.990	1.649	0.296
39	−0.79	0.10	3.6	1.374	3.523	2.627	0.342
40	−2.01	0.09	11.3	0.756	2.078	1.855	0.246
41	−1.38	0.09	10.5	1.160	2.680	2.355	0.264
43	−2.01	0.08	–	0.886	2.150	1.580	0.250
45	−0.92	0.10	5.9	1.218	3.317	2.761	0.357
46	−2.17	0.09	13.5	0.834	2.223	1.545	0.244
47	−2.09	0.08	–	0.690	2.062	1.578	0.264
49	−1.85	–	11.5	0.964	2.562	1.891	0.292
50	−0.83	0.10	3.8	1.226	3.166	2.704	0.336
51	−1.54	0.10	10.6	1.128	2.906	2.244	0.331
52	−1.07	0.11	9.7	1.268	3.179	2.676	0.370
53	−1.01	0.10	7.5	1.073	3.386	2.710	0.426
54	−1.61	0.10	–	1.142	2.738	2.226	0.329
55	−0.86	0.10	4.9	1.325	3.343	2.844	0.425
56	−1.42	0.10	12.3	1.186	3.038	2.337	0.397
57	−0.93	0.09	–	1.079	3.097	2.651	0.320
59	−1.00	0.10	8.8	1.262	3.249	2.598	0.419
60	−1.02	0.11	8.0	1.348	3.501	2.786	0.399
61	−1.35	0.10	10.0	1.284	2.998	2.365	0.339
62	−1.92	0.09	–	0.334	2.185	1.838	0.391
63	−0.64	0.11	1.9	1.393	3.742	3.011	0.423
64	−1.10	0.09	9.9	1.372	2.909	2.662	0.402
65	−1.12	0.10	1.6	1.403	3.124	2.602	0.337
66	−1.74	0.09	9.1	0.966	2.683	1.816	0.284
67	−2.30	0.43	7.6	0.740	1.883	1.429	0.236
68	−0.81	0.10	4.6	1.217	3.539	2.786	0.457
69	−0.94	0.11	8.3	1.404	3.504	2.841	0.382
70	−0.96	0.11	6.2	1.516	3.440	2.936	0.454
71	−1.73	0.09	13.4	0.904	2.302	1.858	0.185
72	−0.71	0.10	3.1	1.510	3.581	2.893	0.422

Table A.2 – continued from previous page

Star ID	$[\mathrm{Fe/H}]_{\mathrm{CaT}}$	$\sigma[\mathrm{Fe/H}]_{\mathrm{CaT}}$	age [Gyr]	$\mathrm{EW}_{\mathrm{CaT1}}$	$\mathrm{EW}_{\mathrm{CaT2}}$	$\mathrm{EW}_{\mathrm{CaT3}}$	$\mathrm{EW}_{\mathrm{MgI}}$
73	−0.88	0.10	6.5	1.426	3.459	2.744	0.396
74	−1.43	0.10	12.3	1.161	2.899	2.251	0.310
75	−2.08	0.09	11.6	0.913	2.146	1.781	0.266
76	−1.89	0.08	11.1	1.252	2.058	1.663	0.224
77	−1.02	0.09	5.7	1.216	3.243	2.517	0.345
78	−1.39	0.10	12.6	1.125	3.021	2.403	0.317
79	−1.96	0.09	11.2	0.905	2.288	1.840	0.275
81	−1.91	0.09	–	0.942	2.344	1.671	0.309
82	−2.97	0.08	–	0.504	1.148	0.910	0.150
83	−0.90	0.11	6.1	1.448	3.521	2.830	0.417
84	−0.85	0.11	5.9	1.445	3.549	2.943	0.409
85	−1.05	0.11	2.3	1.300	3.446	2.727	0.431
86	−1.64	0.10	11.0	1.074	2.661	2.253	0.287
87	−0.86	0.11	6.3	1.445	3.695	2.907	0.426
89	−1.58	0.10	10.9	1.084	2.679	2.248	0.299
90	−0.88	0.10	4.2	1.320	3.361	2.771	0.391
91	−0.91	0.10	4.2	1.380	3.396	2.879	0.428
92	−1.25	0.11	13.2	1.442	2.754	2.585	0.449
96	−1.48	0.10	10.8	1.123	2.898	2.339	0.331
98	−1.81	0.09	12.7	0.938	2.507	1.671	0.234
100	−0.97	0.10	8.0	1.359	3.399	2.638	0.348
101	−0.91	0.10	2.8	1.167	3.291	2.741	0.339
102	−1.12	0.10	–	1.222	3.236	2.541	0.361
103	−2.16	0.08	–	0.780	1.999	1.582	0.290
104	−1.57	0.09	3.6	1.038	2.570	2.087	0.280
105	−1.50	0.10	12.0	1.164	2.921	2.298	0.339
107	−2.34	0.13	–	0.666	1.381	1.763	0.234
108	−0.81	0.11	4.6	1.410	3.562	3.003	0.473
109	−1.19	0.15	5.4	0.813	3.110	2.460	0.355
110	−0.94	0.10	4.9	1.478	3.356	2.827	0.411
111	−0.91	0.11	4.4	1.382	3.426	3.015	0.434
112	−1.48	0.10	11.9	1.231	2.838	2.291	0.296
114	−2.46	0.08	–	0.673	1.719	1.068	0.126
115	−0.67	0.11	4.0	1.246	3.588	2.748	0.406
126	−1.12	0.10	2.9	1.068	3.167	2.504	0.288
127	−1.93	0.10	2.5	0.682	1.984	1.824	0.162
128	−1.85	0.09	7.0	0.145	2.208	1.623	0.161
129	−2.52	0.08	–	0.534	1.258	1.277	0.066
130	−1.77	0.09	13.7	–	2.491	1.940	0.306
133	−0.87	0.11	5.6	1.488	3.576	2.918	0.420
135	−1.34	0.10	–	0.242	2.747	2.154	0.225
136	−0.89	0.11	7.3	1.274	3.418	2.729	0.459
137	−2.23	0.08	–	–	1.841	1.411	0.279
138	−1.40	0.10	5.3	1.086	2.903	2.201	0.333
139	−0.92	0.11	8.0	1.381	3.538	2.711	0.467
142	−1.19	0.10	13.6	1.154	3.074	2.617	0.376
143	−0.95	0.10	2.5	1.171	3.009	2.540	0.345
145	−2.62	0.11	–	–	1.422	1.138	0.169
146	−1.23	0.09	11.4	1.108	2.890	2.407	0.344
147	−0.94	0.09	3.0	1.229	3.074	2.691	0.306
148	−0.94	0.11	5.2	1.336	3.456	2.892	0.406
149	−1.71	0.09	–	1.053	2.456	1.645	0.281
150	−1.83	0.10	8.4	0.911	2.453	2.024	0.291
151	−1.23	0.10	7.2	0.419	2.793	2.550	0.288
152	−0.77	0.11	1.9	1.378	3.470	3.014	0.414
153	−0.91	0.11	4.5	1.169	3.247	2.853	0.399
154	−0.99	0.12	8.5	1.310	3.243	2.789	0.392
155	−1.03	0.10	11.5	1.337	3.381	2.358	0.376
157	−1.51	0.10	14.3	1.100	2.720	2.242	0.298
158	−1.63	0.10	13.3	0.920	2.258	2.315	0.223
160	−1.54	0.09	11.2	1.061	2.681	2.181	0.263
161	−1.13	0.09	1.3	1.124	3.001	2.259	0.349
162	−1.14	0.11	–	1.365	2.999	2.809	0.452
163	−0.97	0.10	7.8	1.235	3.523	2.162	0.365
164	−2.35	0.08	–	0.656	1.734	1.396	0.193
165	−0.92	0.11	–	1.172	3.622	2.843	0.455
167	−0.84	0.10	2.8	1.414	3.424	2.683	0.370

Table A.2 – continued from previous page

Star ID	$[\mathrm{Fe/H}]_{\mathrm{CaT}}$	$\sigma[\mathrm{Fe/H}]_{\mathrm{CaT}}$	age [Gyr]	$\mathrm{EW}_{\mathrm{CaT1}}$	$\mathrm{EW}_{\mathrm{CaT2}}$	$\mathrm{EW}_{\mathrm{CaT3}}$	$\mathrm{EW}_{\mathrm{Mg\,I}}$
168	−1.88	0.08	6.7	0.842	2.111	1.741	0.244
169	−1.06	–	10.7	1.352	3.186	2.688	0.448
170	−1.91	0.09	–	0.786	1.933	1.839	0.246
171	−0.98	0.10	6.5	1.436	3.259	2.144	0.249
173	−1.97	0.09	–	0.328	2.049	1.782	0.281
174	−0.76	–	–	1.154	3.264	2.793	0.271
175	−1.38	0.08	8.1	1.041	2.705	2.172	0.311
176	−1.49	0.13	9.4	0.461	2.220	2.547	0.391
177	−2.59	0.09	–	0.299	1.400	1.237	0.192
178	−1.62	0.09	–	1.104	2.671	2.098	0.310
179	−0.80	0.09	3.7	1.197	3.282	2.658	0.391
180	−0.91	0.09	5.3	1.210	3.364	2.641	0.443
181	−2.27	0.08	–	0.750	1.910	1.476	0.227
182	−1.04	0.10	7.1	1.341	3.241	2.721	0.410
183	−1.46	0.10	13.4	1.479	2.690	2.293	0.305
184	−1.04	0.11	–	1.388	3.372	2.476	0.378
185	−2.37	0.07	–	0.638	1.506	1.325	0.176
186	−0.88	0.09	6.9	1.424	3.207	2.741	0.398
187	−1.50	0.09	7.0	1.089	2.349	2.206	0.307
188	−1.08	0.09	4.9	1.291	3.031	2.270	0.308
189	−0.70	0.11	1.6	1.487	3.372	3.042	0.434
190	−2.00	0.09	4.8	0.851	2.108	1.719	0.165
191	−0.99	0.10	4.1	1.070	3.181	2.694	0.392
192	−0.77	0.11	–	1.507	3.460	2.898	0.408
193	−0.66	0.11	2.5	1.514	3.743	3.071	0.465
194	−1.08	0.10	–	0.867	2.865	2.427	0.315
195	−1.51	0.11	–	1.125	2.718	1.987	0.304
197	−1.06	0.11	6.1	0.994	3.324	2.553	0.383
200	−1.35	0.11	–	1.056	2.810	2.074	0.273
204	−0.55	0.11	1.8	1.432	3.855	2.977	0.387
205	−1.40	0.10	7.0	1.096	2.707	2.342	0.295
207	−1.89	0.09	10.3	0.905	2.279	1.870	0.253
208	−0.87	0.11	–	1.458	3.714	2.809	0.433
209	−2.12	0.09	–	0.639	1.803	1.467	0.252
210	−1.61	0.09	11.1	1.046	2.717	2.081	0.297
211	−1.13	0.10	4.3	1.132	3.054	2.655	0.348
212	−1.12	0.10	10.7	1.220	3.205	2.458	0.340
213	−1.24	0.09	6.7	1.079	2.988	2.321	0.313
214	−0.89	0.11	3.3	1.326	3.441	2.924	0.409
215	−1.82	0.09	11.0	0.284	2.318	1.893	0.262
216	−2.11	0.09	10.0	–	1.880	1.502	0.164
217	−2.65	0.09	–	0.760	1.397	1.058	0.183
219	−1.17	0.10	–	1.123	3.122	2.356	0.335
221	−2.48	–	–	1.130	1.255	1.596	0.163
222	−1.28	0.10	8.7	1.144	2.806	2.379	0.352
224	−0.88	0.11	4.0	1.382	3.559	2.790	0.418
225	−2.11	0.10	–	0.103	1.829	1.570	0.151
227	−0.88	0.09	2.7	1.331	3.123	2.629	0.337
228	−1.23	–	8.6	1.198	2.950	2.186	0.323
229	−0.81	0.10	3.6	1.368	3.594	2.775	0.422
230	−1.17	0.11	7.7	0.103	3.001	2.140	0.334
231	−0.98	0.10	3.1	1.639	2.970	2.648	0.331
232	−1.09	0.11	2.7	1.386	3.123	2.565	0.366
233	−1.02	0.10	7.1	1.556	3.223	2.737	0.360
234	−1.08	0.10	3.7	1.163	3.323	2.131	0.346
235	−2.30	0.08	4.5	0.593	1.643	1.377	0.184
236	−1.94	–	10.3	0.979	2.181	1.822	0.277
237	−1.68	0.09	5.8	1.207	2.660	1.865	0.341
238	−0.87	0.10	2.7	1.403	3.391	2.716	0.386
239	−2.18	0.08	8.5	0.623	1.815	1.363	0.193
240	−2.36	0.08	–	0.737	1.478	1.503	0.191
241	−1.85	0.08	3.5	0.956	2.042	1.855	0.202
242	−1.09	2.14	–	0.331	2.991	2.466	–
243	−1.24	0.09	–	0.974	2.974	2.135	0.311
244	−2.41	0.09	9.5	0.698	1.583	1.407	0.232
245	−1.10	0.09	9.3	1.126	2.936	2.385	0.428
248	−0.88	0.12	4.8	1.400	3.207	2.714	0.404

Table A.2 – continued from previous page

Star ID	$[\mathrm{Fe/H}]_{\mathrm{CaT}}$	$\sigma[\mathrm{Fe/H}]_{\mathrm{CaT}}$	age [Gyr]	$\mathrm{EW}_{\mathrm{CaT1}}$	$\mathrm{EW}_{\mathrm{CaT2}}$	$\mathrm{EW}_{\mathrm{CaT3}}$	$\mathrm{EW}_{\mathrm{MgI}}$
249	−0.97	0.09	3.1	0.504	3.186	2.490	0.323
250	−1.10	0.11	–	0.904	2.716	2.402	0.233
251	−2.50	0.09	–	–	1.421	1.047	0.178
252	−2.32	0.08	–	0.405	1.655	1.402	0.235
253	−1.86	0.08	–	1.037	2.232	1.809	0.202
255	−2.14	0.09	11.9	0.704	1.982	1.416	0.237
256	−1.76	0.08	12.9	0.800	2.270	1.861	0.278
257	−0.91	0.10	4.7	1.446	3.431	2.797	0.377
258	−1.73	0.08	10.7	0.844	2.345	1.859	0.288
259	−1.24	0.10	8.2	1.243	3.048	2.453	0.321
260	−2.32	0.08	6.3	0.612	1.643	1.358	0.234
261	−1.99	0.08	8.5	0.857	2.131	1.639	0.206
262	−1.93	0.08	7.2	0.799	2.225	1.733	0.239
263	−1.03	0.10	5.8	1.298	3.318	2.664	0.345
264	−0.91	0.10	4.0	1.207	3.412	2.762	0.366
265	−1.20	0.10	9.5	1.317	2.273	2.706	0.348
266	−1.73	0.10	4.5	0.071	2.241	1.783	0.255
267	−1.19	0.10	–	1.210	3.317	2.164	0.311
268	−0.81	0.10	3.3	1.445	3.563	2.863	0.431
270	−1.20	0.09	13.5	1.078	2.902	2.299	0.363
274	−1.13	0.10	8.6	1.330	3.155	2.263	0.352
275	−2.22	0.10	5.6	0.173	1.831	1.278	0.175
276	−1.78	0.09	–	0.862	2.175	1.839	0.170
277	−1.48	0.09	9.4	1.150	2.729	2.091	0.288
279	−0.88	0.10	1.3	1.322	3.394	2.606	0.316
280	−1.37	0.09	11.9	1.059	2.822	2.329	0.268
281	−1.86	0.08	6.3	0.733	2.177	1.704	0.218
282	−1.98	0.09	6.6	0.825	2.197	1.790	0.249
284	−1.44	0.09	–	0.823	2.614	2.030	0.292
285	−0.88	0.10	3.7	1.508	3.466	2.783	0.367
287	−2.57	0.19	–	0.609	1.394	1.009	0.116
288	−2.05	0.10	–	0.454	1.955	1.428	0.300
289	−1.56	0.11	10.6	1.059	2.261	2.317	0.324
290	−2.36	0.08	8.8	0.011	1.660	1.448	0.231
291	−1.19	0.09	6.9	1.090	2.914	2.407	0.320
294	−2.16	0.08	7.2	0.776	1.639	1.569	0.219
295	−1.67	0.09	9.0	1.041	2.502	2.097	0.274
297	−2.41	0.11	–	0.004	1.567	1.086	0.294
298	−2.46	0.08	–	0.502	1.411	1.232	0.139
299	−0.80	0.10	2.1	1.231	2.991	2.703	0.211
300	−1.07	0.10	6.9	1.169	2.879	2.466	0.328
301	−2.43	0.08	5.1	0.663	1.443	1.387	0.200
302	−2.37	0.12	10.0	0.568	1.263	1.440	0.136
303	−1.56	0.13	–	0.930	2.388	1.868	0.254
304	−0.98	0.10	–	1.129	3.016	2.754	0.289
311	−2.34	0.10	–	–	1.853	1.526	0.218
312	−2.22	0.10	1.7	0.718	1.348	1.620	0.188
313	−2.94	0.09	–	0.393	1.027	0.804	0.087
316	−1.58	0.08	3.1	0.788	2.375	2.026	0.273
317	−2.44	0.07	–	0.694	1.598	1.175	0.262
318	−2.09	0.18	1.6	–	1.681	1.507	0.114
319	−1.53	0.13	9.3	1.097	2.413	1.934	0.132
320	−1.55	0.10	5.6	0.964	2.296	2.051	0.312
321	−0.89	0.11	3.4	1.435	3.635	2.829	0.443
322	−0.68	0.12	1.3	1.631	3.569	2.916	0.345
323	−1.25	0.11	8.9	–	2.644	2.377	0.363
324	−1.65	0.10	7.3	1.066	2.683	2.167	0.362
325	−1.83	0.10	6.5	1.095	2.553	1.774	0.260
326	−1.94	0.10	12.0	1.089	2.548	1.701	0.286
328	−2.21	0.09	4.9	–	1.984	1.397	0.115
332	−1.36	0.11	7.7	1.255	3.286	2.242	0.344
333	−1.90	0.09	11.7	1.356	2.026	1.929	0.298
334	−2.40	0.09	12.3	0.545	1.684	1.346	0.220
335	−2.44	0.09	–	0.125	1.776	1.171	0.195
336	−1.70	0.10	7.9	0.933	2.500	1.899	0.279
337	−0.93	0.11	2.3	1.427	3.420	2.729	0.411
339	−0.84	0.11	3.1	1.322	3.504	2.898	0.421

Table A.2 – continued from previous page

Star ID	$[\mathrm{Fe/H}]_{\mathrm{CaT}}$	$\sigma[\mathrm{Fe/H}]_{\mathrm{CaT}}$	age [Gyr]	$\mathrm{EW}_{\mathrm{CaT1}}$	$\mathrm{EW}_{\mathrm{CaT2}}$	$\mathrm{EW}_{\mathrm{CaT3}}$	$\mathrm{EW}_{\mathrm{Mg\,I}}$
340	−0.95	–	2.5	1.480	3.594	2.741	0.376
341	−0.86	0.11	3.8	1.488	3.540	2.824	0.407
342	−2.63	0.08	–	0.674	1.461	1.256	0.243
343	−0.90	0.11	3.7	1.413	3.564	2.893	0.441
344	−1.42	0.10	11.4	1.134	2.860	2.301	0.352
345	−1.34	0.10	6.2	1.078	2.783	2.459	0.324
347	−1.20	0.10	5.1	1.350	3.112	2.595	0.326
348	−1.36	0.11	7.7	1.244	3.152	2.371	0.365
349	−2.18	0.10	10.6	0.917	2.091	1.628	0.253
350	−0.87	0.11	3.4	1.492	3.592	2.841	0.410
351	−1.49	0.09	8.7	1.249	2.713	2.041	0.237
352	−0.87	0.10	3.6	1.425	3.363	2.611	0.328
353	−1.45	0.10	–	0.795	2.609	2.230	0.283
354	−1.44	–	11.0	0.964	2.305	2.304	0.356
355	−0.95	0.10	4.3	1.461	3.374	2.673	0.334
356	−2.01	0.09	–	1.113	2.191	1.751	0.217
357	−0.95	0.10	2.8	1.295	3.098	2.594	0.342
358	−1.05	0.11	7.7	1.285	3.401	2.694	0.395
359	−1.00	0.10	2.6	1.273	3.339	2.587	0.380
360	−0.84	0.12	3.0	1.522	3.740	2.936	0.421
361	−0.96	0.11	1.3	1.474	3.277	2.825	0.333
362	−0.76	0.12	3.0	1.543	3.803	2.993	0.459
363	−2.43	0.08	5.0	0.594	1.676	1.415	0.179
364	−1.45	0.09	–	1.089	2.657	2.245	0.306
365	−1.49	0.09	7.4	1.027	2.784	2.184	0.344
367	−1.04	0.09	5.2	1.223	3.107	2.602	0.392
368	−0.92	0.10	2.3	1.353	3.465	2.632	0.398
369	−2.30	0.08	8.6	0.776	1.570	1.599	0.234
371	−1.27	0.10	6.8	1.242	3.130	2.480	0.337
372	−0.89	0.11	4.7	1.472	3.571	2.908	0.420
374	−1.49	0.09	7.5	1.000	2.716	2.198	0.325
375	−2.07	0.09	6.3	0.744	1.846	1.587	0.182
377	−1.90	0.09	9.5	0.357	2.089	1.702	0.249
378	−2.10	0.14	8.2	0.841	1.922	1.491	0.215
379	−0.97	0.10	1.6	1.106	3.008	2.522	0.342
380	−1.03	0.11	–	1.298	3.389	2.727	0.404
381	−0.59	0.11	–	1.368	3.774	3.113	0.409
382	−1.07	0.10	3.4	1.073	2.977	2.397	0.239
385	−1.74	0.09	12.3	0.763	2.169	2.064	0.152
386	−1.38	–	–	1.154	2.922	2.348	0.343
387	−1.77	–	10.3	1.000	2.322	2.048	0.337
388	−0.76	0.11	1.9	1.444	3.678	2.921	0.395
389	−0.95	0.11	4.9	1.453	3.513	2.862	0.432
390	−1.89	0.09	–	1.167	2.315	1.774	0.247
391	−0.86	0.12	4.3	1.595	3.773	2.860	0.460
392	−1.34	0.09	7.1	0.986	2.750	2.341	0.391
393	−1.31	0.11	–	1.305	2.949	2.601	0.350
394	−2.04	0.08	9.2	0.733	2.067	1.631	0.206
395	−2.03	0.12	–	0.962	1.810	1.957	0.152
396	−0.95	0.12	–	1.360	3.191	2.889	0.366
397	−1.77	0.09	10.4	1.007	2.484	2.061	0.306
398	−0.95	0.10	2.5	1.212	3.306	2.676	0.250
399	−0.83	0.11	2.9	1.592	3.589	2.981	0.372
400	−2.19	0.07	–	0.809	1.735	1.394	0.201
401	−1.82	0.08	8.1	0.844	2.058	1.794	0.172
402	−1.18	0.10	4.7	1.165	3.055	2.537	0.340
406	−2.60	0.08	–	0.640	1.322	1.222	0.271
407	−1.55	0.10	12.4	1.156	2.684	2.240	0.271
408	−1.27	0.10	6.2	0.513	2.919	2.249	0.288
409	−2.28	0.08	12.3	0.622	1.768	1.335	0.237
411	−1.55	0.09	10.7	1.115	2.566	2.257	0.340
412	−2.05	0.09	9.4	0.800	1.861	1.662	0.227
413	−0.97	0.11	–	0.271	3.564	2.693	0.364
414	−0.48	0.10	–	1.619	3.773	2.941	0.281
415	−2.62	0.08	–	0.551	1.446	1.141	0.131
416	−1.15	0.08	12.3	1.021	2.926	2.315	0.320
417	−1.57	0.10	4.9	0.807	2.352	2.088	0.263

Table A.2 – continued from previous page

Star ID	$[\mathrm{Fe/H}]_{\mathrm{CaT}}$	$\sigma[\mathrm{Fe/H}]_{\mathrm{CaT}}$	age [Gyr]	$\mathrm{EW}_{\mathrm{CaT1}}$	$\mathrm{EW}_{\mathrm{CaT2}}$	$\mathrm{EW}_{\mathrm{CaT3}}$	$\mathrm{EW}_{\mathrm{MgI}}$
418	−0.82	0.10	1.7	1.287	3.418	2.717	0.375
419	−2.02	0.15	9.3	0.667	1.775	1.682	0.260
420	−2.76	0.11	–	0.592	1.308	1.038	0.173
422	−2.33	0.08	8.9	0.569	1.540	1.300	0.184
424	−2.16	0.08	3.7	–	2.006	1.553	0.196
425	−1.80	0.18	–	–	1.545	2.318	0.268
428	−1.19	0.10	5.2	0.474	3.181	2.551	0.410
430	−1.89	0.09	7.7	0.783	1.876	1.826	0.211
431	−1.09	0.10	5.2	1.229	3.062	2.592	0.365

Table A.3: Chemodynamical parameters for field stars and GC members in Fornax – Fe-metallicities, α-abundances. $[\mathrm{Fe/H}]_{\mathrm{HR}}$ refers to the metallicities derived from individual Fe absorption lines. The uncertainties for individual abundances give the statistical error discussed in Hendricks et al. (2014).Column 10 indicates the quality of the spectral fit in terms of a normalized χ^2 value.

Star ID	$[\mathrm{Fe/H}]_{\mathrm{HR}}$	$\sigma[\mathrm{Fe/H}]_{\mathrm{HR}}$	[Mg/Fe]	σ [Mg/Fe]	[Si/Fe]	σ [Si/Fe]	[Ti/Fe]	σ [Ti/Fe]	χ^2
2	−1.57	0.04	–	–	–	–	0.00	0.05	1.90
3	−1.39	0.04	–	–	0.02	0.06	0.39	0.05	2.00
4	−2.22	0.05	–	–	–	–	–	–	2.20
5	−1.36	0.04	–	–	–	–	–	–	2.47
6	−0.95	0.03	–	–	–	–	0.09	0.04	1.70
7	−1.51	0.04	–	–	–	–	−0.02	0.05	2.60
8	−1.34	0.04	0.25	0.06	–	–	–	–	1.69
10	−2.20	0.05	–	–	–	–	–	–	1.71
11	−1.40	0.04	−0.01	0.06	–	–	0.18	0.05	1.83
13	−1.03	0.03	−0.15	0.06	−0.04	0.04	–	–	1.78
14	−0.96	0.03	–	–	–	–	0.33	0.04	1.61
15	−1.94	0.05	–	–	0.16	0.09	–	–	2.83
17	–	–	–	–	–	–	–	–	–
19	−0.91	0.03	−0.25	0.06	−0.01	0.04	0.05	0.04	1.86
20	−1.01	0.03	–	–	−0.06	0.04	–	–	1.49
21	−1.02	0.03	–	–	–	–	0.32	0.04	1.69
22	−1.52	0.04	0.27	0.06	0.07	0.07	0.19	0.05	2.10
23	−0.99	0.03	−0.28	0.06	−0.12	0.04	0.10	0.04	1.84
24	−1.61	0.04	–	–	–	–	–	–	2.33
25	–	–	–	–	–	–	–	–	–
26	−1.80	0.05	0.33	0.08	–	–	−0.01	0.06	1.97
27	−2.56	0.06	–	–	–	–	–	–	2.14
28	−2.47	0.06	–	–	–	–	–	–	1.50
29	−1.05	0.03	−0.11	0.06	0.04	0.04	−0.18	0.04	1.72
30	−1.77	0.05	–	–	–	–	–	–	2.02
31	−0.95	0.03	−0.17	0.06	−0.09	0.04	−0.29	0.04	1.53
32	−0.99	0.03	–	–	–	–	−0.14	0.04	1.59
33	−0.78	0.03	–	–	–	–	−0.05	0.04	1.65
34	−0.90	0.03	−0.18	0.06	−0.05	0.04	−0.12	0.04	1.51
35	−0.86	0.03	−0.24	0.06	–	–	0.23	0.04	1.65
36	−1.76	0.05	–	–	0.00	0.08	0.14	0.06	1.79
37	−1.70	0.04	0.15	0.07	−0.09	0.08	0.05	0.05	1.94
38	−2.11	0.05	–	–	–	–	–	–	1.66
39	−0.92	0.03	–	–	−0.20	0.04	0.15	0.04	2.00
40	−6.83	–	–	–	–	–	–	–	9.99
41	−1.13	0.03	–	–	–	–	–	–	1.91
43	−1.86	0.05	–	–	–	–	–	–	1.67
45	−1.12	0.03	0.01	0.06	0.13	0.05	−0.03	0.04	2.14
46	−2.20	0.05	–	–	0.06	0.11	–	–	1.53
47	−2.28	0.06	–	–	–	–	–	–	1.82
49	–	–	–	–	–	–	–	–	–
50	−0.99	0.03	−0.18	0.06	–	–	–	–	1.66
51	−1.56	0.04	–	–	−0.04	0.07	−0.28	0.05	1.90
52	−0.90	0.03	−0.25	0.06	−0.22	0.04	–	–	1.85
53	−0.87	0.03	−0.24	0.06	−0.24	0.04	0.39	0.04	2.07
54	−1.28	0.04	–	–	–	–	−0.07	0.05	1.57
55	−0.90	0.03	–	–	−0.07	0.04	–	–	1.84
56	−1.18	0.03	0.03	0.06	−0.04	0.05	−0.22	0.04	2.16
57	−1.06	0.03	–	–	–	–	0.59	0.04	1.85
59	−1.09	0.03	0.10	0.06	0.02	0.05	−0.29	0.04	1.63
60	−0.88	0.03	–	–	−0.17	0.04	–	–	1.64
61	−1.29	0.04	−0.11	0.06	0.00	0.06	–	–	1.71
62	−2.44	0.06	–	–	–	–	–	–	2.48
63	−0.77	0.03	0.05	0.06	0.03	0.04	−0.26	0.04	1.68
64	−1.00	0.03	−0.01	0.06	−0.01	0.04	–	–	1.73
65	−0.94	0.03	−0.02	0.06	−0.24	0.04	0.30	0.04	1.87
66	−1.38	0.04	–	–	–	–	0.42	0.05	1.77
67	–	–	–	–	–	–	–	–	–
68	−0.87	0.03	−0.21	0.06	−0.19	0.04	–	–	1.69
69	−0.94	0.03	−0.24	0.06	−0.20	0.04	–	–	1.88
70	−0.84	0.03	−0.19	0.06	–	–	−0.19	0.04	1.72
71	−1.71	0.04	–	–	–	–	–	–	1.83

Table A.3 – continued from previous page

Star ID	$[\mathrm{Fe/H}]_{\mathrm{HR}}$	$\sigma[\mathrm{Fe/H}]_{\mathrm{HR}}$	[Mg/Fe]	σ [Mg/Fe]	[Si/Fe]	σ [Si/Fe]	[Ti/Fe]	σ [Ti/Fe]	χ^2
72	−0.85	0.03	−0.15	0.06	−0.20	0.04	−0.06	0.04	1.92
73	−0.88	0.03	−0.20	0.06	−0.23	0.04	0.00	0.04	1.70
74	−1.33	0.04	–	–	0.07	0.06	–	–	1.66
75	–	–	–	–	–	–	–	–	9.99
76	−2.22	0.05	–	–	–	–	–	–	2.05
77	−1.13	0.03	−0.19	0.06	–	–	−0.02	0.04	1.86
78	−1.22	0.03	–	–	−0.25	0.05	−0.29	0.04	1.59
79	−1.97	0.05	0.40	0.09	0.33	0.09	0.54	0.06	1.66
81	−1.17	0.03	–	–	–	–	–	–	1.53
82	−1.75	0.04	–	–	–	–	–	–	4.21
83	−0.86	0.03	−0.17	0.06	−0.14	0.04	–	–	1.64
84	−1.06	0.03	0.01	0.06	–	–	−0.06	0.04	1.65
85	−0.98	0.03	−0.11	0.06	−0.04	0.04	0.07	0.04	1.80
86	−1.60	0.04	−0.12	0.07	–	–	−0.17	0.05	2.01
87	−0.73	0.03	–	–	–	–	−0.06	0.03	1.67
89	−1.68	0.04	0.23	0.07	0.16	0.08	0.08	0.05	1.53
90	−0.86	0.03	−0.23	0.06	–	–	−0.23	0.04	1.68
91	−1.01	0.03	−0.13	0.06	−0.05	0.04	−0.09	0.04	1.80
92	–	–	–	–	–	–	–	–	–
96	−1.58	0.04	−0.17	0.06	0.10	0.07	0.01	0.05	1.65
98	−1.60	0.04	–	–	0.09	0.07	–	–	1.75
100	−0.97	0.03	−0.01	0.06	−0.12	0.04	0.00	0.04	1.62
101	−0.91	0.03	0.00	0.06	−0.29	0.04	−0.01	0.04	2.07
102	−1.19	0.03	−0.06	0.06	0.03	0.05	–	–	1.65
103	−2.04	0.05	–	–	–	–	–	–	1.75
104	−1.14	0.03	–	–	–	–	–	–	1.99
105	−1.35	0.04	−0.10	0.06	−0.12	0.06	−0.07	0.05	1.63
107	−1.97	0.05	–	–	–	–	–	–	2.01
108	−0.89	0.03	−0.10	0.06	−0.25	0.04	−0.06	0.04	1.51
109	−1.15	0.03	−0.08	0.06	0.07	0.05	−0.04	0.04	2.06
110	−0.81	0.03	−0.26	0.06	–	–	−0.13	0.04	1.85
111	−0.90	0.03	−0.24	0.06	–	–	−0.27	0.04	1.57
112	−1.44	0.04	–	–	0.00	0.07	−0.05	0.05	1.58
114	−2.48	0.06	–	–	–	–	–	–	1.95
115	−0.60	0.03	–	–	−0.11	0.04	0.04	0.03	2.01
126	−1.13	0.03	−0.25	0.06	–	–	0.44	0.04	2.40
127	−1.53	0.04	–	–	–	–	–	–	2.15
128	−2.01	0.05	–	–	–	–	–	–	1.83
129	−2.50	0.06	–	–	–	–	–	–	2.57
130	−2.10	0.05	–	–	0.14	0.10	–	–	2.11
133	−0.85	0.03	−0.14	0.06	–	–	−0.20	0.04	2.29
135	−1.07	0.03	–	–	–	–	–	–	1.52
136	−0.85	0.03	−0.27	0.06	−0.16	0.04	0.09	0.04	2.56
137	−2.12	0.05	–	–	–	–	–	–	2.01
138	−1.49	0.04	0.19	0.06	0.17	0.07	0.15	0.05	2.24
139	−0.89	0.03	−0.12	0.06	−0.17	0.04	−0.12	0.04	1.92
142	−0.99	0.03	−0.28	0.06	–	–	−0.26	0.04	2.05
143	−1.17	0.03	–	–	–	–	–	–	2.71
145	−2.57	0.06	–	–	–	–	–	–	2.85
146	−0.97	0.03	–	–	–	–	–	–	1.73
147	−1.08	0.03	–	–	–	–	–	–	1.64
148	−0.82	0.03	–	–	–	–	0.05	0.04	1.70
149	−1.33	0.04	–	–	–	–	–	–	2.31
150	−2.05	0.05	0.42	0.10	0.30	0.09	–	–	1.94
151	−1.49	0.04	0.11	0.06	–	–	–	–	2.17
152	−0.90	0.03	–	–	–	–	0.07	0.04	1.30
153	−0.83	0.03	−0.27	0.06	−0.25	0.04	0.01	0.04	1.35
154	−0.96	0.03	–	–	−0.20	0.04	–	–	1.98
155	−1.02	0.03	–	–	−0.25	0.04	−0.11	0.04	1.99
157	−1.41	0.04	–	–	−0.08	0.06	–	–	2.15
158	−1.57	0.04	–	–	0.01	0.07	0.50	0.05	1.87
160	−1.53	0.04	–	–	–	–	–	–	2.11
161	−1.57	0.04	−0.04	0.06	0.34	0.07	–	–	2.53
162	–	–	–	–	–	–	–	–	–
163	–	–	–	–	–	–	–	–	–
164	−2.46	0.06	–	–	–	–	–	–	2.11
165	−0.83	0.03	–	–	−0.16	0.04	–	–	2.10

Table A.3 – continued from previous page

Star ID	$[Fe/H]_{HR}$	$\sigma[Fe/H]_{HR}$	[Mg/Fe]	σ [Mg/Fe]	[Si/Fe]	σ [Si/Fe]	[Ti/Fe]	σ [Ti/Fe]	χ^2
167	−1.07	0.03	−0.10	0.06	0.16	0.04	−0.13	0.04	1.60
168	−1.64	0.04	–	–	0.20	0.08	–	–	2.34
169	–	–	–	–	–	–	–	–	–
170	−2.09	0.05	–	–	–	–	–	–	1.97
171	–	–	–	–	–	–	–	–	–
173	−2.43	0.06	–	–	–	–	–	–	1.74
174	–	–	–	–	–	–	–	–	–
175	−1.43	0.04	0.07	0.06	−0.10	0.07	0.03	0.05	2.78
176	–	–	–	–	–	–	–	–	–
177	−2.46	0.06	–	–	–	–	–	–	2.34
178	−1.56	0.04	0.18	0.06	−0.07	0.07	0.06	0.05	1.86
179	−1.08	0.03	–	–	–	–	−0.00	0.04	1.97
180	−1.18	0.03	−0.12	0.06	0.04	0.05	−0.25	0.04	1.90
181	−2.39	0.06	–	–	–	–	–	–	2.33
182	−1.01	0.03	−0.03	0.06	−0.03	0.04	−0.24	0.04	2.15
183	−1.37	0.04	−0.13	0.06	0.04	0.06	–	–	1.95
184	–	–	–	–	–	–	–	–	–
185	−1.83	0.05	–	–	–	–	–	–	2.95
186	−1.11	0.03	0.07	0.06	0.12	0.05	−0.22	0.04	2.84
187	−1.00	0.03	−0.09	0.06	–	–	–	–	2.47
188	−0.57	0.03	–	–	–	–	–	–	1.79
189	−0.84	0.03	−0.02	0.06	−0.26	0.04	0.05	0.04	2.01
190	−1.71	0.04	0.02	0.07	–	–	–	–	2.95
191	−0.97	0.03	–	–	−0.12	0.04	0.04	0.04	2.26
192	−0.90	0.03	−0.13	0.06	–	–	−0.04	0.04	2.34
193	−0.74	0.03	−0.30	0.05	−0.14	0.04	0.04	0.03	2.21
194	−0.29	0.03	–	–	–	–	–	–	2.08
195	−1.24	0.03	−0.22	0.06	−0.30	0.05	0.00	0.04	2.39
197	−1.09	0.03	−0.03	0.06	−0.24	0.05	0.10	0.04	2.29
200	−1.08	0.03	–	–	–	–	–	–	2.52
204	−2.49	0.06	–	–	–	–	–	–	1.99
205	−1.38	0.04	0.04	0.06	0.09	0.06	0.03	0.05	2.33
207	−2.25	0.06	0.32	0.14	0.29	0.11	–	–	1.92
208	−0.91	0.03	−0.16	0.06	−0.21	0.04	–	–	1.93
209	–	–	–	–	–	–	–	–	2.67
210	−1.66	0.04	0.34	0.07	0.09	0.08	0.19	0.05	2.36
211	−1.06	0.03	–	–	–	–	−0.02	0.04	2.31
212	−0.89	0.03	–	–	–	–	–	–	1.84
213	−1.27	0.04	–	–	−0.18	0.06	–	–	2.17
214	−1.11	0.03	−0.04	0.06	0.10	0.05	–	–	2.44
215	−1.36	0.04	–	–	–	–	–	–	2.23
216	−2.31	0.06	–	–	–	–	–	–	2.61
217	−0.61	0.03	–	–	–	–	–	–	2.51
219	−1.16	0.03	–	–	−0.00	0.05	–	–	1.90
221	–	–	–	–	–	–	–	–	–
222	−1.47	0.04	−0.09	0.06	−0.03	0.07	–	–	2.00
224	−1.04	0.03	−0.26	0.06	−0.17	0.04	0.11	0.04	1.81
225	−1.25	0.04	–	–	–	–	–	–	2.66
227	−1.39	0.04	−0.05	0.06	0.24	0.06	−0.23	0.05	1.40
228	–	–	–	–	–	–	–	–	–
229	−0.88	0.03	−0.26	0.06	−0.29	0.04	−0.20	0.04	1.83
230	−1.12	0.03	–	–	–	–	–	–	1.84
231	−1.12	0.03	0.21	0.06	−0.06	0.05	0.33	0.04	4.57
232	−1.03	0.03	−0.05	0.06	−0.07	0.04	0.24	0.04	2.12
233	−1.04	0.03	−0.29	0.06	−0.22	0.04	0.15	0.04	2.58
234	−0.99	0.03	0.01	0.06	−0.08	0.04	0.10	0.04	2.08
235	−2.49	0.06	–	–	–	–	–	–	2.82
236	–	–	–	–	–	–	–	–	–
237	−1.50	0.04	–	–	−0.13	0.07	–	–	2.74
238	−0.90	0.03	−0.14	0.06	−0.16	0.04	0.12	0.04	2.02
239	−2.31	0.06	–	–	–	–	–	–	2.97
240	−2.33	0.06	–	–	–	–	–	–	2.58
241	−2.03	0.05	–	–	–	–	–	–	1.67
242	−1.21	0.03	−0.16	0.06	−0.14	0.05	–	–	2.28
243	−0.89	0.03	–	–	–	–	–	–	2.35
244	−2.21	0.05	–	–	–	–	–	–	1.88
245	−1.16	0.03	–	–	0.16	0.05	–	–	2.43

Table A.3 – continued from previous page

Star ID	$[\mathrm{Fe/H}]_{\mathrm{HR}}$	$\sigma[\mathrm{Fe/H}]_{\mathrm{HR}}$	[Mg/Fe]	σ [Mg/Fe]	[Si/Fe]	σ [Si/Fe]	[Ti/Fe]	σ [Ti/Fe]	χ^2
248	−0.90	0.03	0.30	0.06	–	–	0.04	0.04	2.81
249	−1.11	0.03	−0.22	0.06	–	–	0.15	0.04	2.12
250	−1.53	0.04	–	–	0.13	0.07	–	–	2.83
251	−1.99	0.05	–	–	–	–	–	–	1.96
252	−2.56	0.06	–	–	–	–	–	–	1.75
253	−1.52	0.04	–	–	–	–	–	–	1.87
255	−1.94	0.05	–	–	–	–	–	–	2.62
256	−1.89	0.05	0.33	0.08	0.28	0.09	0.18	0.06	2.57
257	−0.88	0.03	–	–	–	–	0.01	0.04	2.15
258	−1.96	0.05	–	–	–	–	–	–	3.18
259	−1.05	0.03	–	–	–	–	−0.23	0.04	2.11
260	−2.53	0.06	–	–	–	–	–	–	1.57
261	−2.09	0.05	–	–	–	–	–	–	2.62
262	−2.18	0.05	–	–	0.35	0.10	–	–	2.33
263	−1.11	0.03	–	–	–	–	0.01	0.04	2.27
264	−0.99	0.03	−0.24	0.06	−0.06	0.04	0.19	0.04	2.60
265	−1.65	0.04	–	–	–	–	–	–	1.51
266	−2.25	0.06	–	–	–	–	–	–	2.48
267	–	–	–	–	–	–	–	–	–
268	−0.90	0.03	−0.20	0.06	−0.22	0.04	0.12	0.04	2.89
270	–	–	–	–	–	–	–	–	–
274	−1.12	0.03	−0.04	0.06	−0.03	0.05	0.15	0.04	2.36
275	−2.24	0.05	–	–	–	–	–	–	2.47
276	–	–	–	–	–	–	–	–	–
277	−1.31	0.04	–	–	−0.19	0.06	0.01	0.05	2.28
279	−1.10	0.03	–	–	–	–	–	–	2.60
280	−1.27	0.04	−0.17	0.06	−0.16	0.06	0.18	0.05	1.74
281	−1.98	0.05	–	–	0.02	0.09	–	–	2.32
282	−2.29	0.06	–	–	–	–	–	–	2.46
284	–	–	–	–	–	–	–	–	–
285	−0.93	0.03	–	–	−0.18	0.04	0.13	0.04	1.98
287	–	–	–	–	–	–	–	–	0.00
288	−2.39	0.06	–	–	–	–	–	–	2.17
289	−1.24	0.03	–	–	−0.14	0.05	0.22	0.04	4.36
290	−2.46	0.06	–	–	–	–	–	–	1.68
291	−1.18	0.03	–	–	–	–	–	–	1.86
294	−2.28	0.06	–	–	–	–	–	–	2.79
295	−1.77	0.05	0.31	0.08	−0.06	0.08	−0.06	0.06	2.02
297	−2.43	0.06	–	–	–	–	–	–	1.72
298	–	–	–	–	–	–	–	–	–
299	−1.14	0.03	−0.08	0.06	0.02	0.05	–	–	2.17
300	−0.96	0.03	–	–	−0.18	0.04	–	–	1.88
301	−2.45	0.06	–	–	–	–	–	–	2.97
302	–	–	–	–	–	–	–	–	0.00
303	−1.34	0.04	–	–	–	–	–	–	2.17
304	−1.34	0.04	−0.18	0.06	0.03	0.06	–	–	1.13
311	−0.97	0.03	–	–	–	–	–	–	1.61
312	−2.57	0.06	–	–	–	–	–	–	2.92
313	−0.93	0.03	–	–	–	–	–	–	2.69
316	−1.51	0.04	0.19	0.06	−0.19	0.07	–	–	2.46
317	−2.00	0.05	–	–	0.58	0.09	–	–	1.94
318	–	–	–	–	–	–	–	–	–
319	–	–	–	–	–	–	–	–	–
320	−1.54	0.04	–	–	–	–	–	–	2.77
321	−0.94	0.03	−0.17	0.06	−0.26	0.04	−0.10	0.04	1.97
322	−1.39	0.04	–	–	0.39	0.06	0.51	0.05	2.27
323	−1.23	0.03	–	–	–	–	–	–	2.65
324	−1.77	0.05	–	–	–	–	–	–	2.06
325	−1.83	0.05	–	–	–	–	–	–	2.09
326	−1.59	0.04	–	–	–	–	–	–	1.87
328	−1.80	0.05	–	–	–	–	–	–	2.28
332	−1.25	0.04	–	–	−0.15	0.06	0.38	0.04	2.70
333	−1.61	0.04	–	–	–	–	–	–	2.14
334	−1.93	0.05	–	–	–	–	–	–	1.89
335	−1.93	0.05	–	–	–	–	–	–	2.38
336	−2.24	0.05	–	–	–	–	–	–	2.31
337	−0.99	0.03	–	–	0.05	0.04	0.69	0.04	3.49

Table A.3 – continued from previous page

Star ID	$[\mathrm{Fe/H}]_{\mathrm{HR}}$	$\sigma[\mathrm{Fe/H}]_{\mathrm{HR}}$	[Mg/Fe]	σ [Mg/Fe]	[Si/Fe]	σ [Si/Fe]	[Ti/Fe]	σ [Ti/Fe]	χ^2
339	−0.98	0.03	–	–	–	–	−0.14	0.04	2.50
340	–	–	–	–	–	–	–	–	–
341	−1.11	0.03	−0.12	0.06	−0.12	0.05	0.20	0.04	1.87
342	−2.23	0.05	–	–	–	–	–	–	1.86
343	−1.07	0.03	−0.26	0.06	−0.27	0.04	0.05	0.04	2.28
344	−1.26	0.04	–	–	–	–	–	–	1.89
345	−1.34	0.04	–	–	–	–	0.30	0.05	2.38
347	−1.27	0.04	–	–	–	–	0.02	0.05	1.98
348	−1.32	0.04	–	–	−0.12	0.06	–	–	2.32
349	−2.57	0.06	–	–	0.48	0.13	–	–	1.78
350	−0.96	0.03	–	–	−0.15	0.04	−0.17	0.04	2.52
351	−1.64	0.04	–	–	–	–	–	–	1.74
352	−1.44	0.04	–	–	0.37	0.07	0.23	0.05	2.27
353	−1.92	0.05	–	–	–	–	–	–	1.49
354	–	–	–	–	–	–	–	–	–
355	−1.10	0.03	0.17	0.06	–	–	−0.18	0.04	1.80
356	−2.26	0.06	–	–	–	–	–	–	1.97
357	−1.15	0.03	–	–	–	–	–	–	2.50
358	−1.02	0.03	–	–	–	–	–	–	2.10
359	−0.85	0.03	–	–	–	–	–	–	2.33
360	−0.86	0.03	−0.04	0.06	−0.13	0.04	−0.12	0.04	2.42
361	−0.92	0.03	–	–	−0.21	0.04	–	–	1.89
362	−0.75	0.03	−0.14	0.06	−0.24	0.04	0.05	0.04	2.08
363	−2.60	0.06	–	–	0.37	0.13	–	–	1.97
364	−1.50	0.04	0.04	0.06	0.06	0.07	0.35	0.05	1.96
365	−1.40	0.04	–	–	–	–	–	–	2.14
367	−1.07	0.03	–	–	−0.17	0.04	0.10	0.04	2.21
368	−0.89	0.03	0.08	0.06	–	–	−0.19	0.04	2.39
369	−2.25	0.06	–	–	–	–	–	–	1.88
371	−1.24	0.03	–	–	−0.07	0.05	−0.01	0.04	2.14
372	−0.77	0.03	–	–	–	–	−0.02	0.04	2.08
374	−1.32	0.04	–	–	–	–	–	–	1.87
375	−2.00	0.05	–	–	–	–	–	–	4.57
377	−2.23	0.05	–	–	–	–	–	–	1.53
378	−2.09	0.05	–	–	–	–	–	–	2.16
379	–	–	–	–	–	–	–	–	–
380	−0.97	0.03	−0.17	0.06	−0.26	0.04	−0.17	0.04	2.10
381	−0.73	0.03	–	–	–	–	−0.21	0.03	2.76
382	−1.55	0.04	–	–	–	–	–	–	2.57
385	−1.66	0.04	–	–	–	–	–	–	2.08
386	–	–	–	–	–	–	–	–	–
387	–	–	–	–	–	–	–	–	–
388	−1.03	0.03	–	–	–	–	−0.13	0.04	1.96
389	−0.88	0.03	−0.19	0.06	−0.20	0.04	–	–	1.72
390	−1.69	0.04	–	–	–	–	–	–	1.99
391	−0.75	0.03	−0.12	0.06	−0.12	0.04	−0.11	0.04	2.06
392	−1.44	0.04	0.06	0.06	0.30	0.07	−0.24	0.05	2.92
393	−1.24	0.03	0.08	0.06	0.06	0.05	0.02	0.04	2.70
394	−2.00	0.05	0.25	0.09	–	–	–	–	1.84
395	–	–	–	–	–	–	–	–	–
396	−0.92	0.03	–	–	–	–	–	–	1.85
397	−1.72	0.04	–	–	−0.20	0.08	0.27	0.05	2.16
398	−1.12	0.03	−0.07	0.06	–	–	–	–	2.04
399	−1.04	0.03	–	–	0.05	0.04	−0.23	0.04	2.27
400	−2.19	0.05	–	–	–	–	–	–	2.55
401	−1.69	0.04	0.06	0.07	–	–	–	–	2.19
402	−1.19	0.03	−0.20	0.06	−0.28	0.05	0.08	0.04	1.93
406	−2.43	0.06	–	–	–	–	–	–	2.08
407	−1.55	0.04	−0.08	0.06	−0.28	0.07	−0.15	0.05	2.07
408	−1.41	0.04	–	–	0.22	0.06	−0.11	0.05	1.89
409	0.41	0.03	–	–	–	–	–	–	2.92
411	−1.41	0.04	−0.07	0.06	−0.09	0.06	0.08	0.05	2.50
412	−1.76	0.05	–	–	–	–	–	–	1.97
413	−1.05	0.03	−0.14	0.06	−0.13	0.04	−0.13	0.04	2.52
414	−1.18	0.03	–	–	–	–	–	–	2.44
415	−2.48	0.06	–	–	–	–	–	–	1.81
416	−1.22	0.03	0.12	0.06	−0.01	0.05	–	–	1.98

Table A.3 – continued from previous page

Star ID	$[\mathrm{Fe/H}]_{\mathrm{HR}}$	$\sigma[\mathrm{Fe/H}]_{\mathrm{HR}}$	[Mg/Fe]	σ [Mg/Fe]	[Si/Fe]	σ [Si/Fe]	[Ti/Fe]	σ [Ti/Fe]	χ^2
417	–	–	–	–	–	–	–	–	–
418	−1.16	0.03	–	–	−0.08	0.05	0.05	0.04	1.98
419	−1.77	0.05	–	–	–	–	–	–	2.23
420	−2.77	0.06	–	–	–	–	–	–	1.83
422	–	–	–	–	–	–	–	–	–
424	−2.29	0.06	–	–	–	–	–	–	2.00
425	–	–	–	–	–	–	–	–	–
428	−1.12	0.03	−0.19	0.06	–	–	−0.03	0.04	2.08
430	−1.04	0.03	–	–	–	–	–	–	2.48
431	−1.13	0.03	–	–	–	–	–	–	2.10

B

Magellan M2FS Observations of H4 and close-by Field Stars (presented in Chapter 4).

Table B.1: Basic parameters – positions, photometry, quality of the spectra. The star with ID r_0010 is the target with 99.2% H4 membership probability. “Group” indicates whether the star has been selected within the tidal radius of H4 (A), or whether it is a field star from the central part of Fornax (B). For stars of category A, the separation index m_{sep} is an indicator for the flux contamination of a spectrum, as described in Section 4.2.2 of the main article. The S/N is per pixel of the degraded spectra as they are supplied to SP_ACE. The effective wavelength range $\Delta\lambda_{eff}$ gives the final wavelength range which is used in the chemical analysis after critical regions flagged in various pixel masks have been removed. The star with ID r_0010 is the target with 99.2% H4 membership probability.

ID	α	δ	Group	V	σV	$V-I$	$\sigma(V-I)$	m_{sep}	S/N	$\Delta\lambda_{eff}$[Å]
r_0006	2h40m10.15s	−34d31m48.83s	A	18.892	0.007	1.260	0.009	10.01	23.8	301.6
r_0007	2h40m9.19s	−34d32m59.89s	A	19.540	0.010	1.116	0.013	6.87	15.9	393.9
r_0008	2h40m5.51s	−34d32m42.86s	A	18.326	0.005	1.586	0.006	8.16	40.2	439.2
r_0009	2h40m8.84s	−34d32m47.83s	A	19.249	0.008	1.196	0.011	6.82	18.0	214.2
r_0010	2h40m7.69s	−34d32m0.92s	A	18.805	0.007	1.231	0.009	5.95	33.7	345.7
r_0011	2h40m8.30s	−34d32m37.28s	A	18.818	0.007	1.327	0.009	8.49	27.4	450.6
r_0014	2h39m41.20s	−34d34m50.09s	B	18.242	–	1.260	–	–	33.4	434.7
r_0016	2h40m6.63s	−34d32m25.80s	A	20.068	0.004	1.041	0.005	4.70	13.8	175.3
r_0017	2h40m7.22s	−34d31m44.94s	A	19.488	0.003	1.174	0.004	4.75	17.3	304.7
r_0018	2h40m7.07s	−34d31m25.79s	A	19.196	0.008	1.142	0.011	4.73	19.4	379.4
r_0019	2h39m31.50s	−34d46m45.12s	B	18.082	–	1.020	–	–	34.4	423.2
r_0020	2h39m4.80s	−34d41m31.49s	B	18.422	–	1.230	–	–	43.8	463.3
r_0021	2h39m12.29s	−34d44m38.54s	B	17.912	–	1.240	–	–	39.5	478.8
r_0022	2h40m4.01s	−34d32m13.60s	A	19.312	0.009	1.144	0.012	8.84	21.3	378.0
r_0024	2h40m4.46s	−34d31m38.64s	A	19.532	0.010	1.161	0.013	5.62	18.5	360.6
b_0001	2h39m11.42s	−34d29m22.27s	B	18.012	–	1.320	–	–	16.6	277.0
b_0003	2h39m39.90s	−34d43m7.21s	B	18.362	–	1.110	–	–	51.1	375.9
b_0005	2h39m36.30s	−34d51m25.99s	B	18.062	–	1.710	–	–	19.5	379.4
b_0007	2h40m5.97s	−34d32m0.89s	A	18.367	0.006	1.397	0.007	7.56	38.1	403.0
b_0008	2h40m6.09s	−34d31m38.28s	A	18.883	0.007	1.236	0.009	4.22	20.3	311.7
b_0009	2h39m55.38s	−34d45m56.05s	B	18.282	–	1.480	–	–	26.9	355.3
b_0010	2h39m53.79s	−34d38m55.50s	B	18.322	–	1.160	–	–	29.4	175.3
b_0011	2h39m52.62s	−34d45m44.60s	B	17.982	–	1.290	–	–	55.5	426.4
b_0015	2h40m5.09s	−34d35m41.75s	B	18.332	–	1.160	–	–	51.6	281.2
b_0016	2h40m2.73s	−34d38m30.05s	B	18.162	–	1.260	–	–	33.8	352.0
b_0017	2h39m57.10s	−34d49m7.03s	B	18.412	–	1.080	–	–	27.8	372.3
b_0018	2h40m10.92s	−34d32m4.31s	A	19.913	0.004	1.053	0.005	6.50	11.1	277.7
b_0019	2h40m11.20s	−34d31m46.78s	A	19.627	0.010	1.143	0.013	7.20	11.1	236.1
b_0020	2h40m21.48s	−34d25m57.43s	B	18.402	–	1.320	–	–	13.2	175.0
b_0023	2h40m30.22s	−34d38m53.81s	B	18.142	–	1.210	–	–	37.1	447.7

Table B.2: Chemical abundances – [Fe/H], alpha-elements. The star with ID r_0010 is the target with 99.2% H4 membership probability.

ID	v	σv	[Fe/H]	[Fe/H]$_+$	[Fe/H]$_-$	[Ca/H]	[Ca/H]$_+$	[Ca/H]$_-$	[Ti/H]	[Ti/H]$_+$	[Ti/H]$_-$
r_0006	53.26	0.50	−1.71	−1.83	−1.56	–	–	–	–	–	–
r_0007	70.38	0.61	−1.16	−1.26	−1.11	−1.15	−1.26	−1.02	−0.73	−0.87	−0.53
r_0008	72.10	0.20	−0.62	−0.72	−0.54	−0.84	−0.99	−0.66	−1.01	−1.10	−0.77
r_0009	58.10	0.40	−0.84	−1.04	−0.78	−0.46	−0.65	−0.22	−1.06	–	−0.78
r_0010	48.16	0.36	−1.50	−1.54	−1.45	−1.44	−1.53	−1.37	−1.77	–	−1.54
r_0011	49.89	0.28	−0.78	−0.89	−0.77	−0.97	−1.03	−0.88	−0.98	−1.02	−0.88
r_0014	48.94	0.25	−1.13	−1.18	−1.11	−1.46	−1.51	−1.38	−1.38	−1.49	−1.32
r_0016	46.56	0.82	−1.68	−1.95	−1.55	–	–	–	–	–	–
r_0017	47.17	2.12	−0.46	−0.54	−0.19	−0.63	−0.84	−0.47	–	–	–
r_0018	72.78	1.83	−2.30	–	−2.25	−1.92	−2.15	−1.67	–	–	–
r_0019	64.60	0.34	−1.34	−1.61	−1.29	−1.34	−1.67	−1.15	−1.59	–	−1.21
r_0020	58.98	1.44	−1.58	−1.65	−1.55	−1.49	−1.57	−1.43	−1.60	−1.76	−1.51
r_0021	65.38	0.27	−1.74	−1.81	−1.72	−1.71	−1.79	−1.64	−1.70	−1.85	−1.64
r_0022	55.72	0.28	−0.84	−0.99	−0.82	−1.07	−1.16	−0.95	−0.96	−1.12	−0.79
r_0024	61.77	0.50	−0.58	−0.70	−0.55	−0.87	−1.02	−0.72	−1.20	–	−1.01
b_0001	74.85	1.07	−1.40	−1.50	−1.30	−1.94	−2.05	−1.69	−1.61	−1.81	−1.26
b_0003	67.45	0.48	−2.36	−2.72	−2.28	−2.19	−2.61	−1.96	−1.77	–	–
b_0005	39.52	0.48	−0.82	–	–	–	–	–	–	–	–
b_0007	50.57	0.19	−1.02	−1.11	−0.99	−1.09	−1.18	−0.94	−1.49	−1.61	−1.31
b_0008	45.67	0.44	−0.57	−0.72	−0.55	−0.77	−0.85	−0.65	–	–	–
b_0009	51.13	0.33	−1.34	–	–	–	–	–	−1.06	–	–
b_0010	44.28	0.56	−2.00	−2.19	−1.88	−1.86	−2.11	−1.49	−2.18	–	−1.68
b_0011	47.57	0.22	−2.06	−2.08	−1.91	−2.31	−2.38	−2.17	−1.98	−2.18	−1.79
b_0015	45.82	0.26	−1.87	−1.96	−1.86	−1.71	−1.77	−1.68	−1.62	−1.70	−1.55
b_0016	69.05	0.24	−1.65	−1.72	−1.63	−1.60	−1.71	−1.56	−1.64	−1.73	−1.49
b_0017	70.52	0.63	−1.98	−2.36	−1.81	−1.97	–	−1.76	–	–	–
b_0018	47.18	0.77	−1.46	–	−0.90	–	–	–	–	–	–
b_0019	60.68	1.16	−0.21	−0.37	–	−1.20	–	−0.20	−0.88	–	−0.36
b_0020	67.04	0.66	−1.65	−2.01	−1.57	−1.84	–	−1.57	–	–	–
b_0023	57.07	0.15	−0.33	−0.42	−0.22	−0.09	−0.34	0.08	−0.10	−0.37	−0.01

Table B.3: Chemical abundances – iron-peak elements. The star with ID r_0010 is the target with 99.2% H4 membership probability.

ID	[V/Fe]	[V/Fe]$_+$	[V/Fe]$_-$	[Cr/Fe]	[Cr/Fe]$_+$	[Cr/Fe]$_-$	[Co/Fe]	[Co/Fe]$_+$	[Co/Fe]$_-$	[Ni/Fe]	[Ni/Fe]$_+$	[Ni/Fe]$_-$
r_0006	−1.54	−2.00	−1.33	−1.56	–	−1.04	−1.09	−1.33	–	−1.79	–	−1.33
r_0007	−0.91	−1.01	−0.70	–	–	–	−0.94	−1.10	−0.73	−1.26	−1.36	−1.11
r_0008	−0.92	−1.00	−0.68	−0.95	−1.16	−0.61	−0.96	−1.10	−0.73	−1.00	−1.19	−0.83
r_0009	−0.25	−0.58	–	−0.50	−0.78	−0.14	−1.06	–	−0.82	−0.55	−0.86	−0.36
r_0010	−1.65	−1.73	−1.49	−1.47	−1.64	−1.25	−1.83	−1.95	−1.70	−1.59	−1.67	−1.49
r_0011	−1.12	−1.16	−0.99	−0.81	−0.92	−0.70	−1.04	−1.13	−0.94	−1.16	−1.26	−1.11
r_0014	−1.41	−1.49	−1.32	−1.64	–	−1.47	−1.21	−1.29	−1.13	−1.22	−1.29	−1.17
r_0016	–	–	–	–	–	–	−1.21	−1.68	−0.89	−1.44	−1.84	−1.11
r_0017	−0.76	–	−0.58	−0.62	–	−0.31	−0.53	−0.77	−0.27	−0.75	−0.91	−0.54
r_0018	–	–	–	–	–	–	−1.65	−2.48	–	−2.30	–	−2.01
r_0019	−1.91	–	−1.38	–	–	–	−1.82	–	−1.25	−1.69	–	−1.43
r_0020	−2.15	–	−2.05	−1.58	−1.83	−1.28	−2.01	–	−1.85	−1.84	−1.97	−1.76
r_0021	−2.03	−2.18	−1.96	−2.31	–	−1.97	−1.95	−2.14	−1.81	−2.15	−2.31	−2.07
r_0022	−1.11	−1.17	−0.85	−0.97	−1.21	−0.68	−0.96	−1.11	−0.79	−1.10	−1.21	−1.00
r_0024	−0.86	−0.97	−0.64	−0.63	−0.90	−0.35	−0.79	−1.11	−0.54	−1.00	−1.15	−0.91
b_0001	−1.99	−2.11	−1.66	–	–	–	−1.62	−1.93	−1.30	–	–	–
b_0003	−2.23	–	–	–	–	–	−2.80	–	−1.77	−2.85	–	−2.45
b_0005	−0.92	–	–	−1.12	–	–	–	–	–	−1.03	–	–
b_0007	−1.55	−1.62	−1.34	−1.51	−1.70	−1.25	−1.21	−1.38	−1.08	−1.35	−1.49	−1.26
b_0008	−0.91	−1.00	−0.69	−0.92	−1.16	−0.67	−0.96	−1.09	−0.83	−0.91	−1.06	−0.83
b_0009	−1.04	–	–	−1.37	–	–	−1.34	–	–	–	–	–
b_0010	–	–	–	–	–	–	−1.49	−1.97	–	−2.16	–	−1.84
b_0011	−2.65	–	−2.37	–	–	–	–	–	–	−2.58	–	−2.41
b_0015	–	–	–	–	–	–	−2.20	–	−2.07	−1.70	−1.77	−1.65
b_0016	−1.83	−2.00	−1.78	–	–	–	−1.99	–	−1.91	−1.68	−1.81	−1.62
b_0017	–	–	–	–	–	–	−1.76	–	–	−2.16	–	–
b_0018	–	–	–	–	–	–	–	–	–	–	–	–
b_0019	–	–	–	–	–	–	–	–	–	−0.99	–	−0.51
b_0020	–	–	–	–	–	–	–	–	–	–	–	–
b_0023	0.11	−0.19	0.20	−0.20	−0.58	0.01	−0.35	−0.62	−0.13	−0.56	–	−0.34